

THE NATURE OF DUST-OBSCURED GALAXIES AT $Z \sim 2$

by

Robert Shane Bussmann

A Dissertation Submitted to the Faculty of the

DEPARTMENT OF ASTRONOMY

In Partial Fulfillment of the Requirements
For the Degree of

DOCTOR OF PHILOSOPHY

In the Graduate College

THE UNIVERSITY OF ARIZONA

2 0 1 0

THE UNIVERSITY OF ARIZONA
GRADUATE COLLEGE

As members of the Dissertation Committee, we certify that we have read the dissertation prepared by Robert Shane Bussmann entitled The Nature of Dust-Obscured Galaxies at $z \sim 2$ and recommend that it be accepted as fulfilling the dissertation requirement for the Degree of Doctor of Philosophy.

_____ Date: 3 September 2010
Christopher K. Walker

_____ Date: 3 September 2010
Arjun Dey

_____ Date: 3 September 2010
Baruch Thomas Soifer

_____ Date: 3 September 2010
Romeel A. Davé

_____ Date: 3 September 2010
Yancy L. Shirley

Final approval and acceptance of this dissertation is contingent upon the candidate's submission of the final copies of the dissertation to the Graduate College.

I hereby certify that I have read this dissertation prepared under my direction and recommend that it be accepted as fulfilling the dissertation requirement.

_____ Date: 3 September 2010
Dissertation Director: Christopher K. Walker

_____ Date: 3 September 2010
Dissertation Director: Arjun Dey

STATEMENT BY AUTHOR

This dissertation has been submitted in partial fulfillment of requirements for an advanced degree at The University of Arizona and is deposited in the University Library to be made available to borrowers under rules of the Library.

Brief quotations from this dissertation are allowable without special permission, provided that accurate acknowledgment of source is made. Requests for permission for extended quotation from or reproduction of this manuscript in whole or in part may be granted by the head of the major department or the Dean of the Graduate College when in his or her judgment the proposed use of the material is in the interests of scholarship. In all other instances, however, permission must be obtained from the author.

SIGNED: Robert Shane Bussmann

ACKNOWLEDGMENTS

This is the section where I acknowledge the help from all those who have supported me over the past six-plus years. For a brief time, I had actually considered saying only “Thanks to everyone” and leaving it at that. That way I could be sure that I wouldn’t forget anyone by naming people in particular. But you know what? That would be really really weak. So here goes. If I forget anyone, sorry. I didn’t mean to.

Let me start by thanking my thesis advisor, Arjun Dey. I remember talking to Arjun four years ago to see if he had any projects we could work on together. He mentioned some *HST* data on some “dusty galaxies” (we hadn’t come up with the DOG nickname at that point yet) he wanted to study. As we ended that meeting, he summarized the project by saying “this will be fun!”. I think that captures the spirit of working with Arjun in a nutshell. Work hard, but make sure you are having fun doing it. That is the philosophy I hope to keep with me throughout my academic career.

Next up is my first advisor in graduate school, Chris Walker. Under Chris’ guidance, I gained a variety of skills. This included lab skills like soldering and building/testing electronics boxes as well as scientific research into the nature of protostellar outflows. Chris treated me like an old friend the moment I first stepped into his office and helped make the transition to graduate school a smooth one for me. My long-term interests in sub-millimeter astronomy are surely a result of the good times I enjoyed as his student my first three years in graduate school.

I want to thank Yancy Shirley, who has been both a colleague and a mentor to me during most of my time in graduate school. Yancy has always been there for me when I need someone to talk to or to help solve any other problems (e.g. with my thesis committee!). We worked together on a side project between my second year project with Chris and my thesis work with Arjun. Although that research does not appear in my thesis, I hope in the future to tie the two paths of research into one.

I would be remiss if I did not thank Kyle Dawson, assistant professor at the University of Utah Department of Physics & Astronomy. Kyle is a friend of mine from our days at UC Berkeley — we both worked for the same professor in the physics department, he as a grad student and me as an undergrad. He helped me obtain an office at the University of Utah from which to finish writing my thesis. I owe him a tremendous debt of gratitude for this.

I have benefited greatly from the help of a number of collaborators over the years. Among these are Tom Soifer, Buell Januzzi, Vandana Desai, Jason Melbourne, Jen Lotz, and Alex Pope.

It is very important to me that I thank Michelle Cournoyer. She has been the point person for virtually every administrative hurdle that I have had to clear. She does her job extremely well and in so doing has made my life much much easier. Along similar lines, I want to thank all the administrative and support staff at

Steward that have provided so much help for me over the past six years.

We transition now to friends!

First off, I must thank the original Dogg himself, Cordozar Calvin Broadus.

My fellow classmates Suresh, Aleks, Wayne, and Jon, thank you. In some ways it seems like yesterday that we were all fresh out of college and eager to start something new. But then I see the new class of first year students and I realize it's been over six years and it's time to move on.

To those in the years above and below me, thanks for your support too. I especially want to thank Eric Nielsen for over a decade of inane conversations (yes, going back to undergrad), Moire and Kristian for unquestioning support, Desika and Brandon for making me laugh, Amy for keeping it real, Steph & Steph and Steph & Jared for being kind, good-hearted people and Kevin for making so much noise.

Finally, let me thank the No Anchovies We Hate Astronomy But Love Beer club. Although I was never officially a mug-toting member, I have fond memories of Nimbus pints for cheap. Aleks, Maggie, & Will, Jon, Desika & Marie, Brandon Kelly, Iva, Ben O., The three Stephs and Jared, Kevin, Brandon Swift, Andy & Linda, THANKS!

From No Anchovies to Anime night to softball to poker to basketball to racquetball (and nailing Aleks and John Moustakas in the back with wayward passing shots!) to Ultimate frisbee to biking along Speedway wearing strange hats, I've had plenty of fun extra-curricular activities in grad school. Thanks to all my friends who participated in those.

Last but certainly not least, the family!

To Sirius, a shining example of a DOG in the local universe!

To my big sister Jeffra who has always supported and encouraged me to keep going in astronomy. Sometimes I think she's more interested in my research than I am!

To Mom and Dad, words simply cannot express how grateful I am for your support and love over the 29 years I have been alive. Not only have you always been there for me, but you have taught me the greatest lesson of all: have respect for everyone and be a good person. Being a good scientist isn't worth a hill of a beans if you aren't a good person too. Thanks to both of you — I love you so much.

Finally, to Tiffany, my love. You have always been there for me, always supported me. But more than that, you have inspired me to do so much more in life than what I ever thought was possible. This goes far beyond academics. I have had a full and enriching life and it is thanks to you. So thank you, Tiffany.

DEDICATION

I wish to dedicate this thesis to my family. To Grandpa Frank and Grandma Kay, to Grandma Eleda and Grandpa Keith, to my aunts and uncles and cousins, to Tiffany and Jayme and Jay and Mary, to Jeffra, and to Mom and Dad. This is the culmination of over six years of effort, and I dedicate it to all of you.

TABLE OF CONTENTS

| | |
|---|-----|
| LIST OF FIGURES | 10 |
| LIST OF TABLES | 12 |
| ABSTRACT | 14 |
| CHAPTER 1 INTRODUCTION | 16 |
| 1.1 Models for the Formation of Galaxies in the Universe | 16 |
| 1.2 Finding Massive Galaxies in the Process of Formation | 17 |
| 1.3 The Nature of Dust-Obscured Galaxies | 19 |
| CHAPTER 2 MORPHOLOGIES OF POWER-LAW DOMINATED DOGs | 22 |
| 2.1 Introduction | 22 |
| 2.2 Data | 26 |
| 2.2.1 Sample Selection | 26 |
| 2.2.2 Observations | 30 |
| 2.2.3 Astrometry | 33 |
| 2.2.4 Photometry | 33 |
| 2.2.5 Images of DOGs | 34 |
| 2.3 Methodology: Morphological Analysis | 42 |
| 2.3.1 Visual Classification | 42 |
| 2.3.2 GALFIT Modeling | 43 |
| 2.3.3 Non-parametric Classification | 46 |
| 2.4 Results | 50 |
| 2.4.1 Photometry | 50 |
| 2.4.2 Morphologies | 50 |
| 2.5 Discussion | 63 |
| 2.5.1 Dust and Stellar Mass Estimates | 63 |
| 2.5.2 Comparison to other high redshift galaxy populations | 70 |
| 2.5.3 Implications for the Evolution of the Most Massive Galaxies | 77 |
| 2.6 Conclusions | 78 |
| CHAPTER 3 MORPHOLOGIES OF BUMP-DOMINATED DOGs | 81 |
| 3.1 Introduction | 82 |
| 3.2 Data | 86 |
| 3.2.1 Bump DOGs | 87 |
| 3.2.2 Power-law DOGs | 93 |
| 3.2.3 SMG Data | 94 |
| 3.2.4 XFLS Data | 95 |
| 3.3 Images | 95 |
| 3.4 Methodology | 101 |

TABLE OF CONTENTS — *Continued*

| | | |
|---|---|-----|
| 3.4.1 | Photometry | 101 |
| 3.4.2 | Morphology | 103 |
| 3.5 | Results | 110 |
| 3.5.1 | Photometry | 110 |
| 3.5.2 | Morphologies | 111 |
| 3.6 | Discussion: Implications for Models of Massive Galaxy Evolution . . | 123 |
| 3.7 | Conclusions | 128 |
| CHAPTER 4 DOGS ARE WARM-DUST DOMINATED ULIRGS AT $z \sim 2$. | | 131 |
| 4.1 | Introduction | 132 |
| 4.2 | Observations | 134 |
| 4.2.1 | Sample Selection | 134 |
| 4.2.2 | SHARC-II 350 μ m Imaging and Photometry | 135 |
| 4.2.3 | CARMA 1mm Imaging and Photometry | 139 |
| 4.2.4 | Optical, near-IR, mid-IR, and far-IR Photometry | 140 |
| 4.3 | Results | 142 |
| 4.3.1 | Qualitative SED Comparison | 142 |
| 4.3.2 | IR Luminosities | 149 |
| 4.3.3 | Constraints on Dust Properties | 152 |
| 4.3.4 | Dust Masses | 154 |
| 4.3.5 | Stellar Masses | 157 |
| 4.4 | Discussion | 162 |
| 4.4.1 | Related $z \approx 2$ Galaxy Populations | 162 |
| 4.4.2 | Comparison of Measured Properties | 164 |
| 4.4.3 | Implications for Models of Galaxy Evolution | 167 |
| 4.5 | Conclusions | 169 |
| CHAPTER 5 THE STELLAR MASSES AND STAR-FORMATION HISTORIES OF DOGS AT $z \sim 2$ | | 172 |
| 5.1 | Introduction | 173 |
| 5.2 | Data | 179 |
| 5.2.1 | DOGS | 179 |
| 5.2.2 | SMGs | 193 |
| 5.3 | Stellar Population Synthesis Models | 194 |
| 5.3.1 | General Methodology | 194 |
| 5.3.2 | Initial Mass Functions | 196 |
| 5.3.3 | SPS Star-formation Histories | 198 |
| 5.4 | Results | 199 |
| 5.4.1 | SEDs | 199 |
| 5.4.2 | Stellar Population Synthesis | 201 |

TABLE OF CONTENTS — *Continued*

| | | |
|------------|---|-----|
| 5.5 | Discussion | 210 |
| 5.5.1 | Comparing Stellar Mass Estimates | 211 |
| 5.5.2 | Improving Estimates of Stellar Population Age | 212 |
| 5.5.3 | Implications for Galaxy Evolution at $z \sim 2$ | 213 |
| 5.6 | Conclusions | 215 |
| CHAPTER 6 | CONCLUSION | 221 |
| 6.1 | Summary of the Nature of DOGs | 221 |
| 6.2 | Possible Paths Forward in the Future | 222 |
| APPENDIX A | SMG AND XFLS ULIRG NON-PARAMETRIC MORPHOLOGIES | 225 |
| APPENDIX B | TESTS OF FOUR SPS LIBRARIES | 230 |
| REFERENCES | | 233 |

LIST OF FIGURES

| | | |
|-----|--|-----|
| 2.1 | $R - 24$ color vs. $24\mu\text{m}$ magnitude distribution for DOGs in the ND-WFS Boötes field | 28 |
| 2.2 | Distribution of spectroscopic redshifts for DOGs in the Boötes Field . | 29 |
| 2.3 | Cutouts of the 31 DOGs observed by <i>HST</i> | 36 |
| 2.3 | Continued. | 37 |
| 2.3 | Continued. | 38 |
| 2.3 | Continued. | 39 |
| 2.4 | Optical and near-IR color-magnitude diagram for DOGs. | 52 |
| 2.5 | Distributions of effective radii for DOGs | 56 |
| 2.6 | Color-magnitude diagram for extended and unresolved components of DOGs | 59 |
| 2.7 | Gini coefficient vs. M_{20} for DOGs | 61 |
| 2.8 | Expected A_V vs. redshift for DOGs | 65 |
| 2.9 | Stellar masses of DOGs | 67 |
| 3.1 | $R - 24$ color vs. $24\mu\text{m}$ magnitude distribution for DOGs in the ND-WFS Boötes field | 90 |
| 3.2 | Spectroscopic redshift distribution of DOGs | 91 |
| 3.3 | Cutouts of the 22 DOGs observed by <i>HST</i> | 97 |
| 3.3 | Continued. | 98 |
| 3.3 | Continued. | 99 |
| 3.4 | Optical near-IR color-magnitude diagram for bump DOGs, power-law DOGs, SMGs, and XFLS ULIRGs at $z > 1.4$ | 112 |
| 3.5 | C as a function of r_p for $z > 1.4$ ULIRGs | 116 |
| 3.6 | Gini coefficient vs. M_{20} for $z > 1.4$ ULIRGs | 118 |
| 3.7 | Comparison of sizes of $z > 1.4$ ULIRGs | 122 |
| 3.8 | Sérsic index n as a function of point source fraction from GALFIT modeling | 124 |
| 4.1 | $R - 24$ color vs. $24\mu\text{m}$ magnitude for DOGs in the NDWFS Boötes field | 136 |
| 4.2 | SEDs of 5 DOGs detected by SHARC-II at $350\mu\text{m}$ | 143 |
| 4.3 | SEDs of 7 DOGs not detected by SHARC-II at $350\mu\text{m}$ | 144 |
| 4.4 | Optical through sub-mm SEDs of DOGs in the SHARC-II sample . . | 147 |
| 4.5 | $350\mu\text{m}/24\mu\text{m}$ and $1200\mu\text{m}/24\mu\text{m}$ flux density ratios as a function of $R - 24$ color | 150 |
| 4.6 | Constraints on dust properties of DOGs | 155 |
| 4.7 | Constraints on stellar masses of DOGs | 160 |

LIST OF FIGURES — *Continued*

| | | |
|------|--|-----|
| 5.1 | Cartoon picture illustrating the two star-formation histories examined in this paper | 176 |
| 5.2 | $R - 24$ color vs. $24\mu\text{m}$ magnitude distribution for DOGs in the ND-WFS Boötes field | 181 |
| 5.3 | Spectroscopic redshift distribution of DOGs in the Boötes Field . . . | 182 |
| 5.4 | Star-formation histories used in stellar population synthesis models . | 200 |
| 5.5 | Rest-frame UV through near-IR SEDs of the median power-law DOG, bump DOG, and SMG | 202 |
| 5.6 | Cumulative distribution function for the stellar masses of power-law DOGs, bump DOGs, and SMGs derived using using the CB07 library, a Chabrier IMF, and a simple stellar population | 204 |
| 5.7 | Similar to previous figure, but assuming a major merger SFH and a Salpeter IMF | 206 |
| 5.8 | Similar to previous figure, but assuming a smooth accretion SFH . . . | 209 |
| 5.9 | Stellar mass assembly history for a major merger SFH | 216 |
| 5.10 | Stellar mass assembly history for a smooth accretion dominated SFH | 217 |

LIST OF TABLES

| | | |
|-----|--|-----|
| 2.1 | Observations | 31 |
| 2.2 | Non-parametric Morphological Classifications | 49 |
| 2.2 | Non-parametric Morphological Classifications | 50 |
| 2.3 | Photometric Properties ^b | 51 |
| 2.4 | GALFIT Results | 54 |
| 2.4 | GALFIT Results | 55 |
| 2.5 | PSF Subtraction Analysis | 58 |
| 2.6 | DOG Mass Estimates | 69 |
| 2.6 | DOG Mass Estimates | 70 |
| 3.1 | Observations | 88 |
| 3.2 | Photometric Properties | 102 |
| 3.2 | Photometric Properties | 103 |
| 3.3 | NICMOS GALFIT Results ^a | 109 |
| 3.3 | NICMOS GALFIT Results ^a | 110 |
| 3.4 | Visual Morphological Classifications | 113 |
| 3.5 | NICMOS Non-parametric Morphological Classifications | 114 |
| 3.5 | NICMOS Non-parametric Morphological Classifications | 115 |
| 3.6 | NICMOS Morphology Contingency Table Data | 119 |
| 4.1 | SHARC-II 350 μ m Observations | 137 |
| 4.2 | CARMA 1mm Observations | 137 |
| 4.3 | Photometry ^a | 141 |
| 4.4 | Luminosities | 151 |
| 4.5 | Dust Masses and Stellar Properties | 156 |
| 4.6 | Average High- z Galaxy Properties | 165 |
| 5.1 | Basic DOG Spectroscopic Sample Properties | 183 |
| 5.1 | Basic DOG Spectroscopic Sample Properties | 184 |
| 5.1 | Basic DOG Spectroscopic Sample Properties | 185 |
| 5.1 | Basic DOG Spectroscopic Sample Properties | 186 |
| 5.2 | NDWFS and NEWFIRM Photometry of DOGs ^a | 188 |
| 5.2 | NDWFS and NEWFIRM Photometry of DOGs ^a | 189 |
| 5.2 | NDWFS and NEWFIRM Photometry of DOGs ^a | 190 |
| 5.3 | SDWFS and MIPS24 Photometry of DOGs ^a | 191 |
| 5.3 | SDWFS and MIPS24 Photometry of DOGs ^a | 192 |
| 5.3 | SDWFS and MIPS24 Photometry of DOGs ^a | 193 |
| 5.4 | Best-fit χ^2_ν , M_* , and associated uncertainty for PL DOGs, bump DOGs, and SMGs using the CB07 library. | 208 |

| | | |
|-----|---|-----|
| A.1 | SMG NICMOS Morphological Classifications | 227 |
| A.2 | XFLS NICMOS Morphological Classifications | 228 |
| A.2 | XFLS NICMOS Morphological Classifications | 229 |

ABSTRACT

I use observational evidence to examine the nature and role in galaxy evolution of a population of dust-obscured galaxies (DOGs) at $z \sim 2$. These objects are selected with the *Spitzer Space Telescope*, are bright in the mid-infrared (mid-IR) but faint in the optical, and contribute a significant fraction of the luminosity density in the universe at $z \sim 2$.

The first component of my thesis is a morphological study using high spatial resolution imaging with the *Hubble Space Telescope* of two samples of DOGs. One set of 33 DOGs have mid-IR spectral features typical of an obscured active galactic nucleus (AGN) (called power-law DOGs), while the other set of 20 DOGs have a local maximum in their spectral energy distribution (SED) at rest-frame $1.6\mu\text{m}$ associated with stellar emission (called bump DOGs). The host galaxy dominates the light profile in all but two of these DOGs. In addition, bump DOGs are larger than power-law DOGs and exhibit more diffuse and irregular morphologies; these trends are consistent with expectations from simulations of major mergers in which bump DOGs evolve into power-law DOGs.

The second component of my thesis is a study of the dust properties of DOGs, using sub-mm imaging of 12 power-law DOGs. These power-law DOGs are hyper-luminous ($2 \times 10^{13} L_{\odot}$) and have predominantly warm dust ($T_{\text{dust}} > 35 - 60$ K). These results are consistent with an evolutionary sequence in which power-law DOGs represent a brief but important phase when AGN feedback heats the interstellar medium and quenches star-formation.

The third component of my thesis is a study of the stellar masses and star-formation histories of DOGs, using stellar population synthesis models and broad-band photometry in the rest-frame ultra-violet, optical, and near-IR. The best-

fit quantities indicate bump DOGs are less massive than power-law DOGs. The relatively low stellar masses found from this line of analysis favor a merger-driven origin for ULIRGs at $z \sim 2$.

CHAPTER 1

INTRODUCTION

1.1 Models for the Formation of Galaxies in the Universe

Galaxy formation can be described in the broadest terms as the cooling and condensing of baryons into gravitationally-bound, luminous systems. In the currently favored cosmogony, the Λ -cold-dark-matter model (Λ CDM; Spergel et al., 2007), a negative pressure called dark energy constitutes $\approx 70\%$ of the entire energy budget of the universe. Baryons — i.e., the directly observable universe — comprise only $\approx 4\%$ of the total energy in the universe. The remainder consists of dark matter; although not directly observable, the essential properties of dark matter have been established by a wealth of theoretical studies and indirect observations. Dark matter is assembled hierarchically; large haloes are created by the self-similar gravitational clustering of many smaller haloes. Since baryons cool and condense preferentially in the deepest dark matter potential wells, it is expected that galaxies are also assembled hierarchically (White & Rees, 1978).

Early models of galaxy evolution based on the CDM paradigm predicted that (1) over half of the stellar mass in the universe was assembled at $z < 1$; and (2) the most massive galaxies in the local universe should also have the highest star-formation rates (SFRs) (e.g., White & Frenk, 1991). However, observations in ensuing years have established that massive galaxies are dominated by old stellar populations and have little on-going star-formation (Kauffmann et al., 2003). Moreover, the SFRs in massive galaxies ($M_* \geq 10^{11} M_\odot$) are relatively low from $z \sim 0$ to $z \sim 1$, but then rise sharply until $z \sim 2$. Generally speaking, less massive galaxies reach their peak SFR at lower redshifts — a phenomenon that has been termed “down-sizing” (e.g., Cowie et al., 1996; Juneau et al., 2005). Together with the observational fact

that the most massive galaxies in the local universe stopped forming stars billions of years ago, this phenomenon is apparently at odds with the simplest possible theory for galaxy formation in a Λ CDM universe.

Recent theories employing empirical halo occupation models to study the formation of massive galaxies focus on the role played by mergers (Hopkins et al., 2008a). These authors argue that quasar feedback plays a critical role in causing every major merger to leave behind a spheroidal system with little on-going star-formation. This black hole-regulated feedback model provides a natural explanation for the observed correlation between the bulge mass and black hole mass in galaxies (Magorrian et al., 1998) and also correctly reproduces the evolution of the massive galaxy luminosity function. The notion that feedback effects from the growth of a central supermassive black hole regulate the ultimate growth of its host galaxy has gained some traction recently (c.f. Croton et al., 2006; Bower et al., 2006), yet it is not without controversy. In particular, the details of the physical mechanisms governing this process are currently unknown (simulations of major mergers lack the physical resolution needed to probe down to the pertinent size scales). Moreover, the importance of mergers in driving this process remains difficult to quantify observationally. Testing these theories by finding and studying massive galaxies while they are in the process of forming is therefore of critical importance.

1.2 Finding Massive Galaxies in the Process of Formation

In the local universe, massive galaxy formation is a rare phenomenon. The best studied cases are ultra-luminous infrared galaxies (ULIRGs), which are systems with extremely high infrared (IR) luminosities ($L_{\text{IR}} > 10^{12} L_{\odot}$). Discovered with pioneering surveys at mid-IR wavelengths (Rieke & Low, 1972), ULIRGs were identified in large numbers by the *InfraRed Astronomical Satellite* (IRAS; Neugebauer

et al., 1984). These objects have spectral energy distributions (SEDs) that are dominated by the presence of vast quantities of dust; this dust absorbs ultra-violet and optical light and re-radiates it in the IR (Soifer et al., 1986). ULIRGs at $z \sim 0$ have been associated with a critical phase of galaxy evolution linking mergers (Armus et al., 1987) with quasars and red, dead elliptical galaxies (Sanders et al., 1988a,b). While rare locally, ULIRGs are more commonplace in the distant universe, to the extent that they contribute a significant component of the bolometric luminosity density of the universe at $z > 1$ (e.g. Franceschini et al., 2001; Le Floc’h et al., 2005; Pérez-González et al., 2005). This realization has inspired a host of new techniques for identifying ULIRGs at $z > 1$.

One such technique is imaging at sub-millimeter (sub-mm) wavelengths. This method makes use of the fact that as dusty galaxies move out in redshift, the peak of their SED is shifted towards longer wavelengths, effectively compensating for the reduction in brightness due to the inverse square law (this is commonly called a “negative K -correction”). The advent of bolometer arrays at sub-mm and mm wavelengths (most notably the Sub-mm Common User Bolometer Array or SCUBA and the Max Planck Millimetre Bolometer array or MAMBO; Holland et al., 1999; Kreysa et al., 1999) has allowed wide-field surveys at $850\mu\text{m}$ and 1.2mm which have identified hundreds of sub-millimeter selected galaxies (SMGs). Follow-up spectroscopy (Chapman et al., 2005) has indicated that they lie at $z \sim 2$ and have number densities that are comparable to luminous ($> 4L^*$) red galaxies in the local universe ($n \approx 2.5 \times 10^{-5} h_{70}^3 \text{ Mpc}^{-3}$; Wake et al., 2006). Furthermore, studies of the clustering properties of SMGs have found that they inhabit very massive dark matter haloes ($M_{\text{DM}} \approx 10^{12} M_{\odot}$; Blain et al., 2004). This provides evidence that SMGs may be linked with the most massive galaxies ($\approx 3L^*$) in the local universe.

Another method of finding high redshift ULIRGs is the selection of IR-bright,

optically-faint sources identified with the $24\mu\text{m}$ channel of the Multiband Imaging Photometer for Spitzer (MIPS; Rieke et al., 2004) instrument for the *Spitzer Space Telescope* (Yan et al., 2004; Houck et al., 2005; Weedman et al., 2006b; Fiore et al., 2008; Dey et al., 2008; Fiore et al., 2009). In particular, Dey et al. (2008) select sources from the 9 deg^2 NOAO Deep Wide-Field Survey (NDWFS) Boötes field that satisfy $R - [24] > 14$ (Vega magnitudes; $\approx F_{24\mu\text{m}}/F_R > 1000$) and $F_{24\mu\text{m}} > 0.3\text{ mJy}$. These objects are called dust-obscured galaxies (DOGs), lie at $z \approx 2 \pm 0.5$ (Houck et al., 2005; Weedman et al., 2006a; Desai et al., 2009, Soifer et al., in prep.), have a space density of $(2.82 \pm 0.05) \times 10^{-5} h_{70}^3\text{ Mpc}^{-3}$ (Dey et al., 2008), and inhabit massive dark matter haloes ($M_{\text{DM}} \sim 10^{12.3} M_{\odot}$; Brodwin et al., 2008). These results imply DOGs are undergoing a very luminous, short-lived phase of activity characterized by both vigorous stellar bulge and nuclear black hole growth.

In addition, DOGs can be divided into two groups according to the nature of their mid-IR SEDs. Those with a peak or bump at rest-frame $1.6\mu\text{m}$ produced by the photospheres of old stars (“bump DOGs”), and those dominated by a power-law in the mid-IR (“power-law DOGs”). The SED shapes, as well as spectroscopy in the near-IR (Brand et al., 2007; Sajina et al., 2008) and mid-IR (Yan et al., 2007; Sajina et al., 2007a; Farrah et al., 2008; Desai et al., 2009; Huang et al., 2009) indicate that bump DOGs are dominated by star-formation, while power-law DOGs are dominated by obscured active galactic nucleus (AGN).

1.3 The Nature of Dust-Obscured Galaxies

Although some of the basic properties of DOGs are now understood, many significant questions remain. For example, what is the connection between bump DOGs and power-law DOGs? Is there a relationship between DOGs and SMGs? Are DOGs the progenitors of the most massive galaxies in the universe? The purpose of this

thesis is to make progress in answering these questions and in so doing advance our understanding of the formation of massive galaxies.

In chapter 2, we study the morphologies of a sample of 31 power-law DOGs using *Hubble Space Telescope* (*HST*) imaging in the optical and near-IR. Although these objects show spectral features in the mid-IR that are typical of obscured AGN, the host galaxy dominates the optical and near-IR light profile in all but one source. Very few sources show obvious signs of on-going mergers and relaxed morphologies are more common than disturbed/irregular morphologies in this sample. This implies that power-law DOGs either represent (1) a phase near the end of a major merger or (2) a secularly evolving system whose power output is driven by smooth accretion of gas rather than major mergers.

In chapter 3, we extend the morphological study of chapter 2 by adding to it optical and near-IR *HST* imaging of 22 bump DOGs with mid-IR spectral features indicating vigorous on-going star-formation. Bump DOGs are larger and have more irregular morphologies than power-law DOGs — trends which are consistent with expectations from simulations of major mergers. In this chapter, we also present a morphological analysis of SMGs and other ULIRGs at $z \sim 2$. Sources that are less obscured (i.e., $R - [24] < 14$) typically show morphologies more similar to power-law DOGs than bump DOGs, implying that these objects are unlikely to be early stage major mergers.

In chapter 4, we turn away from the morphological studies of the previous two chapters and center our attention on the dust properties of DOGs. Using $350\mu\text{m}$ and 1.3mm imaging of a handful of power-law DOGs, we determine that these objects are ULIRGs with dust temperatures higher than SMGs by $> 10 - 20$ K. This result is consistent with expectations of the dust properties of obscured AGN based on a major merger driven model for galaxy evolution in which AGN feedback plays a

significant role in quenching star-formation by heating the surrounding gas and dust particles near the end of final coalescence.

In chapter 5, we analyze the rest-frame ultra-violet through near-IR SEDs of bump DOGs, power-law DOGs, and SMGs using stellar population synthesis models. The best-fit quantities are consistent with an evolutionary scenario in which the stellar mass grows as SMGs evolve into bump DOGs which then evolve into power-law DOGs. The uncertainty in these relative stellar mass estimates is roughly a factor of 2 (due primarily to the degeneracy between dust extinction and stellar population age), large enough that additional data from future studies will be needed to confirm this trend. A star-formation history driven by a major-merger yields stellar mass estimates that are consistent with the minimal stellar mass needed in the merger simulations to produce ULIRG luminosities at $z \sim 2$. Meanwhile, more quiescent star-formation histories dominated by smooth accretion of gas result in stellar masses that are a factor of 2-4 (depending on the adopted IMF) lower than expected from cosmological simulations. While neither model provides a perfect fit, the relatively low stellar masses found from this line of analysis generally favor a merger-driven origin for ULIRGs at $z \sim 2$.

In chapter 6, we use the morphologies, dust properties, and star-formation histories of DOGs to describe their role in galaxy evolution. Finally, we outline important future steps that must be taken to continue advancing our understanding of how galaxy formation occurs in the distant universe, with an emphasis on two aspects. One is the ability of new mid-IR and sub-mm space telescopes to conduct wide-field surveys and increase the number of ULIRGs identified at high redshift by orders of magnitude. The other is measurements of the gas properties of ULIRGs at high redshift obtained with sub-mm interferometers.

CHAPTER 2

MORPHOLOGIES OF POWER-LAW DOMINATED DOGS

We present high spatial resolution optical and near-infrared imaging obtained using the ACS, WFPC2 and NICMOS cameras aboard the *Hubble Space Telescope* of 31 $24\mu\text{m}$ -bright $z \approx 2$ Dust Obscured Galaxies (DOGs) identified in the Boötes Field of the NOAO Deep Wide-Field Survey. Although this subset of DOGs have mid-IR spectral energy distributions dominated by a power-law component suggestive of an AGN, all but one of the galaxies are spatially extended and not dominated by an unresolved component at rest-frame UV or optical wavelengths. The observed $V - H$ and $I - H$ colors of the extended components are $0.2 - 3$ magnitudes redder than normal star-forming galaxies. All but 1 have axial ratios > 0.3 , making it unlikely that DOGs are composed of an edge-on star-forming disk. We model the spatially extended component of the surface brightness distributions of the DOGs with a Sérsic profile and find effective radii of $1 - 6$ kpc. This sample of DOGs is smaller than most sub-millimeter galaxies (SMGs), but larger than quiescent high-redshift galaxies. Non-parametric measures (Gini and M_{20}) of DOG morphologies suggest that these galaxies are more dynamically relaxed than local ULIRGs. We estimate lower limits to the stellar masses of DOGs based on the rest-frame optical photometry and find that these range from $\sim 10^{9-11} M_{\odot}$. If major mergers are the progenitors of DOGs, then these observations suggest that DOGs may represent a post-merger evolutionary stage.

2.1 Introduction

One of the most important questions concerning the evolution of galaxies is when and how the most massive galaxies formed. It has been known since the analysis of

the *InfraRed Astronomical Satellite (IRAS)* data that in the local universe the most bolometrically luminous galaxies have their spectral energy distributions (SEDs) dominated by infrared (IR) light (Soifer et al., 1986), suggesting that these systems are highly obscured by dust, which absorbs ultra-violet (UV) and optical light and re-radiates it in the IR. While these ultra-luminous IR galaxies (ULIRGs) are rare in the local universe, they become an increasingly important phenomenon at high redshift (e.g., Franceschini et al., 2001; Le Floch et al., 2005; Pérez-González et al., 2005).

Following the launch of the *Spitzer Space Telescope*, numerous investigators have identified and studied populations of high redshift galaxies that are IR-bright yet optically faint (Yan et al., 2004; Houck et al., 2005; Weedman et al., 2006b; Fiore et al., 2008; Dey et al., 2008). In particular, Dey et al. (2008) and Fiore et al. (2008) present a simple and economical method for selecting these systems using only *R*-band and $24\mu\text{m}$ Multiband Imaging Photometer for Spitzer (MIPS; Rieke et al., 2004) data. Dey et al. (2008) employ a color cut of $R - [24] > 14$ (Vega magnitudes; $\approx F_\nu(24\mu\text{m})/F_\nu(R) > 1000$) to identify objects they call Dust Obscured Galaxies (DOGs) in the Boötes field of the NOAO Deep Wide-Field Survey (NDWFS¹; Jannuzi et al., in prep.; Dey et al., in prep.).

The broadband photometry, redshift distribution, and number density of the DOGs imply that they are undergoing an extremely luminous, short-lived phase of stellar bulge and nuclear black hole growth and may be the progenitors of the most luminous ($\sim 4L^*$) present-day galaxies. Ground-based photometry from the NDWFS suggests magnitudes of $R \approx 24 - 27$, $I \approx 24 - 26$, and $K \approx 17.5 - 20.5$ for the sample of DOGs with $F_\nu(24\mu\text{m}) > 0.3$ mJy. DOGs are relatively rare, with a surface density of ≈ 0.089 arcmin⁻² for sources with $F_{24} > 0.3$ mJy. Spec-

¹<http://www.noao.edu/noaodeep>

troscopic redshifts determined for a sub-sample of DOGs using the Deep Imaging Multi-Object Spectrograph (DEIMOS; Faber et al., 2003) and the Low Resolution Imaging Spectrometer (LRIS; Oke et al., 1995) on the telescopes of the W. M. Keck Observatory (43 DOGs), as well as the Infrared Spectrometer (IRS; Houck et al., 2004) on *Spitzer* (43 DOGs) have shown that the DOGs have a redshift distribution centered on $z \approx 2$ with a dispersion of $\sigma_z \approx 0.5$. While DOGs are rare, they are sufficiently luminous that they contribute up to one-quarter of the total IR luminosity density from all $z \sim 2$ galaxies, and constitute the bulk of ULIRGs at $z \sim 2$ (Dey et al., 2008).

Based on their observed properties, Dey et al. (2008) suggest DOGs may represent a transition stage between sub-millimeter-selected galaxies (SMGs) and unobscured quasars or galaxies. Evidence in support of this scenario is that DOGs and SMGs have similar space densities and clustering properties (Brodwin et al., 2008). An important test of this scenario is to study their morphologies with high spatial resolution imaging. For example, one of the primary motivations for the merger-driven scenario for the formation of ULIRGs is their disturbed structure at optical wavelengths (Sanders et al., 1988a). Studies of numerical simulations of galaxy mergers have suggested that they can produce very red, luminous systems that are highly dust-obscured (Jonsson et al., 2006). Recently, Lotz et al. (2008) have applied non-parametric methods of quantifying galaxy morphologies to similar merger simulations and have found that mergers are most easily identified during the first pass and at the final coalescence of their nuclei.

In addition to identifying merger activity, morphological information can constrain the size-scale of the emitting region. Sources with active star formation on several kiloparsec (kpc) scales have larger sizes than objects dominated by an Active Galactic Nucleus (AGN) or a very compact, nuclear starburst. Studies of Distant

Red Galaxies (DRGs) have shown a relation between star formation and size at rest-frame optical wavelengths, in the sense that quiescent DRGs are all very compact with effective radii (R_{eff}) less than 1 kpc, while active DRGs tend to be more extended ($1 < R_{\text{eff}} < 10$ kpc; Zirm et al., 2007; Toft et al., 2007). Analysis of SMGs in GOODS-N shows extended emission on scales of 5-15 kpc (Pope et al., 2005). Recent NICMOS imaging of a sample of 33 high- z ULIRGs by Dasyra et al. (2008) has shown these extreme objects (which are similar in their selection criteria to DOGs) to have effective radii in the range ~ 1.5 -5 kpc. About half of their sample shows signs of interactions, but only 2 are merging binaries with a luminosity ratio $\leq 3:1$, i.e., qualifying as major mergers.

High spatial resolution imaging of the DOGs is essential to understanding their relation to other galaxy populations as well as their role in galaxy evolution in general. We have begun an effort to obtain high resolution imaging using laser guide star and natural guide star adaptive optics on the Keck telescopes. These (on-going) efforts have resulted in high resolution K -band images of a handful of DOGs found near bright stars (Melbourne et al., 2008, , in prep.). A complementary method of obtaining deep, high spatial resolution imaging is with the *Hubble Space Telescope* (*HST*). With the Advanced Camera for Surveys (ACS) and the Wide Field Planetary Camera 2 (WFPC2), we can probe the rest-frame UV emission of the DOGs that is sensitive to the ionizing sources associated with on-going star formation. Meanwhile, NICMOS data allow the study of the rest-frame optical morphology, which better traces the stellar mass and dust-enshrouded AGN.

In this paper we present ACS/WFPC2 and NICMOS images of 31 DOGs and analyze their morphologies. The DOGs studied in this paper have spectroscopic redshifts from either *Spitzer*/IRS DEIMOS/LRIS, were selected primarily based on their large $24\mu\text{m}$ flux densities ($F_{24\mu\text{m}} > 0.8$ mJy), and have power-law SEDs in the

mid-IR. In a future paper, we will study a sample of DOGs with fainter $24\mu\text{m}$ flux densities that have mid-IR bump SEDs (Bussmann et al., in prep.). In section 2.2 we detail the sample selection, observations, and data reduction. Section 2.3 contains a description of the methods we use in our morphological analysis, and in section 2.4, we report the results this analysis. In section 2.5, we estimate some intrinsic properties of the DOGs in our sample and we compare our findings with what is seen in other high redshift galaxy populations. Finally, we present our conclusions in section 2.6.

Throughout this paper we assume $H_0 = 70 \text{ km s}^{-1} \text{ Mpc}^{-1}$, $\Omega_m = 0.3$, and $\Omega_\lambda = 0.7$. At $z = 2$, this results in $8.37 \text{ kpc}''$.

2.2 Data

In this section, we describe our sample selection and give details regarding the *HST* observations and our data reduction procedure, as well how we measure our photometry. Finally, we show postage stamp images and provide a brief qualitative description of each target.

2.2.1 Sample Selection

As outlined in section 2.1, a sample of ≈ 2600 DOGs from Dey et al. (2008) was originally identified using the 9.3 deg^2 Boötes Field of the NDWFS. For details of the selection criteria and photometric analysis, we refer the reader to Dey et al. (2008). In this paper, we analyze *HST* imaging from program HST-GO10890 of 31 of the brightest DOGs at $24\mu\text{m}$ (all have $F_{24\mu\text{m}} > 0.8 \text{ mJy}$). The bolometric luminosity of DOGs with bright $24\mu\text{m}$ flux densities is typically dominated by AGN emission, while the opposite is true for $24\mu\text{m}$ faint DOGs ($0.1 \text{ mJy} < F_{24\mu\text{m}} < 0.3 \text{ mJy}$), which are dominated by star-formation (Pope et al., 2008a). Additionally, IRAC photometry shows that the objects in this paper are dominated by a power-law

component in the mid-IR. The most likely cause of this emission is the presence of warm dust heated by an AGN (Donley et al., 2007).

Shallow X-ray coverage of the Boötes field exists and has yielded a full catalog of X-ray sources (Murray et al., 2005; Kenter et al., 2005; Brand et al., 2006). Within a $2''$ search radius, two of the DOGs studied in this paper (SST24 J143102.2+325152 and SST24 J143644.2+350627) have a single X-ray counterpart, and one DOG has two counterparts (SST24 J142644.3+333051). A full analysis of the X-ray data is beyond the scope of this paper, but these basic results suggest that most DOGs are either not strong X-ray emitters or are heavily obscured. The latter view is supported both by mid-IR spectral features and the fact that this subset of $24\mu\text{m}$ bright DOGs shows some of the reddest $R - [24]$ colors of the entire DOG population. Figure 2.1 shows the color-magnitude diagram in $R - [24]$ vs. $[24]$ space for the full DOG population in Boötes and highlights the subsample of objects studied in this paper.

Previous work has shown that objects dominated by a power-law signature in the mid-IR tend to have AGN indicators in their mid-IR spectra, usually silicate absorption but no PAH emission (Weedman et al., 2006a; Polletta et al., 2008; Brand et al., 2008). Indeed, IRS spectra of these sources have revealed redshifts based on the $9.7\mu\text{m}$ Silicate absorption feature, and all are located at $z \sim 2$. Of the 31 objects in this sample, 17 have spectra from Houck et al. (2005), 2 have spectra from Weedman et al. (2006b), and the remaining spectra will be presented in future work (Higdon et al. in prep.). Subsequent Keck/NIRSPEC (Brand et al., 2007), Keck/LRIS, and Keck/DEIMOS spectroscopy has yielded more precise redshifts for 4 of the DOGs. The redshift distribution of the sample studied in this paper compared to the overall distribution of spectroscopic redshifts for the DOGs from the Boötes field is shown in Figure 2.2.

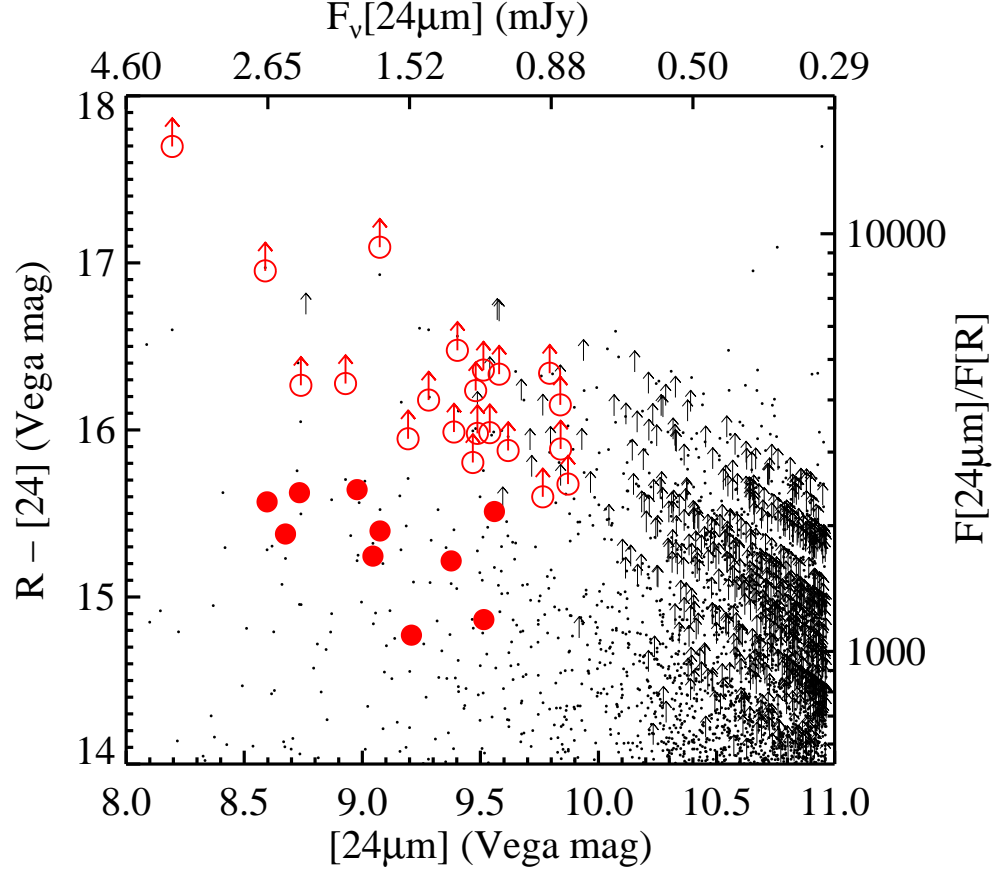


Figure 2.1 $R - [24]$ color vs. $24\mu\text{m}$ magnitude distribution for DOGs in the NDWFS Boötes field. Bottom and top abscissae show the $24\mu\text{m}$ magnitude and flux density, respectively, and the left and right ordinates show the color in magnitudes and the $F_{24\mu\text{m}}/F_R$ flux density ratio, respectively. Black dots and upward arrows show the full sample of DOGs, with and without an R -band detection, respectively. The subsample studied in this paper is represented by red circles (open symbols show lower limits).

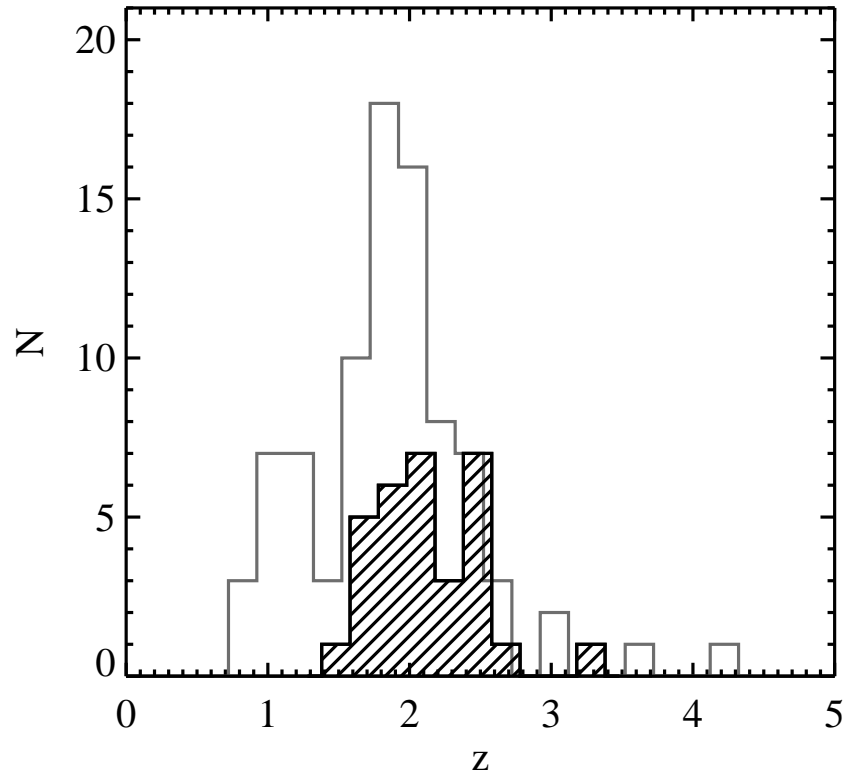


Figure 2.2 Distribution of redshifts for DOGs in the Boötes Field with spectroscopic redshifts (either from *Spitzer/IRS* or Keck DEIMOS/LRIS). The redshift distribution of the sub-sample of objects studied in this paper is shown with the hatched histograms and is representative of the full sample of DOGs.

2.2.2 Observations

The 31 DOGs we study here were observed with *HST* from 2006 November to 2008 February. Nine were imaged in the Wide Field Channel (WFC) mode of ACS (Ford et al., 1998) before the failure of the instrument. We have observed the remaining 22 DOGs with WFPC2 (Trauger et al., 1994). All 31 DOGs were observed with the NICMOS NIC2 camera. Table 2.1 summarizes the details of the observations. All data were processed using IRAF². In the following sections we provide more details about the processing of the ACS, WFPC2, and NICMOS images used in this paper.

2.2.2.1 ACS

Each DOG was observed over a single orbit through the F814W filter using a four point dither pattern (ACS-WFC-DITHER-BOX) with a point spacing of $0.265''$, a line spacing of $0.187''$ and a pattern orientation of 20.67° . Total exposure time was ≈ 2000 sec. Bias-subtraction and flat-fielding was performed using the standard ACS pipeline (Pavlovsky et al. 2004). The MultiDrizzle routine was used to correct for geometric distortions, perform sky-subtraction, image registration, cosmic ray rejection and final drizzle combination (Koekemoer et al., 2002). We used a square interpolation kernel and set the output pixel scale at $0.05'' \text{ pix}^{-1}$.

2.2.2.2 WFPC2

Following the failure of ACS in the middle of Cycle 15 observing, the Wide Field Camera CCD 3 of WFPC2 was used to image the remainder of the DOG population. For these observations, single-orbit data through the F606W filter were used to take advantage of WFPC2's superior sensitivity at this wavelength compared to other WFPC2 filters. We used a four point dither pattern (WFPC2-BOX) with a point

²IRAF is distributed by the National Optical Astronomy Observatories, which are operated by the Association of Universities for Research in Astronomy, Inc., under cooperative agreement with the National Science Foundation. <http://iraf.noao.edu/>

Table 2.1. Observations

| Source Name | RA (J2000) | DEC (J2000) | z | Optical Exposures | | Infrared Exposures | | ID [§] |
|------------------------|--------------|--------------|--------------------|-------------------|------------|--------------------|------------|-----------------|
| | | | | Instrument/Filter | UT Date | Instrument/Filter | UT Date | |
| SST24 J142538.2+351855 | 14:25:38.155 | +35:18:56.19 | 2.26 ^a | WFPC2/F606W | 2007-04-29 | NIC2/F160W | 2007-06-16 | 19 |
| SST24 J142622.0+345249 | 14:26:22.032 | +34:52:49.69 | 2.00 ^c | ACS/F814W | 2006-11-25 | NIC2/F160W | 2007-03-13 | 9 |
| SST24 J142626.4+344731 | 14:26:26.538 | +34:47:31.53 | 2.13 ^a | WFPC2/F606W | 2007-12-31 | NIC2/F160W | 2007-01-04 | 16 |
| SST24 J142644.3+333051 | 14:26:44.321 | +33:30:52.20 | 3.312 ^d | WFPC2/F606W | 2007-04-10 | NIC2/F160W | 2007-02-25 | 31 |
| SST24 J142645.7+351901 | 14:26:45.701 | +35:19:01.17 | 1.75 ^a | WFPC2/F606W | 2007-04-24 | NIC2/F160W | 2007-05-05 | 2 |
| SST24 J142648.9+332927 | 14:26:48.970 | +33:29:27.56 | 2.00 ^c | ACS/F814W | 2007-01-17 | NIC2/F160W | 2006-12-19 | 10 |
| SST24 J142653.2+330220 | 14:26:53.285 | +33:02:21.37 | 1.86 ^a | ACS/F814W | 2006-12-29 | NIC2/F160W | 2007-03-01 | 6 |
| SST24 J142804.1+332135 | 14:28:04.133 | +33:21:34.97 | 2.34 ^a | WFPC2/F606W | 2007-04-17 | NIC2/F160W | 2007-05-01 | 20 |
| SST24 J142924.8+353320 | 14:29:24.811 | +35:33:21.30 | 2.73 ^a | WFPC2/F606W | 2007-03-18 | NIC2/F160W | 2007-02-13 | 30 |
| SST24 J142958.3+322615 | 14:29:58.354 | +32:26:15.17 | 2.64 ^a | WFPC2/F606W | 2007-03-14 | NIC2/F160W | 2007-06-22 | 29 |
| SST24 J143001.9+334538 | 14:30:01.910 | +33:45:38.54 | 2.46 ^a | WFPC2/F606W | 2007-04-12 | NIC2/F160W | 2007-04-28 | 22 |
| SST24 J143025.7+342957 | 14:30:25.764 | +34:29:57.29 | 2.545 ^e | WFPC2/F606W | 2007-04-26 | NIC2/F160W | 2007-04-13 | 26 |
| SST24 J143102.2+325152 | 14:31:02.220 | +32:51:52.10 | 2.00 ^b | WFPC2/F606W | 2007-04-26 | NIC2/F160W | 2008-01-07 | 11 |
| SST24 J143109.7+342802 | 14:31:09.823 | +34:28:02.34 | 2.10 ^c | WFPC2/F606W | 2007-04-12 | NIC2/F160W | 2007-01-04 | 13 |
| SST24 J143135.2+325456 | 14:31:35.309 | +32:54:56.84 | 1.48 ^c | WFPC2/F606W | 2007-03-21 | NIC2/F160W | 2007-06-17 | 1 |
| SST24 J143225.3+334716 | 14:32:25.433 | +33:47:16.67 | 2.00 ^c | ACS/F814W | 2006-12-07 | NIC2/F160W | 2007-06-17 | 12 |
| SST24 J143242.5+342232 | 14:32:42.569 | +34:22:32.23 | 2.16 ^a | WFPC2/F606W | 2007-04-19 | NIC2/F160W | 2007-12-07 | 18 |
| SST24 J143251.8+333536 | 14:32:51.873 | +33:35:35.89 | 1.78 ^a | WFPC2/F606W | 2007-03-20 | NIC2/F160W | 2008-01-14 | 3 |
| SST24 J143312.7+342011 | 14:33:12.734 | +34:20:11.10 | 2.119 ^d | WFPC2/F606W | 2007-04-20 | NIC2/F160W | 2007-06-19 | 15 |
| SST24 J143325.8+333736 | 14:33:25.884 | +33:37:36.90 | 1.90 ^c | WFPC2/F606W | 2007-05-01 | NIC2/F160W | 2007-04-20 | 7 |
| SST24 J143358.0+332607 | 14:33:58.077 | +33:26:07.46 | 2.414 ^f | ACS/F814W | 2006-12-10 | NIC2/F160W | 2008-01-24 | 21 |
| SST24 J143447.7+330230 | 14:34:47.762 | +33:02:30.46 | 1.78 ^a | WFPC2/F606W | 2007-03-19 | NIC2/F160W | 2006-12-23 | 4 |
| SST24 J143504.1+354743 | 14:35:04.166 | +35:47:43.79 | 2.13 ^a | WFPC2/F606W | 2007-04-26 | NIC2/F160W | 2007-01-03 | 17 |
| SST24 J143508.4+334739 | 14:35:08.518 | +33:47:39.44 | 2.10 ^c | WFPC2/F606W | 2007-04-12 | NIC2/F160W | 2007-04-22 | 14 |
| SST24 J143520.7+340418 | 14:35:20.801 | +34:04:18.30 | 1.79 ^a | WFPC2/F606W | 2007-03-16 | NIC2/F160W | 2007-01-03 | 5 |
| SST24 J143523.9+330706 | 14:35:24.005 | +33:07:06.84 | 2.59 ^a | ACS/F814W | 2007-01-01 | NIC2/F160W | 2007-01-06 | 27 |
| SST24 J143539.3+334159 | 14:35:39.360 | +33:41:59.20 | 2.62 ^a | WFPC2/F606W | 2008-05-13 | NIC2/F160W | 2007-02-15 | 28 |
| SST24 J143545.1+342831 | 14:35:45.137 | +34:28:31.42 | 2.50 ^c | ACS/F814W | 2006-12-06 | NIC2/F160W | 2007-02-15 | 23 |
| SST24 J143644.2+350627 | 14:36:44.269 | +35:06:27.12 | 1.95 ^a | WFPC2/F606W | 2008-01-07 | NIC2/F160W | 2007-03-14 | 8 |
| SST24 J143725.1+341502 | 14:37:25.186 | +34:15:02.37 | 2.50 ^c | ACS/F814W | 2007-01-07 | NIC2/F160W | 2007-01-18 | 24 |
| SST24 J143808.3+341016 | 14:38:08.352 | +34:10:15.55 | 2.50 ^c | ACS/F814W | 2006-12-28 | NIC2/F160W | 2007-02-16 | 25 |

^aRedshift from *Spitzer*/IRS (Houck et al., 2005)^bRedshift from *Spitzer*/IRS (Weedman et al., 2006a)^cRedshift from *Spitzer*/IRS (Higdon et al. in prep)^dRedshift from Keck NIRSPEC (Brand et al., 2007)^eRedshift from Keck DEIMOS^fRedshift from Keck LRIS[§]Panel number in Figure 2.3

and line spacing of $0.559''$ and a pattern orientation of 26.6° . Total exposure time was ≈ 1600 sec. The standard WFPC2 pipeline system was used to bias-subtract, dark-subtract, and flat-field the images (Mobasher et al., 2002). MultiDrizzle was then used to correct for geometric distortions, perform sky-subtraction, image registration, cosmic ray rejection and final drizzle combination (Koekemoer et al., 2002). We used a square interpolation kernel and output pixel scale of $0.045'' \text{ pix}^{-1}$, leading to a per-pixel exposure time of ≈ 340 sec. Due to the irregular performance of WF4 and the PC CCDs, we have restricted our analysis to the WF2 and WF3 CCDs.

2.2.2.3 NICMOS

Single orbit data of the DOGs were acquired with NIC2 and the F160W filter. We used a two-point dither pattern (NIC-SPIRAL-DITH) with a point spacing of $0.637''$. Total exposure time was ≈ 2600 s. To reduce the data, we followed the standard reduction process outlined in the NICMOS data handbook (McLaughlin & Wikland 2007). We used the IRAF routine `nicpipe` to pre-process the data, followed by the `biaseq` task to correct for non-linear bias drifts and spatial bias jumps. We then used `nicpipe` a second time to do flat-fielding and initial cosmic-ray removal. The IRAF task `pedsky` was used to fit for the sky level and the quadrant-dependent residual bias. Significant residual background variation remained after this standard reduction process. To minimize these residuals, we constructed a normalized, object-masked median sky image based on all of our NIC2 science frames. This sky image was then scaled by a constant factor and subtracted from each science image. The scaling factor was computed by minimizing the residual of the difference between the masked science image and the scaled sky image. Mosaicing of the dithered exposures was performed using `calnicb` in IRAF, resulting in a pixel scale of $0.075'' \text{ pix}^{-1}$.

2.2.3 Astrometry

Each ACS/WFPC2 and NICMOS image is aligned to the reference frame of the NDWFS, which itself is tied to the USNO A-2 catalog. We first run Source Extractor (SExtractor, Bertin & Arnouts, 1996) on a cutout of the *I*-band NDWFS corresponding to the appropriate ACS/WFPC2 Field Of View (FOV) to generate a list of comparison objects. The IRAF task `wcsctran` is used to convert this list into pixel coordinates on the ACS/WFPC2 image. Another IRAF task, `imcentroid`, is used to improve the accuracy of the pixel coordinates. Finally, the IRAF task `ccmap` applies a first order fit to correct the zero point of the astrometry and update the appropriate WCS information in the header of the ACS/WFPC2 image. This aligned ACS/WFPC2 image is then used as the reference frame for correcting the astrometry of the NICMOS image and the IRAC images (since the IRAC images of the Boötes Field are not tied to the USNO A-2 catalog, but instead to the $2\mu\text{m}$ All-Sky Survey frames, see Eisenhardt et al., 2004). Using the properly aligned, multi-wavelength dataset, identifying the proper counterpart to the MIPS source is relatively straightforward, since inspection of the four IRAC channels reveals a single source associated with the $24\mu\text{m}$ emission for all but one source (this source is undetected in all four IRAC channels). The absolute uncertainty in the centroid of the IRAC $3.6\mu\text{m}$ emission ranges from $0''.3$ - $0''.5$.

2.2.4 Photometry

We perform $2''$ diameter aperture photometry on each DOG in both the rest-optical and rest-UV, choosing the center of the aperture to be located at the peak flux pixel in the NICMOS images. We remove foreground and background objects using SExtractor (see Section 2.4.2.2) and calculate the sky level using an annulus with an inner diameter of $2''$ and a width of $1''$. We found that in some cases (particularly those NICMOS images where significant residual non-linearities remained), the flux

density radial profile did not flatten at large radii. When this occurred, we determined the appropriate sky value by trial-and-error. We computed the background level and photometric uncertainty by measuring the sigma-clipped mean and RMS of fluxes measured in N $2''$ diameter apertures, where $N \approx 10$ and $N \approx 50$ for the NICMOS and ACS/WFPC2 images, respectively.

We compute $4''$ diameter aperture photometry in the NDWFS B_W , R , and I images centered on the IRAC $3.6\ \mu\text{m}$ centroid of emission. Sky background levels were computed in a $3''$ wide annulus with an inner diameter of $4''$. Limiting magnitudes were determined by measuring the flux within a $4''$ aperture at several sourceless locations near the DOG and computing the rms variation of the flux values.

We verified the accuracy of our ACS and WFPC2 photometric zeropoints by comparing well-detected sources common to both our *HST* and NDWFS imaging. For our ACS/F814W observations, we compared to the NDWFS I -band imaging and found negligible offsets (-0.03 ± 0.10 magnitudes). For our WFPC2/F606W observations, we compared to the NDWFS R -band (after correcting for color terms due to the dissimilarity of the R and F606W filter bandpasses) and again found negligible offsets (0.05 ± 0.15 magnitudes).

2.2.5 Images of DOGs

Figure 2.3 shows $2'' \times 2''$ cutout images of the DOGs in order of increasing redshift. Each cutout is centered roughly on the centroid of emission as seen in the NICMOS image. A red plus sign shows the centroid of IRAC $3.6\ \mu\text{m}$ emission and is sized to represent the $1\text{-}\sigma$ uncertainty in the position, which includes independent contributions from the centroiding error on the $3.6\ \mu\text{m}$ emission ($\approx 0''.2\text{--}0''.4$, depending on S/N), the relative astrometric calibration uncertainty within the $3.6\ \mu\text{m}$ map ($\approx 0''.2$), and the uncertainty in tying the $3.6\ \mu\text{m}$ map to the *HST* images ($\approx 0''.1$). The 1σ rms offset between IRAC and NICMOS centroids of the sample is $0''.2$. In most cases, the

offset in centroids is negligible, but those cases where it is not are associated with faint $3.6\mu\text{m}$ emission (when the absolute astrometric uncertainty may be as large as $0''.5$). This suggests there is no significant offset between the near-IR and mid-IR centroids, although we note that we cannot rule out offsets at the < 1 kpc scale.

The DOGs exhibit a wide range of morphologies, with most being well-resolved. Only one object (SST24 J142644.3+333051) shows strong Airy rings and is clearly an unresolved point source. Here we give a brief qualitative description of the morphology of each object.

(1) **SST24 J143135.2+325456:** F606W: Weak detection. F160W: Large-scale emission with a faint tail extending northeast.

(2) **SST24 J142645.7+351901:** F606W: No significant detection. F160W: Two compact, resolved components separated by $\approx 0''.5$.

(3) **SST24 J143251.8+333536:** F606W: Faint emission slightly NE of NICMOS centroid; possible second source $\sim 0''.5$ northwest (NW) of NICMOS centroid. F160W: Extended object; possible point source contamination.

(4) **SST24 J143447.7+330230:** F606W: No significant detection. F160W: Irregular, diffuse object.

(5) **SST24 J143520.7+340418:** F606W: Compact, resolved object. F160W: Very compact object, but no evidence for Airy rings.

(6) **SST24 J142653.2+330220:** F814W: Large scale, irregular, and diffuse emission. F160W: Large-scale, irregular, and diffuse, but with bright compact nuclear component.

(7) **SST24 J143325.8+333736:** F606W: Compact, resolved object. F160W: Bright compact and extended components.

(8) **SST24 J143644.2+350627:** F606W: Compact, resolved object. F160W: Extended object; possible point source contamination. This object has a counterpart

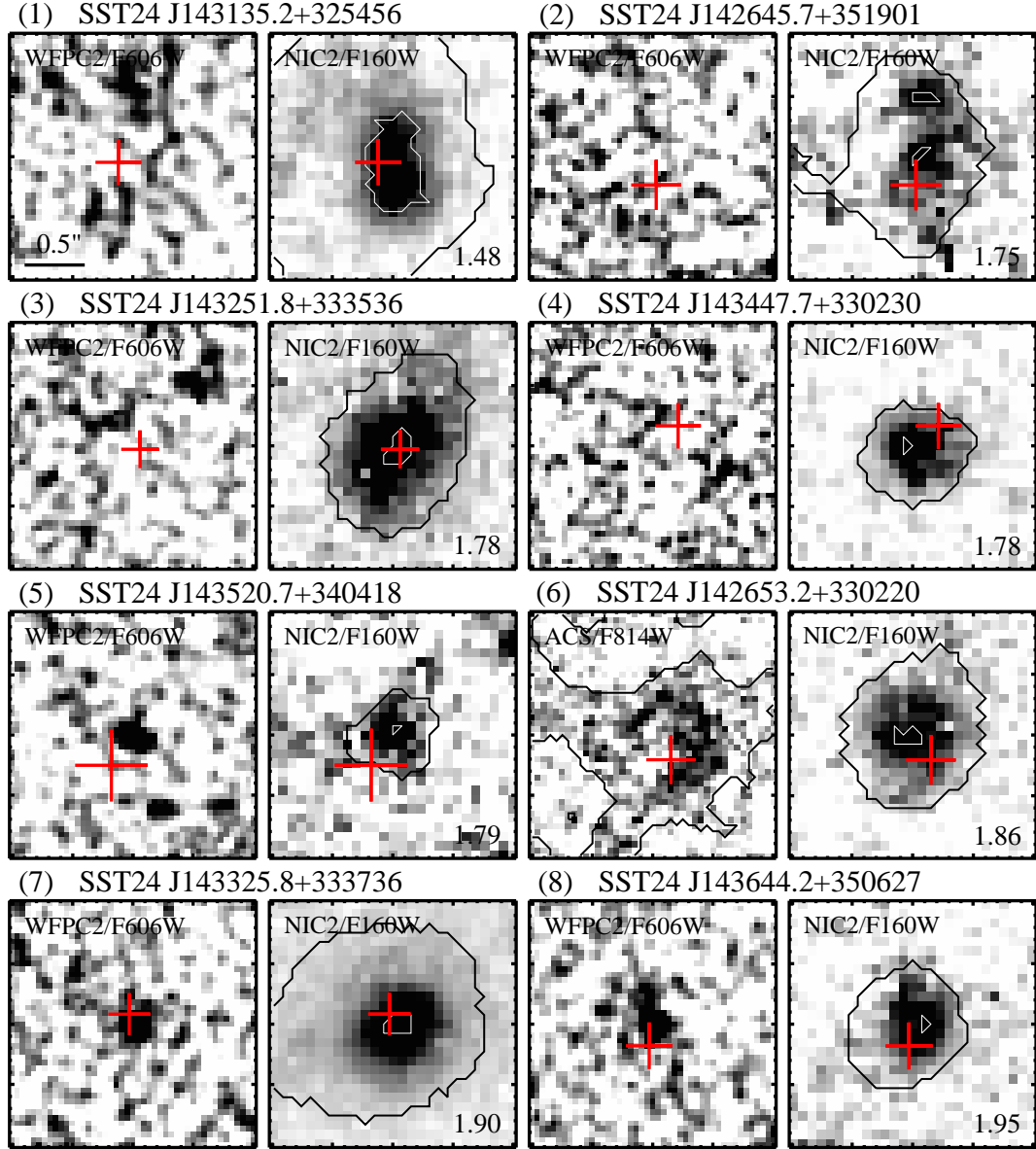


Figure 2.3 Cutouts of the 31 DOGs observed by *HST*, shown with a linear stretch. Columns 1 and 3 are the rest-UV images from either ACS F814W or WFPC2 F606W. Columns 2 and 4 are the rest-optical images from NIC2 F160W. Each cutout is 2'' on a side and is oriented north up and east left. The objects are arranged in order of increasing redshift, and the redshift is printed in the lower right corner of each NICMOS image. A red cross denotes the position and 1- σ uncertainty in the centroid of the IRAC 3.6 μ m emission. In NICMOS images where the S/N per pixel is greater than 2, white contours outline the brightest 20% pixels,

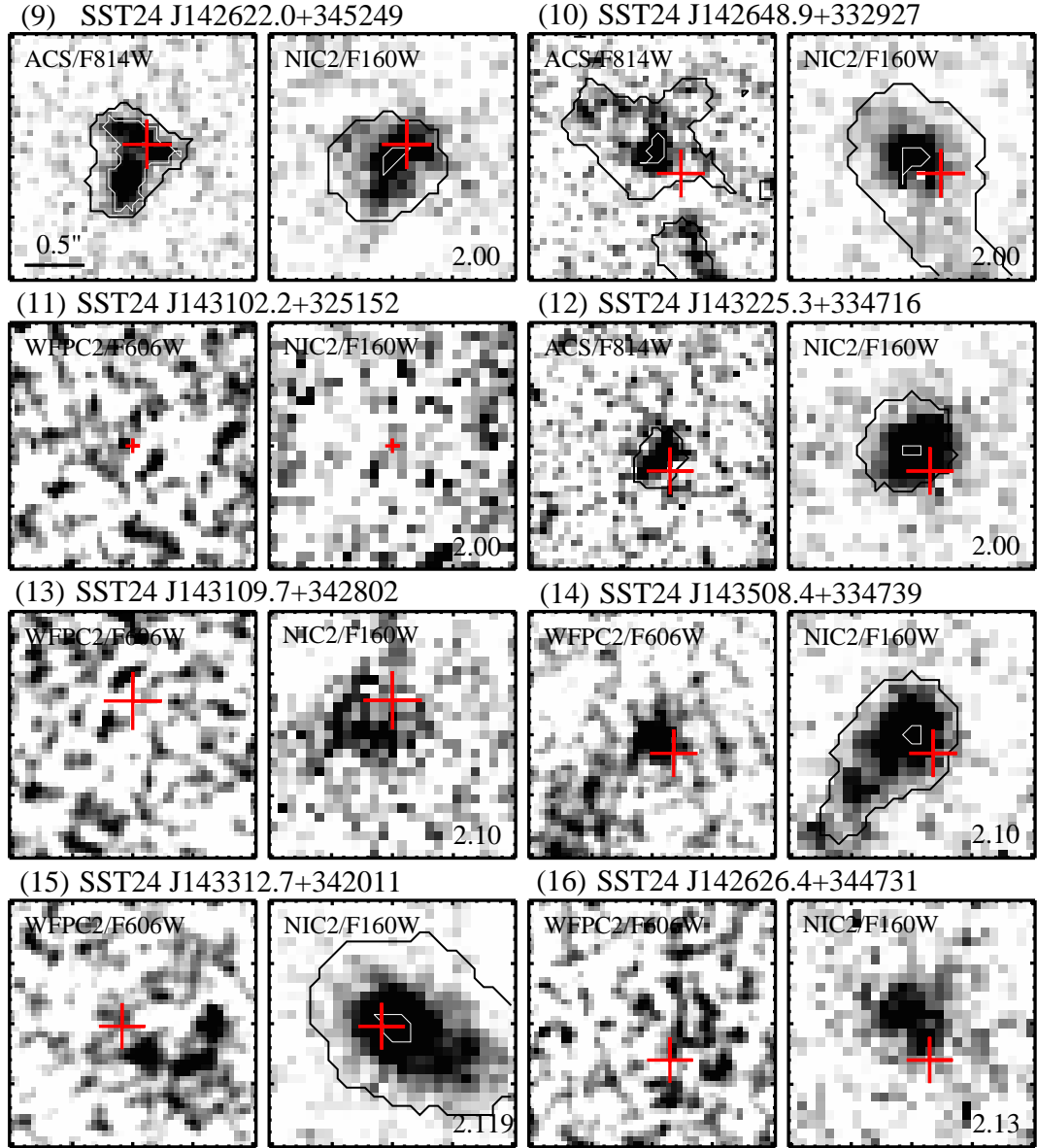
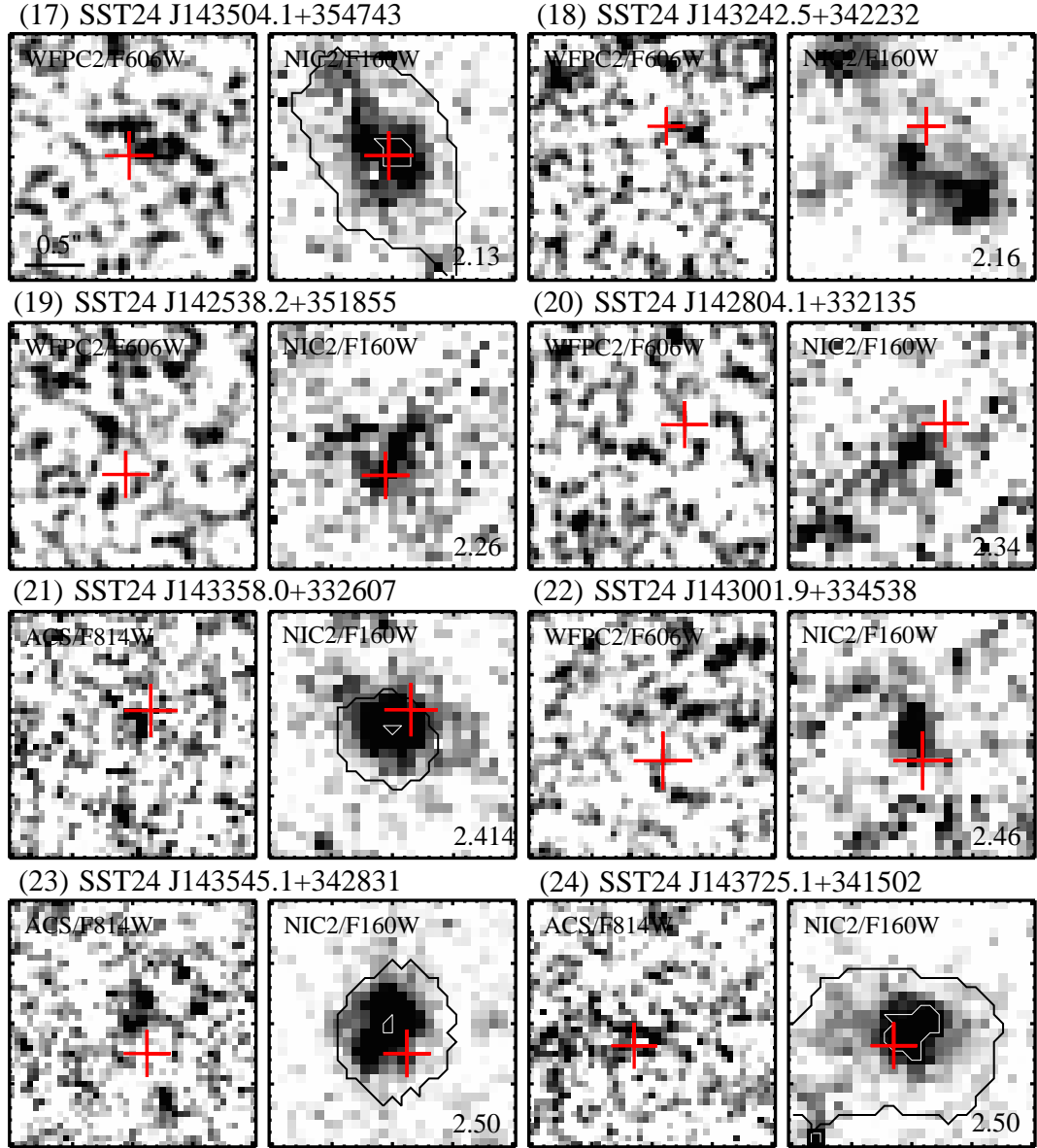


Figure 2.3 Continued.



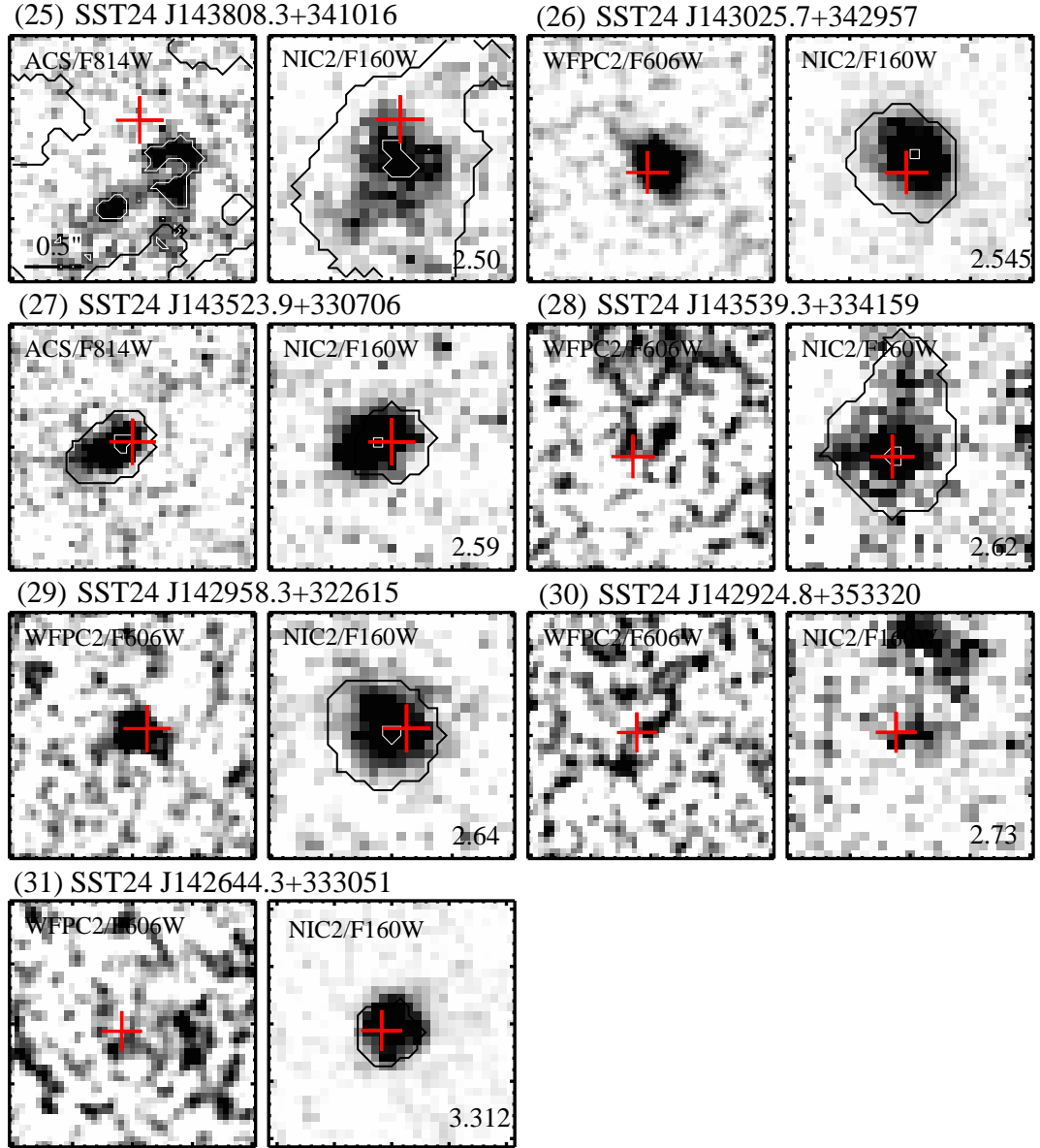


Figure 2.3 Continued.

in the XBoötes catalog (Brand et al., 2006).

(9) SST24 J142622.0+345249: F814W: Four compact, resolved clumps spread in a ‘T’ shape with no visible central component. F160W: Similar irregular ‘T’ shape, but components are not as distinct. NE component is bluer than other components.

(10) SST24 J142648.9+332927: F814W: Compact, resolved object. Chain of sources extends towards southwest. One of these sources is within 1'' of the DOG and is included in the photometric and morphological measurements, since there is no clear evidence to suggest it is not associated with the system. F160W: Similar compact, resolved object; possible point source contamination.

(11) SST24 J143102.2+325152: F606W: No significant detection. F160W: No significant detection. This object is also not detected in any of the IRAC images, but does have a counterpart in the XBoötes catalog (Brand et al., 2006).

(12) SST24 J143225.3+334716: F814W: Compact, irregular object. F160W: Compact, resolved object; possible point source contamination.

(13) SST24 J143109.7+342802: F606W: No significant detection. F160W: Irregular, diffuse object.

(14) SST24 J143508.4+334739: F606W: Compact, resolved, and irregular central component with tail of emission to southeast (SE). F160W: Very similar, but central component is stronger relative to tail.

(15) SST24 J143312.7+342011: F606W: Four compact components in a semi-circle offset from the centroid of NICMOS emission. F160W: Extended object; possible point source contamination.

(16) SST24 J142626.4+344731: F606W: No significant detection. F160W: Irregular, diffuse object.

(17) SST24 J143504.1+354743: F606W: Faint source barely detected. F160W: Irregular, extended object; possible point source contamination.

(18) SST24 J143242.5+342232: F606W: No significant detection. F160W: Faint, compact component near $3.6\mu\text{m}$ centroid with emission leading to second, brighter peak $\sim 0''.5$ to southwest (SW). Possible multiple-component system.

(19) SST24 J142538.0+332607: F606W: No significant detection. F160W: Irregular object elongated in NW-SE direction.

(20) SST24 J142804.1+332135: F606W: No significant detection. F160W: Faint, irregular object.

(21) SST24 J143358.0+332607: F606W: Faint, irregular object. F160W: Extended object with possible point source contamination.

(22) SST24 J143001.9+334538: F606W: No significant detection. F160W: Faint, irregular object.

(23) SST24 J143545.1+342831: F814W: Faint, compact irregular objects; possibly two component system. F160W: Extended emission; possible point source contamination.

(24) SST24 J143725.1+341502: F814W: Very faint, low surface brightness feature extending to east. F160W: Diffuse emission with compact object; faint Airy ring present.

(25) SST24 J143808.3+341016: F814W: Faint, compact, resolved components offset from centroid of NIC2 emission. F160W: Compact, central component with extension to SE overlapping ACS emission centroid.

(26) SST24 J143025.7+342957: F606W: Compact, resolved object. F160W: Compact, resolved object; possible point source contamination.

(27) SST24 J143523.9+330706: F814W: Compact, resolved object with tail of emission to SE; possible point source contamination. F160W: Compact, resolved object; possible point source contamination.

(28) SST24 J143539.3+334159: F606W: Possible faint diffuse emission N of

NIC2 centroid. F160W: Compact, resolved object; possible point source contamination; possible tail of emission towards N.

(29) SST24 J142958.3+322615: F606W: Compact resolved object; possible point source contamination. F160W: Extended object with bright nuclear source; possible point source contamination.

(30) SST24 J142924.8+353320: F606W: No significant detection. F160W: Very compact, irregular, faint object near IRAC $3.6\mu\text{m}$ centroid. Larger, brighter object $\sim 0''.8$ to north.

(31) SST24 J142644.3+333051: F606W: Weak detection. F160W: Dominated by point source emission; clear Airy ring. This source has two X-ray counterparts in the XBoötes catalog (Brand et al., 2006).

2.3 Methodology: Morphological Analysis

We undertook three different, complementary approaches to analyzing the morphology of the DOGs in our sample: a visual classification experiment, multi-component GALFIT modeling, and non-parametric quantification. In this section, we describe the details of our methodology. The results are described in section 2.4.

2.3.1 Visual Classification

We first undertook a visual classification of the DOGs by conducting the following experiment: for each ACS/WFPC2 image, we generate a $5'' \times 5''$ cutout image of both the DOG and 14 other randomly selected galaxies in the same FOV with the same magnitude range as our DOG sample. Eight of the coauthors then classified all 15 galaxies in each FOV (the DOG was not identified), placing them into one of the following bins: Elliptical/Compact (E/C), Disk, Irregular/Multi-component, Irregular/Diffuse, or Too Faint to Tell. In practice, since these galaxies are selected to be faint in the optical and generally have low S/N, we group together the E/C

and Disk categories into a “Regular” bin and the two irregular categories into an “Irregular” bin. This results in a total of 3600 independent classifications, of which 240 pertain to the DOGs. In an effort to explore the robustness of our results, we flag and remove from the sample all objects where fewer than six classifiers were in agreement. This has the effect of reducing the fraction of “Too Faint To Tell” responses, but the ratio of the Regular to Irregular classifications changes by less than 15%. A similar experiment was done on the NICMOS images, without the control sample, since the NIC2 FOV is so small.

Interpretation of the results of our visual classification analysis is hampered by low S/N (in the case of the ACS/WFPC2 images) or the lack of a control sample (in the case of the NICMOS images), so we forego a detailed analysis and instead present the mode of the classifications for each DOG along with an indication of whether the eight coauthors were in general agreement in our morphological results table in section 2.4.2.2. This is useful as a qualitative assessment of the morphology for comparison with the more quantitative methods discussed below.

2.3.2 GALFIT Modeling

In many of the NICMOS images, there is a compact component that is not seen in the corresponding ACS/WFPC2 image, implying there is significant obscuration in the central region of many of the DOGs. In this section, we describe the method we use to explore the degree to which each DOG is dominated by a central, unresolved component. Our tool in this effort is GALFIT (Peng et al., 2002), which uses a 2-dimensional χ^2 minimization to search the parameter space of a set of predefined functions and identify the parameters that best describe the observed 2-D profile.

Because the DOGs are small and have low S/N compared to more typical applications of GALFIT, we restrict the size of the fitting region to be 41×41 pixels (corresponding to an angular and physical size of $3''$ and ≈ 24 kpc, respectively) and

include the minimum necessary components in our model. For a variety of reasons, we expect AGN to be important contributors to the emitted radiation from these sources. Therefore, we model the observed emission with three components which are described by a total of 10 free parameters. The number of degrees of freedom, N_{DOF} , is calculated as the number of pixels in the image being modeled minus the number of free parameters. This implies that the maximum N_{DOF} is 1671. Those cases where $N_{\text{DOF}} < 1671$ are associated with images where pixels were masked out because they were associated with residual instrumental noise and prevented convergence with GALFIT. We note that because NIC2 is a Nyquist-sampled array ($0.075'' \text{ pix}^{-1}$ compared to $0.16''$ FWHM beam), the pixels in our image may not be completely independent. As a result, the χ^2_ν values should be interpreted in a relative sense rather than an absolute one.

The first element in our GALFIT model is a sky component whose amplitude is chosen to obtain flat radial profiles at large radii and is not allowed to vary. The second is an instrumental PSF generated from the TinyTim software (Krist and Hook 2004), which can simulate a PSF for NICMOS, WFPC2, and ACS. For the NICMOS and WFPC2 images, the DOG is positioned in nearly the same spot on the camera. In the case of WFPC2 this is pixel (400,400) of chip 3 and pixel (155, 164) for NICMOS. Meanwhile, a different region of the ACS camera is used for each DOG. Therefore, we generate a unique PSF at each position on the appropriate chip in which a DOG is observed. We use a red power-law spectrum ($F_\nu \propto \nu^{-2}$) as the object spectrum. The PSF is computed out to a size of $3.0''$, and for the WFPC2 PSF we oversample by a factor of 2 to match the pixel scale of the drizzled WFPC2 images.

The final component is a Sérsic profile (Sersic, 1968) where the surface brightness scales with radius as $\exp[-\kappa((r/R_{\text{eff}})^{1/n} - 1)]$, where κ is chosen such that half of the

flux falls within R_{eff} . We attempted to place as few constraints as possible so as to optimize the measurement of the extended flux (i.e., non-point source component). However, in certain cases, the Sérsic index had to be constrained to be positive to ensure convergence on a realistic solution. For the NICMOS images, we used the uncertainty image output by `calnicb` as the error image required by GALFIT to perform a proper χ^2 minimization. The TinyTim NIC2 PSF is convolved with the Sérsic profile prior to performing the χ^2 minimization. The initial guesses of the magnitude, half-light radius, position angle, and ellipticity were determined from the output values from SExtractor. Varying the initial guesses within reasonable values (e.g., plus or minus two pixels for the half-light radius) yielded no significant change in the best-fit model parameters. We used the NICMOS centroid as the initial guess for the (x,y) position of both the PSF and extended components, but in a few cases these guesses had to be modified by 1-2 pixels in order to result in convergence.

We note that we tested two-component models as well (single component Sérsic profile plus sky background) and found larger reduced χ^2 values, especially when the point source fraction in our three-component model was large (see further discussion in section 2.4.2.1). In cases where the point source fraction was small, the two-component model had similar parameter values as the three-component model, as we would expect.

It is important to note here that NIC2 cannot spatially resolve objects smaller than 1.3 kpc at $z \approx 2$. This limit is large enough to encompass a compact stellar bulge as well as an active galactic nucleus, implying that we cannot, from these data alone, distinguish between these two possibilities as to the nature of the central, unresolved component.

After the best-fit parameters are found in the NICMOS image, we run GALFIT

with a simplified model on the DOGs in the ACS/WFPC2 images. The primary simplification is to fix the position of the PSF based on the best-fit NICMOS PSF location (allowing up to 2 pixel wiggle room to account for astrometric uncertainties, which can be as large as $0''.1$). In many cases, GALFIT required an upper limit to be placed on the magnitude of the PSF component in order to reach convergence. We choose to use the magnitude of a point source detected at the $2\text{-}\sigma$ level for this upper limit. We note that our Sérsic profile model for the extended DOG flux is not representative of the rest-UV morphology of many of the DOGs (i.e., the reduced χ^2 values are large), but it does adequately recover their total flux.

2.3.3 Non-parametric Classification

The Gini coefficient (G) and M_{20} parameter are known to be reliable tools for the characterization of faint-object morphologies (Lotz et al., 2004). G was originally created to measure how evenly the wealth in a society is distributed (Glasser, 1962). Recently, Abraham et al. (2003) and Lotz et al. (2004) applied this method to aid in the classification of galaxies, with G defined such that low (high) values imply an equal (un-equal) distribution of flux. M_{20} is the logarithm of the second-order moment of the brightest 20% of the galaxy’s flux, normalized by the total second-order moment (Lotz et al., 2004). This means that higher values of M_{20} imply multiple bright clumps offset from the second-order moment center. Lower values, on the other hand, suggest a system dominated by a central component.

Prior to computing G or M_{20} , we first generate a catalog of objects using SExtractor. We use a detection threshold of 1.5σ (corresponding to $24.5 \text{ mag arcsec}^{-2}$) and a minimum detection area of 15 pixels. The center of the image as well as the ellipticity and position angle computed by SExtractor are used as inputs for computing morphological measures. In addition, we use catalog sources selected to have magnitudes within the range of all 24 DOGs analyzed in this paper as a “field”

galaxy sample for comparison to DOGs.

Much of the methodology in this section relies on morphology code written by J. Lotz and described in detail in Lotz et al. (2004). Here, we summarize the relevant information. Postage stamps of each object in the SExtractor catalog (and the associated segmentation map) are created with foreground/background objects masked out. Using a small region of the cutout devoid of sources, a sky value is computed and subtracted from the postage stamp. Next, we determine which pixels in each postage stamp belong to the galaxy and which do not. Since the isophotal-based segmentation map produced by SExtractor is subject to the effects of surface brightness dimming at high redshift, we use a segmentation map based on the mean surface brightness at the Petrosian radius $\mu(R_p)$. Pixels with surface brightness above $\mu(R_p)$ are assigned to the galaxy while those below it are not. We define R_p as the radius at which the ratio of the surface brightness at R_p to the mean surface brightness within R_p is equal to 0.2.

Using the new segmentation map, we recompute the galaxy's center by minimizing the total second-order moment of the flux. A new value of R_p is then computed and a revised segmentation map is used to calculate G and M_{20} . Finally the morphology code produces an average S/N per pixel value using the pixels in the revised segmentation map (Eqs. 1 through 5 in Lotz et al., 2004).

One of the most common methods of characterizing galaxy morphologies in the literature is to measure the concentration index C (Abraham et al., 1994), the rotational asymmetry A (Schade et al., 1995), and the residual clumpiness, S (Conselice, 2003). Given sufficiently high S/N and spatial resolution, the CAS system has had demonstrated success in measuring morphological parameters and identifying mergers at low (Conselice, 2003) and high redshift (Conselice et al., 2008). Unfortunately, the objects in our sample do not meet simultaneously the S/N and spatial resolution

requirements to be reliably placed in CAS space. Because computation of A and S involves differencing two images, the necessary per-pixel S/N to measure these parameters reliably is twice as high as those that do not involve subtracting images. We find per-pixel S/N values ranging from ~ 2 -5 for the DOGs, whereas reliable measurements of A and S require $S/N \geq 5$ (Lotz et al., 2004). In principle, the data are of sufficient quality to measure C (see Tab. 2.2), but in practice we find that the inherent assumption of circular symmetry does not apply well to the DOGs, making the interpretation of C values difficult.

Table 2.2. Non-parametric Morphological Classifications

| Source Name | Visual ^a | ACS/WFPC2 | | | | | Visual ^a | NICMOS | | | | |
|------------------------|---------------------|-----------|-----------|------|----------|-----|---------------------|--------|-----------|------|----------|-------------------|
| | | S/N | R_p (") | G | M_{20} | C | | S/N | R_p (") | G | M_{20} | C |
| SST24 J142538.2+351855 | TFTT | — | — | — | — | — | <i>Reg</i> | — | — | — | — | — |
| SST24 J142622.0+345249 | Irr | 5.2 | 0.6 | 0.45 | -0.8 | 3.6 | <i>Irr</i> | 3.0 | 0.5 | 0.44 | -1.0 | 2.1 |
| SST24 J142626.4+344731 | Irr | — | — | — | — | — | <i>Reg</i> | — | — | — | — | — |
| SST24 J142644.3+333051 | TFTT | — | — | — | — | — | Reg | 10.7 | 0.3 | 0.56 | -1.8 | 3.3 |
| SST24 J142645.7+351901 | TFTT | — | — | — | — | — | Irr | 2.7 | 0.8 | 0.42 | -0.7 | 4.3 |
| SST24 J142648.9+332927 | <i>Irr</i> | 2.7 | 0.6 | 0.46 | -0.8 | 4.9 | <i>Reg</i> | 2.6 | 0.6 | 0.50 | -1.7 | 2.9 |
| SST24 J142653.2+330220 | Irr | 2.2 | 0.8 | 0.42 | -0.7 | 3.6 | <i>Reg</i> | 3.9 | 0.6 | 0.43 | -1.2 | 2.2 |
| SST24 J142804.1+332135 | TFTT | — | — | — | — | — | TFTT | — | — | — | — | — |
| SST24 J142924.8+353320 | TFTT | — | — | — | — | — | Irr | — | — | — | — | — |
| SST24 J142958.3+322615 | Reg | — | — | — | — | — | Reg | 3.8 | 0.5 | 0.46 | -1.4 | 2.3 |
| SST24 J143001.9+334538 | TFTT | — | — | — | — | — | TFTT | — | — | — | — | — |
| SST24 J143025.7+342957 | Reg | — | — | — | — | — | Reg | 6.1 | 0.6 | 0.54 | -1.7 | 2.9 |
| SST24 J143102.2+325152 | TFTT | — | — | — | — | — | TFTT | — | — | — | — | — |
| SST24 J143109.7+342802 | TFTT | — | — | — | — | — | Irr | — | — | — | — | — |
| SST24 J143135.2+325456 | TFTT | — | — | — | — | — | <i>Irr</i> | 2.8 | 1.3 | 0.52 | -2.5 | 4.7 |
| SST24 J143225.3+334716 | <i>Irr</i> | 3.9 | 0.4 | 0.37 | -1.6 | 2.4 | Reg | 5.1 | 0.5 | 0.50 | -1.4 | 2.8 |
| SST24 J143242.5+342232 | TFTT | — | — | — | — | — | Irr | — | — | — | — | — |
| SST24 J143251.8+333536 | TFTT | — | — | — | — | — | <i>Reg</i> | 4.7 | 0.9 | 0.47 | -1.7 | 2.7 |
| SST24 J143312.7+342011 | Irr | — | — | — | — | — | <i>Reg</i> | 3.8 | 1.1 | 0.51 | -1.4 | 3.3 |
| SST24 J143325.8+333736 | Reg | — | — | — | — | — | Reg | 5.1 | 1.0 | 0.54 | -1.9 | -2.1 ^b |
| SST24 J143358.0+332607 | Reg | — | — | — | — | — | Reg | 4.1 | 0.5 | 0.50 | -1.4 | 3.1 |
| SST24 J143447.7+330230 | TFTT | — | — | — | — | — | <i>Reg</i> | 4.3 | 0.5 | 0.46 | -1.2 | 2.0 |
| SST24 J143504.1+354743 | TFTT | — | — | — | — | — | <i>Reg</i> | 2.2 | 0.9 | 0.49 | -0.9 | -2.1 ^b |
| SST24 J143508.4+334739 | <i>Irr</i> | — | — | — | — | — | <i>Reg</i> | 4.1 | 0.8 | 0.53 | -1.2 | 2.9 |
| SST24 J143520.7+340418 | Reg | — | — | — | — | — | <i>Reg</i> | 3.3 | 0.4 | 0.47 | -0.9 | 3.3 |
| SST24 J143523.9+330706 | <i>Reg</i> | 5.2 | 0.5 | 0.56 | -1.2 | 2.8 | <i>Irr</i> | 6.3 | 0.4 | 0.47 | -1.2 | 2.3 |
| SST24 J143539.3+334159 | TFTT | — | — | — | — | — | Reg | 2.7 | 0.7 | 0.50 | -1.7 | 3.4 |
| SST24 J143545.1+342831 | TFTT | — | — | — | — | — | <i>Reg</i> | 4.6 | 0.6 | 0.55 | -1.6 | 3.2 |
| SST24 J143644.2+350627 | TFTT | — | — | — | — | — | <i>Reg</i> | 3.1 | 0.6 | 0.52 | -1.7 | 2.7 |
| SST24 J143725.1+341502 | TFTT | — | — | — | — | — | Reg | 2.5 | 0.9 | 0.52 | -2.1 | 3.7 |
| SST24 J143808.3+341016 | Irr | 2.3 | 1.3 | 0.44 | -0.9 | 3.6 | Irr | 2.3 | 1.0 | 0.48 | -1.6 | 3.2 |

Table 2.2 (cont'd)

| ACS/WFPC2 | | | | | | | NICMOS | | | | | | |
|-------------|---------------------|-------|-----------|-----|----------|-----|---------------------|-------|-----------|-----|----------|-----|--|
| Source Name | Visual ^a | S/N | R_p (") | G | M_{20} | C | Visual ^a | S/N | R_p (") | G | M_{20} | C | |

^a Mode of visual classification. Italics indicate multiple users disagreed with the mode.

^b Negative C value indicates r_{20} was too small to be measured accurately.

2.4 Results

2.4.1 Photometry

In Figure 2.4, we show the color-magnitude diagram for DOGs and a sample of galaxies in the HDF whose photometric redshifts are comparable to DOGs ($1.5 < z_{\text{phot}} < 2.5$). For DOGs where the measured flux is below the 2σ detection limit, we use an open plotting symbol and an upward pointing arrow. DOGs range in H -band magnitude from 21.93 to 25.1 AB mags. In both $V-H$ and $I-H$, DOGs are redder than a typical high- z galaxy by 0.2-3 AB mags. In particular, the LBGs from the HDF-N (Papovich et al., 2001) are comparably bright in H , but fainter in V by ≈ 2 AB mags than DOGs. There is substantial overlap between the colors of DOGs and DRGs, suggesting that we might expect to see similarities in the morphologies between these two populations. Table 2.3 summarizes the photometric information derived from the NDWFS and the *HST* imaging.

2.4.2 Morphologies

2.4.2.1 GALFIT Results

The results of our GALFIT analysis for the extended component Sérsic profile fit to the NICMOS images are shown in Table 2.4, along with $1-\sigma$ uncertainties in the best-fit parameters. The Sérsic indices (n) range from 0.1 to 2.2 (median $n = 0.9$).

Table 2.3. Photometric Properties^b

| Source Name | B_W | R | I | V (F606W) | I (F814W) | H (F160W) | F_{24} (mJy) | $R - [24]^c$ |
|------------------------|----------|----------|----------|-------------|-------------|-------------|----------------|--------------|
| SST24 J142538.2+351855 | > 26.6 | > 25.9 | > 25.5 | > 26.0 | — | 24.0±0.1 | 0.85±0.05 | > 16.1 |
| SST24 J142622.0+345249 | 24.5±0.1 | 24.5±0.3 | 24.0±0.3 | — | 24.18±0.06 | 23.6±0.1 | 1.29±0.05 | 15.2 |
| SST24 J142626.4+344731 | > 26.6 | > 25.4 | > 25.2 | > 26.4 | — | 23.7±0.1 | 1.17±0.04 | > 16.0 |
| SST24 J142644.3+333051 | > 26.5 | 24.3±0.2 | 24.3±0.2 | 25.9±0.3 | — | 21.93±0.02 | 1.14±0.04 | 14.9 |
| SST24 J142645.7+351901 | > 26.6 | > 25.8 | 24.5±0.3 | > 26.2 | — | 23.31±0.09 | 1.14±0.05 | > 16.3 |
| SST24 J142648.9+332927 | 25.1±0.2 | > 25.0 | 24.1±0.1 | — | 24.9±0.2 | 23.3±0.1 | 2.33±0.07 | > 16.3 |
| SST24 J142653.2+330220 | > 26.6 | > 26.1 | 24.7±0.3 | — | 25.0±0.2 | 22.7±0.1 | 0.88±0.05 | > 16.3 |
| SST24 J142804.1+332135 | > 26.4 | > 25.7 | > 25.3 | > 26.6 | — | 25.1±0.5 | 0.84±0.03 | > 15.9 |
| SST24 J142924.8+353320 | > 26.6 | > 25.4 | > 24.9 | > 26.1 | — | 24.7±0.3 | 1.04±0.05 | > 15.9 |
| SST24 J142958.3+322615 | 25.6±0.1 | > 25.7 | > 25.4 | 25.5±0.3 | — | 23.26±0.09 | 1.18±0.05 | > 16.2 |
| SST24 J143001.9+334538 | > 26.4 | > 25.8 | > 25.1 | > 26.5 | — | 24.9±0.3 | 3.84±0.06 | > 17.7 |
| SST24 J143025.7+342957 | 24.6±0.1 | 24.0±0.1 | 23.9±0.1 | 24.21±0.07 | — | 22.29±0.03 | 2.47±0.05 | 15.4 |
| SST24 J143102.2+325152 | > 25.7 | > 25.2 | > 25.2 | > 26.0 | — | > 25.1 | 1.19±0.05 | > 15.8 |
| SST24 J143109.7+342802 | > 26.4 | > 25.5 | > 25.2 | > 26.3 | — | 23.6±0.1 | 1.11±0.04 | > 16.0 |
| SST24 J143135.2+325456 | 24.7±0.1 | 23.9±0.1 | 23.5±0.1 | 25.1±0.2 | — | 22.04±0.03 | 1.51±0.05 | 14.8 |
| SST24 J143225.3+334716 | > 26.9 | > 25.3 | > 25.2 | — | 26.0±0.4 | 22.8±0.1 | 1.28±0.05 | > 16.0 |
| SST24 J143242.5+342232 | > 26.5 | > 25.3 | > 25.1 | > 26.7 | — | 22.68±0.04 | 0.91±0.04 | > 15.6 |
| SST24 J143251.8+333536 | > 26.5 | > 25.5 | > 25.1 | > 26.5 | — | 22.20±0.03 | 0.82±0.04 | > 15.7 |
| SST24 J143312.7+342011 | 24.5±0.1 | 24.2±0.2 | 23.9±0.1 | 24.7±0.1 | — | 22.23±0.04 | 1.76±0.04 | 15.2 |
| SST24 J143325.8+333736 | 25.6±0.3 | 24.6±0.3 | 23.9±0.2 | 25.6±0.3 | — | 21.52±0.03 | 1.87±0.06 | 15.6 |
| SST24 J143358.0+332607 | > 26.7 | > 25.9 | > 25.3 | — | > 25.9 | 23.09±0.06 | 1.07±0.04 | > 16.3 |
| SST24 J143447.7+330230 | > 26.6 | > 26.1 | > 25.2 | > 26.0 | — | 23.1±0.1 | 1.71±0.04 | > 17.1 |
| SST24 J143504.1+354743 | > 26.6 | > 25.8 | > 25.5 | > 26.4 | — | 23.08±0.09 | 1.26±0.05 | > 16.5 |
| SST24 J143508.4+334739 | 24.6±0.1 | 24.1±0.1 | 23.8±0.1 | 23.87±0.05 | — | 22.69±0.07 | 2.65±0.08 | 15.6 |
| SST24 J143520.7+340418 | 24.8±0.1 | > 25.1 | 24.1±0.2 | > 26.2 | — | 24.0±0.2 | 1.53±0.06 | > 15.9 |
| SST24 J143523.9+330706 | > 26.8 | 25.0±0.2 | 24.9±0.3 | — | 24.7±0.2 | 22.93±0.06 | 1.09±0.05 | 15.5 |
| SST24 J143539.3+334159 | > 26.4 | > 25.5 | 24.7±0.3 | 25.1±0.2 | — | 23.1±0.1 | 2.67±0.06 | > 16.9 |
| SST24 J143545.1+342831 | > 26.9 | > 25.2 | > 25.0 | — | > 26.7 | 22.59±0.05 | 1.95±0.05 | > 16.3 |
| SST24 J143644.2+350627 | 24.7±0.1 | 24.3±0.1 | 24.0±0.2 | 25.6±0.2 | — | 22.70±0.07 | 2.34±0.05 | 15.6 |
| SST24 J143725.1+341502 | 25.4±0.2 | > 25.4 | > 25.2 | — | 26.1±0.6 | 22.70±0.08 | 1.41±0.05 | > 16.2 |
| SST24 J143808.3+341016 | 25.1±0.1 | 24.4±0.3 | 23.9±0.1 | — | 24.7±0.2 | 22.34±0.08 | 1.71±0.05 | 15.4 |

^a magnitude lower limits represent 2σ values.^b magnitudes given in AB system.^c $R - [24]$ color in Vega system.

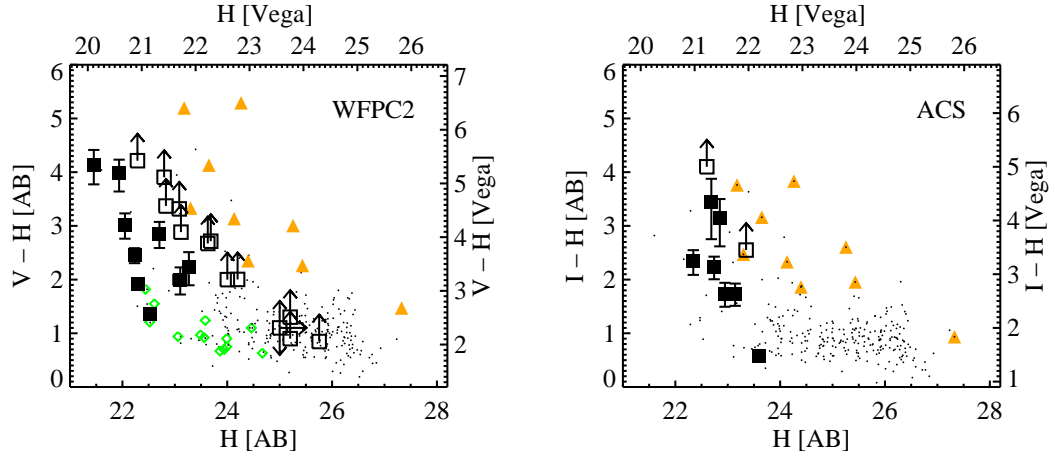


Figure 2.4 Color-magnitude diagram for DOGs. *Left:* $V - H$ vs. H for DOGs observed by WFC2 (filled black squares show detections, open black squares show lower limits). Galaxies spanning the redshift range $1.5 < z < 2.5$ in the HDF-N (Papovich, personal communication) and HDF-S (Labbé et al., 2003) are shown with black dots. Bright LBGs from the HDF-N are shown with green diamonds (Papovich et al., 2001). DRGs in the HDF-S are represented by filled orange triangles. *Right:* $I - H$ vs. H for DOGs observed by ACS. Symbols are the same as in left panel.

For those objects where $n < 1$, we note that constraining n to be equal to 1 does not significantly alter the remaining fit parameters. As the Sérsic index decreases, the radial profile flattens more rapidly within $r < R_{\text{eff}}$ and the intensity drops more steeply beyond $r > R_{\text{eff}}$. For reference, $n = 0.5$ corresponds to a Gaussian profile, $n = 1$ corresponds to an exponential profile, and $n = 4$ corresponds to a de Vaucouleurs profile (Peng et al., 2002). The ratio of the minor to major axis ranges from 0.20 to 0.88 with a median value of 0.53. In comparison, simulated merger remnants tend to have a luminous component in the shape of an oblate spheroid, with axis ratios of 1:1:0.5 (Novak et al., 2006). The projected axial ratio should thus vary between 0.5 and 1.0. Our observed median value of ≈ 0.5 suggests that DOGs have more disk-like profiles than the simulated merger remnants. This may be due to a non-merger origin for DOGs, or it may be an indication that DOGs have not progressed to the merger remnant stage.

Table 2.4. GALFIT Results

| | n | Axial Ratio | R_{eff} (kpc) | χ^2_{ν} ^a | χ^2_{ν} ^b | N_{dof} |
|------------------------|---------|-------------|---------------------------|-----------------------------|-----------------------------|------------------|
| SST24 J142538.2+351855 | 0.7±0.2 | 0.64±0.09 | 2.5±0.4 | 0.35 | 0.36 | 1653 |
| SST24 J142622.0+345249 | 0.1±0.1 | 0.55±0.04 | 2.5±1.0 | 0.92 | 0.92 | 1671 |
| SST24 J142626.4+344731 | 0.8±0.2 | 0.59±0.07 | 3.0±0.4 | 1.35 | 1.35 | 1671 |
| SST24 J142644.3+333051 | 5.6±3.4 | 0.71±0.07 | 1.1±0.3 | 1.16 | 2.58 | 1671 |
| SST24 J142645.7+351901 | 0.1±0.1 | 0.41±0.03 | 4.6±0.2 | 1.08 | 1.08 | 1671 |
| SST24 J142648.9+332927 | 0.7±0.3 | 0.70±0.05 | 1.8±0.1 | 1.08 | 1.08 | 1561 |
| SST24 J142653.2+330220 | 0.4±0.1 | 0.85±0.03 | 2.9±0.1 | 0.95 | 0.96 | 1671 |
| SST24 J142804.1+332135 | 1.0±0.6 | 0.19±0.06 | 6.4±2.6 | 0.95 | 0.96 | 1671 |
| SST24 J142924.8+353320 | 0.8±0.3 | 0.35±0.06 | 2.8±0.4 | 1.04 | 1.07 | 1671 |
| SST24 J142958.3+322615 | 0.4±0.1 | 0.78±0.03 | 2.1±0.1 | 0.36 | 0.39 | 1671 |
| SST24 J143001.9+334538 | 1.0±1.3 | 0.6±0.1 | 1.2±0.3 | 0.49 | 0.49 | 1671 |
| SST24 J143025.7+342957 | 1.0±0.1 | 0.52±0.02 | 1.8±0.1 | 0.90 | 0.96 | 1671 |
| SST24 J143102.2+325152 | — | — | — | — | — | — |
| SST24 J143109.7+342802 | 1.2±0.4 | 0.36±0.05 | 7.0±1.7 | 1.15 | 1.15 | 1671 |
| SST24 J143135.2+325456 | 0.5±0.1 | 0.53±0.01 | 3.8±0.1 | 1.54 | 1.56 | 1671 |
| SST24 J143225.3+334716 | 0.9±0.2 | 0.55±0.03 | 1.9±0.1 | 0.93 | 0.94 | 1671 |
| SST24 J143242.5+342232 | 2.0±0.4 | 0.50±0.06 | 4.0±0.8 | 0.57 | 0.58 | 1601 |
| SST24 J143251.8+333536 | 0.8±0.1 | 0.50±0.02 | 3.3±0.1 | 0.50 | 0.52 | 1671 |
| SST24 J143312.7+342011 | 0.7±0.1 | 0.51±0.01 | 4.0±0.1 | 0.63 | 0.66 | 1671 |
| SST24 J143325.8+333736 | 1.3±0.1 | 0.70±0.01 | 3.1±0.1 | 0.52 | 0.60 | 1671 |
| SST24 J143358.0+332607 | 2.1±0.5 | 0.84±0.07 | 1.4±0.1 | 0.49 | 0.48 | 1671 |
| SST24 J143447.7+330230 | 0.4±0.1 | 0.88±0.04 | 1.9±0.1 | 0.88 | 0.89 | 1671 |
| SST24 J143504.1+354743 | 0.5±0.1 | 0.43±0.03 | 4.6±0.3 | 0.91 | 0.93 | 1671 |
| SST24 J143508.4+334739 | 2.6±0.4 | 0.40±0.03 | 2.2±0.2 | 1.06 | 1.10 | 1671 |
| SST24 J143520.7+340418 | 0.6±0.4 | 0.5±0.1 | 3.4±0.7 | 1.08 | 1.10 | 1671 |
| SST24 J143523.9+330706 | 0.5±0.1 | 0.46±0.02 | 1.5±0.1 | 1.00 | 1.05 | 1671 |
| SST24 J143539.3+334159 | 1.8±0.5 | 0.82±0.09 | 3.7±0.7 | 0.91 | 0.92 | 1671 |
| SST24 J143545.1+342831 | 1.1±0.2 | 0.49±0.03 | 2.2±0.1 | 1.04 | 1.06 | 1671 |
| SST24 J143644.2+350627 | 0.9±0.2 | 0.70±0.05 | 1.9±0.1 | 1.22 | 1.23 | 1670 |
| SST24 J143725.1+341502 | 0.3±0.1 | 0.50±0.03 | 3.4±0.2 | 1.09 | 1.14 | 1424 |
| SST24 J143808.3+341016 | 0.9±0.1 | 0.81±0.04 | 3.0±0.2 | 1.37 | 1.38 | 1671 |

Table 2.4 (cont'd)

| n | Axial Ratio | R_{eff} | | χ^2_{ν} ^a | χ^2_{ν} ^b | N_{dof} |
|-----|-------------|------------------|--|-----------------------------|-----------------------------|------------------|
| | | (kpc) | | | | |

^aAssuming finite PSF contribution^bAssuming zero PSF contribution

It is possible for a degeneracy to arise in the fitting parameters, in the sense that a high- n , low point source fraction model may be comparable to a low- n , high point source fraction model. We have tested this by running GALFIT with the point source fraction set to zero (i.e., removing the PSF component). The resulting n values range from 0.1 to 5.2 with a median of 2.0, which is still below the value of 4 that is typical of early-type galaxies. A total of 7 DOGs have $n > 3$ using this zero-point-source model. The best-fit R_{eff} values change by less than one pixel, with an offset of -0.2 ± 0.8 pixels. In general, as mentioned in section 2.3.2, the removal of the PSF component leads to larger reduced- χ^2 values (see columns 5 and 6 in Tab. 2.4). However, we note that only one case (SST24 J142644.3+333051) is associated with a >0.08 decrease in χ^2_{ν} after adding a non-zero PSF component. This suggests that the PSF component in most of the DOGs in this sample is not dominant at rest-frame optical wavelengths.

We find the effective radius, R_{eff} , ranges from 1.1 to 5.9 kpc with a median value of 2.5 kpc. In the left panel of Figure 2.5, we show the distribution of R_{eff} values for DOGs (dark shaded histogram), Distant Blue Galaxies (diagonal blue hatched; DBGs, i.e., galaxies with $z_{\text{phot}} > 2$ that satisfy $J - Ks < 2.3$; Toft et al., 2007), and DRGs (opposite diagonal red hatched; Zirm et al., 2007; Toft et al., 2007). Two-sided K-S tests show that DOGs are dissimilar from both populations,

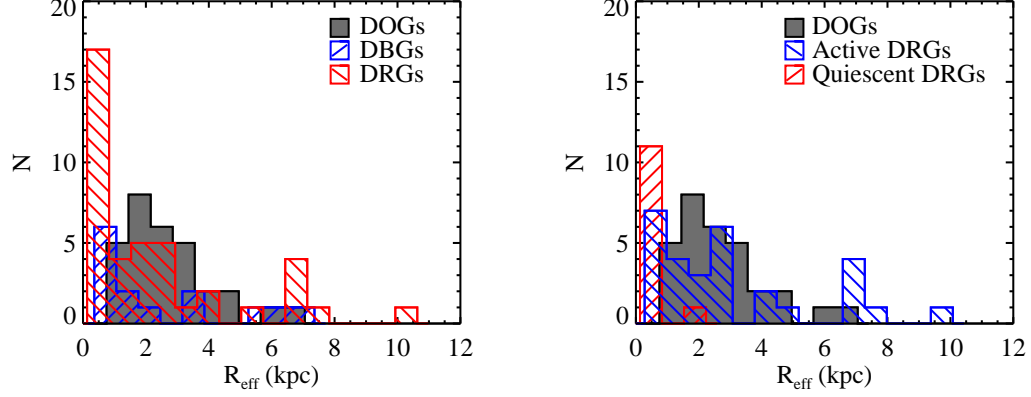


Figure 2.5 *Left*: Distribution of effective radius, R_{eff} , for an unconstrained Sérsic profile matched to the DOGs using GALFIT (filled grey region), DBGs (Distant Blue Galaxies, diagonal hatched blue region) and DRGs (opposite diagonal hatched red region). *Right*: Distribution of R_{eff} values for DOGs (filled grey region), active DRGs (diagonal hatched blue region), and quiescent DRGs (opposite diagonal hatched red region). DBG and DRG data from Zirm et al. (2007) and Toft et al. (2007).

with a $<7\%$ and $<4\%$ chance of being drawn from the same parent distribution, respectively. Based on the nature of their UV-NIR SED, DRGs may be separated into those that are actively forming stars (active DRGs or sDRGs) and those that are not (quiescent DRGs or qDRGs, see Zirm et al., 2007; Toft et al., 2007). The right panel of Figure 2.5 shows the DOG R_{eff} distribution in comparison to active DRGs (diagonal blue hatched) and quiescent DRGs (opposite diagonal red hatched). Quiescent DRGs have much smaller effective radii, while active DRGs are much closer to DOGs. Here the two-sided K-S test gives a 99.9994% and 34% chance of being drawn from different parent distributions, respectively, suggesting that the DOG and active DRG populations may overlap.

In Table 2.5, we give the V , I , and H magnitudes of the nuclear (PSF) component and the extended (galaxy) component, as well as the fraction of light contributed by a point source (including $1\text{-}\sigma$ uncertainties). When the nuclear component is not detected, we quote the $3\text{-}\sigma$ limit on the point source fraction. The magnitude of the PSF component is measured using the same aperture photometry method described in Section 2.2.4, with the exception that the sky background is assumed to be zero. For the extended component, we subtract the PSF component from the science image and compute the photometry in the usual way on the residual image. The fraction of light due to an unresolved component in the rest-optical ranges from 0.04 to 0.78, and the median is 0.12. In the rest-UV, however, this fraction is significantly smaller, with only one object having a detected fraction. This object, SST24 J143523.9+330706, stands out as unique by virtue of having a greater point source fraction in the rest-UV than in the rest-optical. This behavior is unique within our sample (but is expected when the AGN is viewed without obscuration) and is also reflected in the non-parametric measures of its morphology (see Sect. 2.4.2.2 for more detail).

Figure 2.6 shows the $V - H$ and $I - H$ colors of the nuclear, extended, and full galaxy components as a function of H , in AB magnitudes. High- z galaxies and DRGs in the HDF-N and HDF-S are also shown. The full galaxy and extended components have similar colors and H magnitudes, consistent with the nuclear component not dominating the flux. This is why even the extended components of DOGs are redder in both $V - H$ and $I - H$ compared to Lyman break galaxies (LBGs) in the HDF, and suggests that one cannot create a DOG simply by adding an obscured AGN to a star-forming galaxy like an LBG. DRGs show greater overlap with the colors of DOGs but few are as bright in H as the DOGs in our sample.

Table 2.5. PSF Subtraction Analysis

| Source Name | V_{nuc} | I_{nuc} | H_{nuc} | V_{gal} | I_{gal} | H_{gal} | $f_{\text{PSF}}^{\text{opt}}$ | $f_{\text{PSF}}^{\text{ir}}$ |
|------------------------|------------------|------------------|------------------|------------------|------------------|------------------|-------------------------------|------------------------------|
| SST24 J142538.2+351855 | > 28.3 | — | 27±2 | > 26.0 | — | 24.1±0.3 | — | <0.27 |
| SST24 J142622.0+345249 | — | > 27.9 | 27±1 | — | 24.2±0.1 | 23.6±0.2 | <0.01 | <0.15 |
| SST24 J142626.4+344731 | > 27.6 | — | 26.8±0.3 | > 26.4 | — | 23.7±0.2 | — | <0.07 |
| SST24 J142644.3+333051 | > 28.1 | — | 22.3±0.1 | 26.1±0.6 | — | 23.4±0.1 | <0.06 | 0.73±0.07 |
| SST24 J142645.7+351901 | > 27.7 | — | 27±1 | > 26.2 | — | 22.9±0.1 | — | <0.08 |
| SST24 J142648.9+332927 | — | > 28.1 | 25.2±0.3 | — | 24.9±0.4 | 23.3±0.2 | <0.03 | 0.15±0.06 |
| SST24 J142653.2+330220 | — | > 28.3 | 25.8±0.2 | — | 25.0±0.4 | 22.8±0.2 | <0.01 | 0.06±0.03 |
| SST24 J142804.1+332135 | > 27.7 | — | 26.1±0.5 | > 26.6 | — | > 25.2 | — | — |
| SST24 J142924.8+353320 | > 27.9 | — | 25.9±0.5 | > 26.1 | — | > 25.3 | — | — |
| SST24 J142958.3+322615 | > 28.2 | — | 25.0±0.1 | 25.6±0.6 | — | 23.5±0.2 | <0.01 | 0.20±0.03 |
| SST24 J143001.9+334538 | > 27.9 | — | 26.6±0.9 | > 26.5 | — | > 25.5 | — | <0.53 |
| SST24 J143025.7+342957 | > 28.4 | — | 23.9±0.1 | 24.2±0.2 | — | 22.58±0.07 | <0.01 | 0.24±0.03 |
| SST24 J143102.2+325152 | > 27.8 | — | > 27.0 | > 26.0 | — | > 25.1 | — | — |
| SST24 J143109.7+342802 | > 27.9 | — | 27±1 | > 26.3 | — | 23.78±0.3 | — | <0.18 |
| SST24 J143135.2+325456 | > 27.8 | — | 26.1±0.3 | 25.2±0.5 | — | 22.1±0.1 | <0.06 | <0.02 |
| SST24 J143225.3+334716 | — | > 28.3 | 24.8±0.1 | — | 26±1 | 23.0±0.2 | <0.02 | 0.17±0.04 |
| SST24 J143242.5+342232 | > 28.5 | — | 25.4±0.2 | > 26.7 | — | 22.9±0.1 | — | 0.09±0.03 |
| SST24 J143251.8+333536 | > 28.7 | — | 24.9±0.1 | > 26.5 | — | 22.4±0.1 | — | 0.09±0.01 |
| SST24 J143312.7+342011 | > 27.9 | — | 24.6±0.1 | 24.7±0.3 | — | 22.4±0.1 | <0.04 | 0.12±0.02 |
| SST24 J143325.8+333736 | > 27.6 | — | 23.6±0.1 | 25.8±0.7 | — | 21.6±0.1 | — | 0.13±0.02 |
| SST24 J143358.0+332607 | — | 27.5±0.5 | 25.8±0.3 | — | > 25.9 | 23.5±0.2 | — | 0.10±0.05 |
| SST24 J143447.7+330230 | > 27.9 | — | 25.8±0.6 | > 26.0 | — | 23.2±0.2 | — | <0.12 |
| SST24 J143504.1+354743 | > 27.7 | — | 24.9±0.2 | > 26.4 | — | 23.3±0.2 | — | 0.18±0.05 |
| SST24 J143508.4+334739 | 27±2 | — | 24.9±0.3 | 23.9±0.1 | — | 22.6±0.1 | <0.14 | 0.11±0.04 |
| SST24 J143520.7+340418 | > 28.1 | — | 24.9±0.1 | > 26.2 | — | 25.0±0.5 | — | 0.5±0.1 |
| SST24 J143523.9+330706 | — | 26.2±0.2 | 24.9±0.2 | — | 25.0±0.5 | 23.1±0.1 | 0.24±0.04 | 0.17±0.03 |
| SST24 J143539.3+334159 | > 28.4 | — | 25.2±0.2 | 25.2±0.5 | — | 23.3±0.3 | <0.01 | 0.15±0.06 |
| SST24 J143545.1+342831 | — | > 28.0 | 24.2±0.1 | — | > 26.7 | 22.9±0.1 | — | 0.22±0.03 |
| SST24 J143644.2+350627 | 28±1 | — | 24.9±0.3 | 25.7±0.4 | — | 22.9±0.1 | <0.11 | 0.13±0.04 |
| SST24 J143725.1+341502 | — | > 28.1 | 23.6±0.1 | — | > 26.2 | 23.3±0.2 | — | 0.43±0.05 |
| SST24 J143808.3+341016 | — | > 28.3 | 25.9±0.4 | — | 24.7±0.4 | 22.4±0.2 | <0.01 | <0.06 |

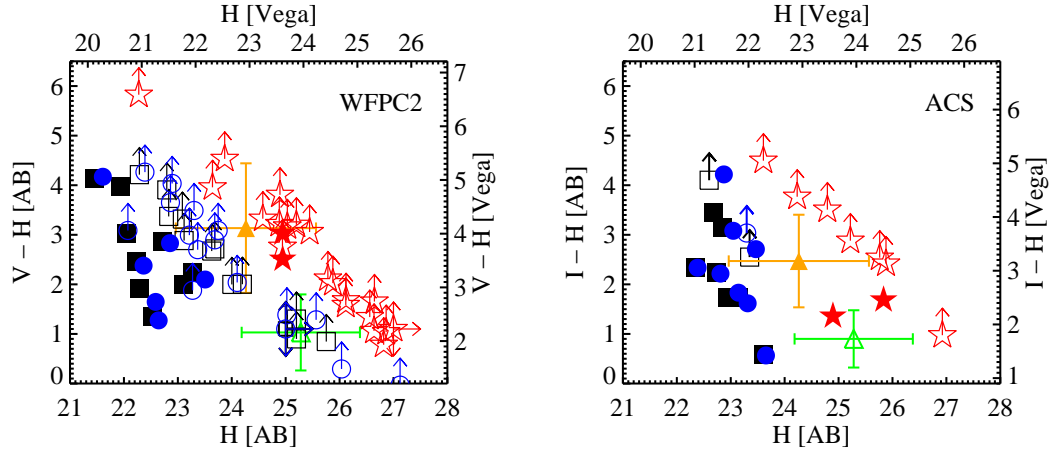


Figure 2.6 Color-magnitude diagram for DOGs, broken down into an extended component (unconstrained Sérsic profile) and an unresolved nuclear component (from TinyTim PSF). *Left:* $V - H$ vs. H for DOGs observed by WFPC2 (black squares). The extended component of each DOG is shown with a blue circle and the point source with a red star. Detections (Lower limits) are plotted with filled (open) symbols. Open green triangles show the median and 1σ dispersion in colors of high- z galaxies from the HDF-N (Papovich, personal communication and HDF-S (Labbé et al., 2003)). The subset of these galaxies qualifying as DRGs are shown with a filled orange triangle. *Right:* $I - H$ vs. H for DOGs observed by ACS. Symbols are same as in left panel.

2.4.2.2 Non-parametric Classification Results

Non-parametric methods of characterizing galaxy morphology are known to require high S/N imaging to yield reliable results (Lotz et al., 2004). In the rest-UV, where the DOGs are very faint, none of the 22 WFPC2 images and only 6 out of 9 ACS images have the per-pixel S/N necessary to compute R_p , G , M_{20} , and C . In the rest-optical, however, DOGs are much brighter and 23 out of 31 NICMOS images have sufficient S/N. Table 2.2 presents the visual and non-parametric measures of DOG morphologies, including the per-pixel S/N, R_p , G , M_{20} , and C values for the ACS/WFPC2 and NICMOS images.

In the left panel of Figure 2.7, we plot G as a function of M_{20} as measured in the rest-UV for DOGs, a field galaxy sample, and simulated $r^{1/4}$ bulges and pure exponential disks (Lotz et al., 2006). None of the DOGs fall within the pure exponential disk- or $r^{1/4}$ bulge-dominated regime. The field galaxy population is composed of sources identified within the ACS FOVs and is selected to span the same magnitude range as the DOGs in our sample. We use our NDWFS data to apply color cuts in $B_W - R$ and $R - I$ space in order to remove objects with colors typical of $z < 0.7$ sources. The morphologies of this field galaxy sample are represented with gray contours. Four out of six DOGs lie in the lower left corner of the plot, with low G and high M_{20} values indicating irregular, diffuse morphologies. In general, low G and high M_{20} values are indicative of dust-enshrouded stellar populations, where obscuration by dust causes a galaxy to appear very clumpy with flux distributed among many pixels (Lotz et al., 2008).

One object (SST24 J143523.9+330706, panel 27 in Fig. 2.3) has a higher G and lower M_{20} value than nearly all of the field galaxies. This is the same object that shows a stronger point-source contribution in the rest-UV than the rest-optical. Visual inspection of this object’s cutout image reveals an extended feature fading

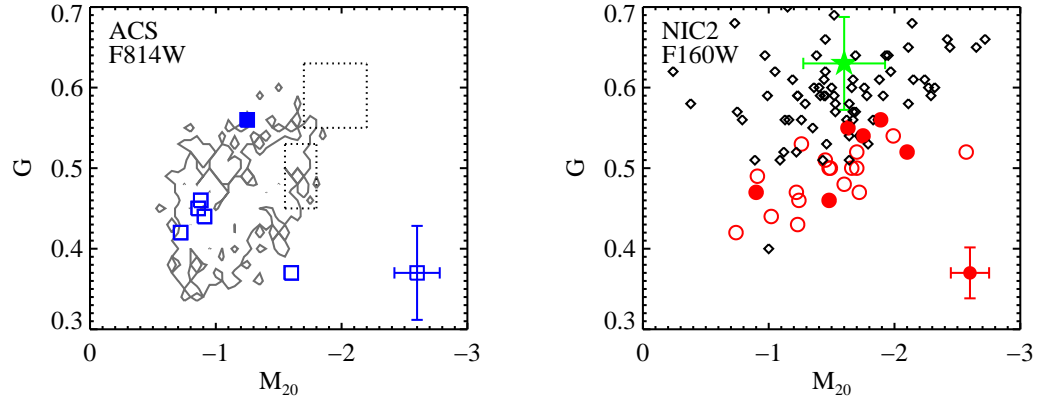


Figure 2.7 Gini coefficient vs. M_{20} . *Left:* Morphological measures from ACS/F814W images of DOGs (blue squares) and field galaxies (grey solid contours, see text). Representative error bars in the lower right corner include uncertainties due both to low S/N and low spatial resolution and are estimated using a method similar to that in Lotz et al. (2004). Filled symbols have greater than 20% point-source contribution. Top and bottom dotted boxes show where simulated face-on bulges and disks lie, respectively (Lotz et al., 2006). *Right:* Same plot but showing results from NIC2/F160W images of DOGs (red circles), HDF-N LBGs (filled green star) and a sample of local ULIRGs (black diamonds) (Lotz et al., 2004).

towards the southeast that is present in both the rest-UV and rest-optical. It appears that the central activity in this source is not quite as obscured as in other DOGs, but it is not yet clear why this is the case.

The right panel in Figure 2.7 shows G and M_{20} values as measured in the rest-optical for DOGs as well as LBGs in the HDF-N and a sample of local ($z < 0.1$) ULIRGs (Lotz et al., 2004). DOGs shift to more typical morphological parameters in the rest-optical compared to the rest-UV, but they are offset from the parameter space occupied by LBGs and local ULIRGs. The median G and M_{20} values for DOGs are 0.49 and -1.24 , respectively, while for LBGs they are 0.63 and -1.6 and for local ULIRGs they are 0.59 and -1.5 . Part of the difference in G and M_{20} compared to LBGs may be that LBGs are more compact, and hence less resolved. The offset to lower G values in DOGs compared to local ULIRGs is remarkable and indicates that either different mechanisms are involved in creating these two populations, or they represent different stages in the evolution of massive galaxies. We note that the ULIRG sample has comparable S/N as the DOGs studied here, and that the rest-frame wavelength of both samples is similar (~ 7000 Å vs. ~ 5300 Å, respectively). While there is a greater relative difference in the spatial resolution of the two samples (≈ 0.2 kpc pix $^{-1}$ vs. ≈ 0.6 kpc pix $^{-1}$, respectively), Lotz et al. (2004) found that systematic offsets at these resolutions should be on the order of 20% or less for C and M_{20} and less than 10% for G . Therefore, the difference in G cannot be explained by spatial resolution effects alone.

As a qualitative consistency check, we examined R -band images of a sample of 56 ULIRGs from Murphy et al. (1996) and determined that 20 (35%) have double nuclei with nuclear separations larger than 2.3 kpc, approximately the resolution limit of our NIC2 images. In comparison, only one DOG has two well-detected, distinct nuclei and three or four have low S/N components separated by $0''.5$ (≈ 4 kpc),

implying that at most 16% of the DOGs in our sample have multiple nuclei with separations larger than 2.3 kpc. This result is qualitatively consistent with the differences seen in G between local ULIRGs and DOGs. An important caveat with this analysis is that our sample of DOGs is dominated by power-law sources, while the ULIRG sample has a variety of rest-frame NIR SED shapes. For reference, we measured the G and M_{20} values of a well-detected, non-DOG point source (S/N per pixel of 18) in one of our NIC2 images, and found values of 0.62 and -1.7 , respectively. The DOG whose morphology is dominated by a point source (see panel 31 in Fig. 2.3) has a lower G value (0.56) but almost the same M_{20} (-1.8). This may be an indication that this DOG contains an underlying extended component, but the data are not conclusive.

2.5 Discussion

2.5.1 Dust and Stellar Mass Estimates

Here we estimate some of the intrinsic properties of DOGs, including lower limits on their reddening (A_V), dust and gas masses, and stellar masses. To do this, we use Simple Stellar Population (SSP) template SEDs from the Bruzual & Charlot (2003) population synthesis library with ages spaced logarithmically from 10 Myr up to 1 Gyr, as well as the median QSO template from Elvis et al. (1994). All models used here have solar metallicity, a Chabrier IMF over the mass range 0.1 - $100M_{\odot}$ (Chabrier, 2003), and use the Padova 1994 evolutionary tracks (Girardi et al., 1996). The reddening law used is a combination of that from Calzetti et al. (2000) and longer wavelength estimates from Draine (2003), and assumes the case of a dust screen in front of the emitting source in order to derive a firm lower limit on A_V .

For each DOG, we estimate A_V needed as a function of age by determining

the amount of extinction necessary to redden the given SSP template such that it reproduces the observed $V - H$ or $I - H$ color. The process is illustrated in Figure 2.8. Each panel shows the colors of DOGs in our sample as a function of redshift. Blue circles represent the extended component and red stars show the point source component of each DOG, as described in section 2.4.2.1. Dotted lines show the expected colors of the SSP templates for varying amounts of extinction. Even with no extinction ($A_V = 0$), the oldest SSP templates are too red to reproduce the colors exhibited by DOGs. The QSO templates, on the other hand, require large A_V values in order to match the DOG nuclear colors.

We use the relation from Bohlin et al. (1978) to convert A_V to the total column density of hydrogen atoms and molecules, N_H . For the 100 Myr SSP, the column densities range from $3 \times 10^{20} - 6 \times 10^{21} \text{ cm}^{-2}$, with a median N_H of $3 \times 10^{21} \text{ cm}^{-2}$. If we assume the dust is distributed in a spherical shell around the source with radius equal to the effective radius, then we can place a lower limit on the dust mass:

$$M_{\text{dust}} \geq \frac{1}{f_{\text{gd}}} \mu_p N_H \times 4\pi R_{\text{eff}}^2. \quad (2.1)$$

Here, f_{gd} is the gas-to-dust mass ratio and μ_p is the mean molecular weight of the gas, which we take to be $1.6m_p$, where m_p is the mass of a proton. We adopt the average gas-to-dust mass ratio of 120 measured for the nuclear regions of local ULIRGs by Wilson et al. (2008). We find dust mass lower limits ranging from $2 \times 10^5 - 6 \times 10^7 M_\odot$, with a median of $9 \times 10^6 M_\odot$ for a 100 Myr SSP.

A complementary method of estimating the dust mass is based on measurements of optically thin sub-mm emission. Because sub-mm photometry for the DOGs in our sample is currently unavailable, we extrapolate from the $24\mu\text{m}$ flux density measurement. We used the Mrk231 template to determine the extrapolated $850\mu\text{m}$ flux density, F_{850} . Using a template SED of a galaxy with colder dust such as Arp220

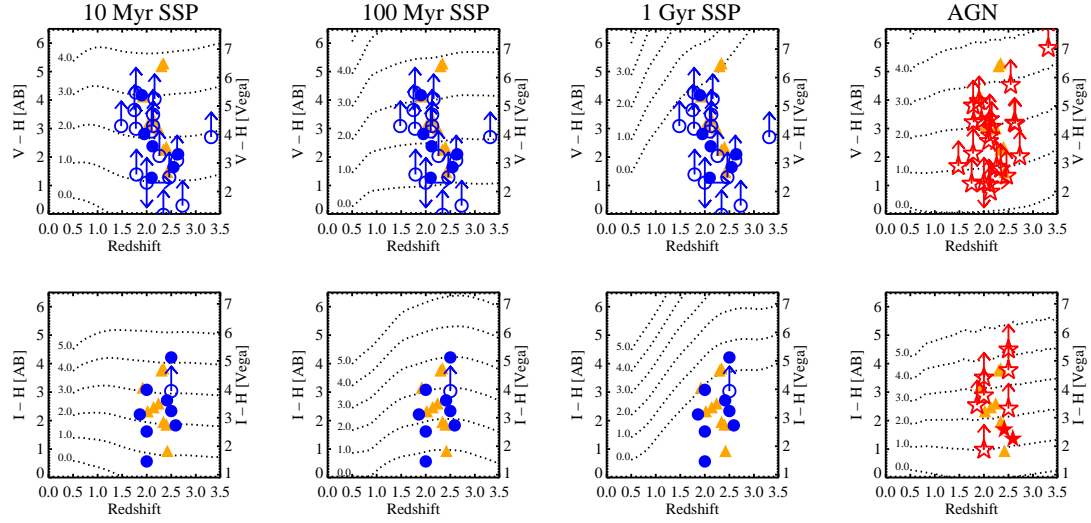


Figure 2.8 $V - H$ (top row) and $I - H$ (bottom row) as a function of spectroscopic redshift for each DOG. The first three columns show the colors of the extended component, while the fourth column shows the colors of the unresolved component (filled symbols are detections, open symbols are lower limits). Filled orange triangles represent DRGs in the HDF-S. Dotted lines trace the evolution of colors with redshift of reddened simple stellar population models from Bruzual & Charlot (2003) with solar metallicity, a Chabrier IMF and at ages of 10 Myr, 100 Myr, and 1 Gyr (three columns on left), as well as of the median QSO template from Elvis et al. (1994).

would increase the inferred $850\mu\text{m}$ flux. We follow Hughes et al. (1997) and estimate the dust mass using:

$$M_{\text{dust}} = \frac{1}{1+z} \frac{F_{850} d_L^2}{\kappa_d B(\nu, T_d)}, \quad (2.2)$$

where d_L is the luminosity distance, κ_d is the rest-frequency mass absorption coefficient, and $B(\nu, T)$ is the value of the modified blackbody function ($\beta = 1.5$) at the rest frequency ν and a temperature T . The appropriate κ_d value is interpolated from Draine (2003), with typical values being $5 \text{ cm}^2 \text{ g}^{-1}$. There is at least a factor of 2 uncertainty in this quantity. We have assumed relatively hot dust ($T_d = 75 \text{ K}$), since we expect AGN heating to play an important role in this sample of DOGs (a dust temperature of 50 K would increase the inferred dust mass by an additional factor of ≈ 1.5). Using this method, we find dust masses of $8 \times 10^7 - 6 \times 10^8 M_\odot$, with the median dust mass being $1.6 \times 10^8 M_\odot$. This is a factor of nearly 20 larger than the median dust mass inferred from the measurements of A_V . This might be expected, given that many of the dust masses based on A_V are lower limits, while the dust masses based on the $24\mu\text{m}$ emission may be overestimates if $T_d > 75 \text{ K}$. On the other hand, this difference may be suggesting that the dust causing the average UV extinction of the extended galaxy component is not the same dust that is causing the thermal emission.

We use the SSP templates to estimate the stellar mass in each DOG. This is computed by reddening each SSP template to match the observed color of the DOG at the appropriate redshift. We then scale the redshifted, reddened template to match the observed H-band photometry. Since the Bruzual & Charlot (2003) models are normalized to a stellar mass of $1 M_\odot$, this scaling factor represents the stellar mass of the DOG.

In Figure 2.9, we show the stellar mass of each DOG as a function of age as

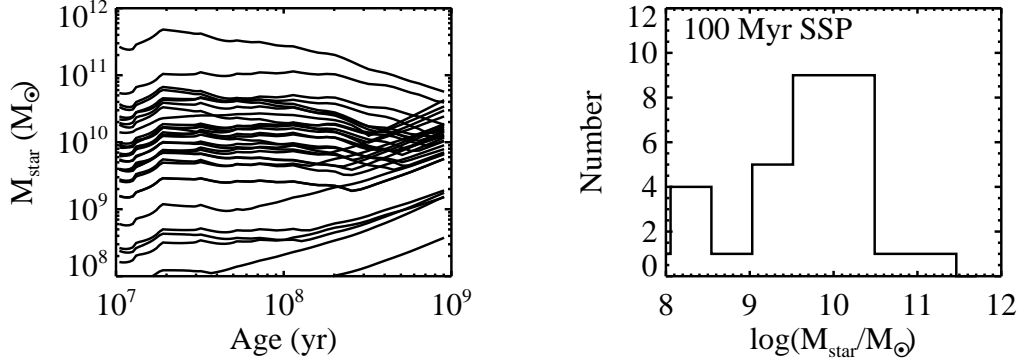


Figure 2.9 *Left*: Stellar mass as a function of SSP age for the DOGs. *Right*: Distribution of stellar masses at an age of 100 Myr.

well as the distribution of stellar masses assuming a 100 Myr SSP model. As stellar populations age, their colors naturally redden, and so less extinction is needed to reproduce the observed colors of the DOGs. For most DOGs, ages greater than ~ 300 Myr require A_V values less than zero and are unphysical. Meanwhile, at younger ages, lower mass-to-light ratios are balanced by the need for greater extinction to match the observed colors. As a result, the inferred stellar masses are relatively constant to within a factor of a few for ages less than 300 Myr. We note that these mass estimates are lower limits because (1) the amount of extinction is a lower limit, especially when there is no detection in the V - or I -band image and (2) our extinction estimate does not take into account grey extinction. For an age of 100 Myr, the stellar masses range from $7 \times 10^8 - 5 \times 10^{11} M_{\odot}$, with the median mass being $1.0 \times 10^{10} M_{\odot}$.

We use our dust mass estimates inferred from the $24\mu\text{m}$ flux densities and a gas-to-dust mass ratio of 120 (Wilson et al., 2008) to obtain an upper limit on the gas masses. This leads to gas masses of $1\text{--}7 \times 10^{10} M_{\odot}$, with a median gas mass of 2×10^{10} .

If we assume a closed-box model and an exponential star-formation history, then we can write $M_{\text{gas}} + M_{\text{dust}} = M_{\text{tot}} \exp(-t/t_0)$, where M_{tot} is the sum of the gas, dust, and stellar masses. The stellar mass is then given by $M_{\text{star}} = M_{\text{tot}}(1 - \exp(-t/t_0))$, which implies

$$\frac{t}{t_0} = \ln \frac{M_{\text{tot}}}{M_{\text{gas}} + M_{\text{dust}}}. \quad (2.3)$$

This quantity represents the fractional lifetime (in units of the scale time for our exponential star-formation rate assumption) of each DOG. Larger values of t/t_0 indicate more evolved systems, as more of the gas has been converted to stars. Our values of t/t_0 represent lower limits on the actual values because our stellar masses are underestimated and our gas masses are based on our $24\mu\text{m}$ flux densities, which likely overestimates the true mass of gas. We find t/t_0 lower limits ranging from 0.01 to 2.4, with a median lower limit of 0.4. This result implies that in half of the DOGs in our sample, at least 40% of one exponential timescale’s worth of star-formation has occurred. The “oldest” DOG in our sample has gone through at least two and a half exponential timescales of evolution. However, we caution that the “youngest” DOGs from this line of analysis are uniformly associated with sources where the dust extinction is most likely underestimated, thereby causing an additional underestimate in the stellar mass and the associated t/t_0 value. In Table 2.6, we present the dust and stellar masses derived in this section, as well as our measure of the lower limit on the fractional lifetime, t/t_0 .

Table 2.6. DOG Mass Estimates

| | $M_{\text{dust}}^{\text{a}}$ ($10^7 M_{\odot}$) | $M_{\text{star}}^{\text{b}}$ ($10^{10} M_{\odot}$) | t/t_0^{c} |
|------------------------|--|---|--------------------|
| SST24 J142538.2+351855 | 0.8 – 11 | 0.8 | 0.5 |
| SST24 J142622.0+345249 | 0.5 – 13 | 0.4 | 0.2 |
| SST24 J142626.4+344731 | 2.0 – 15 | 2.9 | 1.0 |
| SST24 J142644.3+333051 | 0.3 – 32 | 11. | 1.4 |
| SST24 J142645.7+351901 | 5.2 – 13 | 5.1 | 1.5 |
| SST24 J142648.9+332927 | 0.7 – 24 | 1.3 | 0.4 |
| SST24 J142653.2+330220 | 2.9 – 8 | 3.8 | 1.6 |
| SST24 J142804.1+332135 | 2.8 – 12 | 0.02 | 0.02 |
| SST24 J142924.8+353320 | 0.2 – 16 | 0.08 | 0.04 |
| SST24 J142958.3+322615 | 0.5 – 19 | 2.0 | 0.6 |
| SST24 J143001.9+334538 | 0.1 – 60 | 0.1 | 0.02 |
| SST24 J143025.7+342957 | 0.3 – 37 | 2.8 | 0.5 |
| SST24 J143102.2+325152 | — | — | — |
| SST24 J143109.7+342802 | 7.7 – 13 | 2.2 | 0.9 |
| SST24 J143135.2+325456 | 4.9 – 29 | 4.5 | 0.8 |
| SST24 J143225.3+334716 | 1.7 – 13 | 9.6 | 2.0 |
| SST24 J143242.5+342232 | 4.7 – 11 | 13. | 2.4 |
| SST24 J143251.8+333536 | 3.5 – 9 | 13. | 2.6 |
| SST24 J143312.7+342011 | 3.6 – 23 | 4.9 | 1.0 |
| SST24 J143325.8+333736 | 3.8 – 17 | 32. | 2.8 |
| SST24 J143358.0+332607 | 1.1 – 15 | 6.6 | 1.5 |
| SST24 J143447.7+330230 | 0.9 – 18 | 2.4 | 0.7 |
| SST24 J143504.1+354743 | 5.1 – 16 | 5.4 | 1.3 |
| SST24 J143508.4+334739 | 0.4 – 31 | 1.4 | 0.3 |
| SST24 J143520.7+340418 | 0.1 – 16 | 0.1 | 0.05 |
| SST24 J143523.9+330706 | 0.5 – 16 | 3.3 | 1.0 |
| SST24 J143539.3+334159 | 1.1 – 43 | 2.0 | 0.3 |
| SST24 J143545.1+342831 | 2.5 – 30 | 95. | 3.3 |
| SST24 J143644.2+350627 | 1.0 – 22 | 3.7 | 0.9 |
| SST24 J143725.1+341502 | 2.4 – 22 | 13. | 1.8 |
| SST24 J143808.3+341016 | 1.1 – 26 | 12. | 1.6 |

Table 2.6 (cont'd)

| $M_{\text{dust}}^{\text{a}}$ | $M_{\text{star}}^{\text{b}}$ | t/t_0^{c} |
|------------------------------|------------------------------|--------------------|
| $(10^7 M_{\odot})$ | $(10^{10} M_{\odot})$ | |

^aMass range reflects estimates based on A_V and $24\mu\text{m}$ flux density

^bStellar mass estimates represent lower limits on true stellar mass

^c t/t_0 estimates are lower limits based on $24\mu\text{m}$ dust masses

2.5.2 Comparison to other high redshift galaxy populations

It is important to understand how DOGs are related to other populations of high- z galaxies that have been studied in the literature. Here we compare the morphological properties of the DOGs with some of these high-redshift galaxy populations and find that DOG morphologies are distinct from the bulk of LBGs and quiescent high- z galaxies, but are similar to SMGs as well as active DRGs and the extreme subset of faint, diffuse LBGs.

2.5.2.1 Sub-mm Galaxies

SMGs are a particularly interesting population of galaxies to compare with DOGs. First identified by blind sub-mm surveys with the Submillimetre Common User Bolometer Array (SCUBA Holland et al., 1999), SMGs may represent an important, short-lived, and very active phase in the evolution of the most massive galaxies. Their redshift distribution, number density, and clustering properties are similar to DOGs (Chapman et al., 2005; Dey et al., 2008; Blain et al., 2004; Brodwin et al., 2008). However, a sample of DOGs detected at $70\mu\text{m}$ or $160\mu\text{m}$ by *Spitzer*/MIPS tend to show warmer colors (i.e., smaller $70/24\mu\text{m}$ or $160/24\mu\text{m}$ flux density ratios)

compared to SMGs (Tyler et al., submitted). One speculative scenario that may serve as a possible explanation for this behavior is that these two galaxy populations are linked in an evolutionary sense: SMGs represent a cold dust, star-formation dominated stage in the formation of massive galaxies that may precede the DOG phase, when the feedback from the growth of a central black hole has heated the surrounding gas and dust, thereby quenching star formation and shifting the peak of the SED to shorter wavelengths.

If this scenario is correct, then we expect to see major mergers dominate the morphologies of SMGs, while DOGs should show more relaxed morphologies typical of the final merger stage before the remnant. Conselice et al. (2003) analyzed Space Telescope Imaging Spectrograph (STIS) rest-frame UV data of a sample of 11 SMGs at $z \sim 2 - 3$ using the CAS system, and found evidence suggesting a major merger fraction of between 40% and 80%. Although we do not have the S/N in our images to measure A reliably (and thereby determine a major merger fraction in a similar manner), the low G and high M_{20} values we have measured imply diffuse, irregular systems where the light is spread into multiple components rather than 2 separate components. If the DOGs were predominantly major mergers, we would expect our sample to have higher G values. Instead, the low G values we find suggest that we may be looking at the dusty remnant of a major merger, where there are many highly obscured components near each other. However, we caution that dust can have a strong effect on the measured G value in the rest-UV, such that even major mergers might yield lower G values.

The rest-UV morphologies of SMGs have also been analyzed in the GOODS-N field, where a SCUBA super-map exists and has been used to identify robust sub-mm detections (Borys et al., 2003). A sample of 12 sources in the redshift range 1.7-4.0 (comparable to the DOGs) were studied by Pope et al. (2005), who computed

concentration and asymmetry values, finding C to be in the range 2-3.3 and A to be dominated by noise, with the exception of two objects (one is very compact and the other is clearly asymmetric). The comments associated with many of these sources are “faint” and “diffuse”, suggesting that there is large-scale dust obscuration in these systems. This is qualitatively similar to what is seen in many of the DOGs, suggesting that there is some overlap between the two samples.

SMGs have not yet been characterized in terms of G or M_{20} , so direct comparisons based on these quantities are not possible at this time. However, we can compare the sizes of these systems directly via the Petrosian radius. In the rest-UV, the DOGs range in size from $R_p \sim 0.5''$ to $1.5''$, while SMGs range in size from $0.5 - 2.5''$. Indeed, a two-sided KS test reveals that there is only a 5% chance that they are drawn from the same parent distribution. This suggests that, while there are similarities between SMGs and DOGs, SMGs tend to be slightly larger than DOGs. This is consistent with the major merger hypothesis in which DOGs are in a more evolved state where dynamical friction has caused individual components to fall towards the center of mass. However, we caution that this result in itself does not provide evidence for DOGs originating from major mergers. Objects moving at $\sim 100 \text{ km s}^{-1}$ will traverse 8 kpc in $\leq 100 \text{ Myr}$. Simulations of major mergers predict a phase of intense star formation and central black hole growth that lasts of order this timescale, indicating that the size differences are at least consistent with the scenario outlined above (Hopkins et al., 2008b).

Finally, the ratio of the stellar mass to the gas mass holds potential for comparing the evolutionary states of SMGs and DOGs. The ideal comparison study would include statistically significant samples of both populations of galaxies for a range of observed properties such as $24\mu\text{m}$ emission, bolometric luminosity, space density, etc. Unfortunately, such samples do not currently exist — mainly due to

a combination of the limitations of current instrumentation and the fact that these are relatively recently discovered populations of galaxies. While CO linewidths and emission strengths have found gas mass estimates for a handful of SMGs, no such measurements have been published for DOGs. The gas mass estimates for SMGs are typically $\sim 5 \times 10^{10} M_{\odot}$ (Greve et al., 2005; Tacconi et al., 2006, 2008). A number of efforts have been directed at determining the stellar masses of SMGs using SED-fitting algorithms. Average stellar mass values are in the range $3\text{--}6 \times 10^{11} M_{\odot}$ (Borys et al., 2005; Dye et al., 2008). However, when we employ our method of determining the stellar mass (in this case using the $R - K$ color to determine the optimal A_V value for a given SSP and age) using the photometry presented in those papers, we find average stellar masses of $\sim 3 \times 10^{10} M_{\odot}$. These estimates increase by a factor of ≈ 2 if instead of a Chabrier IMF we use a Salpeter IMF (as was done by the previous authors for SMGs). However, this still leaves us a factor of ≈ 5 short of the mass estimates provided in the papers described above. In order to compare DOG stellar masses with SMGs consistently, we adopt the lower stellar mass values that we derive for SMGs. In this case, the median t/t_0 values for SMGs becomes ≈ 0.5 , which is much closer to the median lower limit value of 0.4 found for the DOGs in section 2.5.1.

The large uncertainty inherent in the process of estimating dust and gas masses based on $24\mu\text{m}$ photometry or rest-frame optical A_V measurements currently prevents a strong conclusion being made regarding the evolutionary status using this line of analysis. However, the morphological evidence is suggestive — although not conclusive — of an evolutionary link between the two populations with SMGs serving as the less evolved precursor to the DOG phase.

2.5.2.2 Star-forming Galaxies

A number of selection criteria have been used to identify normal star-forming galaxies at high redshift. Two of these are the LBG dropout (Madau et al., 1996; Steidel et al., 1996) and *BzK* (Daddi et al., 2004) techniques. A direct comparison to our work can be made with a sample of LBGs and emission line galaxies in the GOODS-N field studied by Lotz et al. (2006). These authors compared G , M_{20} , and C values between their sample of 82 $z \sim 4$ LBGs and 55 $z \sim 1.5$ emission line galaxies. In the LBG sample, they found a major-merger fraction of $\sim 10 - 25\%$ (defined by $M_{20} \geq -1.1$) and a bulge-dominated fraction of $\sim 30\%$ ($G \geq 0.55$, $M_{20} < -1.6$). The remainder of the LBGs had G and M_{20} values larger than what is typical for normal galaxies, suggesting active star-formation or a recent merger event. The low- z emission-line sample showed a similar major merger fraction but fewer bulge-dominated systems. It is remarkable then, that so few of the DOGs have G and M_{20} values typical of bulge-dominated systems, even in the rest-optical, despite their luminosity. Furthermore, four out of six DOGs with measureable morphologies in the rest-UV have high M_{20} and low G values that are typical of dusty, irregular systems. This may be an indication of kpc scale dust obscuration, which can bias the G and M_{20} values away from the bulge-dominated regime.

A morphological study of LBGs in GOODS-N by Ravindranath et al. (2006) found axial ratios skewed towards lower values for galaxies at $z > 3$, suggesting high- z LBGs are dominated by edge-on morphologies. In contrast, only one DOG has an axial ratio less than 0.35, indicating that if these sources are disk galaxies, then some selection mechanism must be in place that favors observing DOGs in face-on orientations. Meanwhile, results from numerical simulations of galaxy mergers indicate that remnants end up with axial ratios between 0.5 and 1.0, depending on the viewing angle (Novak et al., 2006). 21 DOGs satisfy this axial ratio criterion, but

the median value in our dataset is ≈ 0.5 . This suggests that either DOGs represent a phase prior to the final remnant stage or they are formed by some other process.

Recently, Law et al. (2007) have used GOODS data to analyze morphologies of 216 LBGs and compare them with other high- z galaxy populations. They found significant overlap between the LBGs and BzK s, indicating that the optical and NIR selection criteria are identifying similar galaxies. While these authors performed a non-parametric morphological analysis, direct comparison between our work and theirs is difficult because (a) they assign pixels to each galaxy based on an isophotal surface brightness criterion rather than the elliptical Petrosian radius as we have done and (b) they create their own parameter to describe the multiplicity (Ψ) of each galaxy, rather than using M_{20} . Nevertheless, there are some apparent differences between the DOGs and LBGs from the Law et al. (2007) study. While the LBGs span the full range of G values in the rest-UV, the DOGs tend to be low G objects. Furthermore, though LBGs span a wide range in G , they are preferentially found to have low Ψ values, implying a small number of distinct components. On the other hand, the DOGs have high M_{20} values, suggesting multi-component structure is commonplace. Law et al. (2007) note a correlation in their plot of G as a function of Ψ , in the sense that objects with many components (large Ψ) tend to be fainter and more nebulous (low G). DOGs resemble this extreme subset of faint diffuse LBGs, but appear highly morphologically distinct from the vast majority of the LBG population.

2.5.2.3 Passively Evolving Galaxies

As mentioned above, the BzK method can be used to identify high- z passively evolving galaxies. This photometric color cut has been used in the Hubble Ultra Deep Field (UDF) to generate a sample of seven luminous early-type galaxies at $z = 1.39\text{--}2.47$ (Daddi et al., 2005). These authors studied the i and z band morphologies

of all seven objects with both parametric (Sérsic profile fitting) and non-parametric (concentration and asymmetry) methods. They found fairly large Sérsic indices ($n \sim 3$) and small effective radii ($r_{\text{eff}} \leq 1 \text{ kpc}$), typical of E/S0 galaxies. In contrast, the best-fit Sérsic profile for DOGs has smaller n values more typical of exponential disks (median $n = 0.9$) and larger effective radii ($R_{\text{eff}} \sim 1 - 6 \text{ kpc}$). Moreover, the passive BzK galaxies have $C > 2.6$ and $A < 0.2$, consistent with early-type systems. In the rest-optical, DOGs tend to show lower C values (S/N is not sufficient to measure A), consistent with an exponential profile. Along with the low G and high M_{20} values that are measured for the DOGs, these morphology results suggest that DOGs and passively evolving high- z galaxies are distinct populations, either because they represent different stages of evolution or because they have different formation mechanisms.

2.5.2.4 Distant Red Galaxies

Another population of high- z galaxies is the so-called Distant Red Galaxies (DRGs). Identified via deep NIR imaging, these objects were first postulated to be the red-denied descendents of LBGs (Franx et al., 2003). Subsequent studies of DRGs in the Extended Groth Strip (EGS) show a wide variety of shapes, with 57% appearing visually as elliptical/compact, 7% as edge-on disks, and the remainder as peculiar/irregular galaxies (Conselice et al., 2007). The low redshift DRGs ($z < 1.4$) have CAS values typical of nearby normal galaxies. The higher z DRGs visually classified as elliptical/compact have higher C values, similar to what is seen locally in massive ellipticals and in the BzK samples. Meanwhile, Law et al. (2007) examined DRGs in the GOODS-N field that did not overlap with the BX or BM LBG color criteria and found that this population of galaxies was substantially fainter and more diffuse than either the star-forming BzK s or the LBGs. They note that this is the behavior one expects from dusty, IR-bright galaxies. The faint, diffuse

nature of these objects is reminiscent of the DOGs, and it is possible that there is significant overlap between these two populations.

Previous work using rest-frame UV-NIR SEDs has separated actively star-forming DRGs (sDRGs) from quiescent ones (qDRGs) (Zirm et al., 2007; Toft et al., 2007). Examination of the morphological differences between these two populations has revealed a correlation between size and star formation activity, in the sense that qDRGs are all very small ($R_{\text{eff}} \leq 1$ kpc), while sDRGs span a larger range in size ($R_{\text{eff}} \sim 1 - 10$ kpc). As is shown in the right panel of Figure 2.5, DOGs appear very similar to sDRGs in terms of their sizes. This is consistent with the qualitative similarity between sDRGs and DOGs described in the preceding paragraph and suggests there is extensive overlap between these two populations.

2.5.3 Implications for the Evolution of the Most Massive Galaxies

In the local universe, there has been evidence for some time that warm dust-dominated ULIRGs may represent a transition stage between cold ULIRGs and optically luminous quasars (Sanders et al., 1988b). If this scenario holds at high redshift, then there is a natural explanation for the observations based on the selection criteria alone: objects selected at long wavelengths (i.e., SMGs) are preferentially cold-dust dominated systems and represent the ‘cold ULIRG’ phase, whereas objects selected at $24\mu\text{m}$ (i.e., DOGs) are dominated by warmer dust and represent the transition phase en route to the optically luminous quasar. As time progresses and the quasar fades in luminosity, the compact, quiescent, elliptical galaxy remnant becomes visible (i.e., quiescent *BzK*s and DRGs).

Again referring to the local universe for guidance, if the triggering mechanism for this activity is a major merger (Sanders et al., 1988a), then we should expect to see a trend in relaxation and size, where the initial stage shows the largest sizes and least relaxation and the end product is a relaxed, compact system. This picture

is apparently consistent with our data, as DOGs tend to be smaller than SMGs, but larger than quiescent DRGs or BzK galaxies. Furthermore, SMGs frequently exhibit signs of major merger activity, whereas passively evolving systems at high- z are very compact with large Sérsic indices. DOGs appear to be intermediate stage objects that typically do not show signs of major mergers, but nonetheless have morphologies indicating they are more dynamically relaxed than SMGs but less so than the quiescent systems.

It is important to emphasize that while our morphological results are consistent with the hypothesis that DOGs act as a transition phase in the process of creating a massive galaxy via a major merger, the morphological information currently available is not sufficient to exclude the possibility that DOGs are created by some other process such as minor merging (for example, minor mergers have the potential to increase size temporarily), or are simply dusty galaxies hosting a powerful, obscured AGN.

Our analysis of the stellar, dust, and gas masses of DOGs currently does not provide compelling evidence to place them within an evolutionary scheme with respect to other massive proto-galaxy candidates such as SMGs. Additional data are needed before conclusive statements can be made based on mass estimates such as these.

2.6 Conclusions

We have analyzed the morphologies of 31 Dust Obscured Galaxies (DOGs) at $z \approx 2$ from the Boötes field using data from *HST* ACS/WFPC2 and NICMOS. Our findings are summarized below.

1. Although these sources were selected to have mid-IR signatures of AGN, we detect spatially resolved emission at rest-frame UV and/or rest-frame optical

wavelengths for all but one of the 31 targets.

2. Using a three component model in GALFIT (sky + PSF + Sérsic profile), we measure significant unresolved components in 28 out of 31 DOGs in the rest-optical, and the median point-source fraction is 0.13. Only 10 DOGs have measureable unresolved components in the rest-UV.
3. The median Sérsic index is 0.9, indicating that disk-like profiles are preferred to bulge-like ones. On the other hand, very few DOG extended components have small axial ratios, indicating that if DOGs are predominantly a population of normal, disk-like galaxies (with an obscured AGN producing the $24\mu\text{m}$ flux), then some selection mechanism(s) must be in place that favors face-on rather than edge-on orientations.
4. DOGs in our sample have effective radii of 1-5 kpc, which places them between SMGs and quiescent DRGs or *BzK* galaxies. If DOGs are formed by a major merger, this trend in sizes is consistent with them acting as a transition stage in the evolution of massive galaxies. If DOG activity is triggered by some other process, such as a minor merger or a dusty AGN in a normal galaxy, then interpretation of this size trend is not as clear.
5. In the rest-optical, DOGs have lower G values than local ULIRGs (median values of 0.49 and 0.59, respectively). This might be expected if DOGs represent a subsequent stage in the merging process (just before coalescence), but might also be expected if the galaxies are not disturbed by a major merger.
6. Simple stellar population modeling reveals that old (>300 Myr) single-burst stellar populations are redder than most DOGs and thus ruled out. If 100 Myr old SSPs are appropriate, then DOGs require substantial amounts of extinction

to produce the observed red colors, with $A_V = 0.2 - 3$. This provides a lower bound on the median dust mass of $10^7 M_\odot$. An upper bound is obtained by extrapolating the $24\mu\text{m}$ flux density to $850\mu\text{m}$ and is found to have a median value of $1.5 \times 10^8 M_\odot$. We find a median stellar mass lower limit of $10^{10} M_\odot$ which is relatively insensitive to age to within a factor of a few.

This work is based in part on observations made with the *Spitzer Space Telescope*, which is operated by the Jet Propulsion Laboratory, California Institute of Technology under NASA contract 1407. We are grateful to the expert assistance of the staff Kitt Peak National Observatory where the Boötes field observations of the NDWFS were obtained. The authors thank NOAO for supporting the NOAO Deep Wide-Field Survey. In particular, we thank Jenna Claver, Lindsey Davis, Alyson Ford, Emma Hogan, Tod Lauer, Lissa Miller, Erin Ryan, Glenn Tiede and Frank Valdes for their able assistance with the NDWFS data. We also thank the staff of the W. M. Keck Observatory, where some of the galaxy redshifts were obtained.

RSB gratefully acknowledges financial assistance from HST grant GO10890, without which this research would not have been possible. Support for Program number HST-GO10890 was provided by NASA through a grant from the Space Telescope Science Institute, which is operated by the Association of Universities for Research in Astronomy, Incorporated, under NASA contract NAS5-26555. The research activities of AD and BTJ are supported by NOAO, which is operated by the Association of Universities for Research in Astronomy (AURA) under a cooperative agreement with the National Science Foundation. Support for E. Le Floch was provided by NASA through the Spitzer Space Telescope Fellowship Program.

CHAPTER 3

MORPHOLOGIES OF BUMP-DOMINATED DOGS

We present *Hubble Space Telescope* (*HST*) imaging of 22 ultra-luminous infrared galaxies (ULIRGs) at $z \approx 2$ with extremely red $R - [24]$ colors (called dust-obscured galaxies, or DOGs) which have a local maximum in their spectral energy distribution (SED) at rest-frame $1.6\mu\text{m}$ associated with stellar emission. These sources, which we call “bump DOGs”, have redshifts derived from mid-IR spectra which show strong polycyclic aromatic hydrocarbon emission — a sign of vigorous ongoing star-formation. Using a uniform morphological analysis, we seek to answer the question of whether quantifiable morphological differences exist between these bump DOGs, power-law DOGs (*Spitzer*-selected ULIRGs with mid-IR SEDs dominated by a power-law and spectral features that are more typical of obscured active galactic nuclei than starbursts), sub-millimeter selected galaxies (SMGs), and ULIRGs from the *Spitzer* extragalactic First Look Survey (XFLS). Bump DOGs are larger than power-law DOGs (median Petrosian radius of 8 kpc vs. 5 kpc) and exhibit more diffuse and irregular morphologies. These trends are consistent with expectations from simulations of major mergers. Galaxies which are less obscured (i.e., non-DOGs) tend to have single-source rather than diffuse and irregular morphologies. This distinction in morphologies may imply that less obscured sources sample the merger near the end of the peak star-formation rate period; alternatively, it may indicate that a significant fraction of the high redshift ULIRG population is associated with more quiescent modes of formation such as smooth gas inflow or the accretion of small satellites.

3.1 Introduction

The discovery of a strong correlation between the stellar bulge mass and the central super-massive black hole (SMBH) mass of galaxies (e.g., Magorrian et al., 1998) has led to detailed theoretical models in which the growth of SMBHs and their host galaxies occur (nearly) simultaneously during a brief period of intense, merger-driven activity (e.g., Hopkins et al., 2006). In these models, the nature of the connection between SMBHs and their host galaxies has important implications for the evolution of massive galaxies.

The observational foundation of this evolutionary link between SMBHs and their host galaxies was established by studies of ultra-luminous infrared galaxies (ULIRGs Sanders & Mirabel, 1996) identified in the local universe using *InfraRed Astronomical Satellite* (Neugebauer et al., 1984) data. ULIRGs are systems whose spectral energy distributions (SEDs) are dominated by dust emission at infrared (IR) wavelengths (Soifer et al., 1986) and whose morphologies tend to show evidence for recent or on-going major merger activity that has been linked to the formation of active galactic nuclei (AGN) and quasars (Sanders et al., 1988a). Although ULIRGs in the local universe are too rare to contribute significantly to the bolometric luminosity density, recent studies with the *Spitzer Space Telescope* have shown that they become increasingly important at higher redshifts (e.g. Le Floch et al., 2005; Maggelli et al., 2009). To understand the physical mechanisms that drive massive galaxy evolution, it is essential to identify and study high-redshift ($z > 1$), dusty, luminous galaxies that show signs of concurrent AGN and starburst activity.

Efforts to identify high-redshift ULIRGs have been increasingly fruitful the last two decades. In particular, blank-field surveys at sub-millimeter or millimeter wavelengths have identified sub-millimeter selected galaxies (SMGs; e.g. Smail et al., 1997; Coppin et al., 2006). More recently, the advent of the Multiband Imaging Pho-

tometer for Spitzer (MIPS; Rieke et al., 2004) on board the *Spitzer Space Telescope* has allowed for the identification of sources which are bright at mid-IR wavelengths but faint in the optical (e.g. Yan et al., 2004; Fiore et al., 2008; Dey et al., 2008; Lonsdale et al., 2009). Follow-up spectroscopy and clustering measurements of both the sub-millimeter-selected and the *Spitzer*-selected populations has demonstrated that they have similar number densities, redshift distributions, and clustering properties that indicate they are undergoing an extremely luminous, short-lived phase of stellar bulge and nuclear black hole growth and may be the progenitors of the most luminous ($\sim 4L^*$) present-day galaxies (Blain et al., 2004; Chapman et al., 2005; Yan et al., 2007; Farrah et al., 2006; Dey et al., 2008; Brodwin et al., 2008).

One intriguing difference between the two populations (as might be expected based on the selection criteria) is that the mid-IR selected ULIRGs have hotter dust than the far-IR selected SMGs (Kovács et al., 2006; Coppin et al., 2008; Sajina et al., 2008; Younger et al., 2009; Lonsdale et al., 2009; Bussmann et al., 2009a; Fiolet et al., 2009). This distinction may be analogous to the warm-dust/cool-dust dichotomy seen in local ULIRGs, where it has been suggested that warm ULIRGs represent an important transition stage between cold ULIRGs and quasars (Sanders et al., 1988b). Furthermore, there are indications based on 1.2 mm photometry that the *Spitzer*-selected population may be divided by dust temperature into two sub-classes: those whose mid-IR SEDs contain a peak near $1.6\mu\text{m}$ (“bump” sources) have cooler dust than those whose SEDs are dominated by a power-law in the mid-IR (“power-law” sources) (Lutz et al., 2005; Sajina et al., 2008; Younger et al., 2009; Lonsdale et al., 2009; Bussmann et al., 2009a; Fiolet et al., 2009). Given that mid-IR spectra of bump sources show strong polycyclic aromatic hydrocarbon (PAH) emission features typical of star-forming regions (Yan et al., 2007; Desai et al., 2009; Huang et al., 2009), while power-law sources have silicate absorption features or

are dominated by continuum emission consistent with obscured AGN (Houck et al., 2005; Weedman et al., 2006b; Yan et al., 2007), these results suggest that there may be a connection between the origin of the bolometric luminosity of a system and its globally averaged dust temperature.

Efforts to understand this connection between mid-IR and far-IR selected high- z ULIRGs within the context of an evolutionary paradigm have been advanced by numerical simulations of galaxy mergers (e.g. Mihos & Hernquist, 1996; Narayanan et al., 2009). In these models, when the merging system approaches final coalescence, the star-formation rate (SFR) spikes and, because it is enshrouded in cold-dust, the system is observed as an SMG. As time proceeds, feedback from the growth of a central super-massive black hole warms the ambient dust and ultimately quenches star-formation. It is during this critical period of galaxy evolution when the system is observable as a *Spitzer*-selected ULIRG. To test the predictions of this model, and in general to understand the physical processes governing galaxy evolution, it is essential to study the *Spitzer*-selected and SMG populations in detail.

The primary goal of this paper is to identify quantifiable morphological differences between SMGs, *Spitzer*-selected bump ULIRGs and *Spitzer*-selected power-law ULIRGs. In particular, morphological differences that test the results of recent efforts to study the morphologies of simulated mergers; these studies find that mergers occupy a distinct morphological phase space during the “final coalescence” period when the SFR peaks (Lotz et al., 2008, 2009b,a). If SMGs and *Spitzer*-selected ULIRGs are related in an evolutionary sequence driven by major mergers, do they occupy the expected region of morphological phase space suggested by the simulations? Using high-spatial resolution *HST* imaging, it is possible to begin to answer this question.

In addition to identifying merger activity, high-spatial resolution data constrain

the size-scale of the dominant emitting region. *HST* imaging of power-law dominated *Spitzer*-selected ULIRGs has shown that these sources are nearly always resolved with effective radii of 1-5 kpc, although few show obvious signs of on-going major merger activity (from a sample of ≈ 50 sources Dasyra et al., 2008; Busmann et al., 2009b). In addition, Keck *K*-band adaptive optics imaging of 15 such objects has revealed a size trend within the *Spitzer*-selected ULIRG population: $24\mu\text{m}$ -bright, power-law dominated sources are more compact than $24\mu\text{m}$ -faint, bump-dominated sources (Melbourne et al., 2008, 2009), consistent with the idea that the brighter $24\mu\text{m}$ sources are more AGN-dominated.

One major component of this paper is the presentation of new *HST* imaging of 22 *Spitzer*-selected bump ULIRGs at $z \approx 2$. The objects in this sample are selected from the Boötes field of the NOAO Deep Wide-Field Survey (NDWFS¹; Jannuzi et al., in prep.; Dey et al., in prep. Jannuzi & Dey, 1999) to have $R - [24] > 14$ (Vega magnitudes; $\approx F_\nu(24\mu\text{m})/F_\nu(R) > 1000$) and are called Dust Obscured Galaxies (DOGs). DOGs in Boötes satisfying $F_{24\mu\text{m}} > 0.3$ mJy have a space density of $\approx 2.8 \times 10^{-5} h_{70}^3 \text{ Mpc}^{-3}$. Although these sources are rare, they are sufficiently luminous that they contribute up to one-quarter of the total IR luminosity density from all $z \sim 2$ galaxies (Dey et al., 2008) and constitute a substantial component of the *Spitzer*-selected ULIRG population. The DOGs studied in this paper were selected to have mid-IR SEDs (based on IRAC shallow survey data Eisenhardt et al., 2004) indicating a peak at rest-frame $1.6\mu\text{m}$ (bump DOGs) and have spectroscopic redshifts from *Spitzer*/Infrared Spectrograph (IRS) data (Desai et al., 2009). For two targets, subsequent deeper mid-IR imaging from the *Spitzer* Deep Wide-Field Survey revealed power-law SEDs rather than bump SEDs. Additionally, one bump target had to be replaced with a power-law target due to scheduling constraints.

¹<http://www.noao.edu/noaodeep>

In this paper we present Wide-Field Planetary Camera 2 (WFPC2 Trauger et al., 1994) and Near-IR Camera and Multi-object Spectrometer (NICMOS Thompson et al., 1998) images of 19 bump DOGs and 3 power-law DOGs and analyze their morphologies.

A second major aspect of this study is the assembly and uniform morphological analysis of *HST* NICMOS imaging of *Spitzer*-selected and sub-mm selected ULIRGs at $z > 1.4$. Including the DOGs studied here and in Paper I, as well as SMGs (Swinbank et al., 2010a) and *Spitzer*-selected ULIRGs at $z > 1.4$ extragalactic first look survey (XFLS; Dasyra et al., 2008), the combined dataset comprises 103 high redshift ULIRGs with uniform morphological analysis and offers the optimal testing ground of models for the formation and evolution of these systems.

In section 3.2 we detail the sample selection, observations, and data reduction. Section 3.3 contains postage stamp cutouts of all 22 DOGs in this sample. In section 3.4, we describe our methodology for measuring photometry and morphologies, including a visual classification experiment, non-parametric quantities, and GALFIT modeling. Section 3.5 contains the results of this analysis, including a comparison of SMG, DOG, and simulated merger morphologies. In section 3.6, we estimate crude stellar masses based on the $I - H$ colors of DOGs, and discuss the implications of our results. Finally, we present our conclusions in section 3.7.

Throughout this paper we assume $H_0 = 70 \text{ km s}^{-1} \text{ Mpc}^{-1}$, $\Omega_m = 0.3$, and $\Omega_\lambda = 0.7$. At $z = 2$, this results in a spatial scale of $8.37 \text{ kpc}''$.

3.2 Data

In this section, we describe the new *HST* observations of bump DOGs and the procedure used to reduce them. We also detail the archival datasets of power-law DOGs, SMGs, and XFLS ULIRGs used subsequently in this paper.

3.2.1 Bump DOGs

The 22 DOGs presented in this paper were observed with *HST* from 2007 December to 2008 May. All were observed with WFPC2 through the F814W filter and with the NICMOS NIC2 camera through the F160W filter. Table 3.1 summarizes the details of the observations. All data were processed using IRAF². The following sections provide more details about the sample selection and processing of the WFPC2 and NICMOS images used in this paper.

3.2.1.1 Sample Selection

A sample of 2603 DOGs was identified by Dey et al. (2008) from the 9.3 deg² Boötes Field of the NDWFS. Keck and *Spitzer* spectroscopy have resulted in redshifts of ≈ 100 DOGs, approximately 60% of which have power-law dominated mid-IR SEDs and 40% have bump SEDs. These are objects which have very high intrinsic to observed UV luminosity ratios, on par with or beyond the most extreme starbursts studied by *Spitzer* in the local universe (Sargsyan et al., 2010).

In Bussmann et al. (2009b, hereafter Paper I), we analyzed *HST* imaging (program HST-GO10890) of 31 of the brightest DOGs at 24 μ m (all have $F_{24\mu\text{m}} > 0.8$ mJy) that have power-law mid-IR SEDs and spectroscopic redshifts based on the 9.7 μ m silicate absorption feature, most likely due to the presence of warm dust heated by an AGN (Weedman et al., 2006a; Donley et al., 2007; Polletta et al., 2008; Brand et al., 2008).

In this paper, we analyze *HST* imaging (program HST-GO11195) of 22 DOGs that show a bump in their rest-frame mid-IR SED (selected using Arp 220 as a template; for details see Desai et al., 2009). This feature indicates that the mid-IR light is dominated by stellar emission in these sources. Furthermore, *Spitzer* mid-IR

²IRAF is distributed by the National Optical Astronomy Observatory, which is operated by the Association of Universities for Research in Astronomy, Inc., under cooperative agreement with the National Science Foundation. <http://iraf.noao.edu/>

Table 3.1. Observations

| Source Name | ID ^a | RA (J2000) | DEC (J2000) | z^b | WFPC2/F814W | NIC2/F160W |
|------------------------|-----------------|---------------|--------------|--------------------|-------------|------------|
| SST24 J142637.3+333025 | 1 | +14:26:37.397 | +33:30:25.82 | 3.200 ^c | 2008-02-11 | 2007-12-31 |
| SST24 J142652.4+345504 | 12 | +14:26:52.555 | +34:55:05.53 | 1.91 | 2008-03-28 | 2008-01-01 |
| SST24 J142724.9+350823 | 4 | +14:27:25.016 | +35:08:24.20 | 1.71 | 2008-07-02 | 2008-01-14 |
| SST24 J142832.4+340850 | 8 | +14:28:32.476 | +34:08:51.23 | 1.84 | 2008-07-03 | 2008-01-15 |
| SST24 J142920.1+333023 | 17 | +14:29:20.164 | +33:30:23.59 | 2.01 | 2008-02-01 | 2008-05-26 |
| SST24 J142941.0+340915 | 13 | +14:29:41.085 | +34:09:15.61 | 1.91 | 2008-05-21 | 2008-03-15 |
| SST24 J142951.1+342041 | 5 | +14:29:51.163 | +34:20:41.33 | 1.76 | 2008-01-28 | 2008-01-14 |
| SST24 J143020.4+330344 | 11 | +14:30:20.537 | +33:03:44.45 | 1.87 | 2008-03-21 | 2008-04-11 |
| SST24 J143028.5+343221 | 21 | +14:30:28.534 | +34:32:21.62 | 2.178 ^d | 2008-05-07 | 2008-01-15 |
| SST24 J143137.1+334500 | 7 | +14:31:37.080 | +33:45:01.26 | 1.77 | 2008-05-20 | 2008-04-12 |
| SST24 J143143.3+324944 | 2 | +14:31:43.400 | +32:49:44.38 | — | 2008-02-10 | 2008-03-15 |
| SST24 J143152.4+350029 | 3 | +14:31:52.463 | +35:00:29.44 | 1.50 | 2008-01-24 | 2008-05-22 |
| SST24 J143216.8+335231 | 6 | +14:32:16.904 | +33:52:32.18 | 1.76 | 2008-02-01 | 2008-03-16 |
| SST24 J143321.8+342502 | 18 | +14:33:21.890 | +34:25:02.62 | 2.10 | 2008-05-21 | 2008-01-15 |
| SST24 J143324.2+334239 | 14 | +14:33:24.269 | +33:42:39.55 | 1.91 | 2008-02-02 | 2008-01-17 |
| SST24 J143331.9+352027 | 15 | +14:33:31.945 | +35:20:27.28 | 1.91 | 2007-12-25 | 2008-01-14 |
| SST24 J143349.5+334602 | 10 | +14:33:49.585 | +33:46:02.00 | 1.86 | 2008-03-18 | 2008-01-07 |
| SST24 J143458.8+333437 | 20 | +14:34:58.953 | +33:34:37.57 | 2.13 | 2008-07-03 | 2008-05-21 |
| SST24 J143502.9+342657 | 19 | +14:35:02.930 | +34:26:58.88 | 2.10 | 2008-05-09 | 2008-01-15 |
| SST24 J143503.3+340243 | 16 | +14:35:03.336 | +34:02:44.16 | 1.97 | 2008-02-29 | 2008-01-07 |
| SST24 J143702.0+344631 | 22 | +14:37:02.018 | +34:46:30.93 | 3.04 | 2008-03-28 | 2007-12-28 |
| SST24 J143816.6+333700 | 9 | +14:38:16.714 | +33:37:00.94 | 1.84 | 2008-07-03 | 2008-01-14 |

^aPanel number in Figure 3.3^bRedshift from *Spitzer*/IRS (Desai et al., 2009) unless otherwise noted^cRedshift from Keck LRIS (Soifer et al., in prep.)^dRedshift from Keck NIRSPEC (Brand et al., 2007)

spectroscopy has provided redshifts for 20/22 of these sources via identification of PAH emission features commonly associated with on-going star-formation (Desai et al., 2009). Subsequent deeper mid-IR imaging from the *Spitzer* Deep Wide-Field Survey (Ashby et al., 2009) has revealed that the two sources lacking PAH features have power-law mid-IR SEDs. One additional target has a power-law mid-IR SED (SST24 J143028.5+343221) and was observed by *HST* because the bump source it replaced could not be observed due to scheduling constraints.

Figure 3.1 shows the $R - [24]$ color and R -band magnitude (Vega system) for the following sources with *HST* imaging: bump and power-law DOGs, SMGs, and XFLS ULIRGs at high redshift. Following careful reanalysis of the R -band photometry, a few DOGs show $R - [24]$ colors below the nominal DOG threshold — we refer to these objects as DOGs in this paper because they satisfy the essential physical characteristics of DOGs: they are $z \sim 2$ ULIRGs that are likely to be a highly obscured stage in massive galaxy evolution. The bump DOGs in this sample have fainter $24\mu\text{m}$ flux densities and less extreme $R - [24]$ colors than the power-law DOGs. These distinctions are qualitatively representative of the photometric properties of the full sample of 2603 DOGs in the Boötes Field.

Figure 3.2 shows the redshift distributions of bump DOGs, power-law DOGs, SMGS, and XFLS ULIRGs with *HST* data in comparison to all DOGs in Boötes with spectroscopic redshifts. Bump DOGs predominantly lie in a relatively narrow redshift range of $1.5 < z < 2.1$. Briefly, this is because at $z = 1.9$, the strong $7.7\mu\text{m}$ PAH feature boosts the $24\mu\text{m}$ flux, pushing sources with weaker continuum into the flux-limited bump DOG sample (for additional details, see Desai et al., 2009).

3.2.1.2 WFPC2 Data

The Wide Field Camera CCD 3 of WFPC2 was used to image the 22 DOGs in this study. These observations consisted of double-orbit data with the F814W filter. We

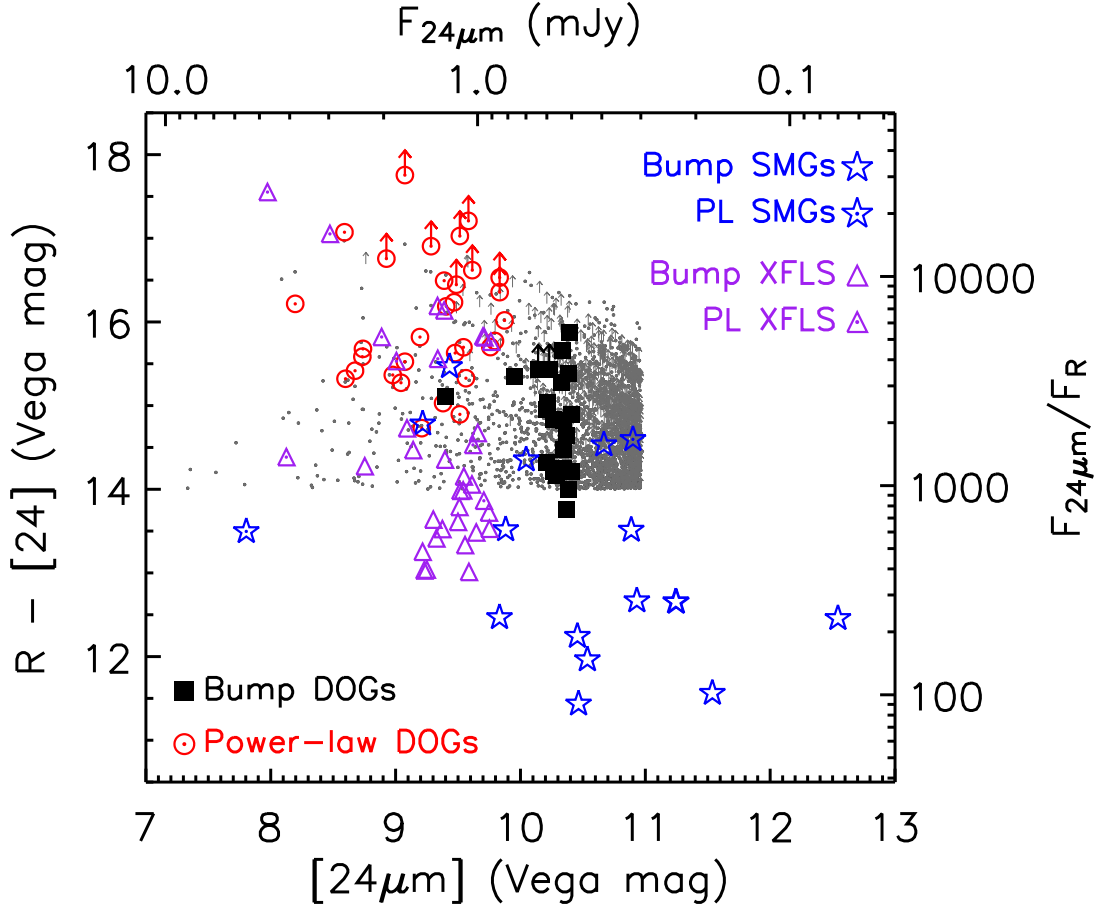


Figure 3.1 $R - [24]$ color vs. $24\mu m$ magnitude distribution for all DOGs in the ND-WFS Boötes field (gray dots). Arrows indicate R -band non-detections (2σ level), and cross symbols highlight power-law dominated sources. Also shown are the samples with high-spatial resolution imaging studied in this paper: power-law DOGs (red circles), bump DOGs (black squares), SMGs (blue stars), and XFLS ULIRGs (purple triangles). Power-law sources tend to be the brightest at $24\mu m$ and the most heavily obscured.

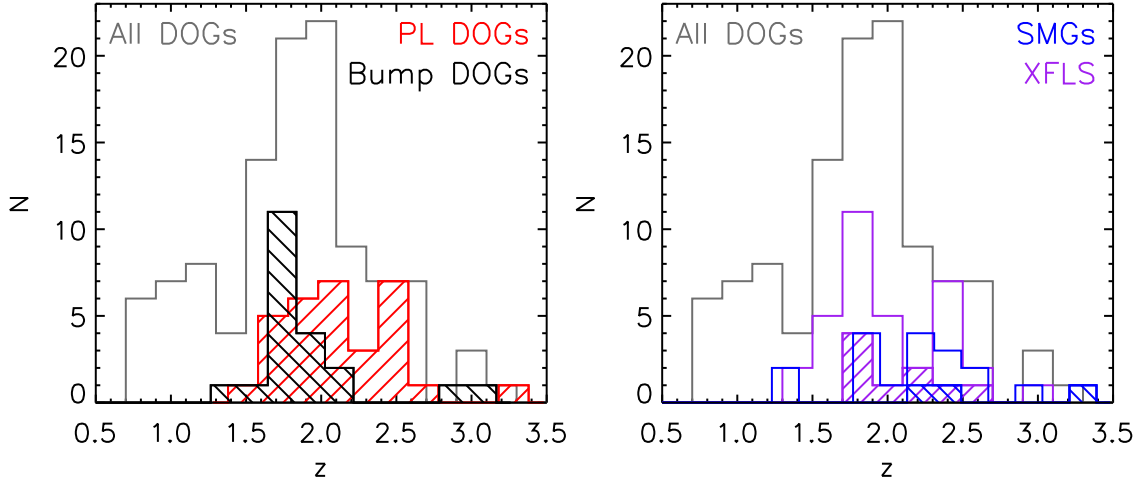


Figure 3.2 *Left*: Redshift distribution of DOGs in the Boötes Field with spectroscopic redshifts (gray histogram; either from *Spitzer/IRS* or Keck DEIMOS/LRIS, Soifer et al. in prep.). The redshift distribution of bump DOGs (black hatched) is relatively narrow due to selection effects (for details see Desai et al., 2009), while power-law DOGs (red hatched) are weighted towards slightly larger redshifts. *Right*: Redshift distribution of SMGs (blue histogram) and XFLS ULIRGs (purple histogram) at $z > 1.4$ studied in this paper. Hatched regions denote the sub-sample qualifying as power-law dominated in the mid-IR.

used a three point dither pattern (WFPC2-LINE) with a point and line spacing of $0''.3535$ and a pattern orientation of 45° . Total exposure duration at the nominal pixel scale of $0''.1 \text{ pix}^{-1}$ was $\approx 3800 \text{ sec}$. The standard WFPC2 pipeline system was used to bias-subtract, dark-subtract, and flat-field the images (Mobasher et al., 2002). MultiDrizzle was then used to correct for geometric distortions, perform sky-subtraction, image registration, cosmic ray rejection and final drizzle combination (Koekemoer et al., 2002). We used a square interpolation kernel and output pixel scale of $0.075'' \text{ pix}^{-1}$, leading to a per-pixel exposure time in the drizzled image of $\approx 2200 \text{ sec}$.

3.2.1.3 NICMOS Data

Single orbit data of the DOGs were acquired with the NIC2 camera and the F160W filter. We used a two-point dither pattern (NIC-SPIRAL-DITH) with a point spacing of $0.637''$. Total exposure time was $\approx 2688 \text{ s}$. We followed the standard data reduction process outlined in the NICMOS data handbook (Viana et al., 2009). We used the IRAF routine `nicpipe` to pre-process the data, followed by the `biaseq` task to correct for non-linear bias drifts and spatial bias jumps. We then used `nicpipe` a second time to do flat-fielding and initial cosmic-ray removal. The IRAF task `pedsky` was used to fit for the sky level and the quadrant-dependent residual bias. Significant residual background variation remained after this standard reduction process. To minimize these residuals, we followed the procedure outlined in Paper I: we constructed an object-masked median sky image based on all of our NIC2 science frames, scaled it by a spatially constant factor and subtracted it from each science image. The scaling factor was computed by minimizing the residual of the difference between the masked science image and the scaled sky image. Mosaicing of the dithered exposures was performed using `calnicb` in IRAF, resulting in a pixel scale of $0.075'' \text{ pix}^{-1}$.

3.2.1.4 Astrometry

Each WFPC2 and NICMOS image is aligned to the reference frame of the NDWFS, which itself is tied to the USNO A-2 catalog. We identify well-detected, unsaturated sources in the *I*-band NDWFS data overlapping the field of view (FOV) of each WFPC2/F814W image using Source Extractor (SExtractor, version 2.5.0, Bertin & Arnouts, 1996). The IRAF tasks `wcsctran` and `imcentroid` are used to convert the RA and DEC values of this list of comparison sources into WFPC2 pixel coordinates. Finally, the IRAF task `ccmap` is used to apply a first order fit which corrects the zero point of the astrometry and updates the appropriate WCS information in the header of the WFPC2 image. The aligned WFPC2 image serves as a reference frame for correcting the astrometry of the NICMOS image as well as the IRAC images (since the IRAC images of the Boötes Field are not tied to the USNO A-2 catalog, but instead to the $2\mu\text{m}$ All-Sky Survey frames, see Ashby et al., 2009) using a similar procedure. The properly aligned, multi-wavelength dataset generally allows for straightforward identification of the proper counterpart to the MIPS source, since inspection of the four IRAC channels reveals a single source associated with the $24\mu\text{m}$ emission for all sources. The absolute uncertainty in the centroid of the IRAC $3.6\mu\text{m}$ emission ranges from $0''.2$ – $0''.4$.

3.2.2 Power-law DOGs

As mentioned in the previous section, in Paper I we analyzed *HST* imaging of 31 power-law DOGs at $z > 1.4$. Although these sources have mid-IR SED features indicative of obscured AGN, their rest-frame optical morphologies nearly all show minor ($< 30\%$) point-source contributions and significant emission on scales of 1–5 kpc. This indicates that the rest-frame optical light of these sources is produced from stars, rather than AGN.

The NICMOS exposure times and *H*-band luminosities of these sources are sim-

ilar to the bump DOGs, facilitating a comparison between the two populations. This particular comparison — between distinct sub-classes of the most extreme dust-obscured ULIRGs — is a major aspect of this study.

3.2.3 SMG Data

The SMG data used in this paper are *HST* NICMOS/F160W imaging of a sample of 25 SMGs selected from a catalog of 73 SMGs with spectroscopic redshifts (Chapman et al., 2005) and were first presented by Swinbank et al. (2010a). Of the 25 SMGs, 23 have single-orbit NIC2 imaging from Cycle 12 *HST* program GO-9856 (Swinbank et al., 2010a) and an additional 6 have multi-orbit NIC3 imaging from GOODS-N (Conselice et al. 2010 in prep.). *HST* optical imaging in the F814W filter is also available for all of these objects.

In this paper, we focus on the subset of 18 SMGs at $z > 1.4$. Of these 18, all have NIC2 imaging and 3 have NIC3 imaging as well (SMM J123622.65+621629.7, SMM J123632.61+620800.1, and SMM J123635.59+621424.1). Although the NIC3 images are significantly deeper, we prefer to use the NIC2 data (each of these sources is well-detected at $S/N > 2$) because of the superior pixel scale of NIC2 and the unusual shape of the NIC3 PSF. Some of these sources have optical *HST* imaging with the Advanced Camera for Surveys (ACS), but the S/N levels are generally insufficient for quantitative analysis and so are not used in this study.

We obtained the NIC2 images of SMGs from the *HST* data archive and reduced them following the same procedure that is outlined in section 3.2.1.3. Most importantly, the methodology used to analyze the photometry and morphology of both SMGs and DOGs in this study is identical and is described in section 3.4.

3.2.4 XFLS Data

A sample of 33 XFLS ULIRGs at $z > 1.4$ was imaged with *HST* NICMOS/F160W in Cycle 15 as part of program GO10858. These data and a morphological analysis of the imaging was presented in Dasyra et al. (2008). We note that in our study, we use only single-orbit NIC2 data of these objects to facilitate comparison with the NIC2 images of the other high- z ULIRG populations studied here, which all have only single-orbit NIC2 data. Double-orbit imaging is available for nearly 50% of the sample and in principle could be used to measure more accurate morphologies of the fainter objects as well as test for systematic errors in the morphologies resulting from low S/N. The data were obtained from the *HST* data archive, reduced, and analyzed using the same methodology that was applied to DOGs and SMGs.

3.3 Images

In this section, we present postage stamp images and provide a brief qualitative description of each of the bump DOGs (as well as one DOG from the Cycle 16 *HST* imaging program that is a power-law source). Figure 3.3 shows $3'' \times 3''$ cutout images of the DOGs in order of increasing redshift (note that redshifts are not available for the first two sources presented). Each cutout is centered roughly on the centroid of emission as seen in the NICMOS image. A red plus sign shows the centroid of IRAC $3.6\mu\text{m}$ emission and is sized to represent the $1\text{-}\sigma$ uncertainty in the position, which includes independent contributions from the centroiding error on the $3.6\mu\text{m}$ emission ($\approx 0''.1\text{--}0''.3$, depending on S/N), the relative astrometric calibration uncertainty within the $3.6\mu\text{m}$ map ($\approx 0''.2$), and the uncertainty in tying the $3.6\mu\text{m}$ map to the *HST* images ($\approx 0''.1$). The 1σ rms offset between IRAC and NICMOS centroids of the sample is $0''.2$. In most cases, the offset in centroids is negligible, but those cases where it is not are associated with faint $3.6\mu\text{m}$ emission (when the

absolute astrometric uncertainty may be as large as $0''.4$). This suggests there is no significant offset between the near-IR and mid-IR centroids at > 1 kpc scales.

The DOGs exhibit a wide range of morphologies, with most being well-resolved. Only one object (SST24 J143143.3+324944) shows strong Airy rings and is clearly an unresolved point source. However, we note that this source has a power-law dominated mid-IR SED and is not representative of the bump DOG population. Here we give a brief qualitative description of the morphology of each object.

(1) SST24 J143143.3+324944: F814W: Faint compact morphology. F160W: Bright, compact morphology; dominated by unresolved component.

(2) SST24 J143152.4+350029: F814W: Faint diffuse morphology. F160W: Bright, extended morphology; low surface brightness extension to southwest.

(3) SST24 J142724.9+350823: F814W: Faint, compact source $\approx 0''.5$ SW of NIC2 centroid. F160W: Bright, extended morphology with tentative evidence of tidal tails or spiral arms.

(4) SST24 J142951.1+342041: F814W: Faint, compact source $\approx 0''.3$ north of NIC2 centroid. F160W: Bright, clumpy morphology.

(5) SST24 J143216.8+335231: F814W: Faint, compact source at eastern edge of NIC2 emission. F160W: Bright, clumpy morphology; two bad pixels within the segmentation map of this galaxy have been masked out in the analysis.

(6) SST24 J143137.1+334500: F814W: No detection. F160W: Extended narrow morphology resembling a giant edge-on disk with semi-major axis larger than $3''$.

(7) SST24 J142832.4+340850: F814W: Faint, compact morphology. F160W: No usable data.

(8) SST24 J143816.6+333700: F814W: Faint, compact morphology. F160W: Bright, compact morphology; no obvious PSF signature.

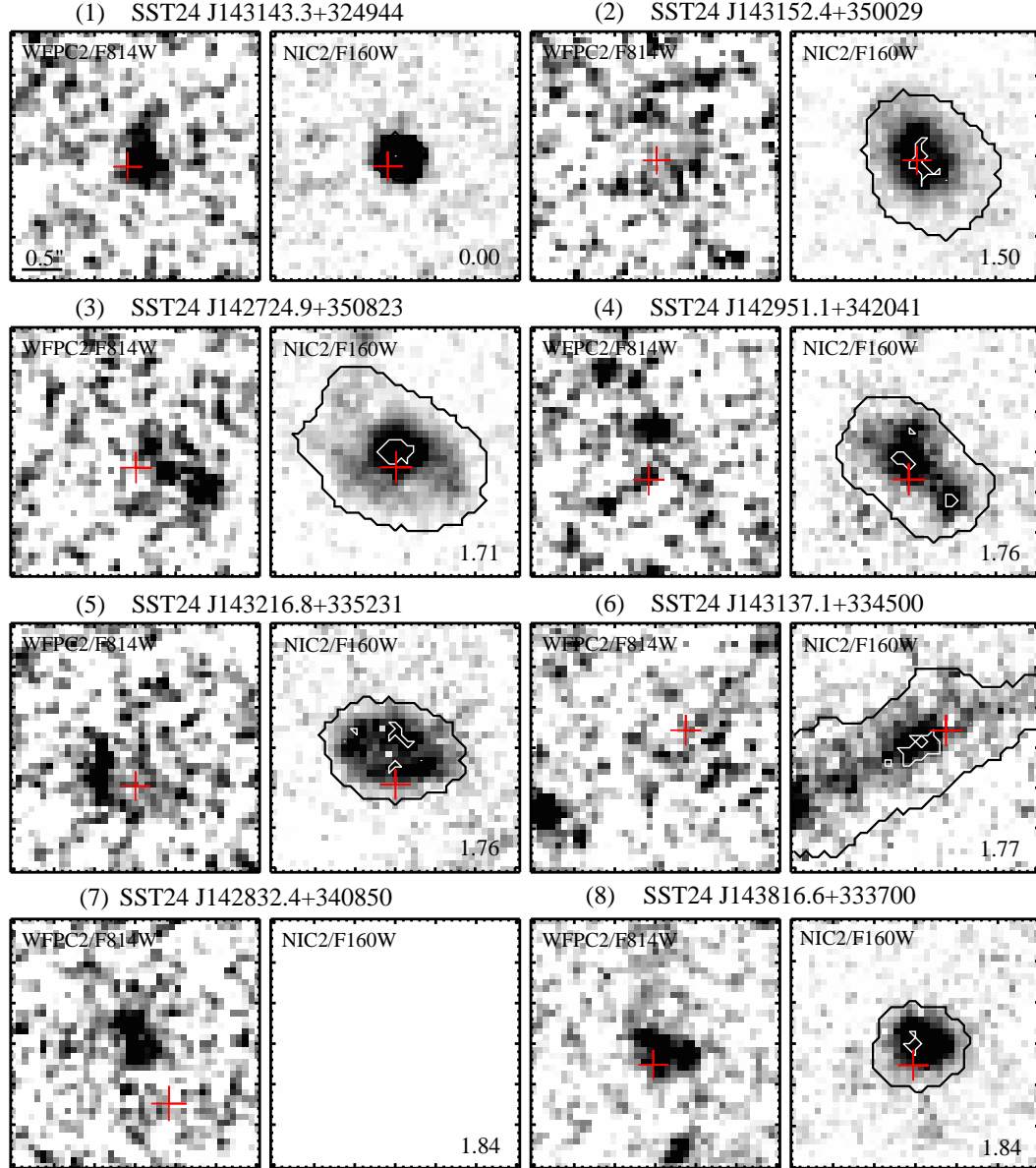


Figure 3.3 Cutouts of the 22 DOGs observed by *HST*, shown with a linear stretch. Columns 1 and 3 are the rest-UV images from WFPC2 F814W and columns 2 and 4 are the rest-optical images from NIC2 F160W. Each cutout is $3''$ on a side and is oriented north up and east left. The objects are arranged in order of increasing redshift, and the redshift is printed in the lower right corner of each NICMOS image. A red cross denotes the position and $1\text{-}\sigma$ uncertainty in the centroid of the IRAC $3.6\mu\text{m}$ emission. In images where the S/N per pixel is greater than 2, white contours outline the brightest 20% pixels (for computing M_{20}), and black contours show the outline of the segmentation map used in measuring the non-parametric morphologies. NICMOS imaging is not available for target SST24 J142832.4+340850.

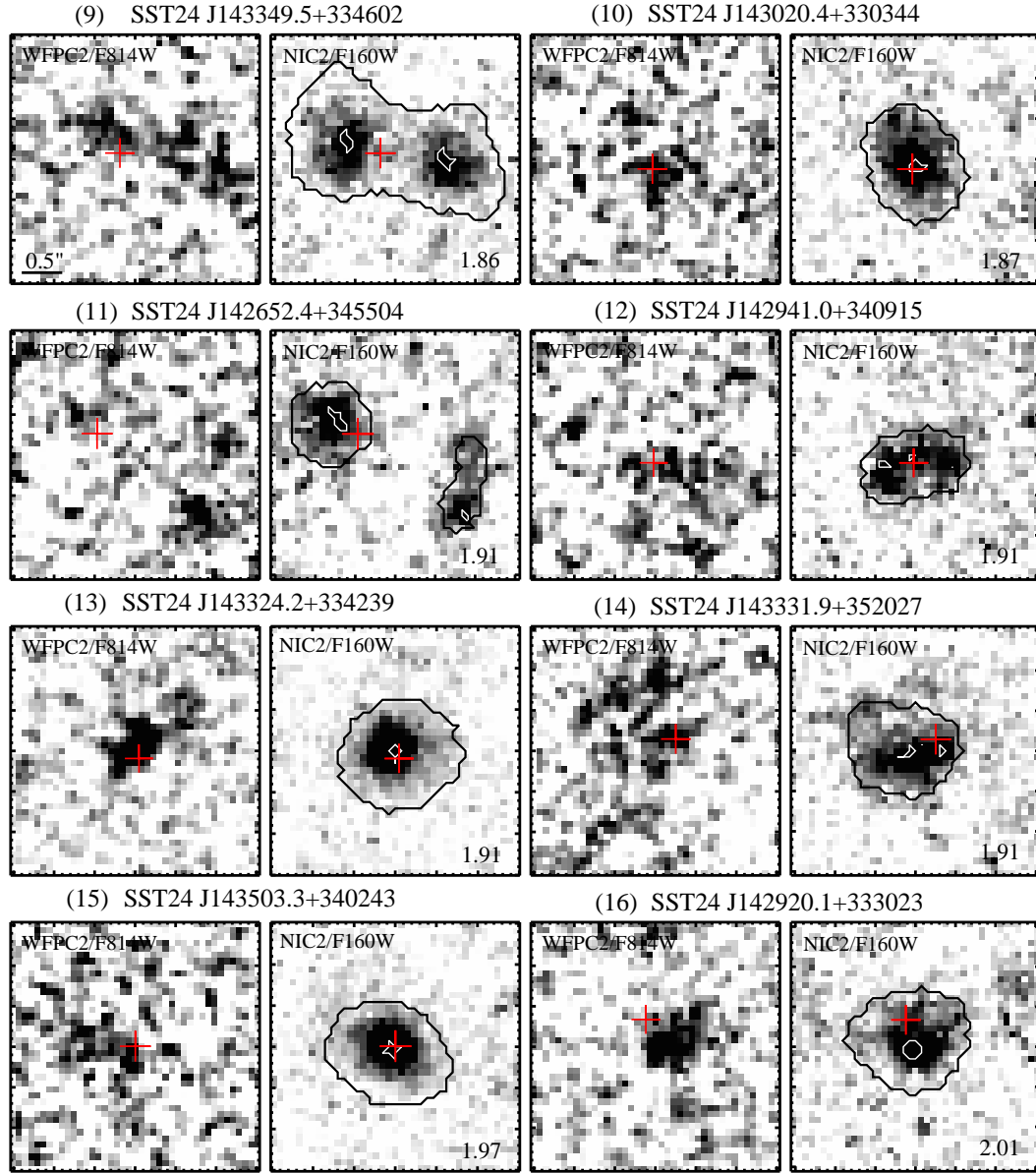


Figure 3.3 Continued.

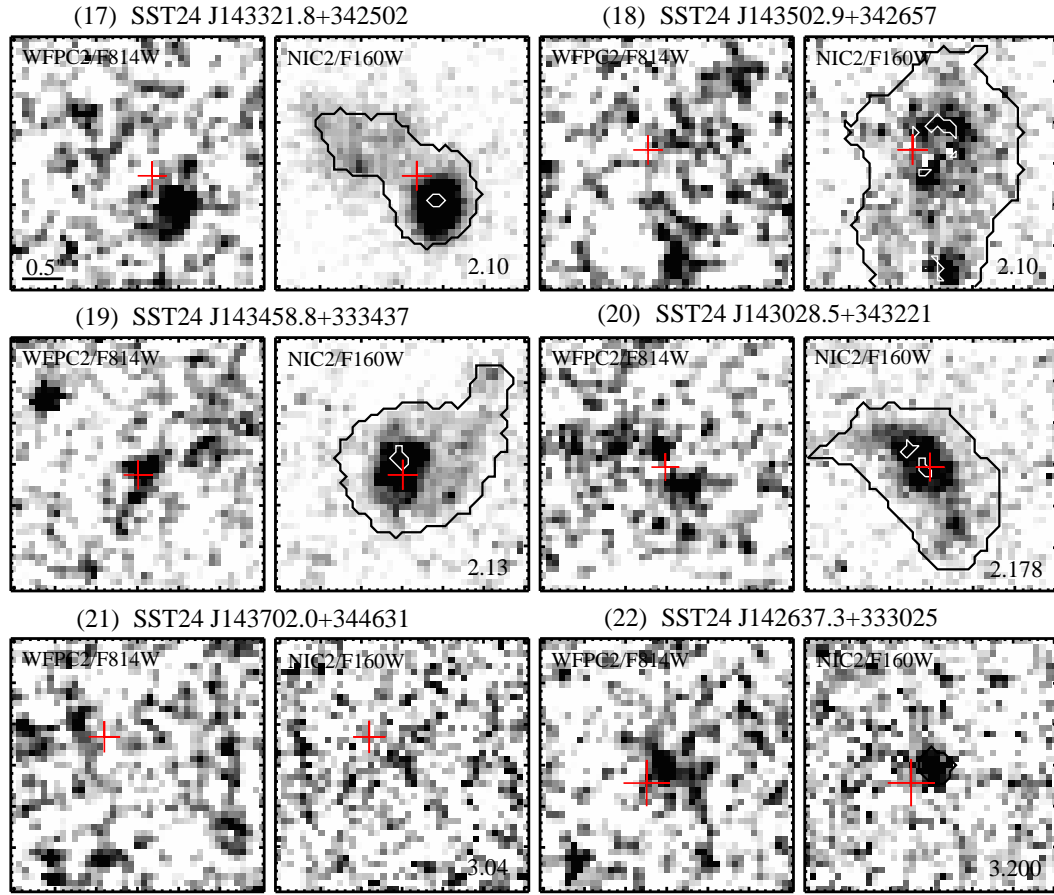


Figure 3.3 Continued.

- (9) **SST24 J143349.5+334602:** F814W: Faint, clumpy morphology. F160W: Two distinct faint, compact sources; IRAC centroid is closer to eastern source.
- (10) **SST24 J143020.4+330344:** F814W: No detection. F160W: Compact morphology; no obvious PSF signature.
- (11) **SST24 J142652.4+345504:** F814W: No detection. F160W: Two faint sources separated by $\approx 2''$; IRAC centroid consistent with northeastern source.
- (12) **SST24 J142941.0+340915:** F814W: No detection. F160W: Clumpy morphology.
- (13) **SST24 J143324.2+334239:** F814W: Faint, compact morphology. F160W: Bright, compact morphology; low surface brightness extension to southwest.
- (14) **SST24 J143331.9+352027:** F814W: Very faint, clumpy morphology. F160W: Bright, clumpy morphology; low surface brightness extension to northeast.
- (15) **SST24 J143503.3+340243:** F814W: No detection. F160W: Bright, compact morphology; no obvious PSF signature.
- (16) **SST24 J142920.1+333023:** F814W: Faint, compact morphology. F160W: Bright, compact morphology.
- (17) **SST24 J143321.8+342502:** F814W: Faint, compact source spatially coincident with peak NIC2 emission. F160W: Bright, compact morphology; no obvious PSF signature; strong low surface brightness feature extending northeast.
- (18) **SST24 J143502.9+342657:** F814W: No detection. F160W: Very clumpy morphology with low surface brightness feature extending to south.
- (19) **SST24 J143458.8+333437:** F814W: Very faint, compact morphology. F160W: Bright, compact morphology; low surface brightness feature to northwest resembles a tidal tail.
- (20) **SST24 J143028.5+343221:** F814W: Very faint, clumpy morphology. F160W: Bright, clumpy morphology; low surface brightness features extending in

eastern and southern directions.

(21) SST24 J143702.0+344631: F814W: No detection. F160W: No detection.

(22) SST24 J142637.3+333025: F814W: Faint compact morphology. F160W: Faint compact morphology; formally detected at 3σ level with $0''.6$ diameter aperture.

3.4 Methodology

In this section, we describe our methods to measure photometry as well as visual, non-parametric, and GALFIT morphologies.

3.4.1 Photometry

We perform $2''$ diameter aperture photometry on each DOG in both the NICMOS and WFPC2 images, choosing the center of the aperture to be located at the peak flux pixel in the NICMOS images. Foreground and background objects are identified and removed using SExtractor (see Section 3.5.2.2). The sky level is derived using an annulus with an inner diameter of $2''$ and a width of $2''$. In cases where the flux density radial profile did not flatten at large radii, the appropriate sky value was determined by trial-and-error. Photometric uncertainty was computed by measuring the sigma-clipped root-mean-square of fluxes measured in N $2''$ diameter apertures, where $N \approx 10$ and $N \approx 100$ for the NICMOS and WFPC2 images, respectively. We verified the accuracy of our WFPC2 photometric zeropoints by comparing well-detected, non-saturated sources common to both the WFPC2/F814W and NDWFS/*I*-band imaging. Photometric measurements of the DOGs are presented in Table 3.2.

Table 3.2. Photometric Properties

| Source Name | F_{F814W} (μJy) | σ_{F814W} (μJy) | F_{F160W} (μJy) | σ_{F160W} (μJy) | F_{24} (mJy) | $R - [24]$ (Vega) |
|------------------------|-----------------------------------|--|-----------------------------------|--|-------------------|----------------------|
| SST24 J142637.3+333025 | 0.36 | 0.19 | 0.45 | 0.57 | 0.64 | >15.0 |
| SST24 J142652.4+345504 | 0.24 | 0.15 | 1.78 | 0.36 | 1.29 | 15.0 |
| SST24 J142724.9+350823 | 0.63 | 0.15 | 6.72 | 0.42 | 0.51 | 14.4 |
| SST24 J142832.4+340850 | 0.59 | 0.16 | — | — | 0.52 | 13.9 |
| SST24 J142920.1+333023 | 0.35 | 0.14 | 2.85 | 0.27 | 0.51 | >13.6 |
| SST24 J142941.0+340915 | 0.30 | 0.13 | 2.47 | 0.46 | 0.59 | >14.6 |
| SST24 J142951.1+342041 | 0.55 | 0.16 | 5.30 | 0.52 | 0.60 | >14.9 |
| SST24 J143020.4+330344 | 0.31 | 0.13 | 4.26 | 0.50 | 0.54 | >15.3 |
| SST24 J143028.5+343221 | 0.59 | 0.16 | 4.92 | 0.31 | 1.27 | 14.7 |
| SST24 J143137.1+334500 | 0.18 | 0.14 | 2.67 | 0.37 | 0.57 | 14.3 |
| SST24 J143143.3+324944 | 0.43 | 0.15 | 6.43 | 0.37 | 1.51 | 14.4 |
| SST24 J143152.4+350029 | 0.54 | 0.16 | 8.21 | 0.31 | 0.52 | 14.3 |
| SST24 J143216.8+335231 | 0.51 | 0.15 | 4.24 | 0.37 | 1.28 | >16.1 |
| SST24 J143321.8+342502 | 0.72 | 0.16 | 7.16 | 0.37 | 0.56 | 14.4 |
| SST24 J143324.2+334239 | 0.96 | 0.17 | 6.67 | 0.47 | 0.53 | 13.8 |
| SST24 J143331.9+352027 | 0.66 | 0.17 | 3.58 | 0.32 | 0.60 | 14.3 |
| SST24 J143349.5+334602 | 0.63 | 0.15 | 4.44 | 0.33 | 0.53 | 14.3 |
| SST24 J143458.8+333437 | 0.49 | 0.20 | 5.14 | 0.51 | 0.57 | 14.0 |
| SST24 J143502.9+342657 | 0.24 | 0.13 | 2.52 | 0.63 | 0.50 | 14.1 |
| SST24 J143503.3+340243 | 0.26 | 0.14 | 3.68 | 0.36 | 0.76 | 14.6 |
| SST24 J143702.0+344631 | 0.10 | 0.11 | 0.17 | 0.33 | 0.33 | 14.2 |

Table 3.2 (cont'd)

| Source Name | F_{F814W} (μJy) | σ_{F814W} (μJy) | F_{F160W} (μJy) | σ_{F160W} (μJy) | F_{24} (mJy) | $R - [24]$ (Vega) |
|------------------------|-----------------------------------|--|-----------------------------------|--|-------------------|----------------------|
| SST24 J143816.6+333700 | 0.68 | 0.16 | 4.22 | 0.22 | 3.28 | 14.8 |

3.4.2 Morphology

To analyze the morphologies of the bump DOGs, we follow a similar procedure to that outlined in Paper I. Here we summarize the three different, complementary approaches used in analyzing the morphology of the DOGs in our sample: a visual classification experiment, multi-component GALFIT modeling, and non-parametric quantification.

3.4.2.1 Visual Classification

For this paper, our visual classification experiment differed significantly from Paper I. The goal of the original experiment outlined in Paper I was to determine if DOGs could be distinguished from normal field galaxies based on a visual classification. This proved difficult to quantify due to the faintness of DOGs in the rest-frame UV (ACS/WFPC2 images) and the small number of field galaxies in the rest-frame optical (NICMOS images).

Our new classification experiment is designed specifically to identify morphological differences found in the NICMOS imaging of bump and power-law DOGs. We generated a $5'' \times 5''$ cutout image of every DOG with NICMOS data (both power-law and bump sources, a total of 53 objects) and arranged them randomly. Seven of the coauthors classified these objects into “Regular”, “Irregular”, or “Too Faint To Tell”. In addition to probing for a difference between bump and power-law DOGs,

the mode of the classifications for each DOG as well as the number of coauthors in agreement with the mode is useful as a qualitative assessment of the morphology for comparison with the more quantitative methods discussed below. Seven of the coauthors submitted morphological classifications. Results are presented in Table 3.4 and discussed in section 3.5.2.1.

3.4.2.2 Non-parametric Classification

A wide variety of tools now exist to quantify the morphologies of galaxies. Five such tools which frequently appear in the literature are the concentration index C (Abraham et al., 1994), the rotational asymmetry A (Schade et al., 1995), the residual clumpiness, S (Conselice, 2003), the Gini coefficient G (Abraham et al., 2003), and M_{20} parameter (Lotz et al., 2004). Of these five, A and S have S/N and spatial resolution requirements that are not satisfied by the imaging of the DOGs in this sample. Therefore, this analysis is focused on C , G , and M_{20} .

The concentration index C is defined as the ratio of the circular radii containing 20% and 80% of the total flux (Bershady et al., 2000):

$$C = 5 \log_{10} \left(\frac{r_{80}}{r_{20}} \right), \quad (3.1)$$

where r_{80} and r_{20} are the circular apertures containing 80% and 20% of the total flux, respectively. G was originally introduced to measure how evenly the wealth in a society is distributed (Glasser, 1962). Recently, Abraham et al. (2003) and Lotz et al. (2004) applied this method to aid in galaxy classification: low values imply a galaxy's flux is well-distributed among many pixels, while high values imply a small fraction of the pixels within a galaxy account for the majority of the total flux. M_{20} is the logarithm of the second-order moment of the brightest 20% of the galaxy's flux, normalized by the total second-order moment (Lotz et al., 2004). Higher values of M_{20} indicate multiple bright clumps offset from the second-order moment center.

Lower values are typical of centrally-dominated systems.

Prior to computing G or M_{20} , we first generate a catalog of objects using SExtractor (Bertin & Arnouts, 1996). We use a detection threshold of 3σ (corresponding to 23.7 mag arcsec⁻²) and a minimum detection area of 15 pixels. The center of the image, the ellipticity, and position angle computed by SExtractor are used as inputs to our morphology code. This code is written by J. Lotz and described in detail in Lotz et al. (2004). Here, we summarize the relevant information.

Postage stamps of each object in the SExtractor catalog (and the associated segmentation map) are created with foreground and background objects masked out. For each source, we adopt the sky value computed in our photometric analysis. Since the isophotal-based segmentation map produced by SExtractor is subject to the effects of surface brightness dimming at high redshift, pixels belonging to the galaxy are computed based on the surface brightness at the elliptical Petrosian radius, $\mu(r_P)$. We adopt the usual generalized definition for r_P as the radius at which the ratio of the surface brightness at r_P to the mean surface brightness within r_P is equal to 0.2 (Petrosian, 1976). The elliptical r_P is derived from surface brightness measurements within elliptical apertures and represents the length of the major axis. Studies have shown that using the Petrosian radius to select pixels associated with a galaxy provides the most robust morphological measurements (Lotz et al., 2004; Lisker, 2008). Pixels with surface brightness above $\mu(r_P)$ are assigned to the galaxy while those below it are not.

Using the new segmentation map, we recompute the galaxy's center by minimizing the total second-order moment of the flux. A new value of r_P is then computed and a revised segmentation map is used to calculate G and M_{20} . Finally, the morphology code calculates an average S/N per pixel value using the pixels in the revised segmentation map (Eqs. 1 through 5 in Lotz et al., 2004). Results of this analysis

are presented in Table 3.5 and will be discussed in section 3.5.2.2.

3.4.2.3 GALFIT Modeling

In Paper I, we reported the existence of a centrally located, compact component that was present in the NICMOS images of power-law DOGs but absent in the ACS/WFPC2 images, signifying the presence of strong central obscuration. To quantify this feature, we used GALFIT (Peng et al., 2002) to model the 2-D light profile of the DOGs. In this paper, we repeat this procedure on the bump DOGs with *HST* NICMOS data. Here, we review our methodology.

We choose the size of the fitting region to be 41×41 pixels (corresponding to angular and physical sizes of $3''$ and ≈ 24 kpc, respectively) because the DOGs are small and have low S/N compared to more typical applications of GALFIT. For the same reason, we wish to include only the minimum necessary components in our model. We model the observed emission with three components which are described by a total of 10 free parameters. The number of degrees of freedom, N_{DOF} , is calculated as the difference of the number of pixels in the image and the number of free parameters. Thus, the maximum N_{DOF} is 1671. Cases where $N_{\text{DOF}} < 1671$ are associated with images where some pixels were masked out because they were associated with obvious residual instrumental noise. NIC2 is a Nyquist-sampled array ($0.075'' \text{ pix}^{-1}$ compared to $0.16''$ FWHM beam), so the pixels in our image are not completely independent and the χ^2_ν values should be interpreted in a relative sense rather than an absolute one.

The first element in our GALFIT model is a sky component whose amplitude is held constant at a value derived from the photometry to yield flat radial profiles. The second is an instrumental PSF generated from the TinyTim software assuming a red power-law spectrum ($F_\nu \propto \nu^{-2}$) as the object spectrum (Krist and Hook 2004), which can simulate a PSF for NICMOS, WFPC2, and ACS. For the NICMOS and

WFPC2 images, the DOG is positioned in nearly the same spot on the camera. In the case of WFPC2 this is pixel (132,144) of chip 3 and pixel (155, 164) for NICMOS. The PSF is computed out to a size of $3.0''$, and for the WFPC2 PSF we oversample by a factor of 1.3 to match the pixel scale of the drizzled WFPC2 images.

The final component is a Sérsic profile (Sersic, 1968) where the surface brightness scales with radius as $\exp[-\kappa((r/R_{\text{eff}})^{1/n} - 1)]$, where κ is chosen such that half of the flux falls within R_{eff} . As few constraints as possible were placed so as to optimize the measurement of the extended flux (i.e., non-point source component). In certain cases, the Sérsic index had to be constrained to be positive to ensure convergence on a realistic solution. When fitting the NICMOS data, the uncertainty image from `calnicb` provides the necessary information required by GALFIT to perform a true χ^2 minimization. The TinyTim NIC2 PSF is convolved with the Sérsic profile prior to performing the χ^2 minimization. The initial guesses of the magnitude, half-light radius, position angle, and ellipticity were determined from the output values from SExtractor. Varying the initial guesses within reasonable values (e.g., plus or minus two pixels for the half-light radius) yielded no significant change in the best-fit model parameters. The NICMOS centroid was used as the initial guess for the (x,y) position of both the PSF and extended components.

A degeneracy potentially exists between our estimates of the point-source fraction (i.e., relative ratio of PSF component flux to Sérsic component flux) and the Sérsic index. Fits using models without the PSF component yield larger reduced χ^2_ν values, especially when the point source fraction in our three-component model was large (see further discussion in section 3.5.2.3). In cases where the point source fraction was small, the no-PSF model had similar parameter values as our fiducial three-component model, as would be expected.

The results of this GALFIT analysis are presented in Table 3.3 and will be

discussed in section 3.5.2.3.

Table 3.3. NICMOS GALFIT Results^a

| | PSF Fraction | R_{eff} (kpc) | n | Axial Ratio | N_{dof} | χ^2_{ν} |
|------------------------|-----------------|---------------------------|---------------|-----------------|------------------|----------------|
| SST24 J142637.3+333025 | 0.45 ± 0.55 | — | 0.1 ± 1.7 | 0.15 ± 0.49 | 1594 | 2.3 |
| SST24 J142652.4+345504 | 0.11 ± 0.20 | 3.3 ± 0.4 | 1.1 ± 0.2 | 0.84 ± 0.06 | 1654 | 1.6 |
| SST24 J142724.9+350823 | 0.04 ± 0.06 | 4.6 ± 0.2 | 1.5 ± 0.1 | 0.69 ± 0.02 | 1656 | 1.1 |
| SST24 J142832.4+340850 | — | — | — | — | — | — |
| SST24 J142920.1+333023 | 0.08 ± 0.09 | 3.3 ± 0.2 | 0.8 ± 0.1 | 0.79 ± 0.04 | 1663 | 2.5 |
| SST24 J142941.0+340915 | 0.07 ± 0.18 | 3.9 ± 1.8 | 0.0 ± 0.1 | 0.57 ± 0.04 | 1635 | 2.1 |
| SST24 J142951.1+342041 | 0.03 ± 0.09 | 5.2 ± 0.1 | 0.3 ± 0.1 | 0.42 ± 0.01 | 1668 | 3.2 |
| SST24 J143020.4+330344 | 0.13 ± 0.11 | 2.9 ± 0.2 | 0.9 ± 0.2 | 0.64 ± 0.04 | 1599 | 3.4 |
| SST24 J143028.5+343221 | 0.05 ± 0.05 | 4.4 ± 0.2 | 0.7 ± 0.1 | 0.39 ± 0.02 | 1639 | 2.8 |
| SST24 J143137.1+334500 | 0.10 ± 0.13 | 10.5 ± 0.8 | 0.7 ± 0.1 | 0.26 ± 0.01 | 1657 | 1.1 |
| SST24 J143143.3+324944 | 0.42 ± 0.05 | — | 1.0 ± 0.4 | 0.66 ± 0.03 | 1665 | 2.7 |
| SST24 J143152.4+350029 | 0.02 ± 0.03 | 3.9 ± 0.1 | 0.7 ± 0.1 | 0.69 ± 0.01 | 1666 | 2.2 |
| SST24 J143216.8+335231 | 0.00 ± 0.08 | 4.2 ± 0.1 | 0.1 ± 0.1 | 0.60 ± 0.01 | 1666 | 2.0 |
| SST24 J143321.8+342502 | 0.13 ± 0.05 | 1.8 ± 0.1 | 1.4 ± 0.1 | 0.61 ± 0.02 | 1659 | 1.6 |
| SST24 J143324.2+334239 | 0.12 ± 0.06 | 2.6 ± 0.1 | 1.2 ± 0.1 | 0.80 ± 0.03 | 1612 | 2.6 |
| SST24 J143331.9+352027 | 0.00 ± 0.08 | 4.7 ± 0.2 | 0.9 ± 0.1 | 0.57 ± 0.03 | 1658 | 2.7 |
| SST24 J143349.5+334602 | 0.05 ± 0.07 | 3.2 ± 0.3 | 0.8 ± 0.1 | 0.67 ± 0.04 | 1660 | 2.4 |
| SST24 J143458.8+333437 | 0.15 ± 0.10 | 4.9 ± 0.5 | 2.1 ± 0.3 | 0.81 ± 0.03 | 1657 | 1.9 |
| SST24 J143502.9+342657 | 0.03 ± 0.25 | 8.8 ± 3.5 | 0.0 ± 0.1 | 0.35 ± 0.02 | 1669 | 1.3 |
| SST24 J143503.3+340243 | 0.09 ± 0.09 | 2.9 ± 0.1 | 1.0 ± 0.1 | 0.62 ± 0.02 | 1659 | 1.8 |
| SST24 J143702.0+344631 | 0.77 ± 0.77 | — | — | — | — | — |

Table 3.3 (cont'd)

| | PSF Fraction | R_{eff} (kpc) | n | Axial Ratio | N_{dof} | χ^2_{ν} |
|------------------------|-----------------|---------------------------|---------------|-----------------|------------------|----------------|
| SST24 J143816.6+333700 | 0.06 ± 0.04 | 2.3 ± 0.1 | 0.4 ± 0.1 | 0.81 ± 0.02 | 1666 | 1.9 |

^aUncertainties represent formal GALFIT measurements and likely underestimate true uncertainties.

It is important to note here that NIC2 cannot spatially resolve objects smaller than 1.3 kpc at $z \approx 2$. This limit is large enough to encompass a compact stellar bulge as well as an active galactic nucleus, implying that we cannot, from these data alone, distinguish between these two possibilities as to the nature of any central, unresolved component.

3.5 Results

In this section, we present our photometry, visual classification, non-parametric classification, GALFIT modeling, and stellar and dust mass results.

3.5.1 Photometry

Table 3.2 presents the photometric information derived from the *HST* imaging. In Figure 3.4, we show the $I - H$ vs. H color-magnitude diagram for bump DOGs, power-law DOGs, XFLS ULIRGs, and a sample of galaxies in the Hubble Deep Field (HDF) whose photometric redshifts are comparable to DOGs ($1.5 < z_{\text{phot}} < 2.5$). Power-law DOGs tend to be the reddest sources ($I - H \approx 2 - 5$ AB mag), followed by bump DOGs ($I - H \approx 2 - 3$ AB mag), XFLS ULIRGs ($I - H \approx 1.5 - 3$), and SMGs, which have $I - H$ colors similar to high- z galaxies in the HDF ($I - H \approx 0 - 2$

AB mag). SMGs and DOGs (both bump and power-law varieties) are comparably bright in H . The bluer color of SMGs relative to DOGs at a given H -band magnitude suggests weaker UV flux from DOGs, either due to older stellar populations in DOGs or a higher dust mass relative to stellar mass in DOGs.

3.5.2 Morphologies

3.5.2.1 Visual Classification Results

From the 7 users who entered classifications of the NICMOS images of DOGs, the main results can be summarized as follows: power-law DOGs were classified as irregular (43%) approximately as frequently as they were classified regular (42%), with 15% being too faint to tell. In contrast, bump DOGs were classified as irregular significantly more often than they were classified as regular (69% vs. 26%, with only 5% being too faint to tell). These results can be subdivided into those with very robust classifications (6 or more users were in agreement), and less robust classifications (fewer than 6 users were in agreement). The trends quoted earlier become stronger when considering only the robust classifications, as the ratio of regular:irregular classifications for this subset is 1.4:1 and 1:3 for power-law and bump DOGs, respectively. Table 3.4 shows the breakdown of visual classifications with this additional subdivision. In Table 3.5 we provide, for each DOG in this sample, the mode of the classifications as well as how many users were in agreement with the mode. Overall, the qualitative morphological assessment indicates that bump DOGs have irregular, diffuse morphologies more frequently than power-law DOGs.

3.5.2.2 Non-parametric Classification Results

The characterization of galaxy morphologies requires high S/N imaging in order to provide reliable results. For non-parametric forms of analysis, typical requirements

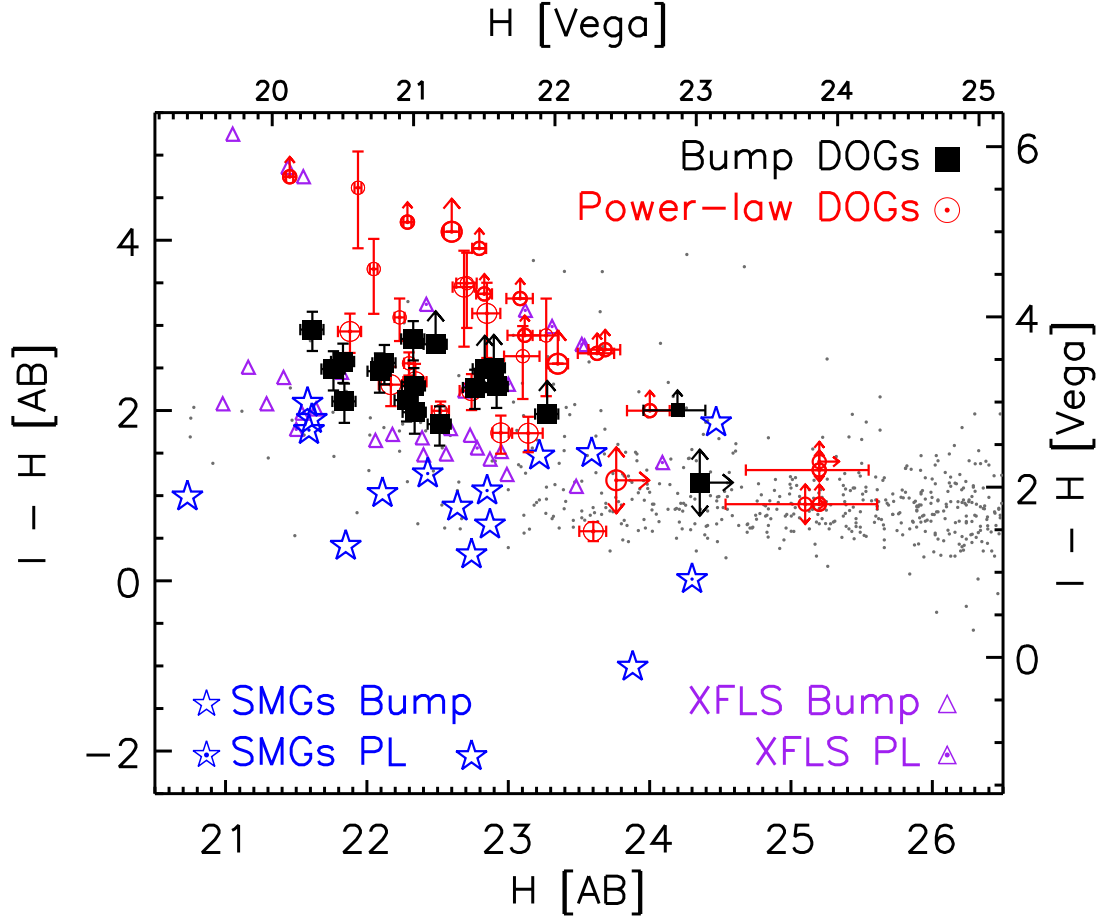


Figure 3.4 Color-magnitude diagram for bump DOGs, power-law DOGs, SMGs, and XFLS ULIRGs at $z > 1.4$ (symbols as in Figure 3.1). Smaller symbols indicate objects where the I -band measurement has been synthesized from the R -band or V -band measurement (Dasyra et al., 2008; Bussmann et al., 2009b), assuming a power-law of the form $F_\nu \propto \nu^{-2}$. Arrows indicate $2\text{-}\sigma$ limits. Galaxies spanning the redshift range $1.5 < z < 2.5$ in the HDF-N (Papovich, personal communication) and HDF-S (Labbé et al., 2003) are shown with grey dots. Power-law DOGs have the reddest $I - H$ colors, followed by bump DOGs, XFLS ULIRGs, and SMGs, which have colors comparable to high- z HDF galaxies.

Table 3.4. Visual Morphological Classifications

| | Regular | | Irregular | | Too Faint | Too Tell |
|----------------|---------|----------|-----------|----------|-----------|----------|
| | Agree | Disagree | Agree | Disagree | Agree | Disagree |
| Power-law DOGs | 34% | 9% | 24% | 18% | 6% | 9% |
| Bump DOGs | 16% | 10% | 48% | 21% | 5% | 0% |

are $S/N_{\text{pixel}} > 2$ and $R_p(\text{Elliptical}) > 2 \times \text{FWHM}$ (Lotz et al., 2004) (hereafter, r_P indicates the elliptical petrosian radius). In the case of the imaging presented here, $\text{FWHM} = 0''.16$. None of the 22 DOGs in GO-11195 observed with WFPC2 have the per-pixel S/N necessary to compute r_P , G , M_{20} , and C . On the other hand, 20 out of 21 bump DOGs with NICMOS observations have sufficient S/N. Table 3.5 presents the visual and non-parametric measures of DOG morphologies, including per-pixel S/N, r_P , G , M_{20} , and C values for the NICMOS images.

Table 3.5. NICMOS Non-parametric Morphological Classifications

| Source Name | Visual ^a | $N_{\text{agree}}^{\text{b}}$ | S/N | r_{P} (kpc) | G | M_{20} | C |
|------------------------|---------------------|-------------------------------|-------|----------------------|------|----------|-----|
| SST24 J142637.3+333025 | TFTT | 4 | 3.1 | — | 0.47 | -1.72 | 2.9 |
| SST24 J142652.4+345504 | Reg | 4 | 3.8 | 8.6 | 0.38 | -0.77 | 3.4 |
| SST24 J142724.9+350823 | Irr | 6 | 4.1 | 12.0 | 0.48 | -1.63 | 4.9 |
| SST24 J142832.4+340850 | — | — | 6.8 | — | — | — | — |
| SST24 J142920.1+333023 | Irr | 6 | 3.4 | 6.9 | 0.48 | -1.00 | 2.8 |
| SST24 J142941.0+340915 | Irr | 7 | 2.8 | 6.6 | 0.40 | -0.99 | 1.7 |
| SST24 J142951.1+342041 | Irr | 6 | 4.0 | 10.7 | 0.46 | -0.98 | 2.8 |
| SST24 J143020.4+330344 | Reg | 7 | 3.3 | 7.0 | 0.49 | -1.63 | 3.0 |
| SST24 J143028.5+343221 | Irr | 6 | 2.5 | 9.7 | 0.51 | -1.18 | 4.0 |
| SST24 J143137.1+334500 | Irr | 4 | 2.5 | 27.5 | 0.44 | -1.00 | 3.2 |
| SST24 J143143.3+324944 | Reg | 7 | 11.3 | — | 0.52 | -1.69 | 3.0 |
| SST24 J143152.4+350029 | Irr | 4 | 5.2 | 8.9 | 0.46 | -1.41 | 4.8 |
| SST24 J143216.8+335231 | Irr | 4 | 4.4 | 8.4 | 0.38 | -0.98 | 2.4 |
| SST24 J143321.8+342502 | Irr | 6 | 5.0 | 8.2 | 0.54 | -0.78 | 3.3 |
| SST24 J143324.2+334239 | Reg | 7 | 3.8 | 6.7 | 0.54 | -1.62 | 3.0 |
| SST24 J143331.9+352027 | Irr | 6 | 4.1 | 8.2 | 0.37 | -0.85 | 2.4 |
| SST24 J143349.5+334602 | Irr | 7 | 2.5 | 11.8 | 0.48 | -0.83 | 1.9 |
| SST24 J143458.8+333437 | Irr | 7 | 2.5 | 9.6 | 0.54 | -1.24 | 3.8 |
| SST24 J143502.9+342657 | Irr | 7 | 2.1 | 14.9 | 0.46 | -0.77 | 2.4 |
| SST24 J143503.3+340243 | Reg | 6 | 4.0 | 7.2 | 0.53 | -1.71 | 2.8 |
| SST24 J143702.0+344631 | TFTT | 7 | — | — | — | — | — |
| SST24 J143816.6+333700 | Reg | 5 | 5.1 | 5.7 | 0.47 | -1.47 | 2.6 |

Table 3.5 (cont'd)

| Source Name | Visual ^a | N_{agree}^b | S/N | r_P (kpc) | G | M_{20} | C |
|-------------|---------------------|----------------------|-------|-------------|-----|----------|-----|
|-------------|---------------------|----------------------|-------|-------------|-----|----------|-----|

^a Mode of visual classification.

^b Number of users in agreement with mode of visual classification.

Figure 3.5 displays C as a function of r_P for power-law DOGs, bump DOGs, SMGs, and XFLS sources. The left panel of Figure 3.5, focusing only on bump and power-law sources that qualify as DOGs, shows that bump DOGs have larger sizes (median $r_P = 8.0$ kpc) than their power-law siblings (median $r_P = 5.4$ kpc). The right panel of Figure 3.5 shows SMGs and XFLS sources which are not DOGs. In this diagram, almost all sources are bumps, and almost all sources have large sizes (median $r_P = 8.5$ kpc).

When no consideration is given to their $R - [24]$ color, SMGs and XFLS sources show a similar distinction in their sizes when dividing the samples into bump (SMG median $r_P = 8.6$ kpc; XFLS median $r_P = 7.6$ kpc) and power-law (SMG median $r_P = 4.6$ kpc; XFLS median $r_P = 6.2$ kpc) varieties. Indeed, considering all $z > 1.4$ ULIRGs regardless of whether they are selected at mid-IR or sub-mm wavelengths, bump sources (median $r_P = 8.0$ kpc) are significantly larger than their power-law counterparts (median $r_P = 5.6$ kpc), and a two-sided Kolmogorov-Smirnov (KS) test indicates there is only a 1.3% chance the two populations could be drawn randomly from the same parent sample. This finding is consistent with results from Keck K -band adaptive optics imaging of DOGs which shows that power-law DOGs are smaller and more concentrated than bump DOGs (Melbourne et al., 2009). One

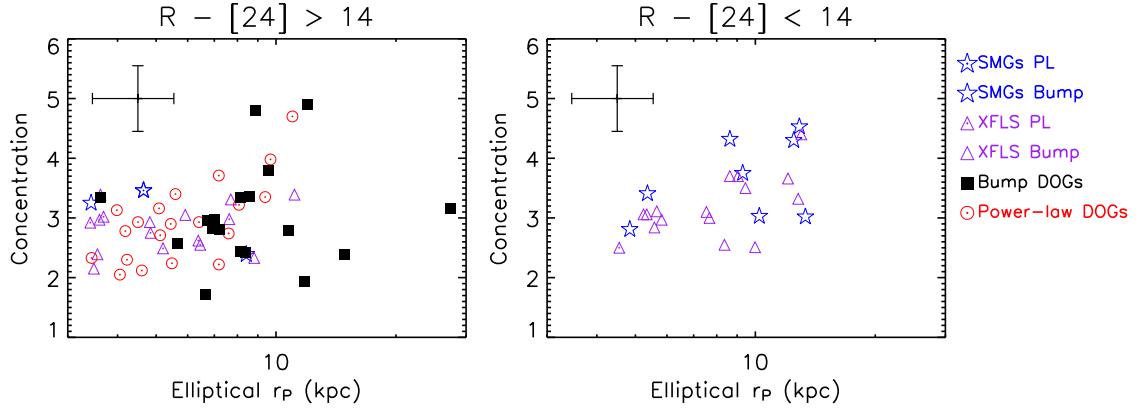


Figure 3.5 C as a function of r_P for $z > 1.4$ ULIRGs (symbols are the same as in Figure 3.1). *Left:* Power-law DOGs, bump DOGs, SMGs that qualify as DOGs, and XFLS ULIRGs at $z > 1.4$ that qualify as DOGs. Error bar in top left corner illustrates typical uncertainty level, computed as a function of S/N and spatial resolution (Lotz et al., 2006). Bump DOGs have larger sizes than power-law DOGs. *Right:* Same as left panel, but only for $z > 1.4$ ULIRGs (SMGs and XFLS) that are not DOGs. Regardless of sample selection criteria, power-law $z > 1.4$ ULIRGs are significantly smaller than their bump counterparts (median r_P of 5.6 kpc vs. 8.0 kpc, for the total respective populations).

caveat with this result is that the bump DOG sample is brighter in H -band than the power-law DOG sample. Considering only the DOGs satisfying $H < 22.5$, the bump and power-law DOGs have similar sizes ($r_P \approx 8$ kpc). At the faint end ($H > 22.5$), power-law DOGs are smaller than bump DOGs (5 kpc vs. 8 kpc, respectively).

The distribution in $G - M_{20}$ space derived from NICMOS imaging of power-law DOGs, bump DOGs, XFLS sources, and SMGs is shown in Figure 3.6. A sample of 73 local ULIRGs ($z < 0.2$) is also shown in this diagram (Lotz et al., 2004), using data from *HST* WFPC2/F814W imaging (Borne et al., 2000). The dotted line separates major mergers from other types of galaxies and is based on measurements at roughly the same rest-frame wavelength ($\approx 5000 - 5500$ Å) of these 73 local ULIRGs (Lotz et al., 2004).

The left panel of Figure 3.6 (including all sources that qualify as DOGs) shows that bump DOGs appear offset to lower G and higher M_{20} values than power-law DOGs. The median $\{G, M_{20}\}$ values for bump and power-law DOGs are $\{0.47, -1.08\}$ and $\{0.49, -1.48\}$, respectively. These types of morphologies are consistent with what is seen in simulations of major mergers during the beginning and end stages, respectively, of the “final coalescence” of the merger when the SFR peaks and begins to turn over (Lotz et al., 2008). In the right panel of Figure 3.6, SMGs and XFLS $z > 1.4$ ULIRGs that are not DOGs are shown. Although nearly all of these sources have bump SEDs, their morphologies bear a greater resemblance to power-law DOGs than bump DOGs. The median $\{G, M_{20}\}$ values for the non-DOGs are $\{0.52, -1.46\}$.

The preceding analysis is largely qualitative in nature. A more quantitative approach involves the use of contingency tables, which offer a means to quantify broad-brush distinctions in the properties of two populations of objects. Three properties are tested here: mid-IR SED shape (bump OR power-law), extent of

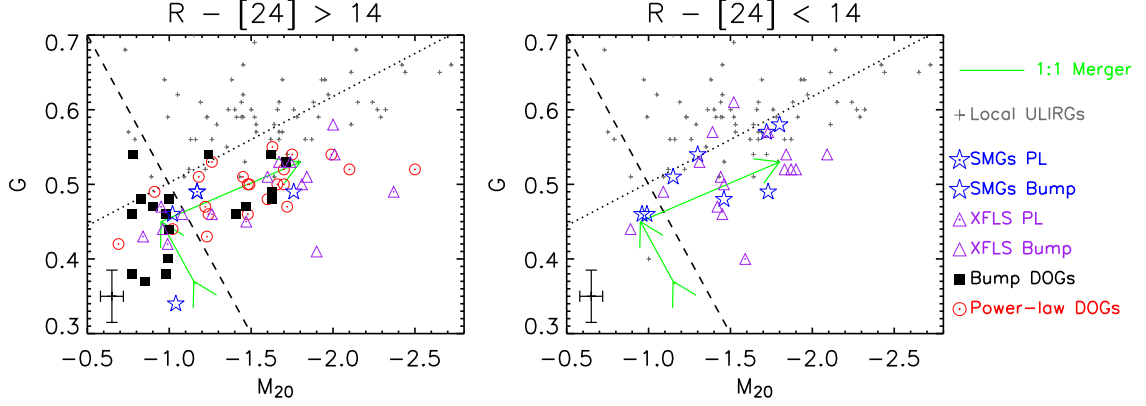


Figure 3.6 Gini coefficient vs. M_{20} derived from NIC2/F160W images of high-redshift ULIRGs (symbols same as in Figure 3.1) and local ULIRGs (gray plus signs, Lotz et al., 2004). The evolution of a typical gas-rich ($f_{\text{gas}} = 0.5$) major merger during its peak SFR period is illustrated by a green vector (Lotz et al., 2008). The dashed line is drawn qualitatively to separate “diffuse” and “single-object” morphologies and bisects the green vector. The dotted line shows the empirically determined (based on measurements of local ULIRGs) demarcation line above which objects are obvious major mergers (Lotz et al., 2004). *Left*: Bump DOGs, power-law DOGs, and SMGs and XFLS ULIRGs qualifying as DOGs. Within this highly obscured subset of the high redshift ULIRG population, bump sources are “diffuse” (low G , high M_{20}) more often than power-law DOGs. In simulations of major mergers, such morphologies occur during the early half of the peak SFR period of the merger. *Right*: Same as left panel, but for SMGs and XFLS $z > 1.4$ ULIRGs that are not DOGs. The distribution of morphologies for non-DOGs is skewed towards the “single-object” region of this diagram. These objects may occur during the late stage of the peak SFR period of a major merger, or they may be associated with more secular evolutionary processes.

Table 3.6. NICMOS Morphology Contingency Table Data

| | $R - [24] < 14$ | | $R - [24] > 14$ | |
|-----------|----------------------|----------------------------|----------------------|----------------------------|
| | Diffuse ^a | Single-source ^b | Diffuse ^a | Single-source ^b |
| Power-law | 0 | 1 | 7 | 24 |
| Bump | 3 | 20 | 15 | 14 |

$$^a G < 0.4M_{20} + 0.9$$

$$^b G > 0.4M_{20} + 0.9$$

obscuration ($R - [24] > 14$ OR $R - [24] < 14$), and morphology (low G , high M_{20} OR high G , low M_{20}). The division based on morphology is derived from simulations of major mergers, which indicate that the high SFR period of a merger is bisected by a line described by the equation $G = 0.4M_{20} + 0.9$ (Lotz et al., 2008). Table 3.6 shows the two 2×2 contingency tables that are needed to account for the three variables used in this analysis.

The first result from this analysis is the paucity of power-law sources in the non-DOG subset. There are 29 bump DOGs, 23 bump non-DOGs, 31 power-law DOGs, and only 1 power-law non-DOGs. The 2×2 contingency table for this dataset indicates a negligible probability (Fisher Exact p-value < 0.0001) that all four sub-populations are drawn randomly from the same parent sample. Could this be due to a selection effect? The non-DOG sample comprises ULIRGs from the XFLS and SMGs. XFLS sources are selected to have high $F_{24\mu\text{m}}/F_{8\mu\text{m}}$ flux density ratios, which tends to favor the selection of bump SEDs over power-law ones. On the other hand, the XFLS sources are selected to be very bright at $24\mu\text{m}$ ($F_{24\mu\text{m}} > 0.8$ mJy. At these

$24\mu\text{m}$ flux densities, power-law sources are more common than bump sources (e.g. Dey et al., 2008). SMGs are selected at sub-mm wavelengths, without any knowledge of the mid-IR SED shape. Presently, it is not obvious that either the XFLS ULIRGs or SMGs are affected by the kind of severe selection effect necessary to produce the observed trends.

The second result from the contingency table data is that, considering only bump sources, non-DOGs have a much more skewed distribution of morphologies than DOGs. Diffuse type morphologies (low G , high M_{20}) are rare in the non-DOG population, while in DOGs they occur much more frequently. A 2×2 contingency table here suggests a very low probability (Fisher Exact p-value = 0.007) that blue ($R - [24] < 14$) and red ($R - [24] > 14$) ULIRGs have morphologies drawn from the same parent distribution. Low G and high M_{20} values suggest irregular and lumpy (less centrally concentrated) morphologies that could be caused by a clumpy distribution of stars or significant dust obscuration (Lotz et al., 2008). Further discussion of the implications of this result are deferred to section 3.6.

Finally, with the highly obscured subset of ULIRGs (DOGs), there is evidence that bump DOGs have diffuse type morphologies more commonly than power-law DOGs. A 2×2 contingency table indicates an extremely low probability (Fisher Exact p-value = 0.003) that bump and power-law DOGs have morphologies drawn from the same parent distribution. As mentioned earlier, this distinction is consistent with expectations from simulations of major mergers during the peak SFR phase of the merger (Lotz et al., 2008).

3.5.2.3 GALFIT Results

The results of our GALFIT analysis of the NICMOS images of the Cycle 16 DOGs are shown in Table 3.3, along with $1\text{-}\sigma$ uncertainties in the best-fit parameters. Included in this table are point source fractions (ratio of flux in the point-source

component to the total flux of the source), effective radius of the Sérsic component (R_{eff}), Sérsic index (n), semi-minor to semi-major axis ratio of the Sérsic component (Axial Ratio), number of degrees of freedom (N_{DOF}), and reduced chi-squared (χ^2_ν).

Figure 3.7 shows a comparison of R_{eff} (the radius within which half the light is enclosed) and r_{P} (the radius at which the ratio of the surface brightness at r_{P} to the mean surface brightness within r_{P} is equal to 0.2) for DOGs, SMGs, and XFLS ULIRGs at $z > 1.4$. For bump DOGs and power-law DOGs, the median R_{eff} values are 3.3 kpc and 2.5 kpc, respectively. Bump sources that are not DOGs (from the SMG and XFLS samples) have a median effective radius of 3.2 kpc. One of the bump DOGs (SST24 J143137.1+334500) has the appearance of an edge-on disk with a semi-major axis of $3''.25$, or 27.5 kpc at its redshift of 1.77. This extremely large R_{eff} value may imply that this object is in fact a merger viewed edge-on. Spatially resolved dynamical information would be particularly useful for answering this question.

Our measurements of SMG sizes (median R_{eff} value for the full SMG population of 3.6 kpc) are in broad agreement, given the different methods used, with those of Swinbank et al. (2010a), who find typical half-light radii of 2.8 ± 0.4 kpc. For XFLS ULIRGs, Dasyra et al. (2008) use GALFIT to find typical effective radii of 2.43 ± 0.80 kpc, consistent with our results (median R_{eff} of 2.5 kpc). As an additional consistency check, a strong correlation is evident between R_{eff} and r_{P} for all populations. Note that $r_{\text{P}} > R_{\text{eff}}$; this is because the Sérsic profile is defined such that half of the galaxy's flux is enclosed within a radius of $r = R_{\text{eff}}$, while r_{P} defines the radius at which the surface brightness is one-fifth the average surface brightness within r_{P} .

Figure 3.8 shows the point source fraction and Sérsic index for DOGs, SMGs, and XFLS ULIRGs at $z > 1.4$. The majority of sources have low point source

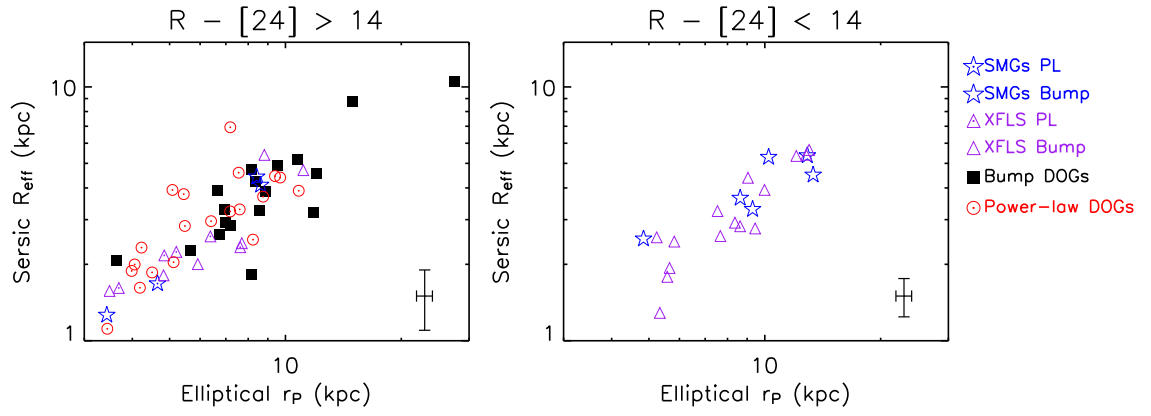


Figure 3.7 Comparison of sizes of $z > 1.4$ ULIRGs (symbols same as in Figure 3.1) as determined by the effective radius of the Sérsic component from GALFIT modeling (R_{eff}) and the elliptical Petrosian radius (r_P). *Left:* Bump DOGs, power-law DOGs, and SMGs and XFLS ULIRGs qualifying as DOGs. *Right:* SMGs and XFLS ULIRGs that are not DOGs. Both size measurements suggest that power-law sources are on average smaller than bump sources, although a significant population of compact bump sources exists.

fractions (point source fraction < 0.3) and disk-type morphologies ($n < 2$). Studies have found that when a point source contributes less than 20% of the total light, it has an insignificant effect on the measured morphologies (Pierce et al., 2010). Considering only DOGs with sufficient S/N to be placed on this diagram (left panel of Figure 3.8), 6/28 power-law DOGs and 0/17 bump DOGs have either $n > 3$ or point source fraction > 0.4 . Such sources have compact, centrally dominated morphologies ($n = 1$ corresponds to an exponential profile, and $n = 4$ corresponds to a de Vaucouleurs profile; Peng et al., 2002). This distinction is consistent with the G and M_{20} results in section 3.5.2.2.

On the other hand, the distinction between bump and power-law sources is not as obvious when considering the SMGs and XFLS sources. For SMGs, 2/3 power-law and 2/11 bump sources satisfy the compact criteria outlined above, while for XFLS ULIRGs the respective numbers are 2/6 (power-law sources) and 3/18 (bump sources). Further discussion of the distinction between the morphological properties of bump and power-law DOGs is deferred to section 3.6.

3.6 Discussion: Implications for Models of Massive Galaxy Evolution

ULIRG activity in the local universe has been known for some time to result from a major merger of two gas-rich disk galaxies (e.g. Armus et al., 1987; Sanders et al., 1988a). Material is funneled towards the center of the system and drives an intense starburst, producing large amounts of cold dust, and begins to feed a nascent central black hole. As the merger evolves, ambient gas and dust particles are heated by feedback processes. This warm-dust ULIRG stage has been suggested to represent a transition stage between cold ULIRGs and optically luminous quasars (Sanders et al., 1988b).

Recently, efforts have been made to extend this paradigm to the ultra-luminous

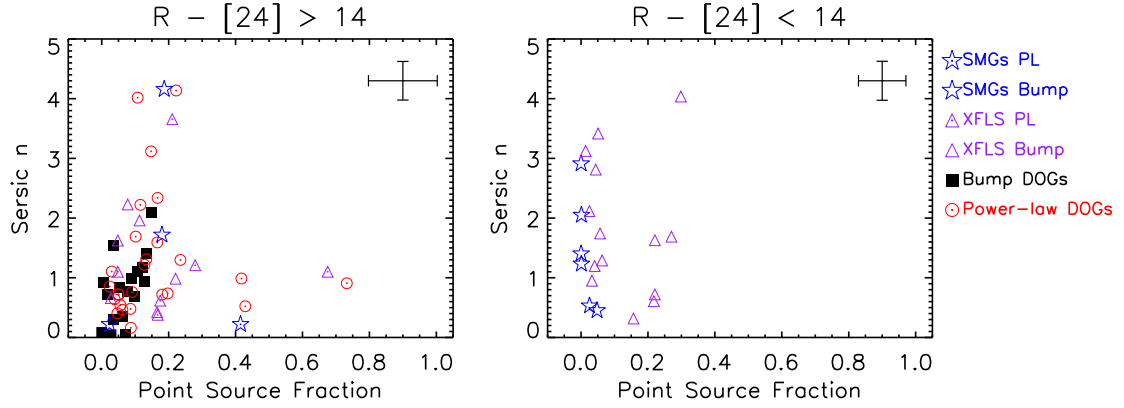


Figure 3.8 Sérsic index n as a function of point source fraction from GALFIT modeling (symbols same as in Figure 3.1). *Left:* Power-law DOGs, bump DOGs, and SMGs and XFLS ULIRGs qualifying as DOGs. Aside from a handful of power-law DOGs with point source fraction > 0.4 or $n > 2.5$, there is strong overlap between the bump and power-law DOG populations in this diagram. *Right:* SMGs and XFLS ULIRGs that do not qualify as DOGs. In contrast to the DOG populations, there are a number of $n > 2.5$ bump sources from the SMG and XFLS samples. As in the analysis of the G and M_{20} values, these could represent objects at the end of the peak SFR period, or they might not be associated with major merger activity at all.

galaxy populations at high-redshift. One possible hypothesis within this scenario is that SMGs represent the cold-dust ULIRGs created during the early stage of the merger, whereas *Spitzer*-selected sources represent the warm-dust ULIRGs formed during the later stages of the merger (e.g., Dey et al., 2008; Dey & The NDWFS/MIPS Collaboration, 2009; Narayanan et al., 2009). This basic picture (that SMGs and *Spitzer*-selected ULIRGs are related) is strengthened by the similarity in the measured clustering strengths of $z \approx 2$ SMGs, DOGs, and QSOs, which suggest that these populations all reside in similar mass halos at similar epochs (e.g. Brodwin et al., 2008; Dey & The NDWFS/MIPS Collaboration, 2009).

In this section, we use the morphological evidence presented in section 3.5 to test the viability of this scenario. On one hand, when considering only the most extremely obscured objects (i.e., DOGs), a clear trend in morphologies emerges. Bump DOGs are larger (i.e., more spatially extended) than power-law DOGs ($r_p \approx 8$ kpc vs. 5 kpc), more diffuse ($\{G, M_{20}\} \approx \{0.47, -1.08\}$ vs. $\{G, M_{20}\} \approx \{0.49, -1.48\}$), and more irregular (67% vs. 50% visually classified as irregular). This trend is consistent with expectations from simulations of major mergers, which indicate that merger morphologies generally evolve from extended, diffuse, and irregular at the beginning of the peak SFR phase to compact and regular when star-formation shuts down and the AGN begins to dominate (Lotz et al., 2008; Narayanan et al., 2009).

On the other hand, the less obscured sources (non-DOGs from the SMG and XFLS sample) show two strong distinctions from their more extreme counterparts. First, there are very few power-law non-DOGs. If power-law SEDs are more frequently associated with objects that are more dust reddened, this may imply a connection between the amount of extinction of the optical light and the nature of the power source producing the mid-IR emission.

Second, within the bump population of non-DOGs, there are very few diffuse

type morphologies (low G , high M_{20}). The prevalence of bump sources with “single-object” morphologies is difficult to understand within the context of a major merger scenario in which bump sources evolve into power-law sources. If the bump phase always precedes the power-law phase, there should be very few bump sources with compact, single-source morphologies. A number of potential explanations exist.

Perhaps the most exciting explanation is that high redshift ULIRGs are related to one another within a single evolutionary scheme driven by major mergers, but with an additional wrinkle related to the degree of obscuration. During the highly dust-obscured period of the merger (represented jointly by both bump and power-law DOGs), the bump phase typically occurs before the power-law phase. In contrast, the less obscured sources (SMGs and XFLS ULIRGs) sample the merger over a broader timescale and so the relationship between bump and power-law sources is not as obvious. For example, there may be a significant population of blue ULIRGs (non-DOGs) that occurs near the very end of the high SFR period of the merger when the obscuring column of dust has decreased and UV light can escape the galaxy.

An alternative, but potentially equally exciting, way to reconcile the morphological evidence is by appealing to more quiescent modes of galaxy assembly for some fraction of the high redshift ULIRG population (e.g. Genzel et al., 2008). Recent theoretical work has suggested that many SMGs may be produced not by major mergers, but instead by smooth gas inflow and the accretion of small gas-rich satellites (Davé et al., 2010). Such an explanation would be surprising, given the evidence already in place favoring a major merger origin for SMGs largely based on dynamical and kinematic arguments (e.g. Greve et al., 2005; Swinbank et al., 2006; Tacconi et al., 2008), yet the results presented here provide some indication that this may be happening more commonly in some of the bluer (i.e., less dust-obscured)

high-redshift ULIRGs.

A third possibility is that the expected trends in morphologies with merger stage are somewhat sensitive both to the initial conditions of the merger — for example, highly radial orbits can have similar G and M_{20} values throughout the “final merger” stage (Lotz et al., 2008) — as well as the viewing time and angle. It would be surprising if unusual initial conditions or viewing times and angles were necessary to explain most high redshift ULIRGs, particularly since they appear to have fairly typical axial ratios (see Table 3.3).

An important consideration related to the XFLS ULIRGs and SMGs analyzed here is that many of these objects are composite starburst and AGN systems with complex mid-IR spectral features. Dasyra et al. (2008) show that the $7.7\mu\text{m}$ PAH feature is usually strong in extended sources, while it varies from strong to weak in compact sources. The mid-IR spectral analysis of these sources (Sajina et al., 2007a) indicates that only a few XFLS ULIRGs are clearly dominated by PAH features or AGN continuum emission. This result is consistent with the nature of their mid-IR SEDs and underscores the fact that these objects are composite systems that are not easily classified by either their mid-IR spectral features or their rest-frame optical morphologies. Only 7 SMGs in the sample studied here have both high-resolution imaging and mid-IR spectroscopy (Menéndez-Delmestre et al., 2009). Of these 7, all are bump sources, 4 have strong PAH emission, and 3 have weak or no PAH emission. It may be the case that the mid-IR SEDs of the SMG and XFLS ULIRG samples are not sufficiently distinct to identify significant morphology differences in the bump vs. power-law sub-samples.

3.7 Conclusions

We have used *HST* imaging to analyze the morphologies of 22 DOGs at $z \approx 2$ from the Boötes field selected to show SED features typical of star-formation dominated systems (bump DOGs). We compare these new data with similar *HST* imaging of DOGs with SED features typical of AGN-dominated systems (power-law DOGs) as well as sub-millimeter-selected galaxies (SMGs), ULIRGs at high- z selected from the *Spitzer* XFLS. Our findings are summarized below.

1. Spatially resolved emission is observed in the rest-frame optical imaging of all bump DOGs. GALFIT modeling indicates that the point source fraction (ratio of flux in the point-source component to total flux of the source) in these objects never exceeds 20% and is typically smaller than that found in power-law DOGs, suggesting a smaller AGN contribution to the rest-frame optical light from bump DOGs.
2. Typical Sérsic indices of the resolved emission of bump DOGs suggest disk-type rather than bulge-type profiles ($n < 2$), similar to power-law DOGs.
3. At $H < 22.5$, bump and power-law DOGs have similar sizes (median $r_P = 8$ kpc). At $H > 22.5$, bump DOGs are significantly larger than power-law DOGs (median value of $r_P = 8$ kpc vs. $r_P = 5.4$ kpc, respectively). This distinction is also true for SMGs and XFLS ULIRGs.
4. In the rest-frame optical, bump DOGs have lower G and higher M_{20} values than power-law DOGs. This difference is consistent with expectations from simulations of major mergers. On the other hand, less obscured objects in our sample (SMGs and XFLS ULIRGs that do not qualify as DOGs) have high G and low M_{20} values that are more typical of “single-object” systems.

Overall, our findings highlight the diversity and complexity of high redshift ULIRG morphologies. Within the highly obscured subset (i.e., DOGs), we find evidence in support of a major merger paradigm in which bump DOGs evolve into power-law DOGs. Within the less obscured subset (i.e., SMGs and XFLS ULIRGs), the picture is not as clear. This may be a result of the timescales over which obscured and less obscured sources can be observed during a major merger, or it may be an indication that more quiescent forms of galaxy assembly are important for a significant fraction of high redshift ULIRGs.

The work is based primarily on observations made with the *Hubble Space Telescope*. This work also relies in part on observations made with the *Spitzer Space Telescope*, which is operated by the Jet Propulsion Laboratory, California Institute of Technology under NASA contract 1407. We are grateful to the expert assistance of the staff Kitt Peak National Observatory where the Boötes field observations of the NDWFS were obtained. The authors thank NOAO for supporting the NOAO Deep Wide-Field Survey. In particular, we thank Jenna Claver, Lindsey Davis, Alyson Ford, Emma Hogan, Tod Lauer, Lissa Miller, Erin Ryan, Glenn Tiede and Frank Valdes for their able assistance with the NDWFS data. We also thank the staff of the W. M. Keck Observatory, where some of the galaxy redshifts were obtained.

RSB gratefully acknowledges financial assistance from HST grants GO-10890 and GO-11195, without which this research would not have been possible. Support for Program numbers HST-GO10890 and HST-GO11195 were provided by NASA through a grant from the Space Telescope Science Institute, which is operated by the Association of Universities for Research in Astronomy, Incorporated, under NASA contract NAS5-26555. The research activities of AD and BTJ are supported by NOAO, which is operated by the Association of Universities for Research in Astronomy (AURA) under a cooperative agreement with the National Science Foundation.

Support for E. Le Floch was provided by NASA through the Spitzer Space Telescope Fellowship Program.

CHAPTER 4

DOGS ARE WARM-DUST DOMINATED ULIRGS AT $z \sim 2$

We present SHARC-II $350\mu\text{m}$ imaging of twelve $24\mu\text{m}$ -bright ($F_{24\mu\text{m}} > 0.8 \text{ mJy}$) Dust-Obscured Galaxies (DOGs) and CARMA 1mm imaging of a subset of 2 DOGs. These objects are selected from the Boötes field of the NOAO Deep Wide-Field Survey. Detections of 4 DOGs at $350\mu\text{m}$ imply infrared (IR) luminosities which are consistent to within a factor of 2 of expectations based on a warm dust spectral energy distribution (SED) scaled to the observed $24\mu\text{m}$ flux density. The $350\mu\text{m}$ upper limits for the 8 non-detected DOGs are consistent with both Mrk 231 and M82 (warm dust SEDs), but exclude cold dust (Arp 220) SEDs. The two DOGs targeted at 1mm were not detected in our CARMA observations, placing strong constraints on the dust temperature: $T_{\text{dust}} > 35 - 60 \text{ K}$. Assuming these dust properties apply to the entire sample, we find dust masses of $\approx 3 \times 10^8 M_{\odot}$. In comparison to other dusty $z \sim 2$ galaxy populations such as sub-millimeter galaxies (SMGs) and other *Spitzer*-selected high-redshift sources, this sample of DOGs has higher IR luminosities ($2 \times 10^{13} L_{\odot}$ vs. $6 \times 10^{12} L_{\odot}$ for the other galaxy populations) that are driven by warmer dust temperatures ($>35\text{-}60 \text{ K}$ vs. $\sim 30 \text{ K}$) and lower inferred dust masses ($3 \times 10^8 M_{\odot}$ vs. $3 \times 10^9 M_{\odot}$). Wide-field *Herschel* and SCUBA-2 surveys should be able to detect hundreds of these power-law dominated DOGs. We use existing *Hubble Space Telescope* and *Spitzer*/IRAC data to estimate stellar masses of these sources and find that the stellar to gas mass ratio may be higher in our $24\mu\text{m}$ -bright sample of DOGs than in SMGs and other *Spitzer*-selected sources. Although much larger sample sizes are needed to provide a definitive conclusion, the data are consistent with an evolutionary trend in which the formation of massive galaxies at $z \sim 2$ involves a sub-millimeter bright, cold-dust and star-formation dominated

phase followed by a $24\mu\text{m}$ -bright, warm-dust and AGN-dominated phase.

4.1 Introduction

In the local universe, the most bolometrically luminous galaxies are dominated by thermal emission from dust which absorbs ultra-violet (UV) and optical light and re-radiates it in the infrared (IR) (Soifer et al., 1986). While rare locally, these ultra-luminous IR galaxies (ULIRGs) are more common at high redshift (e.g., Franceschini et al., 2001; Le Floc'h et al., 2005; Pérez-González et al., 2005). Studies combining the improved sensitivity in the IR of the *Spitzer Space Telescope* with wide-field ground-based optical imaging have identified a subset of this $z \sim 2$ ULIRG population that is IR-bright but also optically faint (Yan et al., 2004; Houck et al., 2005; Weedman et al., 2006b; Fiore et al., 2008; Dey et al., 2008). In particular, Dey et al. (2008) and Fiore et al. (2008) present a simple and economical method for selecting these systems based on R -band and $24\mu\text{m}$ Multiband Imaging Photometer for Spitzer (MIPS; Rieke et al., 2004) data. Dey et al. (2008) employ a color cut of $R - [24] > 14$ (Vega magnitudes; $\approx F_\nu(24\mu\text{m})/F_\nu(R) > 1000$) to identify objects they call Dust-Obscured Galaxies (DOGs). Applied to the 8.6 deg^2 Boötes field of the NOAO Deep Wide-Field Survey (NDWFS) that has uniform MIPS $24\mu\text{m}$ coverage for $F_\nu(24\mu\text{m}) > 0.3 \text{ mJy}$, this selection yields a sample of ≈ 2600 DOGs, or $\approx 302 \text{ deg}^{-2}$.

The extreme red colors and number density of the DOGs imply that they are undergoing a very luminous, short-lived phase of activity characterized by vigorous stellar bulge and nuclear black hole growth. Spectroscopic redshifts determined for a sub-sample of DOGs using the Deep Imaging Multi-Object Spectrograph (DEIMOS; Faber et al., 2003) and the Low Resolution Imaging Spectrometer (LRIS; Oke et al., 1995) on the telescopes of the W. M. Keck Observatory (59 DOGs), as well as the

Infrared Spectrometer (IRS; Houck et al., 2004) on *Spitzer* (47 DOGs) have revealed a redshift distribution centered on $z \approx 2$ with a dispersion of $\sigma_z \approx 0.5$ (Dey et al., 2008).

While DOGs are rare, they are sufficiently luminous ($\approx 90\%$ of DOGs with spectroscopic redshifts have $L_{\text{IR}} > 10^{12} L_{\odot}$) that they may contribute up to one-quarter of the total IR luminosity density from all $z \sim 2$ galaxies (and over half that from all ULIRGs at $z \sim 2$) and may be the progenitors of the most luminous ($\sim 4L^*$) present-day galaxies (Dey et al., 2008; Brodwin et al., 2008). Thus far, the efforts to estimate the IR luminosities of DOGs have primarily relied upon spectroscopic redshifts and the observed $24\mu\text{m}$ flux density. Dey et al. (2008) use an empirical relation between the rest-frame $8\mu\text{m}$ luminosity (computed from the observed $24\mu\text{m}$ flux density) and the IR luminosity, derived by Caputi et al. (2007). However, there is evidence from sources with $F_{24\mu\text{m}} > 0.25$ mJy that methods based on only the $24\mu\text{m}$ flux density can overestimate the IR luminosity by factors of 2-10 (Papovich et al., 2007). Results from deep $70\mu\text{m}$ and $160\mu\text{m}$ imaging of a sub-sample of $24\mu\text{m}$ -bright DOGs are consistent with this, favoring hot-dust dominated spectral energy distribution (SED) templates like that of Mrk 231 (Tyler et al., 2009) which lead to estimates of the IR luminosity that are on the low end of the range in L_{IR}/L_8 conversion factors adopted in Dey et al. (2008).

In this paper, we present $350\mu\text{m}$ and 1mm photometry of a sample of DOGs whose mid-IR spectral features (silicate absorption, power-law SEDs) suggest the presence of a strong active galactic nucleus (AGN). The primary goals of this study are to measure their IR luminosities and constrain their dust properties, in particular the dust masses and temperatures. We also estimate stellar masses for the sources in the sample using published *Hubble Space Telescope* (*HST*) data and *Spitzer* InfraRed Array Camera (IRAC) catalogs from the *Spitzer* Deep Wide-Field Survey (SDWFS;

see Ashby et al., 2009). Comparison of the stellar and dust masses potentially allows us to place constraints on the evolutionary status of these sources.

In section 4.2, we present the details of the observations. Section 4.3 presents the DOG SEDs from $0.4\mu\text{m}$ to 1mm and IR luminosity measurements, constraints on the dust temperature, and dust and stellar mass estimates. In section 4.4, we compare our results with similar studies of sub-millimeter galaxies (SMGs) and *Spitzer*-selected sources from the eXtragalactic First Look Survey (XFLS) and Spitzer Wide InfraRed Extragalactic (SWIRE) survey. We present our conclusions in section 4.5.

Throughout this paper we assume a cosmology where $H_0 = 70 \text{ km s}^{-1} \text{ Mpc}^{-1}$, $\Omega_m = 0.3$, and $\Omega_\lambda = 0.7$.

4.2 Observations

4.2.1 Sample Selection

Dey et al. (2008) identified 2603 DOGs in the 8.6 deg^2 NDWFS Boötes field, selecting all $24\mu\text{m}$ sources satisfying $R - [24] > 14$ (Vega mag) and $F_{24\mu\text{m}} > 0.3 \text{ mJy}$. We identified 12 DOGs with spectroscopic redshifts for follow-up $350\mu\text{m}$ imaging (see Figure 4.1) with the second-generation Submillimeter High Angular Resolution Camera (SHARC-II) at the Caltech Sub-millimeter Observatory (CSO). These targets were selected to have bright $24\mu\text{m}$ flux densities ($F_{24\mu\text{m}} \gtrsim 1 \text{ mJy}$) and a power-law dominated mid-IR SED (based on *Spitzer*/IRAC and $24\mu\text{m}$ MIPS photometry; for details, see section 3.1.2 in Dey et al., 2008). Using the deeper IRAC observations from SDWFS (Ashby et al., 2009), the fraction of DOGs qualifying as power-law sources ranges from $\approx 10\%$ at $F_{24\mu\text{m}} = 0.3 \text{ mJy}$ to $\approx 60\%$ at $F_{24\mu\text{m}} = 1 \text{ mJy}$. As shown in Figure 4.1, our sample spans a broad range in $R - [24]$ color ($\approx 14.5 - 17.5$). *Spitzer*/IRS spectroscopic redshifts have been obtained for these sources based on the $9.7\mu\text{m}$ silicate absorption feature. Power-law continua and silicate absorption

are typical features of AGN-dominated systems (Donley et al., 2007; Weedman et al., 2006a; Polletta et al., 2008; Brand et al., 2008). We note that such systems often exhibit intense star-formation concurrent with the growth of a super-massive central black hole (e.g., Wang et al., 2008).

Details of our observations are presented in Table 4.1. The effective integration time (column 8 of table 4.1) represents the time necessary to reach the same noise level given a completely transparent atmosphere (see Coppin et al., 2008, for details).

We observed two of the twelve DOGs at 1mm using the Combined Array for Research in Millimeter-wave Astronomy (CARMA) interferometer to search for thermal emission from cold dust particles. These were primarily selected to have robust $350\mu\text{m}$ detections to enhance the probability of detection at 1mm and, in the event of a non-detection, allow useful constraints to be placed on the dust properties. The two targets observed with CARMA are SST24 J142827.2+354127 (S2) and SST24 J143001.9+334538 (S3). Table 4.2 presents the date and integration time of the CARMA observations.

4.2.2 SHARC-II $350\mu\text{m}$ Imaging and Photometry

The SHARC-II observations of the 12 target DOGs were carried out over the course of five separate observing runs from 2005 January to 2007 May. Data were collected only when the atmospheric opacity was low and conditions were stable ($\tau_{225\text{GHz}} < 0.06$). Pointing, focus checks, and calibration were performed every hour, using ULIRG Arp 220 as a calibrator ($F_{350\mu\text{m}} = 10.2 \pm 1.0 \text{ Jy}$). Other secondary calibrators (CIT6, CRL2688, 3C345) were used occasionally to verify the Arp 220 calibrations. A non-connecting Lissajous pattern was used to modulate the telescope pointing with amplitudes of $15''$ - $20''$ and periods of 10-20 s. The observations made use of the CSO Dish Surface Optimization System to optimize the dish surface accuracy and beam efficiency (Leong et al., 2006).

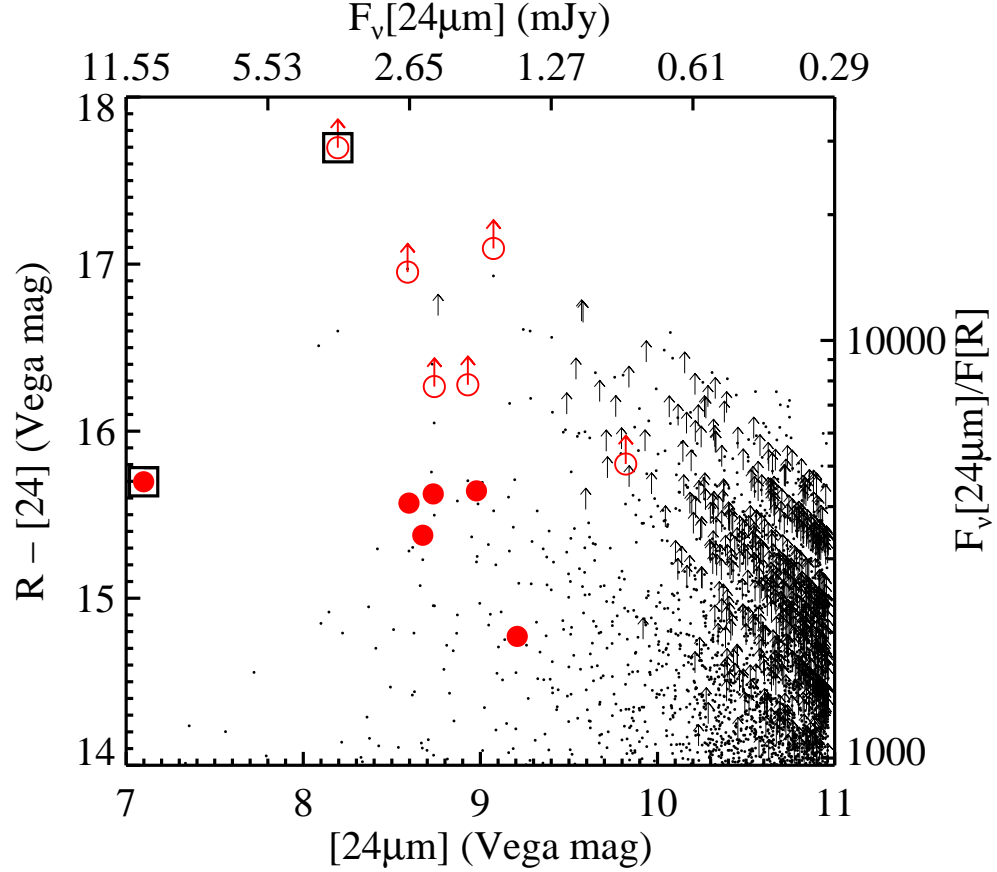


Figure 4.1 $R - [24]$ color vs. $24\mu\text{m}$ magnitude for DOGs in the NDWFS Boötes field. Bottom and top abscissae show the $24\mu\text{m}$ magnitude and flux density, respectively. Left and right ordinates show the color in magnitudes and the $F_{24\mu\text{m}}/F_{0.7\mu\text{m}}$ flux density ratio, respectively. Black dots and upward arrows show the full sample of DOGs, with and without an R -band detection, respectively. The subsample studied in this paper is represented by red circles (open symbols show sources undetected in the R -band data). Two sources observed by CARMA at 1mm are highlighted by a black square. This plot demonstrates that the sample studied in this paper probes the $24\mu\text{m}$ -bright DOGs over a wide range of $R - [24]$ colors.

Table 4.1. SHARC-II 350 μ m Observations

| Source Name | ID | RA (J2000) | DEC (J2000) | z | UT Year-Month | $t_{\text{int}}^{\text{a}}$ (hr) | $t_{\text{eff}}^{\text{b}}$ (min) | σ_{map} (mJy) |
|------------------------|-----|---------------|----------------|--------------------|----------------------------|-------------------------------------|--------------------------------------|--------------------------------|
| SST24 J142648.9+332927 | S1 | 14:26:48.970 | +33:29:27.56 | 2.00 ^c | 2006-Apr | 1.1 | 4.0 | 20 |
| SST24 J142827.2+354127 | S2 | 14:28:27.190 | +35:41:27.71 | 1.293 ^d | 2005-Apr/2006-Apr/2007-May | 3.3 | 11.9 | 10 |
| SST24 J143001.9+334538 | S3 | 14:30:01.910 | +33:45:38.54 | 2.46 ^e | 2005-Apr/2006-Apr/2006-May | 3.6 | 11.4 | 8 |
| SST24 J143025.7+342957 | S4 | 14:30:25.764 | +34:29:57.29 | 2.545 ^f | 2006-Apr | 1.0 | 2.0 | 26 |
| SST24 J143135.2+325456 | S5 | 14:31:35.309 | +32:54:56.84 | 1.48 ^c | 2007-May | 1.2 | 2.0 | 30 |
| SST24 J143325.8+333736 | S6 | 14:33:25.884 | +33:37:36.90 | 1.90 ^c | 2006-Apr | 0.3 | 1.2 | 28 |
| SST24 J143411.0+331733 | S7 | 14:34:10.980 | +33:17:32.70 | 2.656 ^g | 2005-Jan | 3.8 | 12.7 | 8 |
| SST24 J143447.7+330230 | S8 | 14:34:47.762 | +33:02:30.46 | 1.78 ^e | 2007-May | 1.8 | 10.5 | 10 |
| SST24 J143508.4+334739 | S9 | 14:35:08.518 | +33:47:39.44 | 2.10 ^c | 2006-Apr | 1.0 | 0.5 | 35 |
| SST24 J143539.3+334159 | S10 | 14:35:39.364 | +33:41:59.13 | 2.62 ^e | 2005-Apr/2006-Apr | 2.5 | 3.1 | 15 |
| SST24 J143545.1+342831 | S11 | 14:35:45.137 | +34:28:31.42 | 2.50 ^c | 2006-Apr | 0.8 | 3.2 | 22 |
| SST24 J143644.2+350627 | S12 | 14:36:44.269 | +35:06:27.12 | 1.95 ^e | 2006-Apr/2006-May | 2.1 | 6.7 | 10 |

^aActual on-source integration time.

^bEffective integration time for a transparent atmosphere (Coppin et al., 2008).

^cRedshift from *Spitzer*/IRS (Higdon et al. in prep).

^dRedshift from Keck DEIMOS (Desai et al., 2006).

^eRedshift from *Spitzer*/IRS (Houck et al., 2005).

^fRedshift from Keck DEIMOS (Dey et al., in prep.).

^gRedshift from Keck LRIS (Dey et al., 2005).

Table 4.2. CARMA 1mm Observations

| ID | UT Year-Month | t_{int} (hr) ^a |
|----|----------------|------------------------------------|
| S2 | 2008-April/May | 10.3 |
| S3 | 2008-April/May | 7.5 |

^aOn-source integration time.

Data were reduced using the Comprehensive Reduction Utility for SHARC-II (CRUSH) software package with the ‘deep’ option to optimize the signal-to-noise ratio (S/N) for faint (< 100 mJy) point sources (Kovács, 2006). The output map has a pixel scale of $1''.62 \text{ pixel}^{-1}$, and is smoothed with a $9''$ gaussian beam, resulting in an effective image FWHM of $12''.4$.

A $20''$ diameter aperture was used for photometry to compute the instrumental flux density of each source. The sky level and photometric uncertainty were computed by measuring the mean and RMS in ≈ 10 off-source $20''$ diameter apertures. The same procedure was applied to the calibration images, and a scaling factor was derived that converts the instrumental flux density to a physical flux density (using this method, no subsequent aperture correction is required as long as both the science and calibration targets are unresolved and measured in the same aperture).

The aperture photometry is consistent with peak flux density measurements in all but one source, SST24 J142648.9+332927. This source has a radial profile that is significantly more extended than the point spread function of the final map, which results in the peak flux underestimating the aperture flux density measurement. The extended structure in the image is more likely to be noise than signal, so in this case we report the peak flux measurement, which is formally a non-detection.

Flux boosting of low S/N sources can be an important effect in wide-field surveys where source positions are not known a priori (e.g., Coppin et al., 2005). However, because we know our source positions at the $< 1''$ level (from MIPS and IRAC centroids), flux boosting is not a significant effect, and so we do not apply any such corrections to our measurements. Our approach follows that adopted by Laurent et al. (2006) and Kovács et al. (2006) in their $350\mu\text{m}$ follow-up imaging of SMGs.

4.2.3 CARMA 1mm Imaging and Photometry

The CARMA observations were obtained between 2008 April 7 and May 1 in the C-array configuration (beamsize is $\approx 2 \times 1$ sq. arcsec). A total of 7.5 hours and 10.3 hours of integration time in good 1mm weather conditions were spent on sources SST24 J143001.9+334538 (S3) and SST24 J142827.2+354127 (S2), respectively. These sources were selected primarily because of their robust ($S/N > 4.5$) detections at $350\mu\text{m}$. In addition, source S3 is detected with *Spitzer*/MIPS at $70\mu\text{m}$ and $160\mu\text{m}$ (Tyler et al., 2009), while S2 is the subject of a detailed spectroscopic study (Desai et al., 2006).

System temperatures were in the range 250-400 K. A correlator configuration was used with three adjacent 15×31 MHz bands centered on 220 GHz, the frequency at which the CARMA 1mm receivers are most sensitive. The quasar J1310+323 (chosen for its spatial proximity) was observed every 15 minutes for amplitude and phase calibration. Quasars 3C 273 and MWC 349 were used for pointing, pass-band calibration, and flux calibration.

Data were reduced using the Multichannel Image Reconstruction, Image Analysis, and Display (MIRIAD) software package (Sault et al., 1995). Visual inspection of visibilities as a function of baseline length allowed us to identify and flag spurious data. A cleaned map was generated for each track of integration time (ranging from 1 to 5 hours in length) and these tracks were coadded together using a weighted mean to obtain a final image of these sources. No detections were found in either case. Both sources are unresolved in the IRAC images, and NICMOS/F160W imaging of S3 indicates a size of $\leq 0''.5$, implying that it is very unlikely any emission was resolved out by the interferometer. The IMSTAT routine from MIRIAD was used to determine the noise level in the co-added images where we expected to see the source. Table 4.3 shows the photometry from $24\mu\text{m}$ to 1mm, where available.

Non-detections are given as $3\text{-}\sigma$ upper limits.

4.2.4 Optical, near-IR, mid-IR, and far-IR Photometry

The optical and near-IR photometry used in this paper to estimate stellar masses are based on high spatial-resolution *HST* data (WFPC2/F606W, ACS/F814W, and NIC2/F160W) published in Bussmann et al. (2009b). The *HST* data allow the separation of an unresolved nuclear component (flux on scales ≤ 1 kpc) from a more spatially extended component. Because the AGN contribution in the rest-frame UV to optical is uncertain, the photometry of the extended component is used here (measured with $2''$ diameter apertures) to ensure that our stellar mass estimates are not biased by the presence of an obscured AGN (for details on how the extended component is computed, see Bussmann et al., 2009b). Additionally, $4''$ diameter aperture photometry in the optical (B_W , R , and I) from the NDWFS is shown in the SEDs of the objects in this sample (details on how the photometry is computed may be found in Bussmann et al., 2009b).

The mid-IR photometry used in this paper are from the publicly available Data Release 1.1 (DR1.1) catalogs from the SDWFS IRAC coverage of the Boötes field (Ashby et al. 2009). The SDWFS catalogs incorporate the earlier IRAC Shallow Survey of the Boötes field undertaken by the IRAC guaranteed time observation (GTO) programs (Eisenhardt et al., 2004). We identified IRAC counterparts of the DOGs in this paper from the SDWFS catalogs using a $3''$ search radius centered on the $24\mu\text{m}$ position (the MIPS $24\mu\text{m}$ $1\text{-}\sigma$ positional uncertainty is $1''.2$). All of the DOGs in this paper have IRAC counterparts, detected at $> 4\sigma$ in all four IRAC channels. We use the $4''$ (rather than the $6''$) diameter aperture photometry from the DR1.1 SDWFS catalog to reduce contamination from nearby sources. We note that aperture corrections derived from isolated, bright stars have been applied to the SDWFS catalogs.

Table 4.3. Photometry^a

| Source Name | $R - [24]$ (Vega mag) | $F_{24\mu\text{m}}$ (mJy) | $F_{70\mu\text{m}}$ (mJy) | $F_{160\mu\text{m}}$ (mJy) | $F_{350\mu\text{m}}$ (mJy) | $F_{1.2\text{mm}}$ (mJy) | $F_{20\text{cm}}$ ^b (mJy) |
|-------------|--------------------------|------------------------------|------------------------------|-------------------------------|-------------------------------|-----------------------------|---|
| S1 | >16.1 | 2.33 ± 0.07 | — | — | < 66 | — | — |
| S2 | 15.7 | 10.55 ± 0.13 | — | <45 ^c | 74 ± 13 | <1.5 | — |
| S3 | >17.4 | 3.84 ± 0.06 | $9.3 \pm 2.3^{\text{d}}$ | $65 \pm 11^{\text{d}}$ | 41 ± 13 | <1.8 | 0.42 ± 0.04 |
| S4 | 15.1 | 2.47 ± 0.05 | — | — | <81 | — | 0.23 ± 0.03 |
| S5 | 14.5 | 1.51 ± 0.05 | — | — | <100 | — | 0.54 ± 0.12 |
| S6 | 15.4 | 1.87 ± 0.06 | — | — | <137 | — | 0.20 ± 0.03 |
| S7 | 12.4 ^e | 0.86 ± 0.05 | <25 ^f | <90 ^f | 37 ± 13 | — | — |
| S8 | >16.8 | 1.71 ± 0.04 | — | — | 45 ± 12 | — | 0.31 ± 0.06 |
| S9 | 15.3 | 2.65 ± 0.08 | — | — | <150 | — | 0.24 ± 0.04 |
| S10 | >16.7 | 2.67 ± 0.06 | <8.1 ^d | <38 ^d | <50 | — | — |
| S11 | >16.0 | 1.95 ± 0.05 | — | — | <60 | — | — |
| S12 | 15.4 | 2.34 ± 0.05 | 9.1 ± 2.5 | 43 ± 12 | <34 | — | 5.1 ± 0.2 |

^aUpper limits quoted are 3σ values.

^bPhotometry from Westerbork Synthesis Radio Telescope imaging de Vries et al. (2002).

^cPhotometry from Desai et al. (2006).

^dPhotometry from Tyler et al. (2009).

^e R -band photometry includes diffuse emission from Ly- α nebula (Dey et al., 2005).

^fPhotometry from Dey et al. (2005).

Finally, 24, 70, and $160\mu\text{m}$ data over 8.61 deg^2 of the Boötes field are available from GTO programs. The data were reduced by the MIPS GTO team and reach 1σ rms depths of $51\text{ }\mu\text{Jy}$, 5 mJy , and 18 mJy at 24, 70, and $160\mu\text{m}$, respectively. Details of the GTO surveys, such as mapping strategy, data reduction, and source catalogs, will be discussed elsewhere. In addition, several of the DOGs in this paper were targeted for deeper MIPS photometric observations by *Spitzer* General Observer program 20303 (P.I. E. LeFloc'h), and the results are reported in Tyler et al. (2009). We use the Tyler et al. (2009) measurements where they are available.

4.3 Results

In this section, we present SEDs from $0.4\mu\text{m}$ to 1mm for each source in our sample and compare with local starburst (M82) and ULIRG (Arp 220 and Mrk 231) templates. Our approach is to artificially redshift the local galaxy templates and normalize them to match the DOG photometry at observed-frame $24\mu\text{m}$. This allows a simple, qualitative comparison of DOGs and galaxies with properties ranging from warm dust, star-formation dominated (M82), to cool dust, star-formation dominated (Arp 220), to warm dust, AGN-dominated (Mrk 231). We will use the SED that provides the best fit over the sampled wavelength range (observed optical through sub-mm) to estimate the IR luminosities of the DOGs.

Later in this section, we use our limits at 1mm from CARMA to place constraints on the dust temperatures and limits on the dust masses of DOGs. Finally, we use *HST* and *Spitzer*/IRAC data to estimate stellar masses of DOGs.

4.3.1 Qualitative SED Comparison

Figures 4.2 and 4.3 show the SEDs of the sources, divided respectively into those with and those without detections at $350\mu\text{m}$. Note that the rest-frame UV photometry for source S7 is contaminated by emission from nearby sources and will be treated

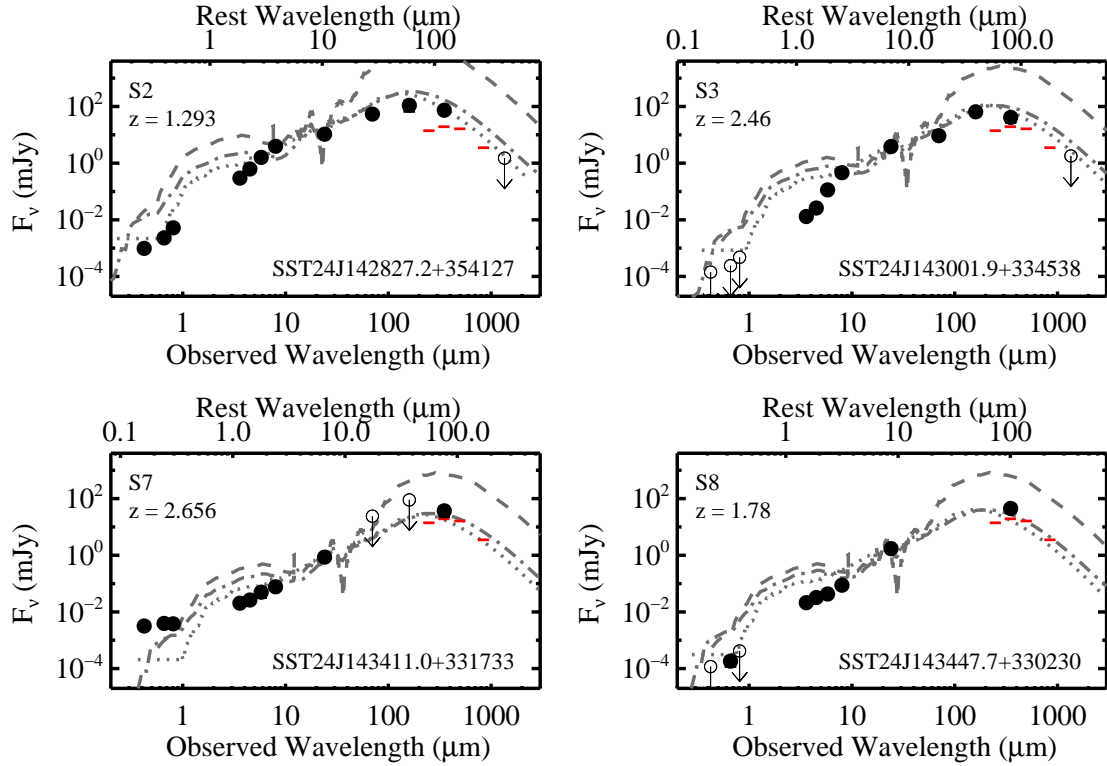


Figure 4.2 SEDs of 5 DOGs detected by SHARC-II at $350\mu\text{m}$. Dotted, dashed, and dot-dashed lines show the Mrk 231, Arp 220, and M82 template SEDs, respectively, placed at the appropriate redshift and scaled to match the observed $24\mu\text{m}$ flux density. Red horizontal lines show the $5\text{-}\sigma$ sensitivity limits (ignoring confusion) from the planned wide-field *Herschel* surveys at 250, 350, and $500\mu\text{m}$, and SCUBA-2 surveys at $850\mu\text{m}$. The cool dust SED of Arp 220 significantly overpredicts the $350\mu\text{m}$ flux density in all cases. The warm dust SED of M82 provides a better fit in the far-IR, but Mrk 231 provides the best fit in both the far-IR and the optical.

in more detail in a future paper (Prescott et al., in prep.).

Overplotted in each panel are M82 (Silva et al., 1998)¹, Mrk 231 (Chary 2008, private communication), and Arp 220 (Rieke et al., 2008) templates, placed at the

¹We use a slightly updated SED obtained from <http://adlibitum.oat.ts.astro.it/silva/grasil/modlib/modlib.html>

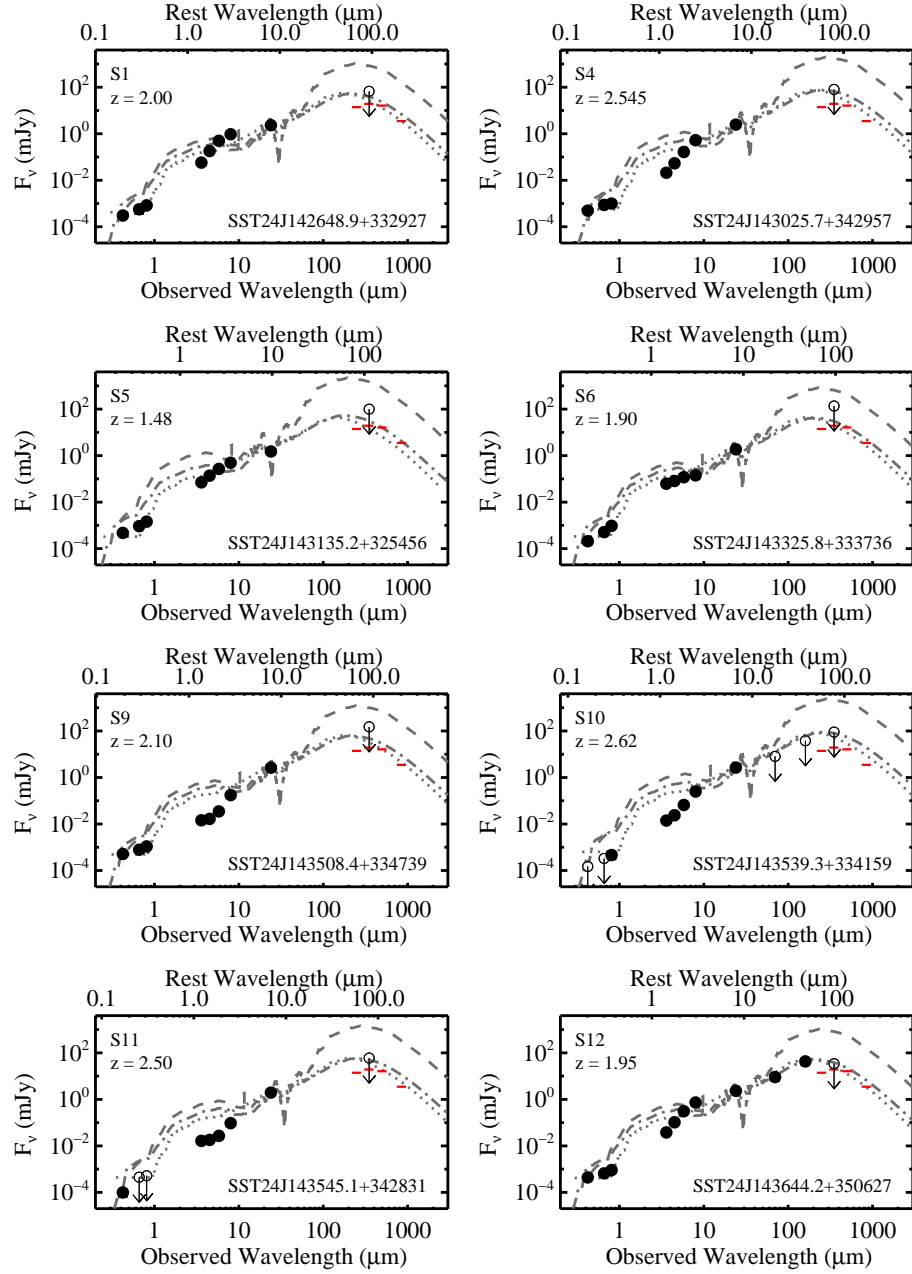


Figure 4.3 Same as Figure 4.2, except showing SEDs of 7 DOGs not detected by SHARC-II at $350\mu\text{m}$. The limits at $350\mu\text{m}$ are all inconsistent with the Arp 220 SED. The $250\mu\text{m}$ channel of *Herschel* should be very efficient for detecting power-law DOGs in wide-field surveys, assuming that Mrk 231 is an appropriate representation of the far-IR SED.

appropriate redshift and scaled to match the flux density observed in the MIPS $24\mu\text{m}$ band. The scaling factors derived for the three templates range over 200-900, and 2-10, 70-700, respectively (the deep silicate absorption feature in Arp 220 and the strong PAH emission feature of M82 make the scaling factors closer to each other than a simple estimate based on the ratio of the IR luminosities would imply). For the Arp 220 and Mrk 231 templates, we have interpolated the spectrum in the UV to match Galaxy Evolution Explorer photometry (in the case of Arp 220) and International Ultraviolet Explorer data as well as *HST* Faint Object Spectrograph data (in the case of Mrk 231; Hutchings & Neff, 1987; Gallagher et al., 2002).

These templates were chosen because they sample a range of dust temperatures and AGN/starburst contributions. M82 is one of the closest ($d_L = 3.86$ Mpc) galaxies undergoing a starburst, as it was triggered by a recent interaction with M81. Although it is less luminous than DOGs ($L_{\text{IR}} \approx 6 \times 10^{10} L_{\odot}$; ² Sanders et al., 2003), its nucleus is dominated by a warm dust component ($T_{\text{dust}} = 48$ K; Hughes et al., 1994). Arp 220 is a nearby ($d_L = 77.3$ Mpc) ULIRG ($L_{\text{IR}} \approx 1.6 \times 10^{12} L_{\odot}$; Sanders et al., 2003) dominated by cold dust ($T_{\text{dust}} = 35$ K; Rigopoulou et al., 1996). Mrk 231 is another nearby ($d_L = 175.1$ Mpc) ULIRG ($L_{\text{IR}} \approx 3.2 \times 10^{12} L_{\odot}$; Sanders et al., 2003), but has a warm dust ($T_{\text{dust}} = 51$ K; Yang & Phillips, 2007) SED dominated by an obscured AGN.

Qualitatively, the Mrk 231 template provides a much better fit than the Arp 220 template to the $350\mu\text{m}$ photometry in every case. M82 fits the $24\mu\text{m}$ and $350\mu\text{m}$ photometry reasonably well (although not as well as Mrk 231), but it fares poorly in the mid-IR and optical, where a strong stellar component in M82 is not seen in the DOGs in this sample (which are dominated by a power-law in the mid-IR). Additionally, M82 shows strong PAH emission which is not seen in the power-law

² L_{IR} is the luminosity integrated over 8-1000 μm

DOGs.

The red horizontal bars in Figures 4.2 and 4.3 show $5\text{-}\sigma$ limits (ignoring confusion) from planned wide-field ($> 8 \text{ deg}^2$) surveys with the *Herschel* Space Observatory (shown for the channels at 250, 350, and $500\mu\text{m}$) and with the Sub-mm Common-User Bolometer Array-2 (SCUBA-2) instrument at $850 \mu\text{m}$. Most of the power-law DOGs studied in this paper have SEDs that peak around observed-frame $250\mu\text{m}$, which is where the *Herschel* wide-field maps will be the deepest ($5\text{-}\sigma$ limit of 14 mJy). If all of the $24\mu\text{m}$ -bright DOGs are detected at $250\mu\text{m}$ in the two wide-field surveys that are planned to reach the depths assumed here (Lockman Hole east, 11 deg^2 ; Extended Chandra Deep Field South, 8 deg^2), then a total of ≈ 600 power-law DOGs should be detected in the $250\mu\text{m}$ *Herschel* catalogs of these two fields. The SCUBA-2 surveys of these fields should be deep enough ($5\text{-}\sigma$ limit of 3.5 mJy at $850\mu\text{m}$) to detect many of these sources, allowing dust temperature constraints to be placed on a statistically significant sample of these rare, important objects.

Figure 4.4 shows all of the DOG SEDs on the same plot, normalized by the rest-frame $8\mu\text{m}$ flux density (which is estimated from the observed-frame $24\mu\text{m}$ flux density by assuming a power law of the form $F_\nu \propto \nu^\alpha$, where $\alpha = -2$). The SEDs M82, Arp 220, Mrk 231, and a composite SMG template SED spanning mid-IR to sub-mm wavelengths are also shown. The composite SMG template is derived from bright ($F_{850\mu\text{m}} > 5 \text{ mJy}$) SMGs from the Great Observatories Origins Deep Survey North (GOODS-N) field with mid-IR spectra (Pope et al., 2008b).

One striking feature of this plot is the steep slope shown by DOGs in the rest-frame $1\text{--}4\mu\text{m}$. Whereas Mrk 231, M82, and Arp 220 all exhibit a bump in the $1\text{--}2\mu\text{m}$ regime, no such feature is apparent in the DOG SEDs. This could be due to the presence of an obscured AGN outshining the stellar light, in the rest-frame near-IR. This is in contrast to rest-frame UV and optical wavelengths, where *HST* imaging

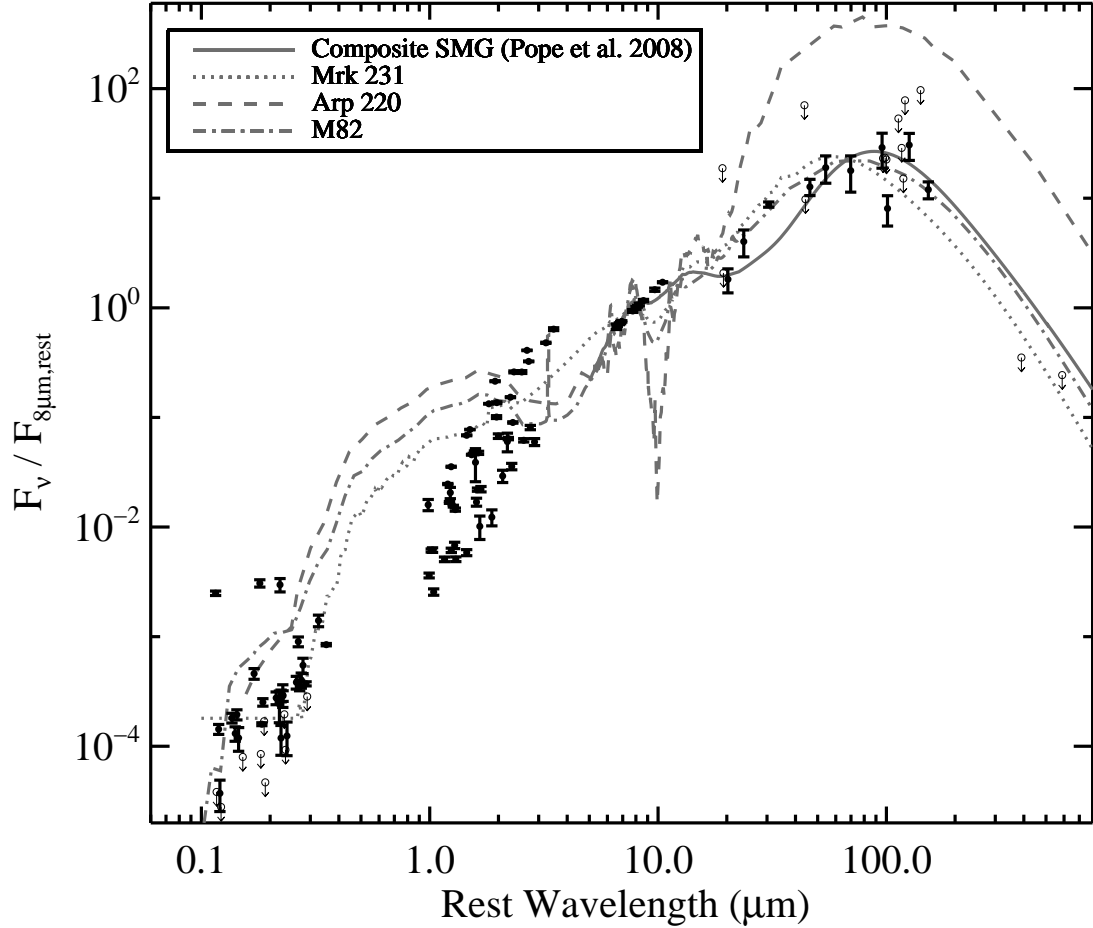


Figure 4.4 Optical through sub-mm SEDs of DOGs in the SHARC-II sample. Flux densities have been normalized by the rest-frame $8\mu\text{m}$ flux density, computed from the observed $24\mu\text{m}$ flux density. Of the three local galaxy templates shown, Mrk 231 provides the best fit over the rest-frame UV through sub-mm range because it has a warm dust SED (unlike Arp 220) and because it lacks a strong stellar component (unlike both Arp 220 and M82). None of the template SEDs match the steepness of the rest-frame near-IR photometry of the power-law DOGs. This may indicate that obscured AGN dominate stellar emission to a greater extent in power-law DOGs than in Mrk 231.

has revealed that stellar light appears to dominate (Bussmann et al., 2009b). As noted previously, DOGs have far-IR to mid-IR flux density ratios more similar to Mrk 231 than Arp 220. The composite SMG template overpredicts the far-IR flux for a given mid-IR flux in all cases where we have $350\mu\text{m}$ detections. We note that adding an additional warm dust component ($T_{\text{dust}} = 350$ K; possibly powered by an AGN) to the composite SMG SED (as was done in Pope et al., 2008a) improves the quality of the fit over the rest-frame 8-100 μm . However, this composite SMG + AGN template retains a strong cool dust ($T_{\text{dust}} \approx 30$ K) component that overpredicts the amount of emission at 1mm. If this type of SED was appropriate for the power-law DOGs investigated in this paper, they would have been easily detected by CARMA.

An alternative way of displaying this information is shown in Figure 4.5. In each panel, the flux density ratio far-IR:mid-IR is plotted as a function of the flux density ratio mid-IR:optical ($F_{24\mu\text{m}}/F_{0.7\mu\text{m}}$). The top two panels show $F_{350\mu\text{m}}/F_{24\mu\text{m}}$ on the y-axis, while the bottom two panels show $F_{1200\mu\text{m}}/F_{24\mu\text{m}}$ on the y-axis. SMGs and various *Spitzer*-selected sources are shown in the plots, divided into those that are detected in the (sub-)mm on the left and those that are not detected on the right. The SMG, XFLS, and SWIRE *R*-band data come from Dye et al. (2008), Yan et al. (2007), and Lonsdale et al. (2009), respectively. For SMGs without detections at $1200\mu\text{m}$, $F_{1200\mu\text{m}}$ is estimated using the $850\mu\text{m}$ flux density and the dust temperature from Coppin et al. (2008), and is represented by a red cross symbol. Dotted, dashed, and dot-dashed lines indicate the evolution of Mrk 231, Arp 220, and M82, respectively, on this diagram over redshifts of 1 – 3. Compared to SMGs, DOGs in this sample have redder flux density ratios in the mid-IR:optical but bluer far-IR:mid-IR ratios. This cannot be explained by an enhancement of the $24\mu\text{m}$ flux due to PAH emission, since mid-IR spectra of these DOGs show power-law continua

with silicate absorption and weak or absent PAH emission features (Houck et al., 2005). Instead, the most likely explanation is that obscured AGN emission boosts the mid-IR continuum (e.g., Rieke & Lebofsky, 1981) relative to both the optical and far-IR.

4.3.2 IR Luminosities

In this section, we provide the best available estimates of the total IR luminosities (L_{IR} ; 8-1000 μm rest-frame) of the sample in this paper based on the 350 μm imaging. We then compare these with estimates based solely on the 24 μm flux density, and also with estimates of the far-IR luminosity (L_{FIR} ; 40-500 μm , rest-frame) based on a modified black-body which has been scaled to match the sub-mm photometry.

The qualitative SED comparison from section 4.3.1 suggests that Mrk 231 provides a reasonable fit to the far-IR photometry. In addition, analysis of 70 μm and 160 μm photometry of a sample of these types of AGN-dominated DOGs has suggested that Mrk 231 provides a reasonable approximation of the full SED (Tyler et al., 2009, see table 4.3 for overlap between that study and this one). Therefore, as the best measure of L_{IR} , we integrate (over 8-1000 μm rest-frame) a redshifted Mrk 231 template which has been scaled to match the observed 350 μm flux density (or 3- σ limit, in the case of a non-detection). These values are tabulated in the first column of Table 4.4. For sources with detections at 350 μm , L_{IR} is in the range of $(2.0 - 2.6) \times 10^{13} L_{\odot}$, with a median value of $2.2 \times 10^{13} L_{\odot}$.

The second column of Table 4.4 shows the rest-frame 8 μm luminosity, $\nu L_{\nu}(8\mu\text{m})$, while the third column shows the total IR luminosity (8-1000 μm , rest-frame) based on the spectroscopic redshift and an empirically determined relationship between $\nu L_{\nu}(8\mu\text{m})$ and L_{IR} : $L_{\text{IR}} = 1.91 L_8^{1.06}$ (Caputi et al., 2007). This approach was used by Dey et al. (2008) in determining the contribution of DOGs to the total IR luminosity density of all $z \sim 2$ galaxies. L_{IR} values range over $(0.5-8.1) \times 10^{13} L_{\odot}$, with a

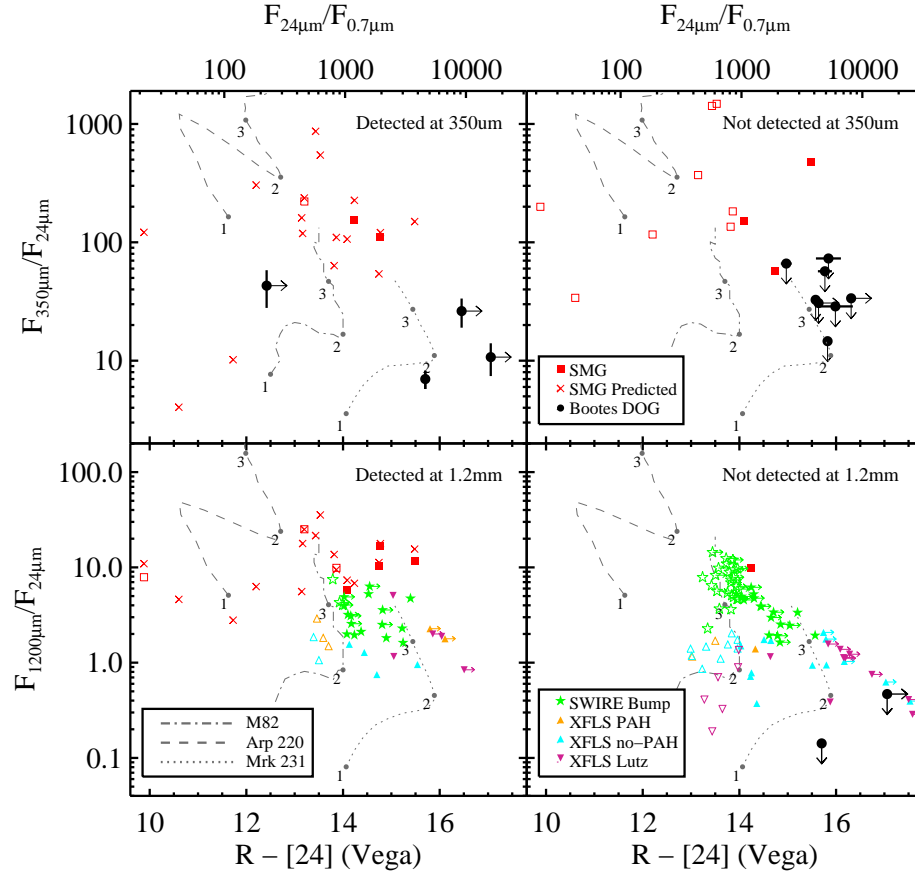


Figure 4.5 Top and bottom panels show $350\mu\text{m}/24\mu\text{m}$ and $1200\mu\text{m}/24\mu\text{m}$ flux density ratios, respectively, as a function of $R-[24]$ (Vega mag) color. For clarity, sources are separated into those detected at $350\mu\text{m}$ or $1200\mu\text{m}$ on the left and those that are not detected on the right. Objects that qualify as a DOG ($R-[24] > 14$) are shown with a filled symbol. Black circles indicate DOGs in Boötes. Red squares show measurements of SMGs (Coppin et al., 2008), while red crosses show predicted values based on $850\mu\text{m}$ photometry (see text for details). Green stars show *Spitzer*-selected bump sources from SWIRE (Lonsdale et al., 2009). Orange triangles (teal triangles) show similarly identified sources from the XFLS dominated by PAH emission (silicate absorption) features (Sajina et al., 2008). Magenta inverted triangles show XFLS sources from Sajina et al. (2008). Finally, dotted, dashed, and dot-dashed lines show the evolution of Mrk 231, Arp 220, and M82 in this parameter space over redshift 1 to 3. The DOGs studied in this paper have some of the reddest $R-[24]$ colors and lowest far-IR/mid-IR flux density ratios of other $z \sim 2$ ULIRGs like SMGs or other *Spitzer*-selected sources.

Table 4.4. Luminosities

| Source Name | L_{IR}^{a} ($10^{12} L_{\odot}$) | $\nu L_{\nu}(8\mu\text{m})$ ($10^{12} L_{\odot}$) | L_{IR}^{b} ($10^{12} L_{\odot}$) | $L_{\text{FIR}}^{\text{d}}$ ($10^{12} L_{\odot}$) |
|-------------|---|--|---|--|
| S1 | $< 32^{\text{e}}$ | 2.2 | 23 | — |
| S2 | $26 \pm 5^{\text{d}}$ | 2.4 | 25 | 9.1 |
| S3 | $22 \pm 7^{\text{d}}$ | 7.2 | 81 | 10 |
| S4 | $< 44^{\text{e}}$ | 5.2 | 57 | — |
| S5 | $< 40^{\text{e}}$ | 53 | 5.1 | — |
| S6 | $< 64^{\text{e}}$ | 1.5 | 15 | — |
| S7 | $21 \pm 7^{\text{d}}$ | 2.1 | 22 | — |
| S8 | $20 \pm 5^{\text{d}}$ | 1.1 | 11 | — |
| S9 | $< 75^{\text{e}}$ | 2.9 | 31 | — |
| S10 | $< 28^{\text{e}}$ | 6.2 | 69 | — |
| S11 | $< 33^{\text{e}}$ | 3.9 | 42 | — |
| S12 | $< 16^{\text{e}}$ | 2.0 | 21 | — |

^aIntegral over 8-1000 μm of redshifted Mrk 231 template normalized at 350 μm .

^bEstimated from $\nu L_{\nu}(8\mu\text{m}) - L_{\text{IR}}$ relation from Caputi et al. (2007).

^cIntegral over 40-500 μm of best-fit modified black-body (only sources with CARMA 1mm data).

^dUncertainties shown reflect 350 μm photometric uncertainties. Additional systematic uncertainties associated with the adoption of a Mrk 231 template are not included.

^e3 σ upper limits.

median value of $2.3 \times 10^{13} L_{\odot}$. The Caputi et al. derived value for L_{IR} is consistent with the $350\mu\text{m}$ -based estimate (or $3\text{-}\sigma$ limit, in the case of non-detections) in 6/12 of the power-law DOGs studied here. In the remaining half of the sample, the Caputi et al. relation overestimates L_{IR} in 5/6 targets. In only one DOG (S8) is the $350\mu\text{m}$ emission brighter than would be expected based on the $24\mu\text{m}$ flux density, redshift, and the Caputi et al. relation. This implies that measurements of the IR luminosity density of DOGs relying solely on the $24\mu\text{m}$ flux density will tend to overestimate their true contribution, consistent with what has been found in a recent study of faint ($F_{24\mu\text{m}} \sim 100 - 500 \mu\text{Jy}$) DOGs in GOODS-N (Pope et al., 2008a). Quantifying the extent of this effect will require much larger samples of DOGs with sub-mm measurements, the kind that will result from wide field surveys with *Herschel* and SCUBA-2.

Finally, the last column of Table 4.4 shows FIR luminosities computed from the integral over $40\text{--}500\mu\text{m}$ (rest-frame) of the best-fit modified black-body (described in more detail in section 4.3.3). These values are tabulated only for those sources with CARMA 1mm imaging. We find L_{FIR} values of $\approx 10^{13} L_{\odot}$, implying $L_{\text{IR}}/L_{\text{FIR}} \approx 3$. In contrast, Mrk 231 has $L_{\text{IR}}/L_{\text{FIR}} \approx 2$, underscoring the fact that the IR luminosity of these DOGs is dominated by mid-IR emission rather than FIR emission.

4.3.3 Constraints on Dust Properties

Additional constraints can be placed on the nature of the cold dust emission from the two sources (S2 and S3) with CARMA. The 1mm non-detections imply warm dust temperatures. If we compute the predicted flux density at 1mm based on the observed $24\mu\text{m}$ flux density and assuming the three local galaxy SED templates (M82, Arp 220, and Mrk 231) used in the previous sections, we find values of 4.4, 740, 1.8 mJy, and 5.8, 120, 2.7 mJy for the two sources respectively. For S2, this implies that our $3\text{-}\sigma$ limit ($< 1.5\text{mJy}$) is close to the level we would expect if Mrk 231

is an appropriate SED, while the other two SEDs are clearly inconsistent with the data. For S3, the limit (< 1.8 mJy) is inconsistent with each of the SEDs, implying a warmer dust temperature than even Mrk 231.

A more quantitative approach is to minimize the residuals between the $160\mu\text{m}$, $350\mu\text{m}$, and 1mm data and that expected from a modified black body. Doing this, we can constrain the dust temperature, T_{dust} , and the dust emissivity index, β , of each target. The best-fit quantities and their uncertainties are estimated using a bootstrap technique that mimics the procedure used by Dunne et al. (2000). Briefly, for each flux density measurement, a set of 100 artificial flux densities are generated using a Gaussian random number generator. The mean value and dispersion of the distribution of artificial flux densities are set by the measurement value and its 1σ uncertainty, respectively (for non-detections, we assume a mean value of 0 and force artificial flux densities to be positive). Each artificial SED is used to construct a distribution of best-fit scaling factors and associated χ^2_ν values for a modified black-body with a given combination of β and T_{dust} .

Figure 4.6 shows the median χ^2_ν contours for the grid of T_{dust} and β values we have sampled in the model fitting for each source observed by CARMA. The contours show the degeneracy between β and T_{dust} , and illustrate why a perfect fit is not possible in spite of the fact that a model with three parameters is being fit to three data points (i.e., the input parameters are not fully independent). The distribution of T_{dust} found for SMGs based on $350\mu\text{m}$ imaging from Coppin et al. (2008) and Kovács et al. (2006) is displayed in the lower panel. Two-sided Kolmogorov-Smirnov tests suggest that the distribution of T_{dust} (assuming $\beta = 1.5$) for each CARMA target is highly unlikely to be drawn from the same parent distribution as the combined sample of SMGs (4% and 0.008%, for the two CARMA targets respectively). In both of the CARMA targets, warmer dust temperatures are required

due to the non-detection at 1mm. The data cannot rule out models with higher values of β , but models of dust grains as well as Galactic and extra-galactic observations consistently suggest $\beta = 1 - 2$ (Hildebrand, 1983; Dunne & Eales, 2001). For $\beta = 1.5$, we reject $T_{\text{dust}} \leq 33\text{K}$ and 45K at the 95% confidence level, in S2 and S3 respectively. For $\beta = 2$, we can reject $T_{\text{dust}} \leq 25\text{ K}$ and 37 K .

4.3.4 Dust Masses

Assuming optically thin sub-mm emission, cold dust masses can be estimated from the $350\mu\text{m}$ photometry (Hughes et al., 1997):

$$M_{\text{dust}} = \frac{1}{1+z} \frac{S_{\text{obs}} D_L^2}{\kappa_d^{\text{rest}} B(\nu^{\text{rest}}, T_{\text{dust}})} \quad (4.1)$$

where S_{obs} is the observed $350\mu\text{m}$ flux density, and κ_d^{rest} and $B(\nu^{\text{rest}}, T_{\text{dust}})$ are, respectively, the values of the mass absorption coefficient and black-body function at the rest frequency ν^{rest} and dust temperature T_{dust} . The appropriate value for κ_d is uncertain to at least a factor of two (Dunne et al., 2003); we use a κ_d^{rest} value interpolated from Draine (2003) ($\langle \kappa_d^{\text{rest}} \rangle \approx 20\text{ cm}^2\text{ g}^{-1}$).

The results from section 4.3.3 suggest that $T_{\text{dust}} > 35 - 60\text{ K}$ for two of the sources. Adopting the average of these limits ($T_{\text{dust}} = 45\text{ K}$) for all of the sources in this sample, then dust mass limits are in the range $(4.1 - 7.9) \times 10^8 M_{\odot}$ (median value of $5.1 \times 10^8 M_{\odot}$) for the five objects with detections at $350\mu\text{m}$. The 3σ upper limits on the dust masses of the remaining sample range from $(3 - 15) \times 10^8 M_{\odot}$. Warmer values of T_{dust} would lead to smaller inferred dust masses (e.g., increasing the dust temperature by 10 K implies $\approx 50\%$ lower dust masses). The dust masses are presented in Table 4.5.

These values agree with those of Bussmann et al. (2009b), where dust masses of a sample of 31 power-law dominated DOGs were estimated using predicted $850\mu\text{m}$ flux densities based on Mrk 231 templates and the measured $24\mu\text{m}$ flux density.

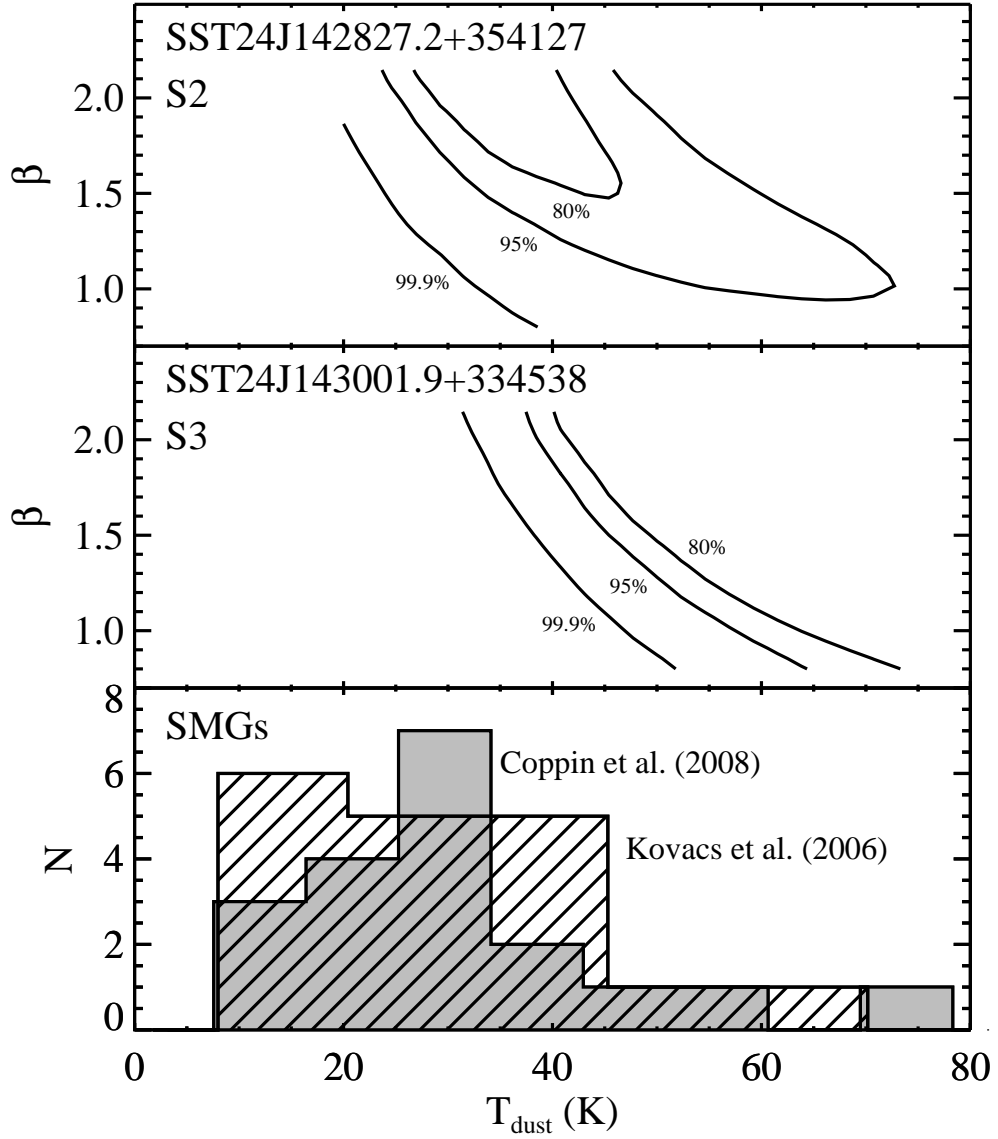


Figure 4.6 χ^2_ν contours based on modified black-body fits to sources with CARMA data. Lines indicate 80%, 95%, and 99.9% confidence intervals. Also shown are T_{dust} distributions for SMGs with $350\mu\text{m}$ data (Kovács et al., 2006; Coppin et al., 2008). The 95% confidence levels for S2 and S3 suggest dust temperature limits that would place them in the warmest 50% and 15%, respectively, of SMGs.

Table 4.5. Dust Masses and Stellar Properties

| Source Name | $M_{\text{dust}}^{\text{a}}$ | $M_{\text{star}}^{\text{b}}$ | $M_{\text{star}}/M_{\text{gas}}$ |
|-------------|------------------------------|------------------------------|----------------------------------|
| | ($10^8 M_{\odot}$) | ($10^{10} M_{\odot}$) | |
| S1 | < 6.3 | (0.3 – 1.5) | 0.05 – 0.24 |
| S2 | 7.9 ± 1.4 | — | — |
| S3 | 4.9 ± 1.5 | < 10 | < 1.7 |
| S4 | < 5.5 | (1 – 3) | $> 0.15 - 0.45$ |
| S5 | < 6.2 | (1.5 – 3) | $> 0.20 - 0.40$ |
| S6 | < 7.5 | (10 – 20) | $> 1.1 - 2.2$ |
| S7 | 2.7 ± 0.7 | — | — |
| S8 | 2.5 ± 0.9 | > 1 | > 0.33 |
| S9 | < 8.5 | (0.6 – 1.1) | $> 0.06 - 0.11$ |
| S10 | < 6.5 | (0.5 – 3) | $> 0.06 - 0.38$ |
| S11 | < 4.0 | (> 10) | > 2.1 |
| S12 | < 1.9 | (1 – 2) | $> 0.44 - 0.88$ |

^aDust mass assuming $T_{\text{dust}} = 45$ K.

^bStellar mass estimated from fitting photometry in the rest-frame UV and optical (V/I and H respectively). Range given reflects 95% confidence intervals based only on photometric uncertainty.

In previous work, we assumed a T_{dust} of 75 K and found a median dust mass of $1.6 \times 10^8 M_{\odot}$. This is consistent with the notion that Mrk 231 accurately characterizes the far-IR SED of power-law DOGs, as described in section 4.3.1 and in Tyler et al. (2009).

Finally, assuming a gas mass to dust mass ratio of 120 (as was found in a study of the nuclear regions of nearby LIRGs; see Wilson et al., 2008), then the gas masses can be estimated as well. Using the assumed ratio, we find gas masses of $(5 - 10) \times 10^{10} M_{\odot}$ (median value of $6 \times 10^{10} M_{\odot}$) for the detected objects and gas mass 3σ limits of $(4 - 18) \times 10^{10} M_{\odot}$ in the remaining sample. We caution that this is very uncertain; Kovács et al. (2006) report a gas mass to dust mass ratio of ≈ 60 for SMGs, assuming $\kappa_d^{\text{rest}} = 15 \text{ cm}^2 \text{ g}^{-1}$. If this gas to dust mass ratio is appropriate for our sample, then the implied gas masses will be a factor of two lower ($2 - 5 \times 10^{10} M_{\odot}$)

4.3.5 Stellar Masses

In this section, we describe the methodology and present estimates for the stellar masses of the DOGs in this sample.

4.3.5.1 Methodology

To estimate stellar masses, we rely on Simple Stellar Population (SSP) template SEDs from the Bruzual & Charlot (2003) population synthesis library. All models used here have ages spaced logarithmically from 10 Myr up to 1 Gyr, solar metallicity, a Chabrier initial mass function (IMF) over the mass range $0.1 - 100 M_{\odot}$ (Chabrier, 2003), and use the Padova 1994 evolutionary tracks (Girardi et al., 1996). The reddening law from Calzetti et al. (2000) is used between $0.12 - 2.2 \mu\text{m}$ and that of Draine (2003) for longer wavelengths. This method is similar to that used in Bussmann et al. (2009b).

For sources at $z \sim 2$ whose mid-IR luminosity is dominated by stellar light, IRAC photometry samples the SED over the wavelength range where emission from asymptotic and red giant branch stars as well as low-mass main-sequence stars produces an emission peak at rest-frame $1.6\mu\text{m}$. In such cases, for given assumptions regarding the star-formation history, metallicity, and IMF, stellar mass estimates can be obtained via stellar population synthesis modeling. One goal of this work is to estimate stellar masses using self-consistent modeling of photometry measured at similar wavelengths for a variety of $z \sim 2$ dusty galaxies. Therefore, we apply this method to determine stellar masses in SMGs as well as XFLS and SWIRE sources. The IRAC data for each of these galaxy populations comes from, respectively, Dye et al. (2008), Lacy et al. (2005), and Lonsdale et al. (2009).

The DOGs studied in this paper have mid-IR SEDs that are dominated by a power-law component, suggesting that obscured AGN emission is overwhelming the stellar flux at these wavelengths. The shape of the mid-IR SED therefore provides limited constraints on the stellar population and additional information is needed to estimate the stellar mass of these sources. To overcome this challenge, SSP models were fit to high spatial-resolution *HST* photometry in the rest-frame UV (WFPC2/F606W or ACS/F814W) and rest-frame optical (NIC2/F160W) from Bussmann et al. (2009b). Two sources currently lack *HST* data (SST24 J142827.2+354127 and SST24 J143411.0+331733³) and so are excluded from this analysis.

In principle, rest-frame near-IR data offer a means to estimate the SSP age and A_V independently, since rest-frame optical and near-IR photometry sample the SED above the 4000 Å break while the rest-frame UV photometry samples galaxy light below the 4000 Å break. However, these data come from the IRAC $3.6\mu\text{m}$ images of the Boötes field (*Spitzer* Deep Wide-Field Survey; Ashby et al., in prep.), where

³*HST* data exist for this source but will be presented in a separate paper (Prescott et al., in prep.)

the spatial resolution is insufficient to resolve the nuclear source from the extended galaxy component. In this case, there are only limited constraints on the amount of non-stellar (i.e., obscured AGN) emission at $3.6\mu\text{m}$. We have explored the effect of this uncertainty on the fitting process by artificially reducing the $3.6\mu\text{m}$ flux by 50% (corresponding to the situation where the $3.6\mu\text{m}$ emission is equal parts starlight and AGN) and re-analyzing the data. Comparing results, we find that higher AGN fractions imply younger inferred SSP ages and higher A_V values. Because the AGN fraction in these sources is currently unknown at $3.6\mu\text{m}$, we are unable to constrain both the age and A_V independently.

Although the usage of photometry at different wavelengths is not ideal for the purposes of comparing stellar masses between galaxy populations, this method remains valuable because the models being fit to the data are the same for each galaxy population. Indeed, recent work has suggested that the dominant source of systematic uncertainty in stellar mass estimates of K -selected galaxies at $z \sim 2.3$ is the use of different stellar population synthesis codes (Muzzin et al., 2009), and that these systematics often dominate the formal random uncertainty. As long as the parameters of the model used here (such as the IMF, star-formation history, metallicity, etc.) do not vary from population to population, then the comparison presented here should be valid in a global sense.

4.3.5.2 Stellar Mass Estimates

Figure 4.7 shows χ^2_ν contours for a grid of SSP ages and A_V values. The contours trace lines of 80%, 95%, and 99.9% confidence intervals allowed by the photometric uncertainties (estimated using a bootstrap method similar to that outlined in section 4.3.3). The solid grey lines trace iso-mass contours and show the range in stellar masses allowed by the photometric uncertainties. The best-fit SSP model parameters (M_{star} and χ^2_ν) are printed in each panel and shown in Table 4.5.

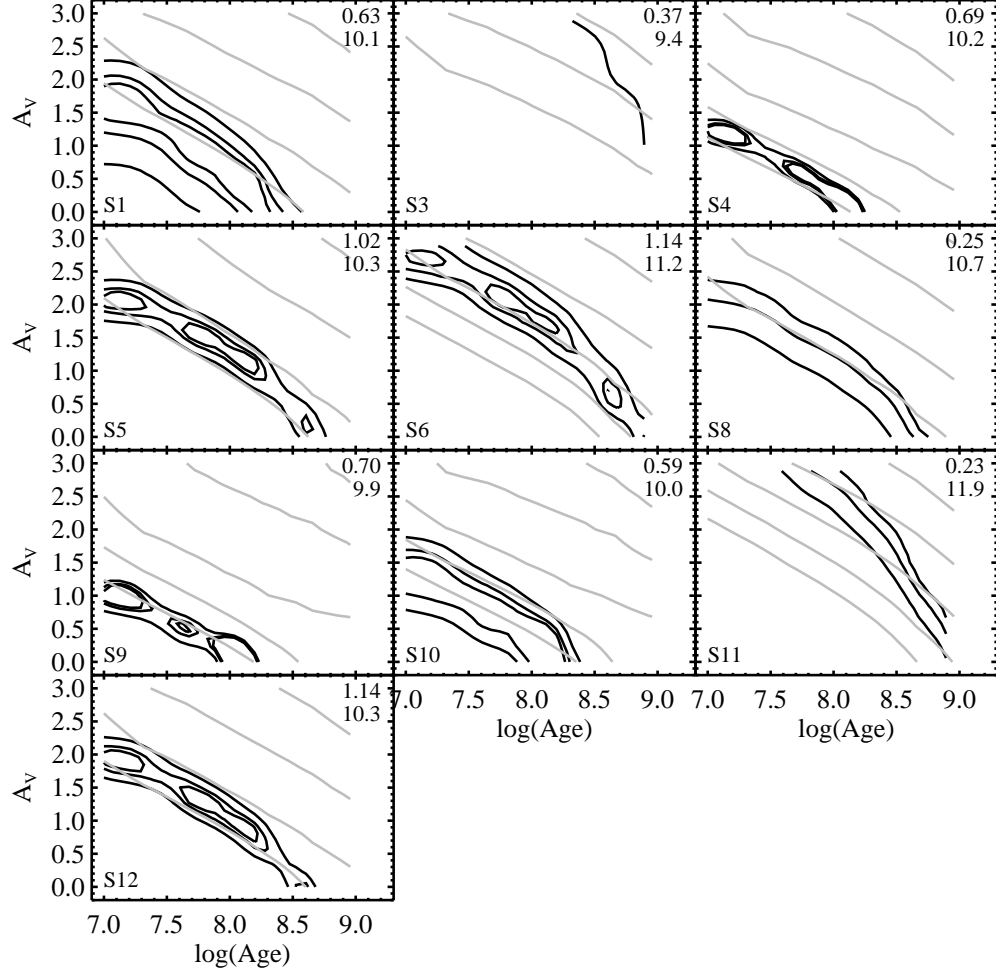


Figure 4.7 χ^2_ν contours based on SSP fits to *HST* imaging in *H*-band and *V*- or *I*-band. Black lines indicate 80%, 95%, and 99.9% confidence intervals. Grey contours trace lines of constant stellar mass for the given *HST* photometry, starting with $M_{\text{star}} = 10^{10} M_{\odot}$ in the bottom left and increasing by 0.5 dex towards the upper right. In the top right corner of each panel is the minimum χ^2_ν value and the associated stellar mass, in units of $\log(M_{\text{star}}/M_{\odot})$. The bottom left corner contains the source identifier. Not shown are sources S2 and S7, since these targets have no *HST* imaging available. The best-fit stellar masses range from $10^{10} - 10^{12} M_{\odot}$.

The stellar masses in the sample range from $(1 - 20) \times 10^{10} M_{\odot}$, with a median value of $2 \times 10^{10} M_{\odot}$. The χ^2_{ν} values range from $0.37 - 1.16$, with a median value of 0.69 . In one case (SST24 J143001.9+334538, or S3), the photometric uncertainty is so large that $\chi^2_{\nu} < 1$ over the full range of A_V and SSP age that we have sampled and so the range of acceptable fits is very large. For this source, we quote the 3σ upper limit on the stellar mass based on the photometric uncertainty.

The ratio of the stellar to gas mass, $\zeta \equiv M_{\text{star}}/M_{\text{gas}}$, is a measure of the evolutionary state of the galaxy, with larger values indicating more processing of gas to stars. Our estimates of ζ , computed assuming $M_{\text{gas}}/M_{\text{dust}} = 120$, are presented in Table 5. We caution that the gas mass to dust mass ratio is highly uncertain. In SMGs, there is evidence suggesting it is ≈ 60 (Kovács et al., 2006). Adopting this lower value would imply lower gas masses by a factor of two and hence double our $M_{\text{star}}/M_{\text{gas}}$ estimates.

Clustering studies suggest that the most luminous DOGs reside in very massive halos ($M_{\text{DM}} \sim 10^{13} M_{\odot}$ Brodwin et al., 2008). It is tempting to attribute the low stellar masses we estimate for DOGs to youth. However, the absolute stellar masses we compute are extremely uncertain. For example, the use of a Salpeter IMF rather than a Chabrier IMF would approximately double our stellar mass estimates (Bruzual & Charlot, 2003). Beyond the choice of what IMF slope to use, the mass-to-light ratio of a model galaxy (for a given rest-frame near-UV - R color) can vary significantly depending on the details of its star-formation history, the clumpiness of its interstellar medium and the associated dust attenuation law, as well as how advanced stages of stellar evolution are treated, such as blue stragglers, thermally-pulsating asymptotic giant branch stars, etc. (Conroy et al., 2010). In light of these uncertainties, the fact that our stellar mass estimates are low ($M_{\text{star}} \sim 10^{10} M_{\odot}$) compared to the dark matter haloes in which we believe they reside is not yet

a cause for concern – a quantitative study of the maximum possible stellar mass allowed by the photometry (by examining results from different stellar population synthesis codes, star-formation histories, metallicities, etc.) would be the best way to approach this issue in the near-term, but is beyond the scope of the current work.

4.4 Discussion

In this section, we seek to understand the role of DOGs in galaxy evolution and their relation to other high- z galaxy populations. We begin by motivating a comparison sample of such objects, including SMGs and *Spitzer*-selected ULIRGs from the XFLS and SWIRE survey. We then examine how the measured properties differ from population to population. We end with the implications of these comparisons for models of galaxy evolution.

4.4.1 Related $z \approx 2$ Galaxy Populations

4.4.1.1 SMGs

SMGs represent an interesting population of galaxies for comparison with DOGs because they are selected at sub-mm wavelengths where the dominant emission component is cold dust ($T_{\text{dust}} \sim 30$ K). In contrast, DOGs are selected predominantly by their brightness at $24\mu\text{m}$ and therefore should be dominated by hot dust. Despite this fundamental distinction, these two galaxy populations have similar number densities and redshift distributions (Chapman et al., 2005; Dey et al., 2008; Blain et al., 2004). Recent evidence suggests that $24\mu\text{m}$ -faint ($F_{24\mu\text{m}} \sim 0.1 - 0.5$ mJy) DOGs have a composite SED whose shape in the far-IR closely mimics that of the average bright ($F_{850} > 5$ mJy) SMG (Pope et al., 2008a). Furthermore, $24\mu\text{m}$ -faint DOGs and SMGs have similar real space correlation lengths ($r_0 \approx 6 \pm 2 h^{-1}$ Mpc), yet there is tentative evidence that DOG clustering strength increases with $24\mu\text{m}$ flux density ($r_0 \approx 13 \pm 3 h^{-1}$ Mpc for DOGs with $F_{24\mu\text{m}} > 0.6$ mJy; Brodwin et al.,

2008). While these results are suggestive of an association between the two populations, the details of such a connection are not yet clear. In an effort to study this connection via their far-IR properties, we will compare the data presented in this paper with SHARC-II $350\mu\text{m}$ and MAMBO 1.2mm imaging of 25 SMGs from the Submillimetre Common User Bolometer Array (SCUBA) Half Degree Extragalactic Survey (Laurent et al., 2006; Kovács et al., 2006; Coppin et al., 2008; Greve et al., 2004).

4.4.1.2 XFLS Sources

A set of *Spitzer*-selected galaxies from the 4 deg^2 XFLS share many properties with the $24\mu\text{m}$ -bright DOGs (Yan et al., 2007). The specific selection criteria are similar, although not necessarily as extreme in their IR-optical flux density ratios: $F_{24\mu\text{m}} \geq 0.9\text{ mJy}$, $\nu F_\nu(24\mu\text{m})/\nu F_\nu(8\mu\text{m}) \geq 3.16$, and $\nu F_\nu(24\mu\text{m})/\nu F_\nu(0.7\mu\text{m}) \geq 10$ (in comparison, DOGs have $\nu F_\nu(24\mu\text{m})/\nu F_\nu(0.7\mu\text{m}) \geq 30$). *Spitzer*/IRS spectroscopy of these objects has revealed strong silicate absorption and in some cases PAH emission features on par with those of SMGs (Sajina et al., 2007b). This suggests that the XFLS sources are composite AGN/starburst systems and may represent a transition phase between (un)obscured quasars and SMGs (Sajina et al., 2008). MAMBO 1.2mm observations of 44 XFLS sources have allowed a detailed study of their far-IR properties and have suggested $\langle L_{\text{IR}} \rangle \sim 7 \times 10^{12} L_\odot$ (Sajina et al., 2008).

4.4.1.3 SWIRE Sources

The last set of comparison galaxies we consider are *Spitzer*-selected sources from the SWIRE survey (Lonsdale et al., 2009). Like DOGs in Boötes and the XFLS sources, they have large IR-optical flux density ratios. However, an additional criterion has been applied to identify sources with significant emission at rest-frame $1.6\mu\text{m}$ due to

evolved stellar populations. For sources at $z = 1.5 - 3$, this means selecting objects whose mid-IR spectrum peaks at $5.8\mu\text{m}$. Although spectroscopic redshifts are not available for most of this sample, SED fitting has suggested photometric redshifts consistent with $z \sim 2$ and stellar masses of $(0.2 - 6) \times 10^{11} M_{\odot}$ (Lonsdale et al., 2009). MAMBO 1.2mm photometry for 61 of these SWIRE sources has indicated far-IR luminosities of 10^{12} - $10^{13.3} L_{\odot}$ (Lonsdale et al., 2009).

4.4.2 Comparison of Measured Properties

Our results from section 4.3 represent our best estimates of L_{IR} , L_{FIR} , T_{dust} , M_{dust} , and M_{star} for the DOGs in the sample. In Table 4.6, we give the median value of these quantities for DOGs in Boötes (from this paper), SMGs, and XFLS and SWIRE sources. In computing these median values, we do not consider sources at $z < 1$; nor do we consider sources without detections at (sub-)mm wavelengths (see discussion on caveats to the analysis at the end of this section). Table 4.6 also makes a distinction between XFLS sources whose mid-IR spectra are dominated by strong PAH features (XFLS PAH) and those that show weak or absent PAH features (XFLS weak-PAH). Each of these galaxy populations is further subdivided into those that qualify as DOGs ($R - [24] > 14$) and those that do not.

The primary feature of this comparison is that the relative uncertainty in the estimated parameters between galaxy populations has been reduced by computing the respective values self-consistently with the methods outlined in section 4.3. The exceptions to this rule are L_{IR} and T_{dust} (note that while the photometry used to determine M_{star} for Boötes DOGs is different than for the other galaxy populations, the methodology used is the same, including the use of the same set of model SSP templates). Our method of computing L_{IR} relies on the assumption that Mrk 231 represents a reasonable approximation of the source SED. For many SMGs as well as XFLS and SWIRE sources, this is an unrealistic assumption. Instead, we estimate

Table 4.6. Average High- z Galaxy Properties

| Source | R -[24] | N | L_{IR} ($10^{12} L_{\odot}$) | L_{FIR} ($10^{12} L_{\odot}$) | T_{dust} (K) | M_d ($10^9 M_{\odot}$) | M_{star} ($10^{10} M_{\odot}$) | $M_{\text{star}}/M_{\text{gas}}^{\text{a}}$ |
|----------------------------|-----------|-----|--|---|--------------------------|-------------------------------|--|---|
| Boötes ^b | > 14 | 5 | 23 | 10 | 45 | 0.5 | > 2 | > 0.3 |
| XFLS ^c | ALL | 11 | 7.7 | 2.7 | 32 | 5.0 | 13 | 0.48 |
| | > 14 | 6 | 8.7 | 1.1 | 27 | 7.3 | 10 | 0.21 |
| | < 14 | 5 | 6.5 | 4.6 | 37 | 2.3 | 16 | 0.58 |
| XFLS PAH ^c | ALL | 5 | 5.7 | 1.8 | 31 | 4.6 | 22 | 0.54 |
| | > 14 | 2 | 6.3 | 1.6 | 29 | 7.5 | 23 | 0.30 |
| | < 14 | 3 | 5.4 | 2.0 | 32 | 2.8 | 22 | 0.69 |
| XFLS weak-PAH ^c | ALL | 6 | 9.4 | 3.4 | 32 | 5.3 | 5.0 | 0.25 |
| | > 14 | 4 | 3.5 | 0.8 | 26 | 7.2 | 3.8 | 0.17 |
| | < 14 | 2 | 14 | 8.0 | 45 | 1.6 | 7.3 | 0.40 |
| SWIRE ^d | ALL | 19 | 6.5 | 3.1 | 32 | 6.7 | 28 | 0.53 |
| | > 14 | 16 | 6.7 | 3.1 | 32 | 6.1 | 28 | 0.56 |
| | < 14 | 3 | 5.5 | 2.6 | 30 | 9.9 | 24 | 0.35 |
| SMG ^e | ALL | 18 | 6.9 | 3.2 | 35 | 1.5 | 10 | 0.60 |
| | > 14 | 4 | 7.8 | 3.6 | 28 | 2.9 | 6.9 | 0.28 |
| | < 14 | 14 | 6.1 | 2.9 | 37 | 1.1 | 12 | 0.71 |

^aComputed using $M_{\text{gas}}/M_{\text{dust}} = 120$.^bIncludes only DOGs detected at $350\mu\text{m}$.^cXFLS sources with MAMBO 1.2mm detections (Sajina et al., 2008).^dSWIRE sources with MAMBO 1.2mm detections (Lonsdale et al., 2009).^eFrom compilation of Coppin et al. (2008).

L_{IR} from L_{FIR} , assuming (1) $L_{\text{IR}} = L_{\text{IR, SB}} + L_{\text{IR, AGN}}$; (2) $L_{\text{IR, SB}} = \alpha L_{\text{FIR}}$; (3) $L_{\text{IR, AGN}} = \epsilon L_{\text{IR}}$, where α is a factor ≈ 1.3 , depending on T_{d} and β (Helou et al., 1988) and ϵ is the typical AGN fraction of the galaxy population. For SMGs, we adopt the conservative upper limit from Pope et al. (2008b) of $\epsilon = 0.3$. For SWIRE sources and XFLS PAH sources, this fraction is ≈ 0.3 (Pope et al., 2008b; Lonsdale et al., 2009; Sajina et al., 2008), while for XFLS weak-PAH sources we use 0.7 (Sajina et al., 2008).

The T_{dust} values given in the literature are adopted for each source. It should be noted that T_{dust} for SWIRE sources are uncertain due to the lack of data near the far-IR peak (i.e., observed-frame 160 or 350 μm). Lonsdale et al. (2009) analyze the stacked signal at 160 μm from these sources and find that the T_{dust} is higher by as much as 10 K than what is assumed in their Table 4.6. For a given 1.2mm flux, increasing T_{d} by 10 K will increase L_{FIR} by a factor of ≈ 3 and decrease M_{dust} by $\approx 50\%$.

The key result from Table 4.6 is that while the DOGs in our sample have lower dust masses than the other galaxy populations by a factor of $\sim 3 - 20$, they have higher total IR and far-IR luminosities by factors of ~ 2 . This distinction is driven by the difference in T_{dust} , as DOGs in the sample have higher values by $\approx 10-20$ K compared to the other galaxy populations.

In terms of the stellar and gas mass estimates, the relationship between DOGs in Boötes (i.e., the sample studied in this paper) and the remaining galaxy populations is unclear. Even if a single dust temperature and a single dust to gas mass ratio for each of the sources studied in this paper is adopted, the uncertainties on the stellar mass estimates are large enough to allow greatly varying stellar mass to gas mass ratios. Sources satisfying $R - [24] > 14$ (i.e., DOGs) tend to have higher gas masses compared to $R - [24] < 14$ sources (under the assumption of a constant

dust-to-gas mass ratio). This difference is at least in part due to a difference in dust temperatures; within this sample, DOGs have lower dust temperatures than non-DOGs. This is in contrast with the evidence for high dust temperatures in the Boötes DOGs studied in this paper and may be an indication that mm-detected DOGs represent a special subset of DOGs that is more representative of the mm-selected galaxy population than the DOG population.

An important caveat to this comparison is that we are dealing with small sample sizes due to incomplete coverage at one or more bands from the mid- to the far-IR. For instance, while every DOG has a measured $24\mu\text{m}$ flux density, very few have been observed at $350\mu\text{m}$, and only two have been observed at 1mm. Similarly, few XFLS and SWIRE sources have been detected at 1mm and even fewer have been observed at $350\mu\text{m}$. Although SMGs are the best-studied class of objects within this set of populations, they too suffer from low-number statistics. Larger sample sizes in the critical 200-500 μm regime will arrive following the analysis of wide-field survey data from the Balloon-borne Large Aperture Submillimeter Telescope (e.g., Pascale et al., 2009) and the *Herschel* Space Observatory.

4.4.3 Implications for Models of Galaxy Evolution

One of the major open questions in galaxy evolution is the effect that AGN have on their host galaxies. In the local universe, there is observational evidence that ULIRGs dominated by warm dust serve as a transition phase between cold dust ULIRGs and optically luminous quasars and that this transition may be driven by a major merger (Sanders et al., 1988a,b). Recent theoretical models of quasar evolution based on numerical simulations of major mergers between gas-rich spirals have suggested that the subsequent growth of a super-massive black hole can regulate star-formation via a feedback effect which re-injects energy into the interstellar medium (ISM) and expels the remaining gas that would otherwise form stars

(Hopkins et al., 2006).

Although the notion that local ULIRGs are associated with mergers is well accepted (e.g., Sanders & Mirabel, 1996), the picture is less clear at high redshift. Morphological studies of high- z galaxies suffer from surface brightness dimming, making the detection of faint merger remnant signatures difficult (e.g., Dasyra et al., 2008; Melbourne et al., 2008; Busmann et al., 2009b; Melbourne et al., 2009). However recent theoretical work on the cosmological role of mergers in the formation of quasars and spheroid galaxies suggests that they dominate the $z \gtrsim 1$ quasar luminosity density compared to secular processes such as bars or disk instabilities (Hopkins et al., 2008b).

If major mergers drive the formation of massive galaxies at high redshift, then one possible interpretation of our results involves an evolutionary scenario in which these sources represent a very brief but luminous episode of extreme AGN growth just prior to the quenching of star formation. In such a scenario, SMGs and the brightest $24\mu\text{m}$ -selected sources represent the beginning and end stages, respectively, of the high star-formation rate, high IR luminosity phase in massive galaxy evolution. Consistent with this scenario is that we find $24\mu\text{m}$ -bright DOGs in Boötes to have higher dust temperatures (possibly from AGN heating of the dust) than SMGs and less extreme *Spitzer*-selected sources. We caution, however, that these results are consistent with any evolutionary model in which the $24\mu\text{m}$ -bright phase follows the sub-mm bright phase, be it driven by major mergers, minor mergers, or some secular process.

Finally, we stress that larger samples of mm and sub-mm imaging of *Spitzer*-selected galaxies are needed in order to understand their role in galaxy evolution fully by comparing samples of similar number density, clustering properties, etc. Much of this will be provided by upcoming *Herschel* and SCUBA-2 surveys. In the more

immediate future, 1mm imaging with currently available instruments such as the Astronomical Thermal Emission Camera (AzTEC) and the MAX-Planck Millimeter Bolometer Array (MAMBO) will be critical to constraining the cold dust properties of *Spitzer*-selected galaxies. Only when these surveys have obtained statistically significant numbers of detections or stringent upper limits will we be able to make definitive conclusions regarding the nature of the link between AGN and starbursts in the formation of the most massive galaxies.

4.5 Conclusions

We present CSO/SHARC-II $350\mu\text{m}$ and CARMA 1mm photometry of DOGs in the Boötes Field. The major results and conclusions from this study are the following:

1. At $350\mu\text{m}$, 4/5 DOGs are detected in data with low rms levels ($\leq 15\text{ mJy}$) and 0/8 DOGs are detected in data with medium to high rms levels ($20 - 50\text{ mJy}$). At 1mm, a subset of two DOGs were observed but not detected.
2. Mrk 231 is confirmed as a valid template for the SEDs of the DOGs in this sample. This suggests the $24\mu\text{m}$ bright ($F_{24\mu\text{m}} \gtrsim 1\text{ mJy}$) population of DOGs is dominated by warm dust, possibly heated by an AGN. Cold dust templates such as Arp 220 are inconsistent with the data in all twelve objects studied.
3. Trends in the flux density ratios $350\mu\text{m}/24\mu\text{m}$ and $1200\mu\text{m}/24\mu\text{m}$ with the R -[24] color ($F_{24\mu\text{m}}/F_{0.7\mu\text{m}}$) show that DOGs in this sample have elevated $24\mu\text{m}$ emission relative to SMGs, most likely due to an obscured AGN.
4. The non-detections at 1mm imply T_{dust} greater than 35-60 K for two objects.
5. If the dust properties of the two DOGs observed at 1mm apply generally to the $24\mu\text{m}$ bright DOGs, then we estimate dust masses for these sources of

$1.6 - 6.1 \times 10^8 M_{\odot}$. Lower T_{dust} would imply higher dust masses and vice versa.

6. In comparison to other $z \approx 2$ ULIRGs, DOGs have warmer dust temperatures that imply higher IR luminosities and lower dust masses. This may be an indication that AGN growth has heated the ambient ISM in these sources.
7. Our stellar mass estimates provide weak evidence indicating that the $24\mu\text{m}$ -bright DOGs may have converted more gas into stars than SMGs or other *Spitzer*-selected sources, consistent with them representing a subsequent phase of evolution. An important caveat to this conclusion is that we have assumed DOGs and SMGs share the same gas mass to dust mass ratio. Testing this assumption will require new data and will be an important goal of future work.

This work is based in part on observations made with the *Spitzer Space Telescope*, which is operated by the Jet Propulsion Laboratory, California Institute of Technology under NASA contract 1407. *Spitzer*/MIPS guaranteed time observing was used to image the Boötes field at $24\mu\text{m}$ and is critical for the selection of DOGs. We thank the SDWFS team (particularly Daniel Stern and Matt Ashby) for making the IRAC source catalogs publicly available. Data from the original IRAC shallow survey were used for initial stellar mass estimates. We thank the anonymous referee for a thorough review of the manuscript that helped improve the paper.

We are grateful to the expert assistance of the staff of Kitt Peak National Observatory where the Boötes field observations of the NDWFS were obtained. The authors thank NOAO for supporting the NOAO Deep Wide-Field Survey. In particular, we thank Jenna Claver, Lindsey Davis, Alyson Ford, Emma Hogan, Tod Lauer, Lissa Miller, Erin Ryan, Glenn Tiede and Frank Valdes for their able assistance with the NDWFS data. We also thank the staff of the W. M. Keck Observatory, where

some of the galaxy redshifts were obtained.

RSB gratefully acknowledges financial assistance from HST grant GO10890, without which this research would not have been possible. Support for Program number HST-GO10890 was provided by NASA through a grant from the Space Telescope Science Institute, which is operated by the Association of Universities for Research in Astronomy, Incorporated, under NASA contract NAS5-26555. The research activities of AD are supported by NOAO, which is operated by the Association of Universities for Research in Astronomy (AURA) under a cooperative agreement with the National Science Foundation. Support for E. Le Floch was provided by NASA through the Spitzer Space Telescope Fellowship Program.

Facilities used: *Spitzer*, CSO, and CARMA. This research made use of CSO (SHARC-II) and CARMA data. Support for CARMA construction was derived from the states of California, Illinois, and Maryland, the Gordon and Betty Moore Foundation, the Kenneth T. and Eileen L. Norris Foundation, the Associates of the California Institute of Technology, and the National Science Foundation. Ongoing CARMA development and operations are supported by the National Science Foundation under a cooperative agreement, and by the CARMA partner universities.

CHAPTER 5

THE STELLAR MASSES AND STAR-FORMATION HISTORIES OF DOGS AT $z \sim 2$

With the goal of elucidating the evolutionary relationship between different populations of dusty high-redshift galaxies, we estimate and compare the stellar masses and star-formation histories of three populations of ultra-luminous infrared galaxies (ULIRGs) at redshifts $z \sim 2$. Two of these are selected at mid-infrared (mid-IR) wavelengths for their extremely red $R-[24]$ colors (dust-obscured galaxies, or DOGs) and one is selected at $850\mu\text{m}$ (sub-millimeter galaxies or SMGs). One set of 39 DOGs has a local maximum in their mid-IR spectral energy distribution (SED) at rest-frame $1.6\mu\text{m}$ associated with stellar emission (“bump DOGs”), while the other set of 51 DOGs has a power-law dominated mid-IR SED with spectral features suggesting obscured AGN (“power-law DOGs”). Using stellar population synthesis models applied self-consistently to photometry in 11 broad-band filters from $0.4\mu\text{m}$ - $24\mu\text{m}$, we find that the best-fit stellar masses of SMGs, bump DOGs and power-law DOGs are $4 \times 10^{10} M_{\odot}$, $5 \times 10^{10} M_{\odot}$, and $6 \times 10^{10} M_{\odot}$, respectively (assuming a simple stellar population and Chabrier IMF). These mass estimates increase by ≈ 0.3 dex when a merger-driven star-formation history using a Salpeter IMF is adopted, values that are consistent with simulations of gas-rich major mergers in which SMGs evolve into bump DOGs and later power-law DOGs. On the other hand, cosmological simulations in which galaxies are assembled primarily by smooth accretion predict stellar masses that are a factor of 2 (4 if a “bottom-light” IMF is assumed) larger than our estimates for DOGs and SMGs. Although neither theoretical model provides a perfect match to the data, the relatively low stellar masses found here generally favor merger-driven star-formation histories.

5.1 Introduction

Ultra-luminous infrared galaxies (ULIRGs) are systems with extremely high infrared (IR) luminosities ($L_{\text{IR}} > 10^{12} L_{\odot}$) generally interpreted as arising from extreme episodes of star-formation ($M_{\odot} > 100 M_{\odot}$) or accretion onto super-massive black holes. These objects are rare in the local universe, yet they have been associated with a critical phase of galaxy evolution linking mergers (Armus et al., 1987) with quasars and red, dead elliptical galaxies (Sanders et al., 1988a,b). ULIRGs are more commonplace in the distant universe, to the extent that they contribute a significant component of the bolometric luminosity density of the universe at $z > 1$ (e.g. Franceschini et al., 2001; Le Floch et al., 2005; Pérez-González et al., 2005). This realization implies that ULIRGs may represent an important evolutionary phase in the assembly history of massive galaxies and has inspired a host of new techniques for identifying ULIRGs at $z > 1$.

The two most successful techniques for identifying high-redshift ULIRGs rely on selection at either mid-infrared or far-infrared wavelengths. Surveys at $24\mu\text{m}$ with the Multiband Imaging Photometer for Spitzer (MIPS; Rieke et al., 2004) instrument for the *Spitzer Space Telescope* have been remarkably successful for the mid-IR identification of ULIRGs (Yan et al., 2004; Houck et al., 2005; Weedman et al., 2006b; Fiore et al., 2008; Dey et al., 2008; Fiore et al., 2009). In particular, Dey et al. (2008) select sources from the 9 deg² NOAO Deep Wide-Field Survey (NDWFS) Boötes field that satisfy $R - [24] > 14$ (Vega magnitudes; $\approx F_{24\mu\text{m}}/F_R > 1000$) and $F_{24\mu\text{m}} > 0.3$ mJy. These objects are called dust-obscured galaxies (DOGs), lie at $z \approx 2 \pm 0.5$ (Houck et al., 2005; Weedman et al., 2006a; Desai et al., 2009, Soifer et al., in prep.), have ULIRG luminosities (e.g. Bussmann et al., 2009a), have a space density of $(2.82 \pm 0.05) \times 10^{-5} h_{70}^3 \text{ Mpc}^{-3}$ (Dey et al., 2008), and inhabit dark matter haloes of mass $M_{\text{DM}} \sim 10^{12.3} M_{\odot}$ (Brodwin et al., 2008). These results imply DOGs

are undergoing a very luminous, short-lived phase of activity characterized by both vigorous stellar bulge and nuclear black hole growth.

In addition, DOGs can be divided into two groups according to the nature of their mid-IR spectral energy distribution (SED). Those with a peak or bump at rest-frame $1.6\mu\text{m}$ produced by the photospheres of old stars (“bump DOGs”), and those dominated by a power-law in the mid-IR (“power-law DOGs”). The SED shapes, as well as spectroscopy in the near-IR (Brand et al., 2007; Sajina et al., 2008) and mid-IR (Yan et al., 2007; Sajina et al., 2007a; Farrah et al., 2008; Desai et al., 2009; Huang et al., 2009) indicate that the bolometric luminosities of bump DOGs are dominated by star-formation, while those of power-law DOGs are dominated by obscured active galactic nuclei (AGN).

Another method of selecting high redshift ULIRGs is imaging at sub-millimeter (sub-mm) wavelengths. The advent of the Sub-mm Common User Bolometer Array (SCUBA; Holland et al., 1999) has allowed wide-field surveys at $850\mu\text{m}$ which have identified hundreds of sub-millimeter selected galaxies (SMGs). These objects have similar redshifts, number densities (Chapman et al., 2005), and clustering properties (Blain et al., 2004) as DOGs.

The fact that SMGs and DOGs have similar properties provides suggestive evidence that these two populations of high redshift ULIRGs might be related in an evolutionary sequence similar to that of ULIRGs in the local universe (e.g. Sanders et al., 1988a). It has been hypothesized that such a sequence does indeed exist (Hopkins et al., 2006; Dey & The NDWFS/MIPS Collaboration, 2009), and that DOGs function as an important intermediate stage between gas-rich major mergers and quasars (which have similar clustering properties as DOGs and SMGs; Brodwin et al., 2008; Shen et al., 2009) at $z \sim 2$.

A theoretical understanding of how this evolutionary sequence might occur has

recently been advanced using N -body/smoothed particle hydrodynamic simulations combined with 3D polychromatic dust radiative transfer models (Narayanan et al., 2009). In these models, simulations are used to follow the evolution of the SED of both isolated disk galaxies and major mergers. These authors find that simulated systems with $F_{24\mu\text{m}} > 0.3$ mJy are associated with gas-rich ($f_g \approx 0.4$) major mergers with a minimum total baryonic mass of $M_b \approx 3 \times 10^{11} M_\odot$.

While there is significant variation associated with different viewing angles, initial orbital configurations, etc., the typical simulated major merger achieves peak star-formation rates (SFRs) of $\sim 1000 M_\odot \text{ yr}^{-1}$ at the beginning of final coalescence when tidal torques funnel large quantities of gas into the nucleus of the system (Mihos & Hernquist, 1996). This period is also when the system is brightest at sub-mm wavelengths and thus can be selected as an SMG. At the same time, central inflows begin to fuel the growth of a supermassive black hole. Approximately 100 Myr after the peak SFR, the black hole accretion rate peaks (at about $1\text{--}2 M_\odot \text{ yr}^{-1}$) and active galactic nucleus (AGN) feedback starts to terminate star-formation (along with consumption of the gas by star-formation). The models indicate that this period of AGN feedback coincides with the DOG phase ($F_{24\mu\text{m}}/F_R > 1000$). As the gas and dust are consumed by star-formation, optical sightlines open up and the system can be optically visible as a quasar. Thus, in these models, the expected evolutionary progression is driven by major mergers and proceeds from SMG to DOG to quasar to red, dead, elliptical galaxy (illustrated qualitatively in the top panel of Figure 5.1).

Alternative theories for the formation of SMGs which do not involve major mergers have also been advanced recently (Davé et al., 2010). These studies rely on numerical simulations of cosmological volumes and select SMGs as the most actively star-forming systems that match the observed number densities of SMGs. These SMGs have stellar masses in the range $M_* = (1 - 5) \times 10^{11} M_\odot$ and SFRs in the

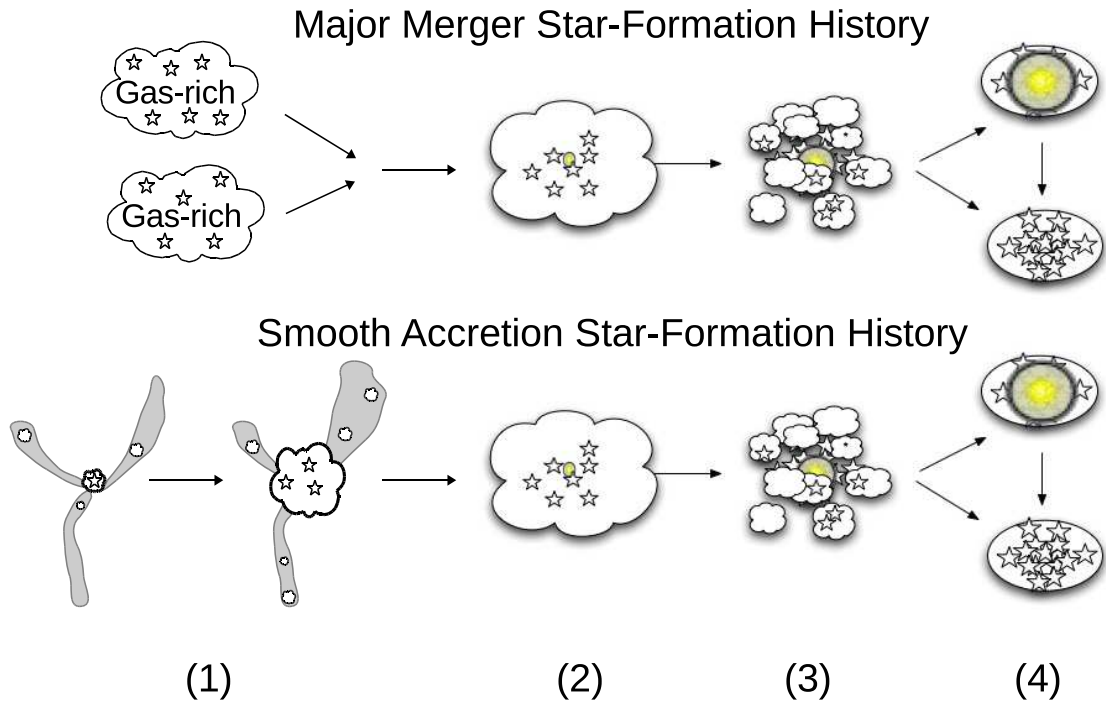


Figure 5.1 Cartoon picture illustrating the two star-formation histories examined in this paper (adapted from Dey & The NDWFS/MIPS Collaboration, 2009). *Top:* (1) A gas rich major merger leads to a (2) dust-enshrouded starburst phase. (3) Energetic feedback from the growth of a central super-massive black hole heats the dust resulting in an increase in the mid-infrared luminosity. (4) The following evolution depends on the relative timescales of AGN fuelling, dust dissipation, and star formation, but the system could be visible briefly as a QSO before settling on the red sequence. *Bottom:* (1) An alternative scenario in which massive galaxies are assembled via smooth accretion of gas and small satellites along filamentary structures. Some mechanism is still needed to quench star-formation; in this cartoon picture, steps (2), (3), and (4) are assumed to be the same as in the major merger driven scenario. One of the primary purposes of this paper is to use the star-formation histories of high redshift ULIRGs to test the two different possibilities illustrated in step (1) of this diagram.

range 200-500 $M_{\odot} \text{ yr}^{-1}$. This is a factor of 3 lower than what is observed in SMGs, which Davé et al. (2010) attribute to systematic effects in the SFR calibration (in particular, a “bottom-light” initial mass function requires lower SFRs to produce the observed IR luminosities of SMGs). Because the star-formation histories (SFHs) which produce these simulated SMGs do not involve major mergers, they are referred to here as “smooth accretion” SFHs (a qualitative illustration of this SFH is given in the bottom panel of Figure 5.1).

Studies attempting to connect the mid-IR and far-IR selected ULIRG population at high redshift have so far focused on their basic properties such as bolometric luminosities (Sajina et al., 2008; Coppin et al., 2008; Lonsdale et al., 2009; Bussmann et al., 2009a; Fiolet et al., 2009), clustering strengths (Blain et al., 2004; Brodwin et al., 2008), and morphologies. In particular, high-spatial resolution imaging (Dasyra et al., 2008; Melbourne et al., 2008, 2009; Bussmann et al., 2009b; Swinbank et al., 2010b) and dynamics (Tacconi et al., 2006, 2008, Bussmann et al., submitted, Melbourne et al., submitted) have identified morphological trends which are consistent with an evolutionary scenario driven by major mergers in which sources that show a bump in their mid-IR SED (i.e., bump DOGs and most SMGs) evolve into those with a power-law dominated mid-IR SED (i.e., power-law DOGs) (Bussmann et al., submitted). To test the origins of these sources further, it is imperative to use alternative, complementary methods of constraining the SFHs of DOGs and SMGs at $z \sim 2$.

This paper is focused on one such technique: stellar population synthesis (SPS) modeling of broad band photometry of DOGs and SMGs with known spectroscopic redshifts. The primary goal of this study is to place the tightest constraints possible on the stellar masses (M_*) and SFHs of bump DOGs, power-law DOGs, and SMGs using a uniform SPS modeling analysis with common model assumptions and fitting

techniques for each ULIRG population. There are several reasons to pursue this goal.

First, constraints on the M_* values and SFHs of *Spitzer*-selected ULIRGs are very limited (Berta et al., 2007; Lonsdale et al., 2009). In particular, the constraints on M_* and SFHs presented here for power-law DOGs are the first such results for this potentially very important population of galaxies.

Second, as SPS modeling methods have become more sophisticated, stellar mass results for a given population have not necessarily converged. For example, Borys et al. (2005) use *Spitzer*/Infrared Array Camera (IRAC; Fazio et al., 2004) data to infer average SMG stellar masses of $M_* \approx 2.5 \times 10^{11} M_\odot$. More recently, Dye et al. (2008) and Michałowski et al. (2010) have found average stellar masses for SMGs of $M_* = 6.3 \times 10^{11} M_\odot$ and $3.5 \times 10^{11} M_\odot$, respectively. Finally, a new study by Hainline et al. (2010) using essentially the same data set as Michałowski et al. (2010) finds significantly lower average SMG stellar masses of $M_* = 7 \times 10^{10} M_\odot$. This emphasizes the significant systematics that affect stellar mass estimates based on SPS modeling and underscores the need for a uniform analysis when comparing different ULIRG populations.

Third, the disagreement in observed stellar masses has significant bearing on theoretical models for the formation of high redshift ULIRGs. As outlined earlier, the cosmological hydrodynamical simulations of Davé et al. (2010) predict that SMGs have large stellar masses that are roughly consistent with the estimates of Borys et al. (2005) and Michałowski et al. (2010), but a factor of ≈ 2 larger than the estimates of Hainline et al. (2010). These mass estimates are also somewhat lower than what is expected from merger simulations (Narayanan et al., 2009), although it should be noted that these expectations are highly dependent on the stage of the merger, viewing angle, etc. A systematic comparison of the stellar masses and SFHs of DOGs and SMGs with both theoretical models is therefore an urgent matter, and

one that is the primary subject of this paper.

In section 5.2, the details of the data used in this analysis are presented, including DOG SEDs from rest-frame ultra-violet (UV) to near-IR. Section 5.3 outlines the general methodology and describes the SPS libraries, initial mass functions (IMFs), and SFHs that are used in the analysis. Results are presented in section 5.4, including constraints on stellar masses, visual extinctions, and stellar population ages. In section 5.5, we compare our results with similar studies of SMGs and other *Spitzer*-selected ULIRGs, identify ways to improve the analysis by obtaining new medium-band photometry, and explain the implications of the results for models of galaxy evolution. Conclusions are presented in section 5.6.

Throughout this paper we assume a cosmology in which $H_0 = 70 \text{ km s}^{-1} \text{ Mpc}^{-1}$, $\Omega_m = 0.3$, and $\Omega_\lambda = 0.7$. All magnitudes are in the AB system.

5.2 Data

The goal of this paper is to study the rest-frame UV through near-IR SEDs of high- z ULIRGs via stellar population synthesis modeling of broad-band photometry. To minimize degeneracies in the models, it is important to limit the analysis to sources with spectroscopic redshifts. Thus, the present sample consists of ULIRGs with spectroscopic redshifts at $z > 1.4$ and broad-band photometry from the rest-frame UV through near-IR. The sample comprises three main sub-groups: two selected with *Spitzer* at $24\mu\text{m}$ (DOGs), and one selected with the Sub-mm Common User Bolometer Array (SCUBA) at $850\mu\text{m}$ (SMGs).

5.2.1 DOGs

5.2.1.1 Sample Selection

For the *Spitzer*-selected ULIRGs, a total of 2603 DOGs satisfying $R - [24] > 14$ (Vega mag) and $F_{24\mu\text{m}} > 0.3 \text{ mJy}$ were identified in the 8.6 deg^2 NDWFS Boötes

field with deep *Spitzer*/MIPS $24\mu\text{m}$ coverage (Dey et al., 2008). This paper focuses on the subset of 90 of these objects that have known spectroscopic redshifts at $z > 1.4$ either from observations with the Keck telescope ($\approx 60\%$, Soifer et al., in prep., 2010) or with the InfraRed Spectrometer (IRS Houck et al., 2004) onboard *Spitzer* (Houck et al., 2005; Weedman et al., 2006b).

Figure 5.2 shows the $R - [24]$ color as a function of $24\mu\text{m}$ magnitude for the subsample studied here (the “spectroscopic sample”) in comparison to the overall sample of DOGs in Boötes. To optimize the spectroscopic detection rate, the spectroscopic sample is biased towards bright $24\mu\text{m}$ sources, although the full range of $R - [24]$ colors is sampled. The spectroscopic sample consists of 39 star-formation dominated “bump” sources (those that show a peak at rest-frame $1.6\mu\text{m}$) and 51 active galactic nucleus (AGN) dominated “power-law” sources. Also shown in this diagram are 58 sub-millimeter galaxies (SMGs) with spectroscopic redshifts from Chapman et al. (2005) (see section 5.2.2). The redshift distributions of these groups of galaxies are shown in Figure 5.3. The positions, $R - [24]$ colors, and nature of mid-IR SED for each DOG in the sample are given in Table 5.1.

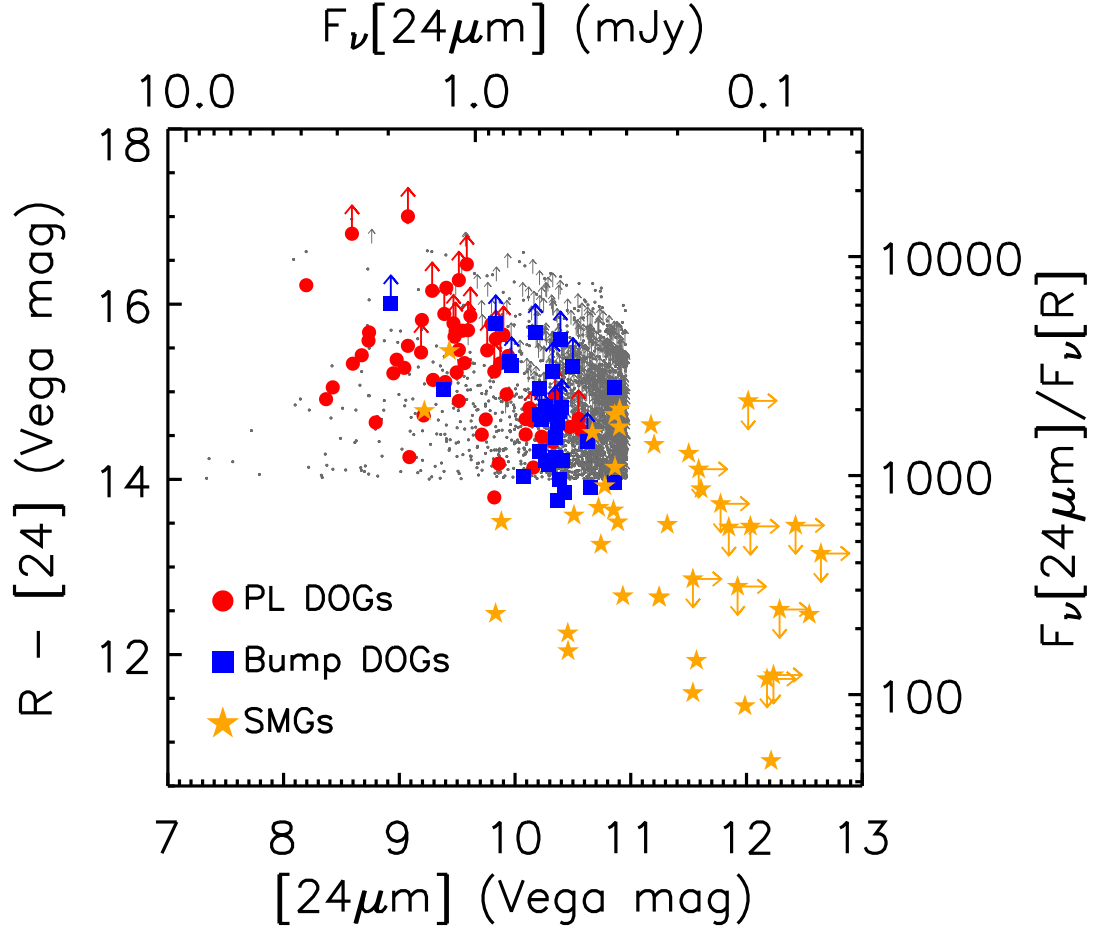


Figure 5.2 $R - [24]$ color vs. $24\mu\text{m}$ magnitude distribution for DOGs in the NDWFS Boötes field. Gray dots and upward arrows show the full sample of DOGs, with and without an R -band detection (2σ limits), respectively. Highlighted are the subsamples with spectroscopic redshifts and either a mid-IR power-law SED (PL DOGs, red circles) or a mid-IR bump SED (Bump DOGs, blue squares). Also shown are SMGs (orange stars) with spectroscopic redshifts from Chapman et al. (2005) and $24\mu\text{m}$ photometry from Hainline et al. (2009).

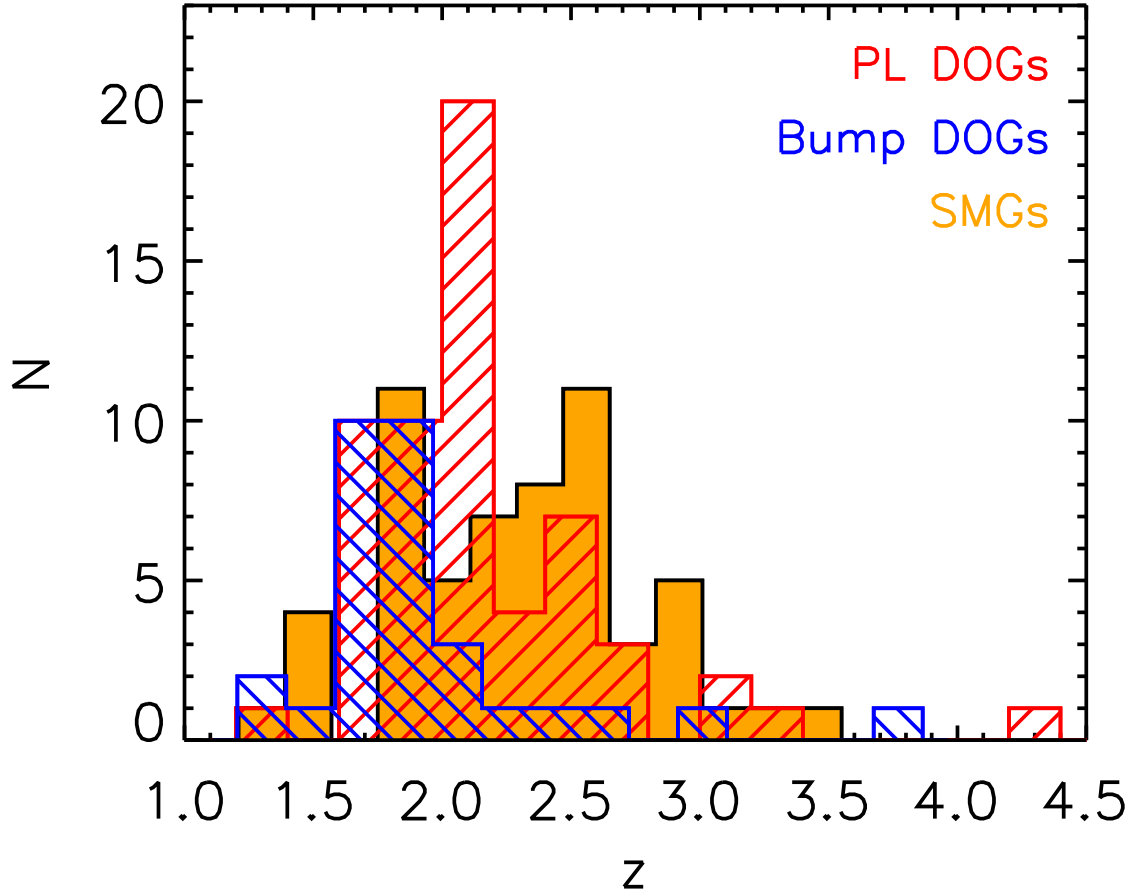


Figure 5.3 Redshift distribution of DOGs in the Boötes Field with spectroscopic redshifts. The redshift distribution of bump DOGs (blue hatched) is relatively narrow due to selection effects (for details see Desai et al., 2009), while power-law DOGs (red hatched) are weighted towards slightly larger redshifts. Also shown is the redshift distribution of SMGs (orange filled region) from Chapman et al. (2005).

Table 5.1. Basic DOG Spectroscopic Sample Properties

| ID | R.A. (J2000) | Dec. (J2000) | Bump/Power-law | |
|------------------------|--------------|--------------|----------------|--------|
| SST24 J142538.2+351855 | 216.4089050 | 35.3156586 | Power-law | > 15.6 |
| SST24 J142541.3+342420 | 216.4219513 | 34.4056931 | Power-law | 14.7 |
| SST24 J142554.9+341820 | 216.4792328 | 34.3057480 | Power-law | 15.5 |
| SST24 J142607.8+330425 | 216.5326385 | 33.0739212 | Power-law | 14.4 |
| SST24 J142622.0+345249 | 216.5918884 | 34.8804398 | Bump | 15.0 |
| SST24 J142626.4+344731 | 216.6102295 | 34.7919617 | Power-law | > 15.7 |
| SST24 J142637.3+333025 | 216.6558075 | 33.5071220 | Power-law | > 14.7 |
| SST24 J142644.3+333051 | 216.6846313 | 33.5143967 | Power-law | 14.9 |
| SST24 J142645.7+351901 | 216.6904144 | 35.3169899 | Power-law | > 16.3 |
| SST24 J142648.9+332927 | 216.7039337 | 33.4908333 | Power-law | 15.7 |
| SST24 J142652.5+345506 | 216.7188568 | 34.9181824 | Bump | 15.0 |
| SST24 J142653.2+330221 | 216.7218781 | 33.0391388 | Power-law | 15.8 |
| SST24 J142724.9+350824 | 216.8541260 | 35.1399765 | Bump | > 14.8 |
| SST24 J142748.4+344851 | 216.9518738 | 34.8142471 | Power-law | 14.6 |
| SST24 J142759.8+351243 | 216.9991150 | 35.2118530 | Power-law | > 15.4 |
| SST24 J142800.6+350455 | 217.0028992 | 35.0819473 | Power-law | 14.7 |
| SST24 J142804.1+332135 | 217.0172119 | 33.3596916 | Bump | > 15.8 |
| SST24 J142810.5+352509 | 217.0439453 | 35.4192238 | Power-law | 14.8 |
| SST24 J142814.2+352245 | 217.0593109 | 35.3795052 | Power-law | 14.2 |
| SST24 J142815.4+324720 | 217.0640869 | 32.7887993 | Power-law | 15.1 |
| SST24 J142827.9+334550 | 217.1163635 | 33.7639198 | Power-law | 15.4 |
| SST24 J142832.4+340849 | 217.1351166 | 34.1473694 | Bump | 13.8 |
| SST24 J142842.9+342409 | 217.1790771 | 34.4030418 | Power-law | 15.1 |
| SST24 J142846.6+352701 | 217.1942139 | 35.4504471 | Bump | > 15.3 |
| SST24 J142901.5+353016 | 217.2565460 | 35.5044174 | Power-law | > 14.7 |

Table 5.1 (cont'd)

| ID | R.A. (J2000) | Dec. (J2000) | Bump/Power-law | |
|------------------------|--------------|--------------|----------------|--------|
| SST24 J142920.1+333023 | 217.3341827 | 33.5063858 | Bump | 14.0 |
| SST24 J142924.8+353320 | 217.3533783 | 35.5559425 | Power-law | > 15.9 |
| SST24 J142928.5+350841 | 217.3685455 | 35.1448898 | Bump | > 14.4 |
| SST24 J142931.3+321828 | 217.3808136 | 32.3076057 | Power-law | > 15.7 |
| SST24 J142934.2+322213 | 217.3932343 | 32.3701096 | Power-law | 15.2 |
| SST24 J142941.0+340915 | 217.4209595 | 34.1542397 | Bump | > 14.7 |
| SST24 J142951.1+342042 | 217.4629822 | 34.3447685 | Bump | > 14.7 |
| SST24 J142958.3+322615 | 217.4930878 | 32.4376068 | Power-law | 15.6 |
| SST24 J143001.9+334538 | 217.5076904 | 33.7603149 | Power-law | 16.2 |
| SST24 J143020.4+330344 | 217.5855865 | 33.0622444 | Bump | > 15.2 |
| SST24 J143022.5+330029 | 217.5941925 | 33.0080185 | Power-law | > 15.7 |
| SST24 J143025.7+342957 | 217.6072998 | 34.4992828 | Power-law | 15.4 |
| SST24 J143028.5+343221 | 217.6188049 | 34.5392456 | Power-law | 15.1 |
| SST24 J143102.2+325152 | 217.7593689 | 32.8645210 | Power-law | > 15.8 |
| SST24 J143109.7+342802 | 217.7908020 | 34.4673615 | Power-law | 15.7 |
| SST24 J143135.2+325456 | 217.8971863 | 32.9158325 | Power-law | 14.7 |
| SST24 J143137.1+334501 | 217.9042053 | 33.7503319 | Bump | 14.8 |
| SST24 J143152.3+350030 | 217.9683838 | 35.0082169 | Bump | 14.6 |
| SST24 J143201.8+340408 | 218.0076141 | 34.0688477 | Power-law | 14.5 |
| SST24 J143216.8+335231 | 218.0702515 | 33.8754730 | Bump | > 14.8 |
| SST24 J143225.3+334716 | 218.1057739 | 33.7878914 | Power-law | > 15.9 |
| SST24 J143242.5+342232 | 218.1771698 | 34.3757019 | Power-law | > 15.5 |
| SST24 J143251.8+333536 | 218.2159729 | 33.5932732 | Power-law | > 15.3 |
| SST24 J143312.7+342011 | 218.3028564 | 34.3364716 | Power-law | 15.3 |
| SST24 J143315.1+335628 | 218.3133240 | 33.9411583 | Power-law | 14.2 |

Table 5.1 (cont'd)

| ID | R.A. (J2000) | Dec. (J2000) | Bump/Power-law | |
|------------------------|--------------|--------------|----------------|--------|
| SST24 J143318.8+332203 | 218.3284149 | 33.3674889 | Power-law | 14.6 |
| SST24 J143321.8+342502 | 218.3410492 | 34.4173508 | Bump | 14.2 |
| SST24 J143324.3+334239 | 218.3508911 | 33.7109337 | Bump | 14.3 |
| SST24 J143325.8+333736 | 218.3575897 | 33.6268959 | Power-law | 15.4 |
| SST24 J143330.0+342234 | 218.3752289 | 34.3762436 | Power-law | 15.2 |
| SST24 J143331.9+352027 | 218.3831787 | 35.3409195 | Bump | 14.3 |
| SST24 J143332.5+332230 | 218.3855133 | 33.3750801 | Bump | > 15.3 |
| SST24 J143335.9+334716 | 218.3996735 | 33.7877769 | Power-law | 14.5 |
| SST24 J143349.5+334601 | 218.4567871 | 33.7671394 | Bump | > 14.7 |
| SST24 J143353.7+343155 | 218.4738007 | 34.5321503 | Bump | 14.0 |
| SST24 J143358.0+332607 | 218.4916382 | 33.4355431 | Power-law | > 16.5 |
| SST24 J143407.4+343242 | 218.5311125 | 34.5451361 | Bump | > 15.7 |
| SST24 J143410.6+332641 | 218.5445557 | 33.4447975 | Power-law | 14.1 |
| SST24 J143411.0+331733 | 218.5457833 | 33.2924194 | Power-law | 13.8 |
| SST24 J143424.4+334543 | 218.6019135 | 33.7619972 | Power-law | > 15.2 |
| SST24 J143447.7+330230 | 218.6988373 | 33.0417976 | Power-law | > 17.0 |
| SST24 J143458.9+333437 | 218.7454834 | 33.5770416 | Bump | 14.2 |
| SST24 J143502.9+342658 | 218.7622208 | 34.4496611 | Bump | 14.2 |
| SST24 J143503.2+340243 | 218.7635042 | 34.0454417 | Bump | 15.3 |
| SST24 J143504.1+354743 | 218.7672272 | 35.7955055 | Power-law | 16.2 |
| SST24 J143508.4+334739 | 218.7854614 | 33.7942467 | Power-law | 15.3 |
| SST24 J143509.7+340137 | 218.7904500 | 34.0269583 | Power-law | 14.6 |
| SST24 J143518.8+340427 | 218.8285065 | 34.0741196 | Bump | 13.9 |
| SST24 J143520.7+340602 | 218.8361969 | 34.1007767 | Bump | 13.8 |
| SST24 J143520.7+340418 | 218.8364868 | 34.0716324 | Power-law | 15.8 |

Table 5.1 (cont'd)

| ID | R.A. (J2000) | Dec. (J2000) | Bump/Power-law | |
|------------------------|--------------|--------------|----------------|--------|
| SST24 J143523.9+330706 | 218.8497772 | 33.1186829 | Power-law | 15.3 |
| SST24 J143539.3+334159 | 218.9140167 | 33.6998062 | Power-law | > 16.8 |
| SST24 J143545.1+342831 | 218.9378204 | 34.4752998 | Bump | > 16.0 |
| SST24 J143631.8+350210 | 219.1326141 | 35.0360146 | Bump | 15.0 |
| SST24 J143632.7+350515 | 219.1362610 | 35.0877495 | Power-law | 14.3 |
| SST24 J143634.3+334854 | 219.1430206 | 33.8151054 | Power-law | 14.9 |
| SST24 J143641.0+350207 | 219.1708542 | 35.0353083 | Bump | 14.0 |
| SST24 J143641.6+342752 | 219.1735382 | 34.4644394 | Power-law | 14.9 |
| SST24 J143644.2+350627 | 219.1842804 | 35.1075211 | Power-law | 15.6 |
| SST24 J143701.9+344630 | 219.2582875 | 34.7751167 | Bump | > 15.6 |
| SST24 J143725.1+341502 | 219.3548889 | 34.2506104 | Power-law | > 16.2 |
| SST24 J143740.1+341102 | 219.4176636 | 34.1841354 | Power-law | 14.5 |
| SST24 J143742.5+341424 | 219.4276276 | 34.2403145 | Power-law | 15.0 |
| SST24 J143808.3+341016 | 219.5347443 | 34.1708908 | Power-law | 15.5 |
| SST24 J143816.6+333700 | 219.5695038 | 33.6167984 | Bump | 14.5 |

5.2.1.2 Optical Photometry

The NOAO Deep Wide Field Survey (NDWFS; Jannuzi & Dey, 1999) is a ground-based optical and near-IR imaging survey of two 9.3 deg^2 fields, one in Boötes and one in Cetus. In this paper, we utilize the optical imaging of the Boötes field, conducted using the NOAO 4m telescope on Kitt Peak. The survey reaches 5σ point-source depths in B_W , R , and I of 27.1, 26.1, and 25.4 (Vega mag), respectively. The NDWFS astrometry is tied to the reference frame defined by stars from the United States Naval Observatory A-2 catalog. NDWFS data products are publicly available

via the NOAO science archive ¹.

Photometry for each DOG was measured in 4'' diameter apertures, centered on the 3.6 μ m centroid position measured from the *Spitzer* Deep Wide-field Survey (SD-WFS; Ashby et al., 2009) imaging data (Ashby et al., 2009). Foreground and background objects were removed using SExtractor, and the sky level was determined using an annulus with an inner diameter of 6'' and a width of 5''. The background level and photometric uncertainty were computed by measuring the sigma-clipped mean and RMS of fluxes measured in roughly fifty 5'' diameter apertures within 1' of the target. Aperture corrections were derived using bright, non-saturated stars for each of the 27 sub-fields that comprise the NDWFS.

5.2.1.3 Near-Infrared Photometry

The NOAO Extremely Wide Field InfraRed iMager (NEWFIRM) has conducted a survey at near-IR wavelengths of the full 9.3 deg² Boötes field using the NOAO 4m telescope on Kitt Peak during the spring semesters of 2008 and 2009. The nominal 5σ limits of the survey within a 3'' diameter aperture in J , H , and Ks are 22.05, 21.3, and 19.8 (Vega mag), respectively. All of the survey data are publicly available (Gonzalez et al., in prep.).

Photometry was computed in the same manner as with the NDWFS images (see section 5.2.1.2). Aperture corrections were computed using bright, non-saturated stars for each of the 52 sub-fields that comprise the NEWFIRM survey of Boötes.

Photometry in the optical and near-IR is presented in Table 5.2.

¹<http://archive.noao.edu/nsa>

Table 5.2. NDWFS and NEWFIRM Photometry of DOGs^a

| ID | F_{BW} | σ_{BW} | F_R | σ_R | F_I | σ_I | F_J | σ_J | F_H | σ_H | F_{K_s} | σ_{K_s} |
|------------------------|----------|---------------|-------|------------|-------|------------|-------|------------|-------|------------|-----------|----------------|
| SST24 J142538.2+351855 | -0.05 | 0.04 | 0.05 | 0.10 | -0.01 | 0.11 | 1.4 | 0.8 | 2.3 | 1.3 | 9.2 | 2.5 |
| SST24 J142541.3+342420 | 0.19 | 0.06 | 0.37 | 0.15 | 0.46 | 0.09 | 0.9 | 0.8 | 1.7 | 1.4 | 2.1 | 2.5 |
| SST24 J142554.9+341820 | 0.19 | 0.04 | 0.30 | 0.13 | 0.54 | 0.12 | 1.2 | 0.8 | 2.2 | 1.3 | 3.8 | 3.0 |
| SST24 J142607.8+330425 | 0.12 | 0.05 | 0.38 | 0.05 | 0.73 | 0.12 | 3.9 | 0.7 | 10.7 | 1.6 | 14.8 | 2.8 |
| SST24 J142622.0+345249 | 0.44 | 0.05 | 0.52 | 0.12 | 0.63 | 0.16 | 0.8 | 1.0 | -4.3 | 3.2 | 5.2 | 2.6 |
| SST24 J142626.4+344731 | 0.04 | 0.05 | 0.00 | 0.13 | -0.15 | 0.21 | -0.5 | 0.9 | 2.3 | 1.3 | 7.0 | 2.8 |
| SST24 J142637.3+333025 | 0.10 | 0.05 | 0.14 | 0.18 | 0.28 | 0.11 | -0.9 | 0.6 | 2.0 | 1.5 | 2.1 | 4.3 |
| SST24 J142644.3+333051 | 0.08 | 0.06 | 0.52 | 0.19 | 0.91 | 0.10 | 3.2 | 0.8 | 4.2 | 2.1 | 21.8 | 5.4 |
| SST24 J142645.7+351901 | 0.04 | 0.03 | 0.07 | 0.07 | 0.30 | 0.13 | 2.2 | 0.7 | 5.0 | 1.1 | 5.3 | 1.5 |
| SST24 J142648.9+332927 | 0.34 | 0.06 | 0.52 | 0.21 | 0.83 | 0.11 | 2.2 | 0.6 | 4.1 | 1.8 | 3.2 | 5.0 |
| SST24 J142652.5+345506 | 0.09 | 0.04 | 0.24 | 0.11 | 0.30 | 0.18 | 1.0 | 0.7 | 4.5 | 1.6 | 2.3 | 1.6 |
| SST24 J142653.2+330221 | 0.10 | 0.04 | 0.18 | 0.08 | 0.42 | 0.16 | 0.8 | 0.8 | 5.3 | 1.4 | 1.7 | 2.9 |
| SST24 J142724.9+350824 | 0.09 | 0.04 | 0.15 | 0.13 | 0.52 | 0.23 | 3.7 | 1.1 | 8.7 | 3.0 | 4.3 | 2.5 |
| SST24 J142748.4+344851 | 1.66 | 0.06 | 1.26 | 0.13 | 0.80 | 0.27 | 2.7 | 0.8 | 5.7 | 1.3 | 5.9 | 2.7 |
| SST24 J142759.8+351243 | 0.34 | 0.04 | 0.40 | 0.21 | 0.47 | 0.32 | 2.9 | 0.6 | 5.9 | 1.0 | 6.5 | 1.4 |
| SST24 J142800.6+350455 | 0.40 | 0.05 | 0.51 | 0.14 | 0.70 | 0.26 | 4.7 | 0.8 | 12.6 | 1.1 | 12.4 | 1.7 |
| SST24 J142804.1+332135 | 0.00 | 0.05 | -0.01 | 0.09 | -0.14 | 0.14 | -1.1 | 0.6 | 2.6 | 2.0 | 1.5 | 4.7 |
| SST24 J142810.5+352509 | 0.14 | 0.03 | 0.32 | 0.11 | 0.73 | 0.09 | 3.3 | 1.0 | 6.6 | 1.4 | 9.9 | 2.6 |
| SST24 J142814.2+352245 | 0.20 | 0.03 | 0.50 | 0.11 | 0.87 | 0.10 | 3.3 | 0.9 | 6.3 | 1.5 | 9.0 | 2.2 |
| SST24 J142815.4+324720 | 0.33 | 0.04 | 0.51 | 0.07 | 0.85 | 0.14 | 2.0 | 1.5 | 4.1 | 2.0 | 8.5 | 3.0 |
| SST24 J142827.9+334550 | 0.20 | 0.04 | 0.22 | 0.09 | 0.37 | 0.14 | 2.4 | 1.2 | 10.2 | 1.6 | 18.7 | 2.7 |
| SST24 J142832.4+340849 | 0.29 | 0.02 | 0.68 | 0.15 | 1.17 | 0.14 | 4.3 | 1.1 | 5.7 | 1.3 | 8.5 | 2.3 |
| SST24 J142842.9+342409 | 1.12 | 0.06 | 1.23 | 0.17 | 2.66 | 0.15 | 13.3 | 1.6 | 16.4 | 1.5 | 24.4 | 2.9 |
| SST24 J142846.6+352701 | 0.10 | 0.05 | 0.18 | 0.12 | 0.31 | 0.15 | 3.3 | 1.6 | 7.1 | 1.4 | 10.9 | 1.7 |
| SST24 J142901.5+353016 | 0.39 | 0.04 | 0.24 | 0.12 | 0.70 | 0.13 | 2.8 | 1.5 | 3.4 | 1.5 | 7.0 | 1.6 |
| SST24 J142920.1+333023 | 0.22 | 0.06 | 0.53 | 0.09 | 0.68 | 0.10 | 3.3 | 0.7 | 3.3 | 1.4 | 8.1 | 2.8 |
| SST24 J142924.8+353320 | 0.08 | 0.04 | 0.09 | 0.10 | 0.15 | 0.08 | -0.2 | 1.8 | 0.4 | 2.5 | -0.2 | 2.1 |
| SST24 J142928.5+350841 | -0.01 | 0.07 | 0.14 | 0.14 | -0.02 | 0.29 | 2.3 | 0.8 | 2.9 | 2.3 | 3.5 | 2.1 |
| SST24 J142931.3+321828 | -0.13 | 0.07 | -0.09 | 0.12 | 0.39 | 0.24 | 0.0 | 0.0 | 0.0 | 0.0 | 0.0 | 0.0 |
| SST24 J142934.2+322213 | 0.61 | 0.04 | 0.39 | 0.06 | 0.57 | 0.12 | 0.9 | 0.8 | 6.5 | 1.9 | 11.2 | 3.9 |
| SST24 J142941.0+340915 | 0.05 | 0.04 | -0.07 | 0.16 | 0.29 | 0.11 | 2.1 | 1.2 | 3.7 | 1.6 | 11.2 | 2.6 |
| SST24 J142951.1+342042 | 0.24 | 0.04 | 0.26 | 0.16 | 0.82 | 0.11 | 1.6 | 1.0 | 4.8 | 1.1 | 9.5 | 2.6 |
| SST24 J142958.3+322615 | 0.20 | 0.04 | 0.27 | 0.09 | 0.31 | 0.13 | 1.3 | 0.9 | 0.1 | 1.5 | 10.2 | 3.4 |
| SST24 J143001.9+334538 | 0.28 | 0.06 | 0.52 | 0.12 | 0.28 | 0.17 | 1.0 | 1.1 | 1.9 | 1.3 | 3.9 | 3.0 |
| SST24 J143020.4+330344 | 0.06 | 0.05 | 0.17 | 0.09 | 0.57 | 0.15 | 3.7 | 0.5 | 9.8 | 1.4 | 7.9 | 2.5 |
| SST24 J143022.5+330029 | 0.01 | 0.05 | 0.16 | 0.09 | 0.05 | 0.11 | 1.2 | 0.8 | 6.5 | 1.8 | 8.1 | 3.2 |
| SST24 J143025.7+342957 | 0.46 | 0.04 | 0.70 | 0.12 | 1.15 | 0.13 | -0.9 | 2.0 | 3.9 | 1.5 | 6.0 | 3.0 |
| SST24 J143028.5+343221 | 0.35 | 0.06 | 0.47 | 0.10 | 0.66 | 0.14 | 3.6 | 1.1 | 6.4 | 1.5 | 7.9 | 2.5 |
| SST24 J143102.2+325152 | -0.04 | 0.04 | 0.16 | 0.12 | 0.69 | 0.17 | -2.0 | 1.1 | 0.7 | 2.2 | -3.2 | 3.0 |
| SST24 J143109.7+342802 | 0.02 | 0.05 | 0.24 | 0.09 | 0.23 | 0.17 | 2.5 | 0.9 | 3.0 | 1.3 | 15.4 | 5.5 |
| SST24 J143135.2+325456 | 0.41 | 0.04 | 0.80 | 0.10 | 1.55 | 0.21 | 6.3 | 1.4 | 9.1 | 3.3 | 23.4 | 5.0 |
| SST24 J143137.1+334501 | 0.17 | 0.06 | 0.28 | 0.12 | 0.80 | 0.15 | 1.5 | 1.2 | 4.7 | 1.9 | 8.2 | 3.3 |
| SST24 J143152.3+350030 | 0.14 | 0.03 | 0.30 | 0.09 | 0.66 | 0.10 | 4.8 | 0.8 | 10.0 | 1.2 | 14.3 | 2.9 |
| SST24 J143201.8+340408 | 0.43 | 0.05 | 0.43 | 0.18 | 1.26 | 0.17 | 4.8 | 1.0 | 12.6 | 1.6 | 17.5 | 2.5 |
| SST24 J143216.8+335231 | 0.11 | 0.05 | 0.23 | 0.12 | 0.39 | 0.12 | 3.4 | 0.8 | 5.6 | 1.5 | 11.9 | 2.6 |

Table 5.2 (cont'd)

| ID | F_{BW} | σ_{BW} | F_R | σ_R | F_I | σ_I | F_J | σ_J | F_H | σ_H | F_{Ks} | σ_{Ks} |
|------------------------|----------|---------------|-------|------------|-------|------------|-------|------------|-------|------------|----------|---------------|
| SST24 J143225.3+334716 | 0.07 | 0.04 | 0.13 | 0.12 | 0.14 | 0.13 | -0.1 | 1.1 | 3.0 | 1.6 | 5.3 | 3.0 |
| SST24 J143242.5+342232 | 0.05 | 0.04 | 0.20 | 0.12 | 0.30 | 0.18 | 3.4 | 1.1 | 3.9 | 1.7 | 12.4 | 2.9 |
| SST24 J143251.8+333536 | 0.06 | 0.05 | 0.13 | 0.13 | 0.34 | 0.14 | 3.3 | 0.6 | 4.2 | 1.4 | 10.9 | 2.1 |
| SST24 J143312.7+342011 | 0.53 | 0.04 | 0.57 | 0.13 | 0.85 | 0.12 | 2.9 | 1.0 | 4.7 | 1.5 | 10.6 | 2.7 |
| SST24 J143315.1+335628 | 0.42 | 0.07 | 0.73 | 0.08 | 0.86 | 0.12 | 3.2 | 0.8 | 7.2 | 1.4 | 12.6 | 2.5 |
| SST24 J143318.8+332203 | 0.28 | 0.05 | 0.27 | 0.06 | 0.15 | 0.10 | 0.6 | 0.7 | 5.0 | 1.5 | -1.4 | 2.3 |
| SST24 J143321.8+342502 | 0.18 | 0.07 | 0.50 | 0.09 | 0.91 | 0.11 | 5.0 | 0.8 | 9.1 | 1.4 | 14.4 | 2.6 |
| SST24 J143324.3+334239 | 0.24 | 0.06 | 0.44 | 0.12 | 1.04 | 0.10 | 4.5 | 1.2 | 7.3 | 1.4 | 13.8 | 2.5 |
| SST24 J143325.8+333736 | 0.20 | 0.06 | 0.55 | 0.10 | 0.92 | 0.13 | 7.8 | 0.7 | 11.2 | 1.4 | 20.7 | 2.0 |
| SST24 J143330.0+342234 | 0.43 | 0.05 | 0.66 | 0.12 | 0.59 | 0.18 | 0.8 | 1.0 | 1.7 | 1.4 | 3.5 | 3.0 |
| SST24 J143331.9+352027 | 0.18 | 0.03 | 0.47 | 0.06 | 0.78 | 0.10 | 3.0 | 1.5 | 5.1 | 1.6 | 8.0 | 3.9 |
| SST24 J143332.5+332230 | 0.09 | 0.05 | 0.14 | 0.07 | 0.17 | 0.13 | 1.0 | 0.8 | -2.3 | 2.0 | -1.0 | 3.4 |
| SST24 J143335.9+334716 | 0.36 | 0.06 | 0.39 | 0.14 | 0.49 | 0.12 | 1.5 | 1.1 | 1.3 | 2.7 | 14.5 | 3.9 |
| SST24 J143349.5+334601 | 0.12 | 0.06 | 0.26 | 0.14 | 0.50 | 0.15 | 4.5 | 1.1 | 9.2 | 1.5 | 12.0 | 3.2 |
| SST24 J143353.7+343155 | 0.33 | 0.04 | 0.69 | 0.13 | 1.10 | 0.17 | 8.6 | 0.8 | 9.0 | 1.5 | 14.3 | 2.5 |
| SST24 J143358.0+332607 | 0.05 | 0.04 | 0.03 | 0.06 | 0.04 | 0.09 | 1.1 | 0.7 | 5.0 | 1.6 | 4.8 | 2.3 |
| SST24 J143407.4+343242 | 0.07 | 0.04 | 0.12 | 0.07 | 0.28 | 0.15 | 0.1 | 1.0 | -0.7 | 1.8 | -1.6 | 2.8 |
| SST24 J143410.6+332641 | 0.72 | 0.06 | 0.58 | 0.06 | 0.93 | 0.10 | 4.1 | 0.8 | 10.5 | 1.4 | 23.2 | 2.6 |
| SST24 J143411.0+331733 | 0.84 | 0.04 | 1.08 | 0.05 | 1.20 | 0.13 | 2.5 | 1.0 | 6.2 | 1.5 | 3.7 | 2.8 |
| SST24 J143424.4+334543 | 0.09 | 0.06 | 0.04 | 0.14 | 0.31 | 0.31 | 2.0 | 1.1 | 3.4 | 1.5 | 5.8 | 2.5 |
| SST24 J143447.7+330230 | 0.00 | 0.05 | 0.03 | 0.06 | -0.01 | 0.11 | 1.2 | 0.7 | 1.5 | 1.7 | 3.8 | 3.1 |
| SST24 J143458.9+333437 | 0.20 | 0.04 | 0.49 | 0.12 | 0.66 | 0.11 | 4.2 | 0.8 | 5.5 | 1.4 | 13.2 | 2.3 |
| SST24 J143502.9+342658 | 0.28 | 0.04 | 0.43 | 0.13 | 0.46 | 0.15 | 2.5 | 1.1 | 2.9 | 1.6 | 11.6 | 2.4 |
| SST24 J143503.2+340243 | 0.03 | 0.06 | 0.23 | 0.11 | 0.38 | 0.12 | 2.6 | 1.1 | 6.5 | 1.6 | 11.3 | 2.8 |
| SST24 J143504.1+354743 | 0.01 | 0.04 | 0.17 | 0.07 | 0.02 | 0.10 | 0.0 | 0.0 | 0.0 | 0.0 | 0.0 | 0.0 |
| SST24 J143508.4+334739 | 0.45 | 0.05 | 0.82 | 0.11 | 0.83 | 0.11 | 3.2 | 0.9 | 5.1 | 1.6 | 11.0 | 4.1 |
| SST24 J143509.7+340137 | 0.07 | 0.06 | 0.28 | 0.11 | 0.55 | 0.15 | 1.2 | 0.8 | 2.5 | 1.4 | 8.4 | 2.9 |
| SST24 J143518.8+340427 | 0.13 | 0.05 | 0.45 | 0.11 | 0.81 | 0.19 | 0.9 | 1.3 | 6.0 | 1.5 | 7.5 | 2.0 |
| SST24 J143520.7+340602 | 0.40 | 0.04 | 0.59 | 0.09 | 1.03 | 0.13 | 2.8 | 1.2 | 8.3 | 1.8 | 11.3 | 2.1 |
| SST24 J143520.7+340418 | 0.37 | 0.06 | 0.30 | 0.13 | 0.67 | 0.22 | 0.0 | 1.0 | 2.0 | 1.5 | 5.7 | 2.1 |
| SST24 J143523.9+330706 | 0.03 | 0.03 | 0.33 | 0.08 | 0.53 | 0.14 | 2.1 | 0.9 | 4.9 | 1.7 | 3.7 | 3.5 |
| SST24 J143539.3+334159 | 0.10 | 0.07 | 0.16 | 0.10 | 0.39 | 0.16 | 1.0 | 1.1 | 0.6 | 2.4 | 3.7 | 3.8 |
| SST24 J143545.1+342831 | 0.22 | 0.06 | 0.13 | 0.16 | 0.40 | 0.12 | 2.6 | 1.2 | 6.1 | 2.0 | 7.1 | 2.3 |
| SST24 J143631.8+350210 | 0.00 | 0.05 | 0.13 | 0.06 | -0.16 | 0.14 | 1.3 | 0.8 | 2.8 | 1.2 | 7.8 | 4.3 |
| SST24 J143632.7+350515 | 1.31 | 0.03 | 1.39 | 0.08 | 1.71 | 0.15 | 6.9 | 0.9 | 10.5 | 1.5 | 16.7 | 3.9 |
| SST24 J143634.3+334854 | 1.02 | 0.05 | 1.47 | 0.06 | 2.27 | 0.14 | 10.9 | 1.0 | 23.4 | 2.4 | 49.0 | 2.9 |
| SST24 J143641.0+350207 | 0.29 | 0.04 | 0.36 | 0.05 | 1.56 | 0.18 | 2.0 | 0.9 | 7.0 | 1.4 | 15.6 | 4.5 |
| SST24 J143641.6+342752 | 0.30 | 0.03 | 0.23 | 0.12 | 0.44 | 0.11 | 1.8 | 1.4 | 5.3 | 1.6 | 8.5 | 2.5 |
| SST24 J143644.2+350627 | 0.39 | 0.04 | 0.57 | 0.06 | 0.79 | 0.16 | 3.4 | 1.0 | 6.4 | 1.5 | 10.5 | 2.5 |
| SST24 J143701.9+344630 | -0.00 | 0.06 | 0.09 | 0.06 | -0.12 | 0.19 | -0.1 | 0.9 | -2.5 | 1.5 | 6.4 | 2.7 |
| SST24 J143725.1+341502 | 0.10 | 0.03 | 0.08 | 0.10 | 0.06 | 0.10 | 1.9 | 1.0 | 6.3 | 1.7 | 12.9 | 4.5 |
| SST24 J143740.1+341102 | 0.43 | 0.04 | 0.62 | 0.12 | 0.50 | 0.12 | 5.1 | 1.0 | 13.4 | 1.7 | 21.6 | 3.9 |
| SST24 J143742.5+341424 | 0.31 | 0.05 | 0.33 | 0.12 | 0.61 | 0.14 | 3.9 | 1.0 | 8.0 | 1.8 | 17.7 | 3.8 |
| SST24 J143808.3+341016 | 0.30 | 0.04 | 0.44 | 0.12 | 0.72 | 0.17 | 2.6 | 0.9 | 7.3 | 1.8 | 13.0 | 2.6 |
| SST24 J143816.6+333700 | 0.18 | 0.04 | 0.36 | 0.10 | 0.71 | 0.14 | 1.6 | 1.5 | 4.2 | 1.1 | 7.0 | 2.5 |

Table 5.2 (cont'd)

| ID | F_{BW} | σ_{BW} | F_R | σ_R | F_I | σ_I | F_J | σ_J | F_H | σ_H | F_{Ks} | σ_{Ks} |
|----|----------|---------------|-------|------------|-------|------------|-------|------------|-------|------------|----------|---------------|
|----|----------|---------------|-------|------------|-------|------------|-------|------------|-------|------------|----------|---------------|

^aAll flux densities given in units of μJy .

5.2.1.4 Mid-Infrared Photometry

The SDWFS is a four-epoch survey of roughly 8.5 deg^2 of the Boötes field of the NDWFS. The first epoch of the survey took place in 2004 January as part of the IRAC Shallow Survey (Eisenhardt et al., 2004). Subsequent visits to the field as part of the SDWFS program reimaged the same area three times to the same depth each time. The final co-added images have 5σ depths (aperture-corrected from a $4''$ diameter aperture) of 19.77, 18.83, 16.50, and 15.85 (Vega mag) at $3.6\mu\text{m}$, $4.5\mu\text{m}$, $5.8\mu\text{m}$, and $8.0\mu\text{m}$, respectively. All SDWFS data are publicly available.

Part of the SDWFS Data Release 1.1 includes band-matched catalogs created with Source Extractor (SExtractor, Bertin & Arnouts, 1996). Astrometry in these catalogs is tied to 2MASS positions within $0''.2$. We identify DOGs in these catalogs using a $3''$ search radius, and use the values in these catalogs for our flux density measurements of DOGs. SExtractor underestimates the true magnitude uncertainties because it does not account for systematic errors associated with the IRAC data. In place of the SExtractor-derived values, we determine our own estimates of the uncertainty on each flux density measurement using $4''$ diameter apertures randomly placed within $1'$ of each object of interest.

Photometry in the mid-IR is presented in Table 5.3.

Table 5.3. SDWFS and MIPS24 Photometry of DOGs^a

| ID | $F_{3.6\mu\text{m}}$ | $\sigma_{3.6\mu\text{m}}$ | $F_{4.5\mu\text{m}}$ | $\sigma_{4.5\mu\text{m}}$ | $F_{5.8\mu\text{m}}$ | $\sigma_{5.8\mu\text{m}}$ | $F_{8.0\mu\text{m}}$ | $\sigma_{8.0\mu\text{m}}$ | $F_{24\mu\text{m}}$ | $\sigma_{24\mu\text{m}}$ |
|------------------------|----------------------|---------------------------|----------------------|---------------------------|----------------------|---------------------------|----------------------|---------------------------|---------------------|--------------------------|
| SST24 J142538.2+351855 | 19.4 | 2.4 | 26.7 | 3.4 | 30.9 | 10.2 | 44.0 | 8.0 | 850 | 85 |
| SST24 J142541.3+342420 | 15.0 | 2.3 | 30.5 | 3.7 | 80.9 | 14.6 | 164.5 | 13.0 | 670 | 67 |
| SST24 J142554.9+341820 | 9.4 | 1.9 | 13.7 | 2.6 | 11.2 | 7.9 | 51.2 | 9.2 | 1140 | 114 |
| SST24 J142607.8+330425 | 32.0 | 3.3 | 44.3 | 4.5 | 75.8 | 13.8 | 131.1 | 12.3 | 540 | 54 |
| SST24 J142622.0+345249 | 4.3 | 1.4 | 4.1 | 1.7 | 0.0 | 5.6 | 37.0 | 7.7 | 1290 | 129 |
| SST24 J142626.4+344731 | 18.3 | 2.7 | 25.2 | 3.4 | 39.8 | 12.1 | 39.3 | 8.3 | 1170 | 117 |
| SST24 J142637.3+333025 | 4.4 | 1.4 | 11.9 | 2.5 | 34.8 | 11.3 | 89.1 | 11.1 | 640 | 64 |
| SST24 J142644.3+333051 | 62.3 | 4.6 | 93.1 | 6.3 | 164.4 | 19.8 | 384.9 | 18.7 | 1140 | 114 |
| SST24 J142645.7+351901 | 32.5 | 3.4 | 52.7 | 4.8 | 84.3 | 14.7 | 156.5 | 12.5 | 1140 | 114 |
| SST24 J142648.9+332927 | 57.4 | 4.5 | 180.4 | 8.8 | 497.8 | 33.1 | 952.7 | 28.6 | 2330 | 233 |
| SST24 J142652.5+345506 | 22.0 | 0.7 | 30.0 | 1.1 | 28.0 | 5.9 | 22.9 | 6.8 | 598 | 50 |
| SST24 J142653.2+330221 | 19.2 | 2.6 | 29.6 | 3.7 | 34.5 | 11.2 | 64.5 | 9.2 | 880 | 88 |
| SST24 J142724.9+350824 | 43.6 | 3.6 | 57.4 | 4.6 | 72.3 | 12.9 | 65.1 | 9.1 | 510 | 51 |
| SST24 J142748.4+344851 | 15.4 | 2.4 | 50.5 | 4.8 | 162.6 | 20.2 | 473.0 | 20.8 | 2210 | 221 |
| SST24 J142759.8+351243 | 48.5 | 4.7 | 78.6 | 6.9 | 181.1 | 23.6 | 333.9 | 21.0 | 1540 | 154 |
| SST24 J142800.6+350455 | 57.2 | 4.4 | 85.9 | 6.1 | 163.8 | 19.4 | 300.2 | 16.5 | 920 | 92 |
| SST24 J142804.1+332135 | 5.6 | 1.5 | 8.5 | 2.1 | 0.0 | 7.0 | 9.0 | 7.1 | 850 | 85 |
| SST24 J142810.5+352509 | 27.3 | 3.1 | 39.7 | 4.1 | 66.4 | 12.9 | 125.2 | 11.8 | 650 | 65 |
| SST24 J142814.2+352245 | 30.1 | 3.2 | 57.4 | 4.9 | 107.1 | 16.3 | 182.1 | 13.4 | 570 | 57 |
| SST24 J142815.4+324720 | 19.6 | 2.5 | 24.5 | 3.2 | 47.0 | 10.8 | 86.3 | 11.5 | 1400 | 140 |
| SST24 J142827.9+334550 | 51.0 | 4.2 | 79.8 | 5.9 | 153.0 | 19.1 | 292.0 | 17.1 | 770 | 77 |
| SST24 J142832.4+340849 | 35.9 | 3.5 | 43.7 | 4.3 | 49.8 | 11.6 | 34.5 | 7.8 | 520 | 52 |
| SST24 J142842.9+342409 | 126.2 | 5.2 | 200.7 | 7.8 | 393.4 | 26.6 | 695.7 | 23.8 | 3110 | 311 |
| SST24 J142846.6+352701 | 42.1 | 3.8 | 68.6 | 5.4 | 120.0 | 17.1 | 169.9 | 13.2 | 750 | 75 |
| SST24 J142901.5+353016 | 25.3 | 3.0 | 50.5 | 4.7 | 94.1 | 15.4 | 194.9 | 13.9 | 440 | 44 |
| SST24 J142920.1+333023 | 19.1 | 2.7 | 24.8 | 3.5 | 36.6 | 11.6 | 16.2 | 8.7 | 510 | 51 |
| SST24 J142924.8+353320 | 6.1 | 1.6 | 10.7 | 2.3 | 21.5 | 8.7 | 71.1 | 10.6 | 1040 | 104 |
| SST24 J142928.5+350841 | 27.2 | 2.9 | 32.6 | 3.6 | 29.6 | 10.7 | 30.0 | 8.2 | 410 | 41 |
| SST24 J142931.3+321828 | 9.8 | 1.9 | 12.7 | 2.5 | 23.0 | 10.1 | 65.3 | 8.9 | 1060 | 106 |
| SST24 J142934.2+322213 | 18.3 | 2.5 | 29.6 | 3.8 | 75.5 | 14.8 | 152.5 | 14.2 | 1160 | 116 |
| SST24 J142941.0+340915 | 31.4 | 3.2 | 42.1 | 4.2 | 47.9 | 11.5 | 41.5 | 8.4 | 590 | 59 |
| SST24 J142951.1+342042 | 42.6 | 3.4 | 54.9 | 4.3 | 60.4 | 12.3 | 42.8 | 7.5 | 600 | 60 |
| SST24 J142958.3+322615 | 28.9 | 3.2 | 48.0 | 4.6 | 111.2 | 16.5 | 219.0 | 14.4 | 1180 | 118 |
| SST24 J143001.9+334538 | 13.1 | 2.5 | 26.0 | 3.6 | 113.4 | 18.7 | 459.8 | 21.7 | 3840 | 384 |
| SST24 J143020.4+330344 | 34.9 | 3.6 | 44.1 | 4.5 | 54.2 | 12.6 | 47.1 | 9.1 | 540 | 54 |
| SST24 J143022.5+330029 | 39.3 | 3.7 | 48.0 | 4.5 | 89.1 | 14.8 | 196.8 | 13.9 | 800 | 80 |
| SST24 J143025.7+342957 | 21.1 | 2.8 | 53.5 | 4.9 | 164.0 | 20.0 | 527.8 | 21.8 | 2470 | 247 |
| SST24 J143028.5+343221 | 28.0 | 3.2 | 47.6 | 4.7 | 120.9 | 17.0 | 288.4 | 16.4 | 1270 | 127 |
| SST24 J143102.2+325152 | 3.9 | 1.4 | 5.9 | 1.8 | 0.0 | 7.7 | 53.2 | 8.3 | 1190 | 119 |
| SST24 J143109.7+342802 | 7.5 | 1.7 | 10.1 | 2.4 | 27.4 | 9.1 | 62.6 | 9.7 | 1110 | 111 |
| SST24 J143135.2+325456 | 70.9 | 4.9 | 137.4 | 7.6 | 268.4 | 24.6 | 494.9 | 21.2 | 1510 | 151 |
| SST24 J143137.1+334501 | 29.4 | 3.0 | 40.4 | 3.9 | 43.2 | 11.1 | 35.6 | 8.2 | 570 | 57 |
| SST24 J143152.3+350030 | 49.0 | 4.0 | 63.1 | 5.1 | 63.3 | 12.7 | 51.7 | 8.9 | 520 | 52 |
| SST24 J143201.8+340408 | 44.8 | 3.9 | 72.3 | 5.5 | 121.2 | 16.8 | 230.3 | 14.7 | 670 | 67 |
| SST24 J143216.8+335231 | 32.4 | 0.7 | 41.4 | 1.1 | 46.6 | 5.7 | 42.1 | 6.5 | 502 | 44 |

Table 5.3 (cont'd)

| ID | $F_{3.6\mu\text{m}}$ | $\sigma_{3.6\mu\text{m}}$ | $F_{4.5\mu\text{m}}$ | $\sigma_{4.5\mu\text{m}}$ | $F_{5.8\mu\text{m}}$ | $\sigma_{5.8\mu\text{m}}$ | $F_{8.0\mu\text{m}}$ | $\sigma_{8.0\mu\text{m}}$ | $F_{24\mu\text{m}}$ | $\sigma_{24\mu\text{m}}$ |
|------------------------|----------------------|---------------------------|----------------------|---------------------------|----------------------|---------------------------|----------------------|---------------------------|---------------------|--------------------------|
| SST24 J143225.3+334716 | 39.1 | 3.7 | 76.2 | 5.8 | 167.9 | 19.7 | 350.0 | 18.0 | 1280 | 128 |
| SST24 J143242.5+342232 | 36.6 | 3.6 | 59.3 | 5.2 | 127.8 | 18.0 | 225.0 | 15.1 | 910 | 91 |
| SST24 J143251.8+333536 | 41.5 | 3.7 | 55.2 | 4.8 | 69.3 | 13.1 | 110.4 | 10.9 | 820 | 82 |
| SST24 J143312.7+342011 | 27.9 | 3.2 | 35.1 | 4.0 | 65.5 | 13.4 | 106.3 | 11.5 | 1760 | 176 |
| SST24 J143315.1+335628 | 35.3 | 3.6 | 55.8 | 5.0 | 102.7 | 16.2 | 164.4 | 13.5 | 830 | 83 |
| SST24 J143318.8+332203 | 11.5 | 2.0 | 18.6 | 2.8 | 31.0 | 9.4 | 56.1 | 9.1 | 430 | 43 |
| SST24 J143321.8+342502 | 32.8 | 3.3 | 41.3 | 4.2 | 56.2 | 12.7 | 48.5 | 9.2 | 560 | 56 |
| SST24 J143324.3+334239 | 41.5 | 3.5 | 54.0 | 4.7 | 50.4 | 11.2 | 52.9 | 8.8 | 530 | 53 |
| SST24 J143325.8+333736 | 62.0 | 4.6 | 81.3 | 6.0 | 118.0 | 16.5 | 141.3 | 12.1 | 1870 | 187 |
| SST24 J143330.0+342234 | 7.0 | 1.7 | 12.3 | 2.6 | 17.7 | 8.2 | 64.7 | 9.8 | 1920 | 192 |
| SST24 J143331.9+352027 | 26.5 | 3.1 | 35.4 | 4.0 | 41.4 | 11.0 | 26.0 | 7.7 | 600 | 60 |
| SST24 J143332.5+332230 | 4.6 | 1.4 | 2.4 | 1.5 | 0.0 | 7.1 | 13.5 | 7.2 | 460 | 46 |
| SST24 J143335.9+334716 | 30.1 | 3.2 | 41.6 | 4.2 | 64.5 | 12.7 | 0.0 | 9.2 | 590 | 59 |
| SST24 J143349.5+334601 | 37.2 | 3.8 | 42.0 | 4.9 | 62.2 | 13.6 | 32.0 | 8.1 | 530 | 53 |
| SST24 J143353.7+343155 | 32.2 | 3.2 | 37.6 | 4.1 | 43.6 | 11.7 | 100.5 | 10.6 | 680 | 68 |
| SST24 J143358.0+332607 | 13.4 | 2.4 | 19.2 | 3.2 | 42.2 | 10.9 | 88.8 | 10.7 | 1070 | 107 |
| SST24 J143407.4+343242 | 0.0 | 1.2 | 0.0 | 1.5 | 0.0 | 6.4 | 0.0 | 7.6 | 620 | 62 |
| SST24 J143410.6+332641 | 50.9 | 4.2 | 80.7 | 5.9 | 148.9 | 18.9 | 271.3 | 15.7 | 630 | 63 |
| SST24 J143411.0+331733 | 20.4 | 2.6 | 26.3 | 3.4 | 49.7 | 16.9 | 76.9 | 15.0 | 860 | 51 |
| SST24 J143424.4+334543 | 14.8 | 2.3 | 23.5 | 3.3 | 73.0 | 14.2 | 156.4 | 13.9 | 860 | 86 |
| SST24 J143447.7+330230 | 21.2 | 2.7 | 32.3 | 3.8 | 42.9 | 11.9 | 87.8 | 10.7 | 1710 | 171 |
| SST24 J143458.9+333437 | 40.0 | 3.7 | 48.6 | 4.6 | 60.5 | 13.0 | 53.9 | 8.4 | 570 | 57 |
| SST24 J143502.9+342658 | 44.7 | 3.4 | 47.2 | 4.3 | 46.2 | 12.5 | 44.0 | 8.4 | 500 | 50 |
| SST24 J143503.2+340243 | 34.3 | 3.5 | 46.2 | 4.6 | 54.5 | 13.0 | 45.1 | 9.0 | 760 | 76 |
| SST24 J143504.1+354743 | 21.0 | 2.7 | 33.8 | 4.0 | 50.8 | 12.1 | 86.6 | 10.8 | 1260 | 126 |
| SST24 J143508.4+334739 | 14.4 | 2.4 | 16.6 | 2.9 | 34.9 | 10.4 | 175.3 | 14.0 | 2650 | 265 |
| SST24 J143509.7+340137 | 13.1 | 1.9 | 15.8 | 2.5 | 32.6 | 8.8 | 53.0 | 9.9 | 470 | 47 |
| SST24 J143518.8+340427 | 23.4 | 2.8 | 31.8 | 3.8 | 53.9 | 12.2 | 48.2 | 8.9 | 400 | 40 |
| SST24 J143520.7+340602 | 29.8 | 3.2 | 35.1 | 4.0 | 40.5 | 11.1 | 25.2 | 8.2 | 490 | 49 |
| SST24 J143520.7+340418 | 5.8 | 1.5 | 7.1 | 2.0 | 15.1 | 8.5 | 7.4 | 7.5 | 1530 | 153 |
| SST24 J143523.9+330706 | 17.7 | 2.6 | 34.1 | 4.1 | 93.5 | 16.0 | 250.3 | 16.4 | 1090 | 109 |
| SST24 J143539.3+334159 | 14.1 | 2.3 | 23.9 | 3.4 | 65.8 | 13.6 | 249.5 | 15.7 | 2670 | 267 |
| SST24 J143545.1+342831 | 16.4 | 2.5 | 18.1 | 3.0 | 27.0 | 9.4 | 95.0 | 10.4 | 1960 | 196 |
| SST24 J143631.8+350210 | 25.4 | 2.8 | 31.5 | 3.4 | 33.0 | 10.0 | 20.7 | 6.6 | 330 | 33 |
| SST24 J143632.7+350515 | 53.2 | 4.2 | 92.2 | 6.2 | 172.8 | 20.1 | 348.1 | 17.9 | 1690 | 169 |
| SST24 J143634.3+334854 | 91.9 | 5.6 | 170.1 | 8.4 | 350.5 | 27.9 | 680.3 | 24.2 | 3280 | 328 |
| SST24 J143641.0+350207 | 20.6 | 2.4 | 26.0 | 3.2 | 30.6 | 9.4 | 43.4 | 8.2 | 330 | 33 |
| SST24 J143641.6+342752 | 23.8 | 2.9 | 38.8 | 4.1 | 77.9 | 14.0 | 162.1 | 13.2 | 530 | 53 |
| SST24 J143644.2+350627 | 37.9 | 3.6 | 103.3 | 6.6 | 308.7 | 26.4 | 734.2 | 25.1 | 2340 | 234 |
| SST24 J143701.9+344630 | 18.0 | 0.8 | 17.9 | 1.3 | 13.2 | 8.8 | 37.0 | 7.7 | 508 | 60 |
| SST24 J143725.1+341502 | 52.9 | 4.3 | 87.9 | 6.1 | 167.5 | 19.6 | 283.4 | 16.3 | 1410 | 141 |
| SST24 J143740.1+341102 | 52.3 | 4.2 | 79.8 | 5.8 | 148.0 | 18.9 | 236.9 | 15.1 | 950 | 95 |
| SST24 J143742.5+341424 | 32.7 | 3.4 | 54.2 | 4.8 | 98.0 | 15.8 | 172.9 | 13.4 | 780 | 78 |
| SST24 J143808.3+341016 | 35.9 | 3.5 | 73.2 | 5.6 | 193.7 | 21.1 | 411.9 | 19.5 | 1710 | 171 |
| SST24 J143816.6+333700 | 24.1 | 0.7 | 29.4 | 1.1 | 31.2 | 6.1 | 19.8 | 6.4 | 530 | 36 |

Table 5.3 (cont'd)

| ID | $F_{3.6\mu\text{m}}$ | $\sigma_{3.6\mu\text{m}}$ | $F_{4.5\mu\text{m}}$ | $\sigma_{4.5\mu\text{m}}$ | $F_{5.8\mu\text{m}}$ | $\sigma_{5.8\mu\text{m}}$ | $F_{8.0\mu\text{m}}$ | $\sigma_{8.0\mu\text{m}}$ | $F_{24\mu\text{m}}$ | $\sigma_{24\mu\text{m}}$ |
|----|----------------------|---------------------------|----------------------|---------------------------|----------------------|---------------------------|----------------------|---------------------------|---------------------|--------------------------|
|----|----------------------|---------------------------|----------------------|---------------------------|----------------------|---------------------------|----------------------|---------------------------|---------------------|--------------------------|

^aAll flux densities given in units of μJy .

5.2.2 SMGs

5.2.2.1 Sample Selection

For the SCUBA-selected SMGs, we use the sample of 58 objects with spectroscopic redshifts at $z > 1.4$ from Chapman et al. (2005). These are sources with precise positional information derived from Very Large Array 1.4 GHz imaging and redshifts obtained with optical ground-based spectroscopy with the Keck I telescope. Their clustering properties indicate they inhabit very massive dark matter haloes ($M_{\text{DM}} \approx 10^{12} M_{\odot}$; Blain et al., 2004), comparable to the dark matter halo masses of DOGs (Brodwin et al., 2008).

5.2.2.2 SMG Photometry

The broad-band photometry of SMGs used in this paper has been collected from a variety of sources. B - and R -band photometry were obtained with several telescopes and were presented in Chapman et al. (2005). I -, J -, and K -band photometry also were obtained with several telescopes and were presented in Smail et al. (2004). These photometry values were derived with $4''$ diameter apertures and have been aperture-corrected. Mid-IR photometry of SMGs was obtained from Hainline et al. (2009), who compute aperture-corrected $4''$ diameter aperture photometry using SExtractor.

5.3 Stellar Population Synthesis Models

Stellar population synthesis (SPS) modeling offers a means of constraining the mass and star-formation history of a galaxy’s stellar population. This section contains a description of the technique adopted here to apply the SPS models to the high- z ULIRG photometry outlined in section 5.2. Additionally, details are provided regarding three initial mass functions (IMFs) and three SFHs that are used in this paper for testing theories for the formation of massive galaxies at high redshift. Results from this analysis are presented in section 5.4.

In all models, the simplifying assumption of a uniform dust screen (A_V ranging from 0 to 3) is adopted which obscures the intrinsic stellar light according to the reddening law for starbursts from Calzetti et al. (2000) for wavelengths between $0.12 - 2.2 \mu\text{m}$ and that of Draine (2003) for longer wavelengths. The quality of currently available data precludes the use of more complex models in which younger stars have different dust obscuration prescriptions than older stars (e.g., Charlot & Fall, 2000).

5.3.1 General Methodology

In principle, it is possible to perform SPS modeling of each individual galaxy in this sample and thereby constraint the mass (M_*), age, and visual extinction (A_V) of the stellar population. However, degeneracies between age and A_V , as well as the uncertainty introduced by the unknown IMF and SFH, lead to large uncertainties on the best fit quantities. Such large errors on each individual absolute measurement suggest that care must be taken when attempting to determine the aggregate properties of a population of such galaxies.

In this study, the goal is to measure the properties of three distinct populations of high redshift ULIRGs using a uniform, self-consistent analysis. This will allow the stellar masses of these objects to be measured in a relative sense and therefore

minimize many of the uncertainties discussed above. The first group comprises DOGs showing a local maximum at rest-frame $1.6\mu\text{m}$ (i.e., the bump DOGs), which typically have strong PAH emission and are thought to be powered by on-going star-formation (e.g., Desai et al., 2009). The second group consists of DOGs showing a mid-IR power-law (i.e., the power-law DOGs), which usually have weak PAH emission and are associated with obscured AGN. Bussmann et al. (2010, submitted) found a distinction in morphology between these two types of sources — bump DOGs are larger and have irregular morphologies more frequently than power-law DOGs — that is consistent with expectations of major mergers. The third grouping is composed of sub-mm galaxies (SMGs), which frequently exhibit bluer $R - [24]$ colors and more UV flux (possibly a reflection of less dust obscuration) than DOGs. An important aspect of this work is to test these conclusions based on morphology using the broadband photometry from the optical through the mid-IR.

The approach used here is to apply SPS models of varying A_V and age values to each galaxy on an individual basis. A probability density function for the stellar mass of each galaxy is then derived from those model fits satisfying $\chi^2 < 12$. Values above this level have a less than 10% chance of occurring randomly (when the number of degrees of freedom is 7, as is the case here). Each individual galaxy’s stellar mass probability density function contributes equally to the final stellar mass probability density function for that population of galaxies.

The use of SPS models to determine intrinsic properties of galaxies assumes that all of the observed flux is emitted by stars. In fact, many of the sources in this study have a significant contribution in the rest-frame near-IR from obscured AGN (this is especially true for the power-law DOGs). Some authors add this component (in the form of a variable slope power-law) to their SPS modelling efforts (e.g., Hainline et al., 2010). Alternatively, it is possible to minimize the AGN contribution by

considering only the first two IRAC channels (i.e., up to observed-frame $4.5\mu\text{m}$). This is the approach that is adopted in this study. For bump DOGs and SMGs, this should provide a reasonably reliable measurement of the stellar light from these objects. For power-law DOGs, there still exists a significant possibility that the observed-frame $4.5\mu\text{m}$ light is contaminated by AGN. For this reason, the stellar mass estimates of power-law DOGs should be regarded as upper limits on the true stellar mass.

Only solar metallicity models are tested in this study. This is a reasonable assumption, since high-redshift dusty galaxies have been found to have near-solar metallicities (Swinbank et al., 2004). Moreover, our broad-band SED data do not provide the ability to constrain metallicity. The adoption of a single metallicity in SPS modeling typically introduces uncertainties at the level of 10-20% (Conroy et al., 2009; Muzzin et al., 2009), which are insignificant compared to systematic uncertainties related to the IMF, SFH, and age of the stellar population.

5.3.2 Initial Mass Functions

One of the most critical adjustable parameters involved in SPS modeling is the IMF. Despite its importance, the detailed nature of the IMF in galaxies at high redshift is poorly constrained. The relevant parameter space is characterized here by three different forms of the IMF, all with a lower mass cutoff of $0.1 M_{\odot}$ and an upper mass cutoff of $100 M_{\odot}$.

The first form of the IMF used here is from Salpeter (1955), and can be characterized as a single power-law of the form $\phi(m) \propto m^{-2.35}$, where $\phi(m)dm$ is the number of stars born with masses between m and $m + dm$.

More recent observations of stars in the Milky Way disk have favored an IMF with a power-law form similar to that of Salpeter (1955) for $M > 1 M_{\odot}$, but a lognormal form below this mass limit (Chabrier IMF; Chabrier, 2003). The primary

effect of this modification is to reduce the relative number of low mass stars and hence decrease the mass-to-light ratio compared to the Salpeter IMF. The Chabrier IMF produces mass-to-light ratios very similar to the Kroupa (2001) IMF.

Finally, in very recent years circumstantial evidence has been building in support of a modified IMF at high redshift (e.g., the “bottom-light” IMF of van Dokkum, 2008; Davé, 2008). Functionally, this is accomplished by adjusting the characteristic mass, m_c , which governs both the cutoff mass at which the lognormal form dominates as well as the shape of the lognormal part of the IMF itself. In particular, van Dokkum (2008) use the color and luminosity evolution of cluster ellipticals to infer $m_c \sim 2 M_\odot$ at $z > 4$. In this study a characteristic mass of $m_c = 0.4 M_\odot$ has been adopted, as this value matches both the (very rough) estimates for SMGs at $z \sim 2$ as well as theoretical expectations based on a model in which the characteristic mass is a function of the CMB temperature: $m_c \propto T_{\text{CMB}}^{3.35}$. The effect of such a change in the characteristic mass is to produce a Salpeter-like slope at $M > 1 M_\odot$ and a turnover at $M \approx 1 M_\odot$. This reduces the number of low-mass stars relative to the high-mass ones, thereby lowering the mass-to-light ratio relative to the Chabrier IMF (for intermediate age stars or younger).

Since observational constraints on the IMF are not readily available, each IMF has been tested with each SFH (see section 5.3.3). In the case of the simple stellar population (ssp), this provides a measure of the uncertainty resulting from the unknown IMF. However, for the purposes of testing the self-consistency of more complicated SFHs of ULIRGs at high redshift, it is necessary to select certain IMFs for each model. The simulations of major mergers tested here (Narayanan et al., 2009) adopt a Salpeter IMF, so that is what is focused on here. Meanwhile, the IMF is a free parameter in the smooth accretion SFH (Davé et al., 2010). However, a Salpeter IMF is disfavored in these simulations because it overpredicts the sub-

mm fluxes of SMGs. A Chabrier IMF is therefore adopted in this paper, with an accompanying thorough discussion of the implications of a more “bottom-light” IMF.

5.3.3 SPS Star-formation Histories

Another critical adjustable parameter in SPS modeling is the star-formation history (SFH). The focus in this paper is placed on three distinct SFHs that broadly encompass a reasonable range of parameter space.

The first SFH adopted here is the simplest one possible: an infinitely short burst of star-formation at time $t = 0$ during which all the stars of the galaxy are formed, followed thereafter by passive evolution. This is called a simple stellar population (SSP), and is used commonly in SPS modeling in the literature. If the objects under study here have recently had star-formation shut off by some process (e.g., AGN feedback), then the SSP model provides constraints on how long ago such an event occurred. Models used here have ages spaced logarithmically from 10 Myr up to 1 Gyr.

The second SFH used in this paper is borrowed from a representative simulation of a major merger which undergoes a very luminous sub-mm phase (SMG) as well as a highly dust-obscured phase (DOG) before star-formation is shut off by AGN feedback effects (Narayanan et al., 2009). This SFH traces the star-formation rate from the beginning of the simulation — before the two gas-rich ($f_g \sim 0.8$) disks begin to interact — through the period of final coalescence when the SFR peaks near $1000 M_\odot \text{ yr}^{-1}$, to the end of the simulation and a red, dead, elliptical galaxy. Models used here have ages spaced roughly linearly from 10 Myr to 0.8 Gyr.

The third SFH adopted in this study comes from cosmological hydrodynamical simulations in which SMGs are posited to correspond to the most rapidly star-forming systems that match the observed number density of SMGs (Davé et al.,

2010). In particular, the SFH and metallicity history of the highest SFR simulated SMG are used. This object has a SFR of $\approx 150 M_{\odot} \text{ yr}^{-1}$ for most of the simulation but is boosted to $\approx 500 M_{\odot} \text{ yr}^{-1}$ at $z = 2$ and reaches a mass of $M_* = 2.8 \times 10^{11} M_{\odot}$ by the same redshift. As nearly all of the mass is assembled in a quiescent mode, this SFH is nearly opposite to a SSP, in which all stars are formed in a single infinitely short burst. Models used here have ages spaced roughly linearly over the full range of the SFH, from 10 Myr to 3 Gyr.

Figure 5.4 shows the SFHs from Narayanan et al. (2009) and Davé et al. (2010) that are used in this analysis.

5.4 Results

This section contains basic photometry results as well as constraints on the median stellar masses (M_*) of bump DOGs, power-law DOGs, and SMGs. The impact of a different choice of SPS library, IMF, and SFH are explored here as well.

5.4.1 SEDs

Since every source in this study has a known spectroscopic redshift, it is possible to construct SEDs showing the luminosity per unit frequency (L_{ν}) as a function of rest-frame wavelength (λ_{rest}). Figure 5.5 shows the median rest-frame SED for each population of ULIRGs in this study: power-law DOGs, bump DOGs, and SMGs. Also shown in this diagram is the SED of a simulated major merger during a time when the system is observable as a DOG and has an IR luminosity of $L_{\text{IR}} \approx 3 \times 10^{12} L_{\odot}$ (Narayanan et al., 2009).

Power-law DOGs have the brightest rest-frame near-IR luminosities, with luminosities at $3\mu\text{m}$ approaching $\nu L_{\nu} = 10^{12} L_{\odot}$. This represents a near-IR excess of a factor of 3-5 compared to bump DOGs and SMGs. Such an excess is an indicator of thermal emission from an obscured nuclear source (i.e., obscured AGN; Rieke,

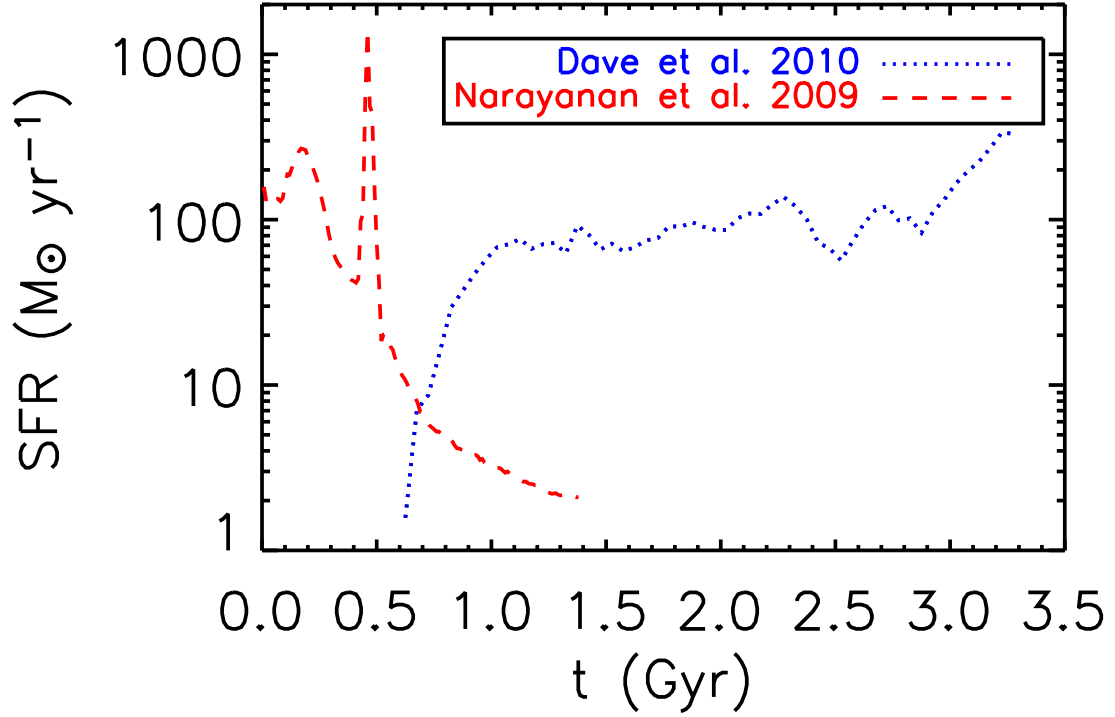


Figure 5.4 Star-formation histories used in stellar population synthesis models. Dotted line represents high- z ULIRGs identified in cosmological hydrodynamical simulations formed via smooth gas inflow and accretion of small satellites (Galaxy A from Figure 4 of Davé et al., 2010). Dashed line represents high- z ULIRGs formed via major mergers of two gas-rich disks (Narayanan et al., 2009).

1978).

Bump DOGs and SMGs have rest-frame optical and near-IR SEDs that qualitatively match the shape of the simulated merger SED shown in Figure 5.5. However, SMGs show a rest-frame UV excess compared to bump DOGs and power-law DOGs. It is not clear with the available data whether this is the result of a selection effect, a difference in dust obscuration, or the luminosity weighted-age of the stellar population. Resolving this issue may require deep, high spatial resolution imaging of SMGs in the rest-frame UV, optical, and near-IR (currently, only UV and optical imaging is available and only for a handful of sources; e.g. Conselice et al., 2003; Swinbank et al., 2010b).

5.4.2 Stellar Population Synthesis

In principle, SPS models can be applied to the broad-band photometry of a galaxy to constrain its stellar mass (M_*), visual extinction (A_V), and stellar population age. However, such a process is dominated by uncertainties resulting from the unknown dust extinction, stellar population age, star-formation history and IMF of that galaxy. Although differences exist in the detailed treatment of various aspects of stellar atmospheres and evolution between various SPS libraries, our results suggest that these details are sub-dominant to the other sources of uncertainty listed above (see section B). The nominal fiducial model chosen in this paper is the CB07 SPS library with a SSP SFH and Chabrier IMF, and is presented in section 5.4.2.1. In later sections, alternative SFHs and IMFs are explored.

5.4.2.1 Simple Stellar Population

The SSP represents a SFH in which all stars form in an infinitely short burst of star-formation and evolve passively thereafter. This is surely an idealized scenario for the formation of massive galaxies, but it is worth studying nonetheless, since

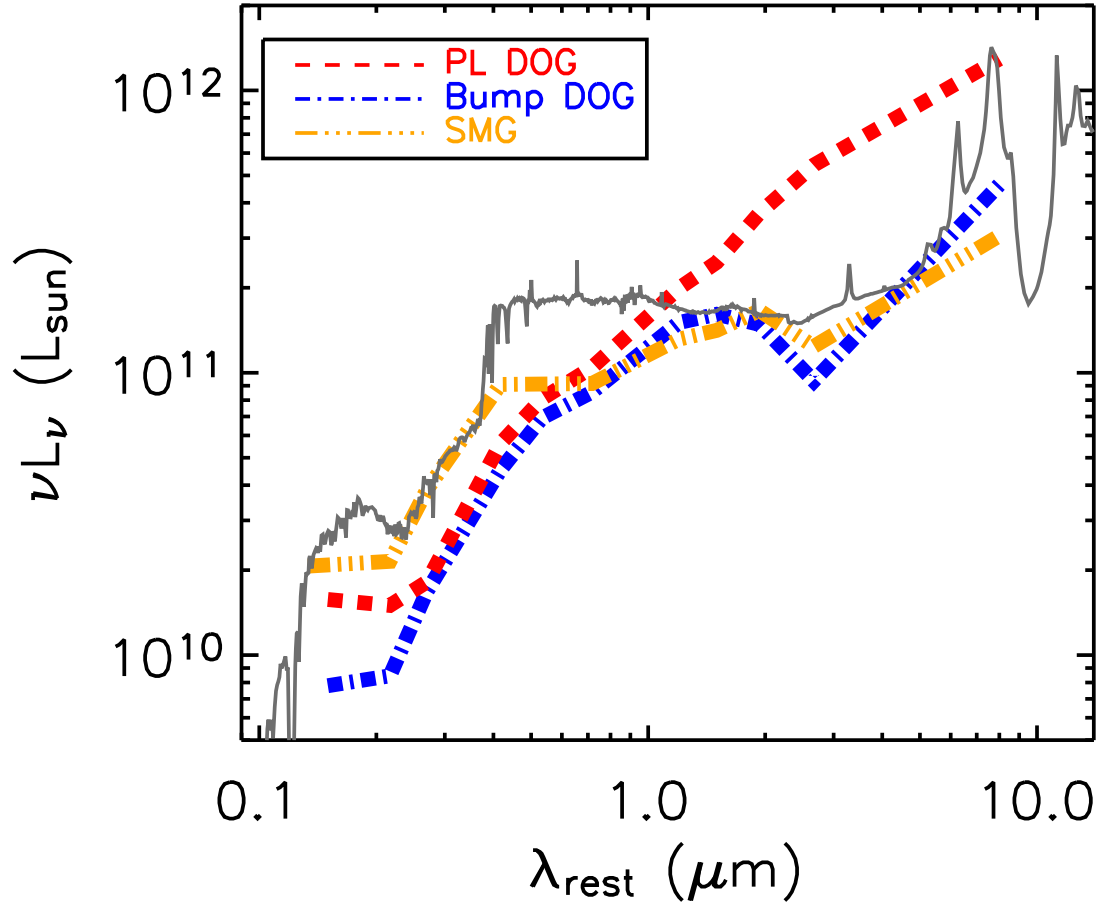


Figure 5.5 Luminosity per unit frequency as a function of rest-frame wavelength for the median power-law DOG (red), bump DOG (blue), and SMG (orange). The SED of a simulated gas-rich major merger at $z = 2$ during a phase when it would be observed as a DOG is overplotted for reference (Narayanan et al., 2009).

SSPs form the building blocks of more complex SFHs and can be used more easily to compare the effect of different SPS libraries and IMFs (see section 5.4.2.4 for more details on this last point).

Figure 5.6 shows the stellar mass cumulative distribution function (derived from the probability density function) resulting from fitting a SSP (computed with the CB07 SPS library and a Chabrier IMF) to the population of power-law DOGs, bump DOGs, and SMGs. In each panel are χ^2_ν and iso-mass contours that illustrate the 1σ range of acceptable M_* , A_V , and stellar age parameters.

All three populations (power-law DOGs, bump DOGs, and SMGs) have a similar range of acceptable M_* values. Power-law DOGs are the most massive systems, followed by bump DOGs and then SMGs. However, their best-fit median stellar masses are separated by only ≈ 0.1 dex, while the spread in their distributions are $\approx 0.3 - 0.4$ dex. This implies that the trends in stellar mass between the populations are suggestive rather than conclusive. The best-fit and 1σ range of acceptable masses for this SFH are given in Table 5.4.

One feature of the fitting process that is not shown in Figure 5.6 is the significant degeneracy between A_V and stellar age – the broad-band photometry of these high- z ULIRGs can be fit either by young (10 Myr) and dusty ($A_V \sim 1.5 - 2$) stellar populations or intermediate age (500 Myr) and less dusty ($A_V \sim 0.0 - 0.5$). Given the large quantities of dust that are known to exist in these systems based on observations at longer wavelengths (e.g., Kovács et al., 2006; Coppin et al., 2008; Bussmann et al., 2009b; Lonsdale et al., 2009; Kovács et al., 2010), it is unlikely that $A_V < 1$ solutions are acceptable. Assuming $A_V = E(B - V)/R_V$ (where $R_V = 3.1$) and the relation between $E(B - V)$ and the hydrogen column density (N_H) from Bohlin et al. (1978), $A_V \sim 1$ implies $N_H \sim 2 \times 10^{21} \text{ cm}^{-2}$. Under the assumption of a spherical shell around the source with radius equal to the effective radius (R_{eff}),

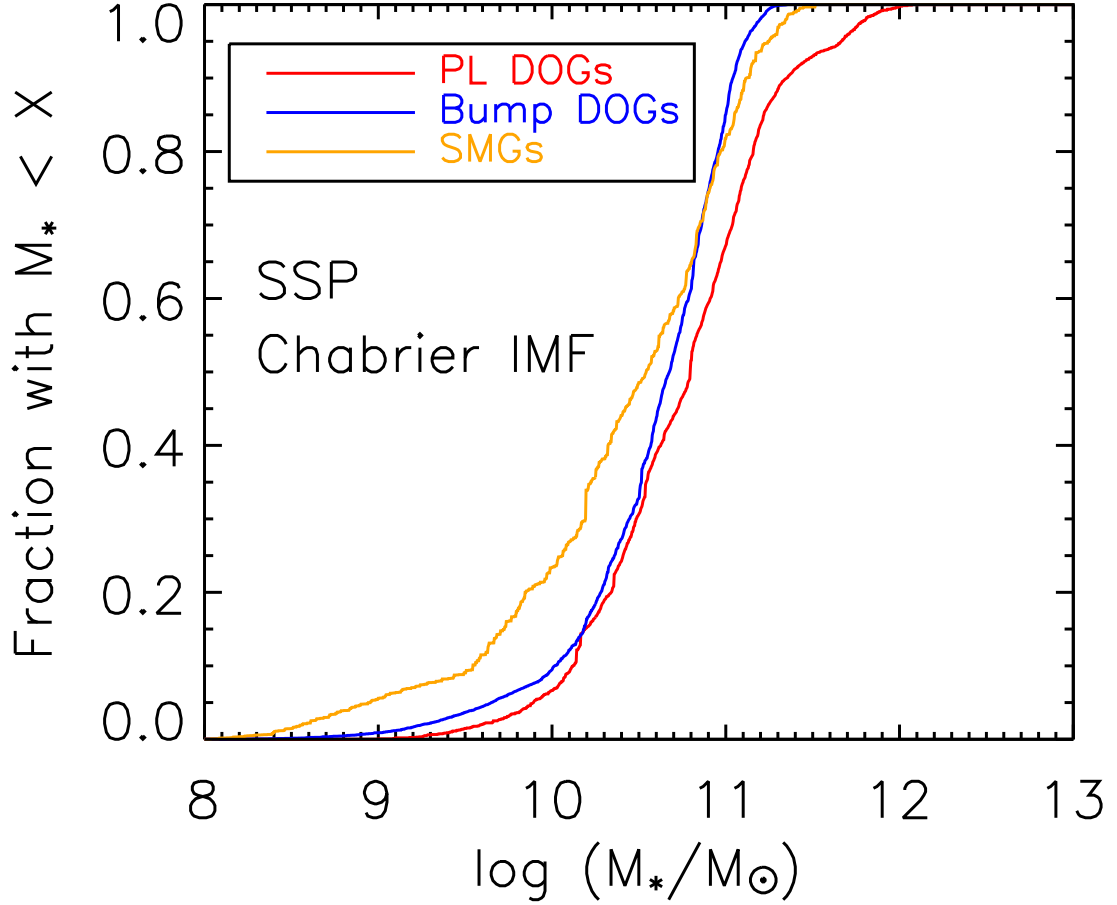


Figure 5.6 Cumulative distribution function for the stellar masses of power-law DOGs (red), bump DOGs (blue), and SMGs (orange) derived using using the CB07 library, a Chabrier IMF, and a simple stellar population SFH. The best-fit median stellar masses are separated by about 0.1 dex, with $M_*(\text{SMG}) < M_*(\text{BumpDOG}) < M_*(\text{PLDOG})$. The 1σ spread in each stellar mass probability distribution is about 0.3-0.4 dex, indicating that these differences between the populations are suggestive rather than conclusive at the current level of precision.

the dust mass can be estimated from N_{H} using:

$$M_{\text{d}} = \frac{1}{f_{\text{gd}}} \mu_{\text{p}} N_{\text{H}} 4\pi R_{\text{eff}}^2, \quad (5.1)$$

where f_{gd} is the gas-to-dust mass ratio (assumed to be 60, the value found appropriate for SMGs; Kovács et al., 2006) and μ_{p} is the mean molecular weight of the gas (assumed to be 1.6 times the mass of a proton). Morphological measurements indicate these objects have typical effective radii of 3-8 kpc (Dasyra et al., 2008; Busmann et al., 2009b; Donley et al., 2010). All together this implies $M_{\text{d}} \sim (0.5-3) \times 10^8 M_{\odot}$, depending on the size of R_{eff} . In fact, based on $350\mu\text{m}$ observations, Kovács et al. (2010) find dust masses of $M_{\text{d}} \approx (5-10) \times 10^8 M_{\odot}$ for *Spitzer*-selected ULIRGs with a mid-IR bump feature. This suggests that $A_{\text{V}} > 1$ and hence age < 200 Myr models should be preferred.

5.4.2.2 Merger-Driven Star-Formation History

One of the major goals of this paper is to go beyond instantaneous burst SFHs (SSPs) and test the self-consistency of more complicated SFHs. Two in particular that are tested here are a major merger-driven SFH (Narayanan et al., 2009) and a more quiescent SFH driven mainly by smooth accretion of gas and nearby small satellites (Davé et al., 2010). The merger-driven SFH is described here, while the smooth accretion SFH is described in more detail in section 5.4.2.3.

Figure 5.7 shows the cumulative distribution function for the best-fit stellar masses of power-law DOGs, bump DOGs, and SMGs derived using a merger-driven SFH (from Narayanan et al., 2009) with the CB07 SPS library and a Salpeter IMF. The best-fit and 1σ range of acceptable M_{\star} values are given for this SFH in Table 5.4. At ages > 0.8 Gyr, the SFR drops below $\sim 30 M_{\odot} \text{ yr}^{-1}$ and this object would not qualify as a ULIRG. Thus we focus on ages < 0.8 Gyr, where the differences in the best-fit stellar mass estimates of power-law DOGs, bump DOGs, and SMGs are

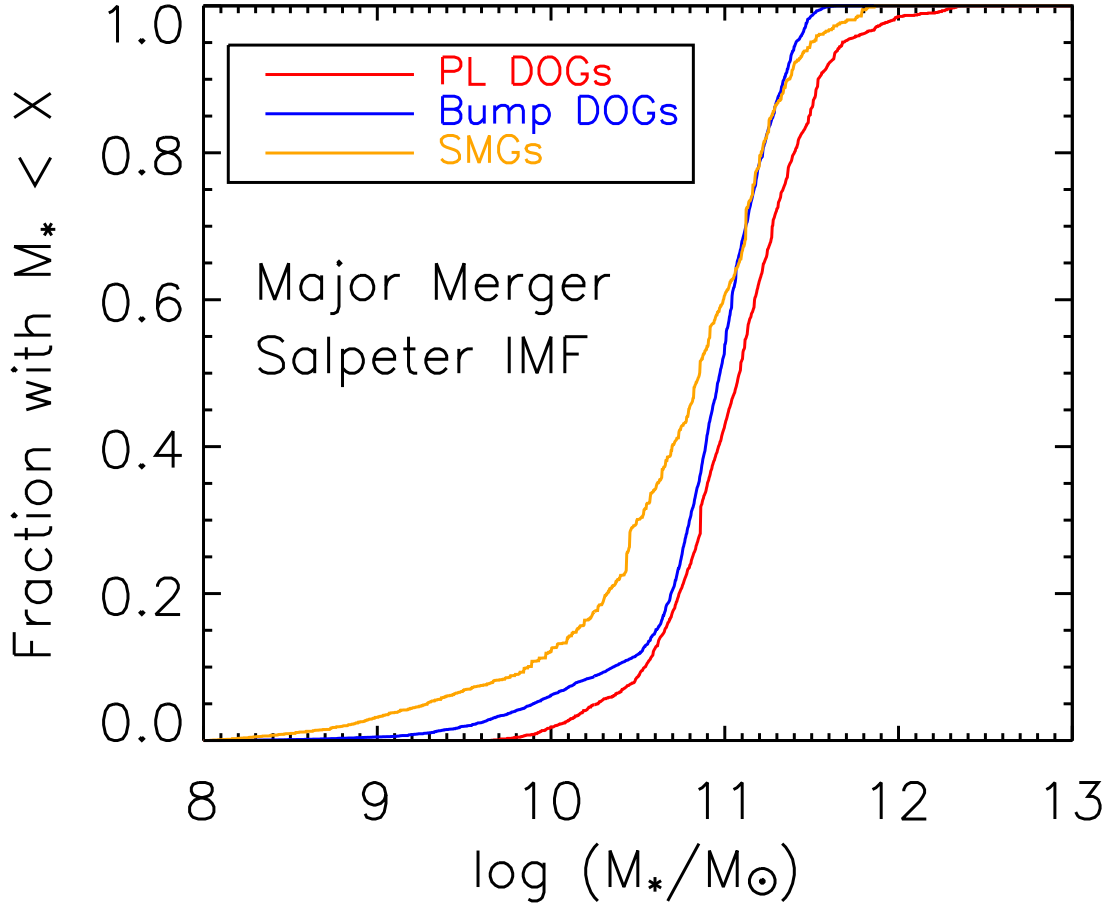


Figure 5.7 Similar to Figure 5.6, but assuming a major merger SFH and a Salpeter IMF (see Figure 5.4 of this paper and Narayanan et al., 2009).

similar to those obtained using the SSP SFH.

In the merger SFH, the DOG phase occurs at the end of the peak SFR period at an age of ≈ 0.75 Gyr. The median M_* for bump DOGs, power-law DOGs, and SMGs at this age is $\approx 1.6 \times 10^{11} M_\odot$. In this simulation, the baryonic mass is initially $M_b = 3 \times 10^{11} M_\odot$, while the stellar mass evolves as gas is converted into stars. At an age of ≈ 0.75 Gyr, the simulated merger has assembled a stellar mass of $M_* \approx 1.8 \times 10^{11} M_\odot$, roughly consistent with the inferred stellar masses

of these ULIRGs. At younger ages (e.g., 0.1 Gyr), the inferred median M_* values for power-law DOGs, bump DOGs, and SMGs are lower ($M_* \approx 5 \times 10^{10} M_\odot$) and would be harder to reconcile with the merger simulations. Furthermore, such objects would have bright, well-separated nuclei which are not typically seen in high-spatial resolution imaging (e.g. Dasyra et al., 2008; Bussmann et al., 2009b; Swinbank et al., 2010b, Bussmann et al., submitted).

5.4.2.3 Smooth Accretion Star-Formation History

In the cosmological hydrodynamical simulations of Davé et al. (2010), SMGs are posited to be the maximally star-forming galaxies whose number densities match the observed number density of SMGs. This results in the typical simulated SMG having a SFH described by a relatively constant SFR of $100\text{--}200 M_\odot \text{ yr}^{-1}$ over a period of 3 Gyr; this leads to a stellar mass in these systems in the range $M_\odot \approx (1 - 5) \times 10^{11} M_\odot$. Davé et al. (2010) note that their simulated SFRs are a factor of ~ 3 lower than the typical values observationally inferred for SMGs, and hypothesize that a “bottom-light” IMF such as that proposed by van Dokkum (2008) and Davé (2008) could explain this discrepancy. This type of IMF would also have the consequence of modifying the M_*/L_V , meaning that at a given L_V , the inferred stellar mass is lower than for other IMFs such as Chabrier or Salpeter. It is for this reason that the constraints on the stellar masses of the high- z ULIRGs with this SFH are of particular interest.

Figure 5.8 shows the cumulative distribution function for the best-fit stellar masses of power-law DOGs, bump DOGs, and SMGs derived using a SFH driven mainly by smooth accretion of gas and nearby satellites (with the CB07 SPS library and a Chabrier IMF). The best-fit and 1σ range of M_* estimates are provided in Table 5.4. In this case, the best-fit stellar masses of the three populations are separated by ≈ 0.2 dex, with power-law DOGs being the most massive and SMGs

Table 5.4. Best-fit χ^2_ν , M_* , and associated uncertainty for PL DOGs, bump DOGs, and SMGs using the CB07 library.

| SFH | PL DOGs | | Bump DOGs | SMGs |
|----------------------------------|---------------------|---------------------|---------------------|------|
| | $\log(M_*/M_\odot)$ | $\log(M_*/M_\odot)$ | $\log(M_*/M_\odot)$ | |
| Instantaneous Burst ^a | 10.8 ± 0.4 | 10.7 ± 0.3 | 10.6 ± 0.5 | |
| Major Merger ^b | 11.1 ± 0.4 | 11.0 ± 0.3 | 10.9 ± 0.4 | |
| Smooth Accretion ^c | 11.0 ± 0.3 | 10.8 ± 0.3 | 10.6 ± 0.5 | |

^aAssuming a Chabrier IMF

^bSFH from Narayanan et al. (2009), assuming a Salpeter IMF

^cSFH from Davé et al. (2010), assuming a Chabrier IMF

being the least massive (note that this is still below the typical 1σ dispersion in the stellar mass estimates of $\approx 0.3 - 0.4$ dex).

For bump DOGs at an age of ≈ 1.5 Gyr, the best-fit stellar masses are $M_* \approx 5 \times 10^{10} M_\odot$. This is roughly a self-consistent result, as integrating this SFH from $t = 0$ to $t = 1.5$ Gyr implies an assembled mass of $\approx 5 \times 10^{10} M_\odot$. For an age of ≈ 3 Gyr, the best-fit stellar mass of bump DOGs is $\approx 10^{11} M_\odot$. Integrating the SFH from $t = 0$ to $t = 3$ Gyr, the assembled mass is $\approx 2 \times 10^{11} M_\odot$. In other words, the rest-frame UV through near-IR luminosities of the high- z ULIRGs studied in this paper are about a factor of 2 lower than they should be if they have been forming stars according to the SFH of Davé et al. (2010) for ~ 3 Gyr.

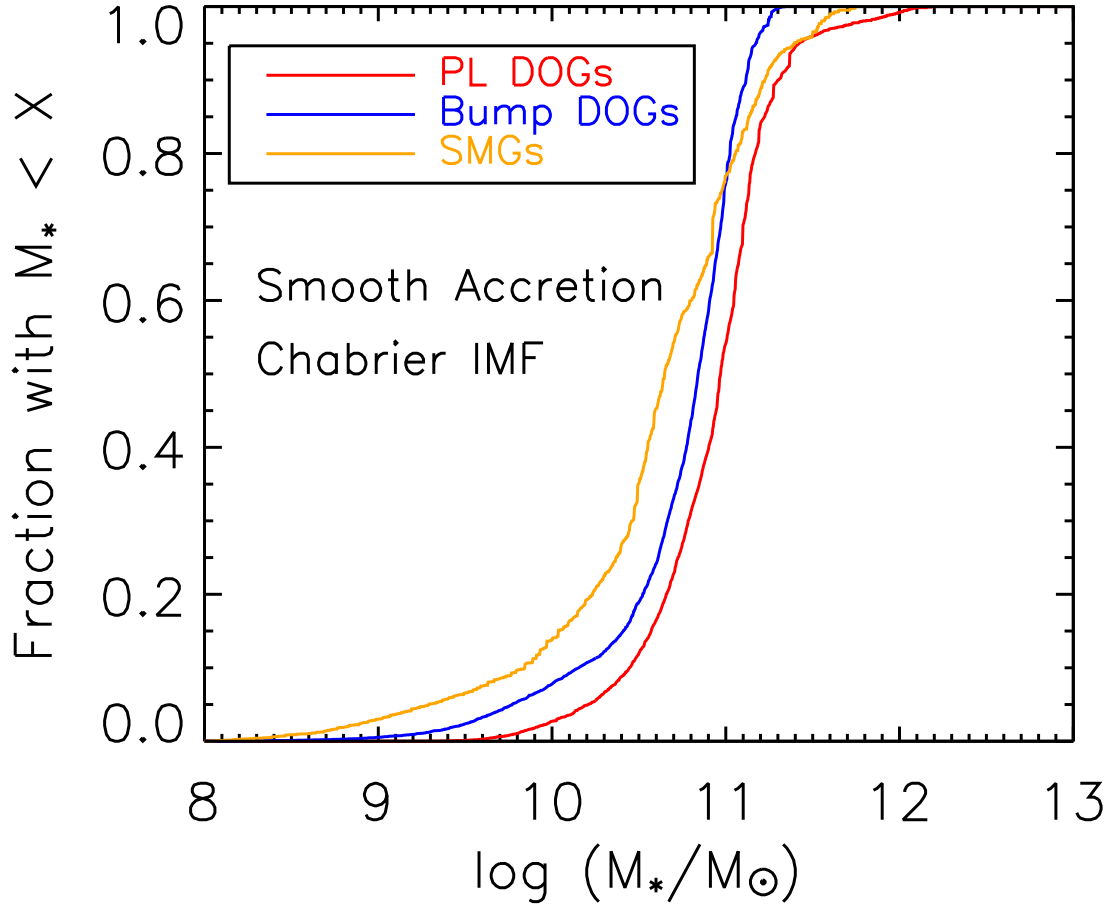


Figure 5.8 Similar to Figure 5.6, but assuming a smooth accretion SFH (see Figure 5.4 of this paper and Davé et al., 2010). The median stellar mass for all three high- z ULIRG populations (power-law DOGs, bump DOGs, and SMGs) is within ≈ 0.2 dex of $M_* = (0.8) \times 10^{11} M_\odot$, depending on the age of the stellar population.

5.4.2.4 Variation with IMF

The importance of the IMF in SPS modeling has mainly to do with the mass-to-light ratio. Bruzual & Charlot (2003) showed that the $B - V$ and $V - K$ colors of SPS models distinguished only by their IMFs (Chabrier vs. Salpeter) are very similar. On the other hand, the Salpeter IMF gives mass-to-light ratios that are ≈ 0.2 dex larger than the Chabrier IMF. Bottom-light IMFs (such as that advocated by van Dokkum, 2008) have more complicated mass-to-light ratios that depend on both the characteristic mass (m_c) and the age of the stellar population. van Dokkum (2008) find that for $m_c = 0.4 M_\odot$ (as adopted here) and ages < 1 Gyr, the mass-to-light ratio is lower by 0.2-0.3 dex compared to a Chabrier IMF. The results of this study are consistent with this finding: assuming a SSP SFH and this bottom-light IMF, the stellar masses of bump DOGs are in the range $M_* = (0.1 - 0.6) \times 10^{11} M_\odot$, or about 0.3-0.4 dex lower than those inferred using a Chabrier IMF. A similar reduction in M_* occurs when using the bottom-light IMF in conjunction with more complicated SFHs such as the merger-driven SFH and the smooth accretion SFH detailed in sections 5.4.2.2 and 5.4.2.3.

5.5 Discussion

The focus of this section is to build upon the constraints on the stellar masses and star-formation histories of bump DOGs, power-law DOGs, and SMGs presented in section 5.4. First, the estimates of M_* presented here are compared with estimates of other dusty high-redshift ULIRGs. Next, possibilities are discussed for improving constraints on the age of the dominant stellar population (the primary source of uncertainty in SPS modeling). Finally, implications for models of galaxy evolution are presented based upon a comparison of the two theoretical SFHs considered in this study (major merger and smooth accretion).

5.5.1 Comparing Stellar Mass Estimates

Studies of other *Spitzer*-selected ULIRGs with a bump mid-IR SED have found median stellar masses of $M_* \approx 10^{11} M_\odot$ (Berta et al., 2007; Lonsdale et al., 2009; Huang et al., 2009). This is a little less than 1σ higher than the median stellar mass found for bump DOGs here. Considering the different sample selection criteria as well as assumptions in IMF, SFH, and SPS libraries, it is remarkably consistent. The difference in stellar mass estimates can probably be fully accounted for by the different selection criteria as well as the use in this study of the new CB07 SPS libraries, which have redder near-IR colors and hence tend towards lower inferred stellar masses (see section 5.4.2.4).

Two recent studies of SMGs using stellar population synthesis modeling have come to differing conclusions regarding their median M_* . While Michałowski et al. (2010) find a median stellar mass of $M_* \approx 2 \times 10^{11} M_\odot$ (using SEDs from Iglesias-Páramo et al., 2007), Hainline et al. (2010) find $M_* = 7 \times 10^{10} M_\odot$ (assuming a Chabrier IMF and models from Maraston, 2005). Hainline et al. (2010) argue that models which do not consider the contribution of an obscured AGN in the mid-IR (particularly in the $5.8\mu\text{m}$ and $8.0\mu\text{m}$ channels of IRAC) can bias stellar mass estimates of SMGs upwards by a factor of ≈ 2 . Our analysis (which excludes these two IRAC channels to minimize the contribution from an obscured AGN) indicates stellar masses that are closer to those of Hainline et al. (2010), with median $M_* = 6 \times 10^{10} M_\odot$. However, inclusion of the additional two IRAC channels increases our stellar mass estimates only by a factor of 30-40% (median $M_* = 8 \times 10^{10} M_\odot$), not by a factor of two. appears

The DOGs and SMGs studied in this paper represent some of the rarest, most actively star-forming systems at $z \approx 2$. More typical star-forming galaxies at this epoch and earlier are frequently selected via their rest-frame UV colors (e.g., Lyman

Break Galaxies or LBGs; Steidel et al., 1996). Stellar population synthesis analysis of these objects have shown that they have stellar masses of $M_* \approx 10^{10} M_\odot$ (Shapley et al., 2005; Erb et al., 2006; Kornei et al., 2010). This is roughly a factor of 7-10 smaller than the typical DOG or SMG. Unless these objects have very high gas fractions ($f_{\text{gas}} > 0.8$), this implies that only the high-mass tail of the distribution of LBGs ($M_* > 5 \times 10^{10} M_\odot$) can contribute as progenitors in merger-driven scenarios for the formation of DOGs or SMGs. An important path of research that is beyond the scope of this work is to examine whether LBGs above this mass threshold are sufficiently numerous given the merger rate at $z \sim 2$ to match the observed number density of ULIRGs at this epoch.

5.5.2 Improving Estimates of Stellar Population Age

The primary uncertainty in the SPS modeling methods used in this paper is the unknown age of the dominant stellar population in the galaxy of interest. This leads to factors of ≈ 3 uncertainty in the stellar mass (M_*) and even larger uncertainties in the extinction (A_V). Obtaining an independent constraint on the stellar population age is therefore the best way to improve upon the procedure followed in this paper. Perhaps the most promising avenue forward on this front is photometry that fully samples the rest-frame 4000 Å break. This feature arises from a collection of spectral absorption lines occurring near 4000 Å. The absorption lines are stronger in older stars (elements in younger stars are multiply ionized and therefore less opaque), so the depth of the 4000 Å break can be used as a tracer of the age of a stellar population (Bruzual A., 1983).

At $z \sim 2$, the 4000 Å break is shifted into the near-IR. Recent efforts to identify this spectral feature in galaxies at $z \sim 2$ have thus relied on medium-band photometry at five near-IR wavelengths: three covering the *J*-band atmospheric window and two covering the *H*-band atmospheric window (NEWFIRM Medium-Band Survey,

NMBS; van Dokkum et al., 2009). This setup ensures the 4000 Å break will be well-sampled for any objects at $1.5 < z < 3.5$. The initial use of these filters in the NMBS focused on obtaining very deep maps (8σ rms level of $K_{AB} = 23.3$) over two relatively small fields ($27' \times 27'$ each). For the DOGs in this study, the median signal of the stacked power-law DOG is $K_s \approx 21.4$ (AB), while for bump DOGs it is $K_s = 21.8$ (AB). Therefore, a shallower survey reaching $K_{AB} \approx 21.5$ and covering several square degrees would be ideal for these objects.

5.5.3 Implications for Galaxy Evolution at $z \sim 2$

Observational evidence indicates that ULIRGs in the local universe are the product of major mergers (Armus et al., 1987) and that they are connected in an evolutionary sense with quasars (Sanders et al., 1988a,b). It is tempting to postulate a similar major-merger origin for the high-redshift ULIRGs. However, conclusive evidence linking these variously selected ULIRG populations to each other and to quasars requires measurements that challenge our current observational capabilities. There are some tantalizing hints that these diverse populations are indeed linked. Brodwin et al. (2008) have demonstrated that the clustering strength of DOGs is comparable to that of both the SMGs and QSOs at similar redshifts. Bussmann et al. (submitted) have shown that the quantitative morphologies of DOGs and SMGs are consistent with an evolutionary picture in which the SMG phase precedes the bump DOG phase, which in turn precedes the PL DOG phase. However, these studies are challenging because of surface brightness dimming and dust-obscuration effects, which prevent a straightforward merger identification via morphological studies (Dasyra et al., 2008; Melbourne et al., 2008; Bussmann et al., 2009b; Melbourne et al., 2009; Bussmann et al., submitted).

This study offers an independent means of testing the merger hypothesis via SPS modeling of broad-band imaging in the rest-frame UV through near-IR. The

approach followed in this paper is to test the self-consistency of two distinct SFHs. One is from Narayanan et al. (2009) and is characterized by a major merger, while the other is from Davé et al. (2010) and is characterized by a more quiescent, steady SFH.

In the major merger SFH, the progenitors each have a baryonic mass of $1.5 \times 10^{11} M_{\odot}$ and gas fractions of $f_g = 0.8$. This represents the minimum mass necessary in these simulations to obtain a DOG and SMG phase. By the end of the merger, much of the gas has been expelled by AGN feedback and the rest has been converted into stars, leaving a system with a stellar mass of $M_* = 1.5 \times 10^{11} M_{\odot}$. Narayanan et al. (2009) note that this system is typically the minimum mass system that satisfies the DOG criteria in the simulations. Figure 5.9 shows the mass assembly history of this simulated merger, as well as the best-fit stellar masses for PL DOGs, bump DOGs, and SMGs derived from the simulated SED at each point during the SFH. The stellar mass estimates assume a Salpeter IMF (as is assumed in the simulations) and are consistent with the assembled mass of the simulated merger both just before final coalescence ($t = 0.4$ Gyr) as well as about 200 Myr after final coalescence ($t = 0.7$ Gyr). If a Chabrier IMF is instead adopted, the estimates of M_* for DOGs and SMGs decrease by a factor of roughly 2.

Turning now to the smooth accretion SFH (Figure 5.10), the best fit stellar masses of DOGs and SMGs match the assembled mass in the simulated galaxy at an age of about 2.0 Gyr. Yet by $t = 3.0$ Gyr, the assembled stellar mass in the simulated system is roughly a factor of 2 larger than those inferred for the median power-law DOG, bump DOG, and SMG from the stellar population synthesis analysis in this paper. Another way of stating this distinction is that roughly 85% of the galaxies in the samples studied here have stellar masses that are lower than the median simulated system at $t = 3$ Gyr. Adopting a Salpeter IMF rather than a

Chabrier IMF would increase the stellar masses by roughly a factor of 2. However, if a Salpeter IMF is truly appropriate for these $z \sim 2$ ULIRGs, then their sub-mm fluxes (typically $F_{850\mu\text{m}} \sim 8$ mJy) would imply SFRs of $\approx 1000 M_{\odot} \text{ yr}^{-1}$. In the cosmological simulations of Davé et al. (2010), SMGs have SFRs that are a factor of ≈ 3 lower than this value.

In fact, Davé et al. (2010) suggest that some or all of the difference between the theoretical and observed SFRs may be due to the use of a “bottom-light” IMF that is lacking in low mass stars compared to a Chabrier IMF (e.g., van Dokkum, 2008; Davé, 2008). However, if a bottom-light IMF is adopted in the SPS models used here, DOGs and SMGs are found to have masses of $M_* \approx 0.5 \times 10^{11} M_{\odot}$ at an age of 3 Gyr, roughly a factor of 4 lower than the assembled M_* of the simulated galaxy at this age. In this case, 95% of the objects studied in this paper have stellar masses that are lower than the median simulated system at $t = 3$ Gyr.

One way to reconcile the rest-frame UV through near-IR luminosities with a bottom-light IMF is by having the DOGs and SMGs begin forming their stars at a later time than is indicated in the smooth accretion model of Davé et al. (2010). For example, if the typical DOG or SMG begins forming stars at a rate of $150 M_{\odot} \text{ yr}^{-1}$ at $z = 3$ (when the universe is ≈ 2 Gyr old) instead of $z = 6$ (when the universe is ≈ 1 Gyr old), then the assembled mass at $z = 2$ is $M_* = 10^{11} M_{\odot}$, significantly closer to what is observed.

5.6 Conclusions

We have attempted to connect the various $z \approx 2$ ULIRG populations (specifically, highly obscured mid-IR selected DOGs and far-IR selected SMGs) in an evolutionary sequence, and determine whether these populations are different stages of major mergers. Previous work by our group (Brodwin et al., 2008) has shown that the

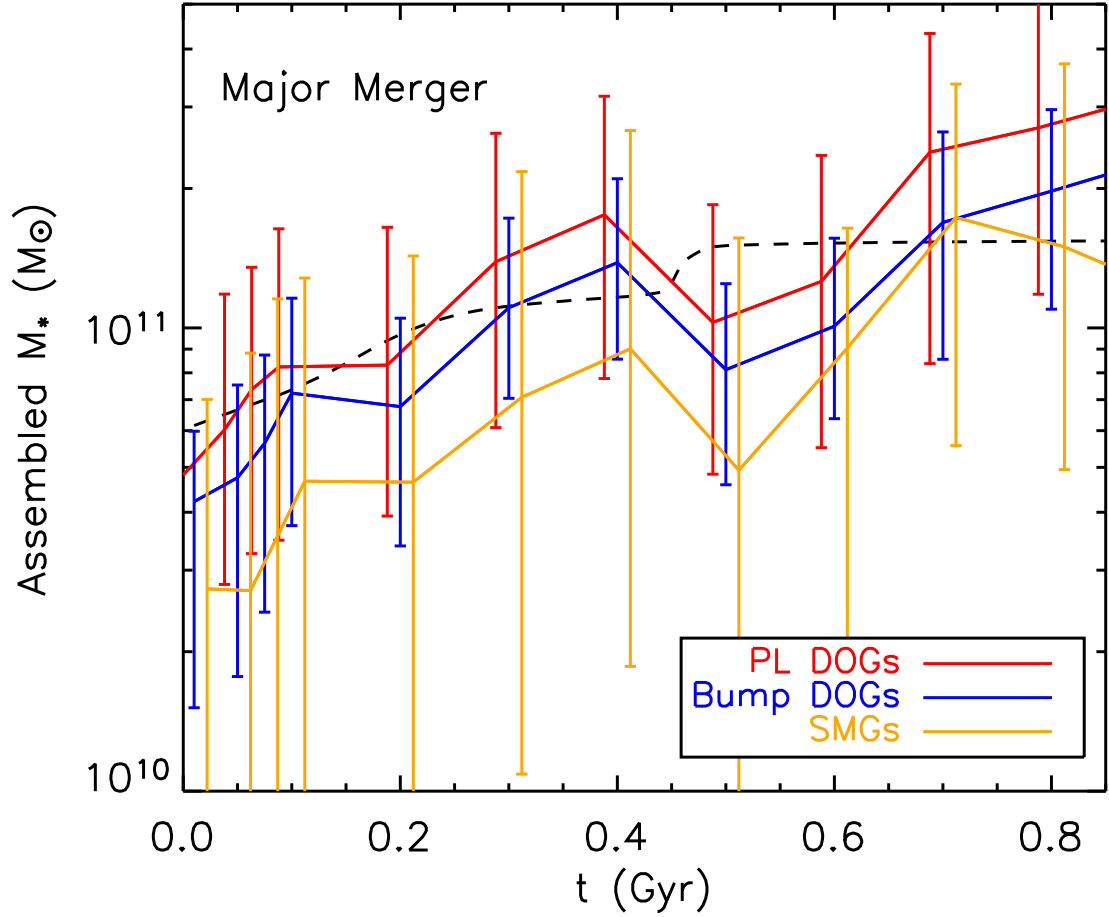


Figure 5.9 Stellar mass assembly history for a major merger SFH (dashed line; Narayanan et al., 2009). Also shown are stellar mass estimates as a function of time for power-law DOGs, bump DOGs, and SMGs assuming a Salpeter IMF (as is used in the simulations). The mass estimates for these objects match the simulated assembled stellar mass just before final coalescence ($t = 0.4$ Gyr) and about 100–200 Myr after final coalescence ($t = 0.65 - 0.75$ Gyr).

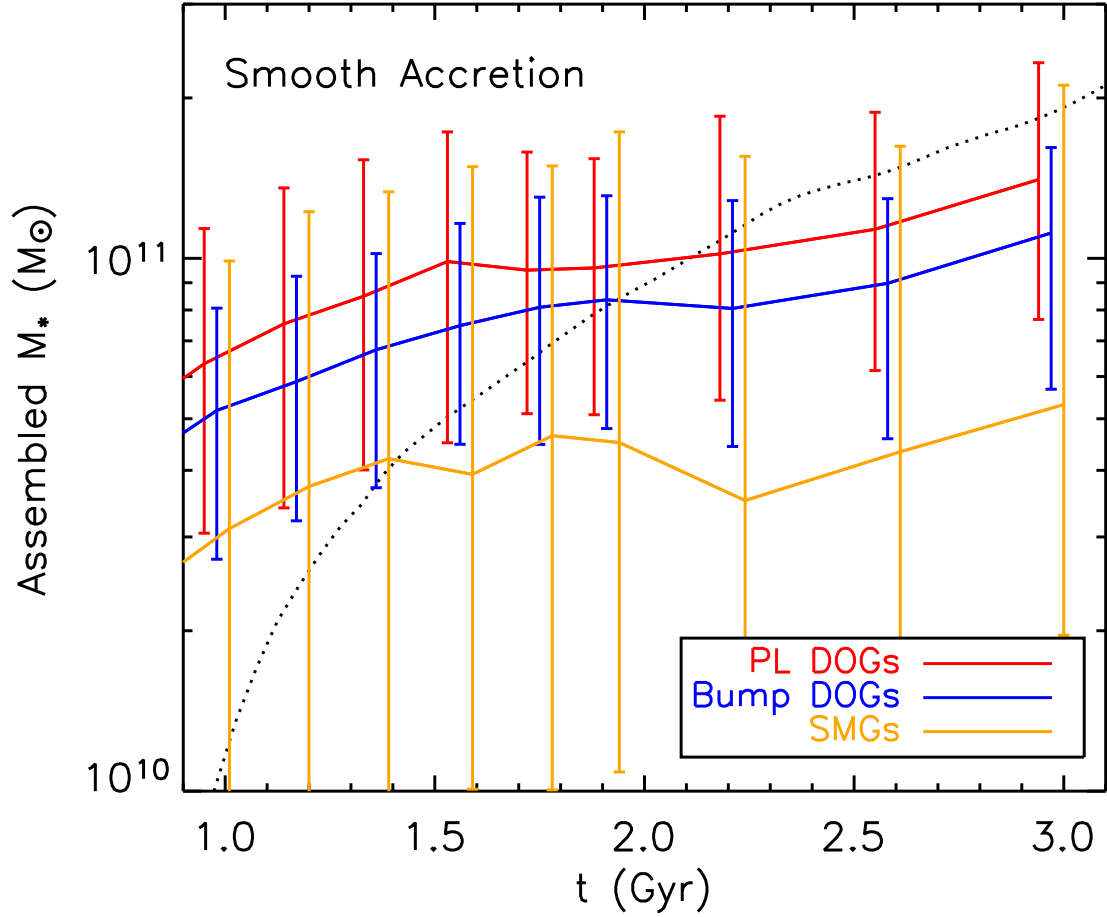


Figure 5.10 Stellar mass assembly history for a smooth accretion dominated SFH (dotted line; Davé et al., 2010) assuming a Chabrier IMF (a Salpeter IMF applied to the cosmological simulations using this SFH implies IR luminosities of simulated ULIRGs that are a factor of 3 lower than observed). The mass estimates are consistent with the simulated assembled M_* at 1.5-2 Gyr, but are a factor of 2 too low at an age of 3 Gyr (i.e., $z \sim 2$, the epoch where these objects are typically found).

clustering measurements of DOGs, SMGs, and QSOs suggests that these three short-lived populations reside in dark matter halos of similar mass. In addition, we have also shown in previous work that the morphologies of these populations suggest they may be placed in an evolutionary scenario where the SMG phase precedes the DOG phases (Bussmann et al., 2009b, Bussmann et al., submitted). In this paper, we analyze the broad-band SEDs of a large sample of DOGs and SMGs with known spectroscopic redshifts. Using stellar population synthesis models, we derive, in a self-consistent manner, estimates of the stellar masses of the DOG and SMG populations and compare these to the theoretical predictions from three different evolutionary scenarios. We list our conclusions below.

- The best-fit stellar masses of SMGs, bump DOGs and power-law DOGs are $4 \times 10^{10} M_{\odot}$, $5 \times 10^{10} M_{\odot}$, and $6 \times 10^{10} M_{\odot}$, respectively (assuming a simple stellar population SFH, a Chabrier IMF, and the CB07 stellar libraries). This trend is consistent with a scenario in which SMGs evolve into bump DOGs which evolve into power-law DOGs, yet uncertainties in the stellar mass estimates are large ($\approx 0.3 - 0.5$ dex, primarily due to the unknown age and dust extinction) and suggest further study is necessary.
- Simulations which produce SMGs and DOGs via gas-rich major mergers require a minimum amount of stellar mass that is consistent with the results reported here for the median SMG, bump DOG, and power-law DOG at $z \sim 2$ (assuming a Salpeter IMF, as is done in the simulations).
- The median stellar mass of simulated SMGs at $z \sim 2$ in smooth-accretion dominated cosmological hydrodynamical simulations is a factor of 2 larger than the median stellar masses found here, assuming a Chabrier IMF. Adoption of a bottom-light IMF in the modeling efforts of this study would increase this

discrepancy to a factor of 4.

There is some tension between the stellar mass estimates reported here and those of the major merger simulations of Narayanan et al. (2009), considering that is the minimum mass model which matches the median DOG and SMG stellar mass estimates. However, we argue that the tension with the smooth accretion simulations of Davé et al. (2010) is greater, particularly when a bottom-light IMF is adopted (without a bottom-light IMF, the SMGs in the smooth accretion simulations have SFRs a factor of 3 too low). On balance therefore, these results favor the major merger scenario, with the obvious caveat that more work remains to be done.

In the near future, wide-field medium-band photometry surveys in the near-IR will provide a finer sampling of the rest-frame 4000 Å break and significantly improve constraints on the primary uncertainty in this analysis, the stellar population age in DOGs and SMGs. Further in the future, the advent of the *James Webb Space Telescope* will provide high-spatial resolution imaging in the mid-IR and provide improved constraints on the amount of stellar emission vs. AGN emission in ULIRGs at high redshift. This is critical information especially for power-law DOGs, but holds significance for bump DOGs and SMGs as well.

This work is based in part on observations made with the *Spitzer Space Telescope*, which is operated by the Jet Propulsion Laboratory, California Institute of Technology under NASA contract 1407. *Spitzer*/MIPS guaranteed time observing was used to image the Boötes field at 24μm and is critical for the selection of DOGs. We thank the SDWFS team (particularly Daniel Stern and Matt Ashby) for making the IRAC source catalogs and imaging publicly available.

We are grateful to the expert assistance of the staff of Kitt Peak National Observatory where the Boötes field observations of the NDWFS were obtained. The authors thank NOAO for supporting the NOAO Deep Wide-Field Survey. In partic-

ular, we thank Jenna Claver, Lindsey Davis, Alyson Ford, Emma Hogan, Tod Lauer, Lissa Miller, Erin Ryan, Glenn Tiede and Frank Valdes for their able assistance with the NDWFS data. We also thank the staff of the W. M. Keck Observatory, where many of the galaxy redshifts were obtained.

RSB gratefully acknowledges financial assistance from HST grants GO10890 and GO11195, without which this research would not have been possible. Support for Programs HST-GO10890 and HST-GO11195 was provided by NASA through a grant from the Space Telescope Science Institute, which is operated by the Association of Universities for Research in Astronomy, Incorporated, under NASA contract NAS5-26555. The research activities of AD and BTJ are supported by NOAO, which is operated by the Association of Universities for Research in Astronomy (AURA) under a cooperative agreement with the National Science Foundation.

Facilities used: *Spitzer Space Telescope*; Kitt Peak National Observatory Mayall 4m telescope; W. M. Keck Observatory; Gemini-North Observatory.

CHAPTER 6

CONCLUSION

In this chapter, we summarize the results and implications of our study of the morphological, dust, and star-formation history properties of DOGs. We also identify potential future steps that promise to advance this field significantly.

6.1 Summary of the Nature of DOGs

In Chapter 2 and Chapter 3, we used *HST* imaging to study the morphologies of power-law DOGs and bump DOGs, and SMGs. We found evidence that very few of these sources are dominated by a point source in the rest-frame optical, yet bump DOGs are larger and have more irregular morphologies than power-law DOGs. These trends are consistent with expectations from simulations of major mergers in which bump DOGs evolve into power-law DOGs near the end of the final coalescence period of the merger when the star-formation rate peaks. The morphological evidence alone cannot rule out alternative, non-merger origins for DOGs. In fact, there is some evidence that high redshift ULIRGs which are less obscured (i.e., do not qualify as DOGs) have morphologies which are expected from a more quiescent mode of galaxy formation.

In Chapter 4, we employed $350\mu\text{m}$ and 1.3mm imaging of a handful of power-law DOGs, to determine that these objects are ULIRGs with dust temperatures higher than SMGs by $> 10 - 20$ K. Meanwhile, other authors have shown that bump DOGs have dust temperatures that are 5-10 K warmer than SMGs. One possible way to interpret these results is in the context of a major merger driven model for galaxy evolution in which AGN feedback plays a significant role in quenching star-formation by heating the surrounding gas and dust particles near the end of

final coalescence. In this scenario, power-law DOGs are warmer than bump DOGs because they occur at a later stage when AGN feedback has had more time to warm the interstellar medium. It should be noted that the observations reported here provide no constraints on the triggering mechanism; for example, a highly turbulent gas-rich disk could potentially lead to a strong inflow of gas which subsequently triggers some kind of AGN feedback.

In Chapter 5, we used synthesized stellar populations and broad-band photometry in the rest-frame ultra-violet, optical, and near-IR to measure the stellar masses and test star-formation histories of bump DOGs, power-law DOGs and SMGs. We found that the best-fit quantities are consistent with an evolutionary scenario in which the stellar mass grows as SMGs evolve into bump DOGs which then evolve into power-law DOGs. In testing a major-merger driven star-formation history, our stellar mass estimates were consistent with the assembled stellar mass of the simulated merger just before final coalescence (potentially the bump DOG phase) as well as 100-200 Myr after final coalescence (potentially the power-law DOG phase). On the other hand, our tests of more quiescent star-formation histories dominated by smooth accretion of gas found stellar masses that were a factor of 2-4 lower than expected from cosmological simulations. The relatively low stellar masses found from this line of analysis therefore favor a merger-driven origin for ULIRGs at $z \sim 2$.

6.2 Possible Paths Forward in the Future

In the next decade, the advent of the Atacama Large Millimeter Array (ALMA), James Webb Space Telescope (JWST), 30-meter class optical telescopes, and other new systems promise to revolutionize the study of massive galaxy evolution at high redshift. ALMA and JWST will be especially valuable, as they will allow detailed kinematical studies on sub-kpc scales of the dust, gas, and stellar emission in galaxies

as faint as our own Galaxy at $z \sim 2$.

In the more immediate future, the most promising way forward is likely to come from wide-field surveys conducted by the *Wide-field Infrared Survey Explorer* (*WISE*), *Herschel* Space Observatory and from the Sub-mm Common User Bolometer Array 2 (SCUBA-2) instrument at the James Clerk Maxwell Telescope. These new instruments are capable of surveying thousands of degrees of sky at wavelengths from $3\mu\text{m}$ to $850\mu\text{m}$ and will provide definitive constraints on the dust properties of DOGs and other high-redshift ULIRGs. The study described in this thesis used data of only a handful of DOGs, yet there are over 2600 DOGs in the 9 deg^2 Boötes field alone!

These surveys will also provide samples of hundreds of lensed ULIRGs at high-redshift that are so bright that they can be used for extensive follow-up observations as ALMA & JWST precursor studies. In particular, sub-mm interferometers have the capability of providing high spatial resolution imaging of the thermal dust emission from these sources. Currently, it is not clear whether the bolometric luminosity of DOGs is dominated by an obscured AGN or by its host galaxy, but high spatial resolution imaging of lensed ULIRGs holds the potential to resolve this question.

Lensed ULIRGs will also be useful for exploring the gas and dynamical properties of high redshift ULIRGs. Sub-mm interferometers again are critical for this effort, as they provide both the spatial and spectral resolution necessary to carry out this type of research. The gas mass can be compared with the stellar mass as one form of evolutionary indicator, as gas is converted into stars during the evolution of a galaxy. The Sub-Millimeter Array (SMA), where I will be doing my post-doc beginning in 2010 November, is capable of carrying out these types of studies; I am looking forward to using it for exactly these purposes! As mentioned earlier, these efforts will act as precursors to subsequent studies with ALMA. I plan to stay

heavily involved in this field and be a regular ALMA user in the future.

Finally, another important near-term project will be to obtain medium-band photometry in the near-IR over as wide a field as possible. These data will provide strong constraints on the 4000 Å break in DOGs and thereby provide an independent measure of the luminosity-weighted age of the stellar population in DOGs. This will be vital to testing the idea that bump DOGs typically evolve into power-law DOGs over the course of 100-200 Myr. Furthermore, a better measurement of the age will provide improved constraints on the stellar masses and thus star-formation histories of DOGs.

APPENDIX A

SMG AND XFLS ULIRG NON-PARAMETRIC MORPHOLOGIES

The morphologies presented herein comprise a large sample of high redshift ULIRGs analyzed in a uniform manner. This minimizes systematic uncertainties in the morphological measurements by facilitating interpretation of the results in a relative sense.

Table A.1 presents the measurements of non-parametric morphologies of SMGs at $z > 1.4$ derived from NIC2 images using the same morphology code used to analyze the imaging of XFLS ULIRGs and DOGs. A total of 18 SMGs meet this requirement, but 2 of these have per-pixel-S/N < 2 and are not included in our analysis here. This table also includes an estimate of whether the source is dominated by a bump or by a power-law in the mid-IR using IRAC data from Hainline et al. (2009) and the same statistical definition originally used for DOGs (Dey et al., 2008).

Swinbank et al. (2010a) present measurements of r_P and G for SMGs, and it is instructive to compare their results with ours here. We find that our size measurements are generally consistent, with median r_P values of 8.4 kpc in our analysis and 8.6 kpc in that of Swinbank et al. (2010a). We also find no systematic offset either at large or small radii in the r_P values.

On the other hand, we find significant offsets in the respective measurements of G . Our median G value for SMGs at $z > 1.4$ is 0.49, while that of Swinbank et al. (2010a) is 0.54. Additionally, aside from a few exceptions, there is tentative evidence that the offset increases with S/N-per-pixel. These offsets may be the result of a different means of selecting which pixels belong to the galaxy in question. As discussed in section 3.4.2.2, pixels with surface brightness above $\mu(r_P)$ are assigned to the galaxy while those below it are not. Meanwhile, Swinbank et al. (2010a) adopt

$1.5r_p$ as their Petrosian radius. Studies of the morphologies of galaxies in the *HST* Ultra-deep field (UDF) have shown that the G coefficient has a strong dependence on the specific definition used for the Petrosian radius (Lisker, 2008). At reliable S/N levels ($S/N > 2$), Lisker (2008) show that using the larger aperture to define a galaxy’s extent can cause an increase in G of up to 0.1, with some evidence for an increase in the offset with S/N. This effect is thus qualitatively consistent with the differences observed between our measurements and those presented in Swinbank et al. (2010a).

The primary takeaway of this comparison is that when comparing morphologies of objects, it is necessary to apply a single systematic method in analyzing all objects in the sample. We note that the central conclusions presented in Swinbank et al. (2010a) are based on measurements of the morphologies of SMGs relative to a population of field galaxies and are therefore robust.

Finally, Table A.2 presents our measurements of non-parametric morphologies of XFLS ULIRGs at $z > 1.4$ derived from NIC2 images using the same morphology code used to analyze the imaging of SMGs and DOGs.

Table A.1. SMG NICMOS Morphological Classifications

| Source Name | Bump/PL | S/N | r_P (kpc) | G | M_{20} | C | PSF Fraction | R_{eff} (kpc) | n | N_{dof} | χ^2_ν |
|-------------|---------|-------|----------------|------|----------|-----|-----------------|---------------------------|----------------|------------------|--------------|
| CFRS03-15 | Bump | 6.1 | 12.5 | 0.57 | -1.72 | 4.3 | 0.00 ± 0.02 | 40.7 ± 34.1 | 18.3 ± 3.8 | 1671 | 4.3 |
| LOCKMAN-03 | Bump | 4.4 | 13.4 | 0.51 | -1.15 | 3.0 | 0.00 ± 0.03 | 4.5 ± 0.2 | 1.2 ± 0.1 | 1671 | 1.4 |
| LOCKMAN-06 | Bump | 3.5 | 10.2 | 0.48 | -1.46 | 3.0 | 0.00 ± 0.05 | 5.3 ± 0.4 | 2.0 ± 0.1 | 1671 | 0.9 |
| LOCKMAN-02 | Bump | 4.0 | 12.9 | 0.46 | -0.99 | 4.5 | 0.03 ± 0.07 | 5.4 ± 0.1 | 0.5 ± 0.0 | 1663 | 0.7 |
| HDFN-082 | Bump | < 2 | — | — | — | — | — | — | — | — | — |
| HDFN-092 | Bump | 2.0 | 8.2 | 0.44 | -0.99 | 5.4 | 0.11 ± 0.16 | 4.1 ± 0.1 | 0.1 ± 0.1 | 1671 | 1.2 |
| HDFN-093 | Bump | 5.8 | 3.4 | 0.49 | -1.76 | 3.2 | 0.19 ± 0.03 | 1.3 ± 0.2 | 4.2 ± 1.2 | 1664 | 0.7 |
| HDFN-105 | Bump | 7.1 | 4.8 | 0.49 | -1.73 | 2.8 | 0.00 ± 0.08 | 2.5 ± 0.2 | 2.9 ± 0.2 | 1671 | 1.4 |
| HDFN-127 | PL | 3.1 | 4.6 | 0.49 | -1.17 | 3.5 | 0.41 ± 0.21 | 1.7 ± 0.2 | 0.2 ± 0.2 | 1671 | 1.4 |
| HDFN-143 | Bump | 3.4 | 8.4 | 0.34 | -1.04 | 2.4 | 0.02 ± 0.08 | 4.4 ± 0.1 | 0.2 ± 0.1 | 1670 | 0.7 |
| HDFN-161 | Bump | 5.5 | 5.4 | 0.58 | -1.80 | 3.4 | 0.01 ± 0.10 | 29.8 ± 41.9 | 20.0 ± 7.6 | 1671 | 1.9 |
| HDFN-172 | Bump | 5.5 | 8.6 | 0.46 | -1.02 | 2.4 | 0.18 ± 0.09 | 4.1 ± 0.3 | 1.7 ± 0.2 | 1671 | 1.7 |
| SA13-332 | PL | 5.1 | 3.2 | 0.51 | -1.62 | 3.0 | 0.47 ± 0.03 | 1.4 ± 0.1 | 0.9 ± 0.3 | 1666 | 0.6 |
| SA13-570 | PL | 3.2 | 7.0 | 0.49 | -1.76 | 2.7 | 0.03 ± 0.18 | 2.9 ± 0.1 | 1.5 ± 0.2 | 1662 | 0.5 |
| CFRS14-3 | Bump | 5.7 | 6.1 | 0.59 | -1.56 | 3.4 | 0.01 ± 0.09 | 1.6 ± 0.1 | 3.4 ± 0.3 | 1671 | 1.4 |
| ELAIS-13 | Bump | < 2 | — | — | — | — | — | — | — | — | — |
| ELAIS-07 | Bump | 4.7 | 8.6 | 0.46 | -0.96 | 4.3 | 0.00 ± 0.08 | 3.7 ± 0.2 | 1.4 ± 0.1 | 1671 | 1.5 |
| ELAIS-04 | Bump | 5.6 | 9.3 | 0.54 | -1.30 | 3.8 | 0.05 ± 0.04 | 3.3 ± 0.0 | 0.5 ± 0.0 | 1671 | 3.3 |

Table A.2. XFLS NICMOS Morphological Classifications

| Source Name | Bump/PL | S/N | r_P (kpc) | G | M_{20} | C | PSF Fraction | R_{eff} (kpc) | n | N_{dof} | χ^2_ν |
|-------------|---------|-------|----------------|------|----------|-----|-----------------|---------------------------|----------------|------------------|--------------|
| MIPS506 | Bump | 5.0 | 5.2 | 0.46 | -1.45 | 3.1 | 0.15 ± 0.24 | 2.6 ± 0.2 | 1.3 ± 0.1 | 1671 | 0.8 |
| MIPS289 | Bump | 5.2 | 11.1 | 0.54 | -2.01 | 3.4 | 0.08 ± 0.03 | 4.7 ± 0.3 | 2.2 ± 0.2 | 1671 | 2.1 |
| MIPS8342 | Bump | 8.0 | 5.3 | 0.57 | -1.73 | 3.1 | 0.11 ± 0.04 | 1.3 ± 0.1 | 2.1 ± 0.1 | 1671 | 1.2 |
| MIPS8242 | Bump | 4.7 | 12.8 | 0.44 | -0.89 | 3.3 | 0.05 ± 0.04 | 5.4 ± 0.1 | 0.5 ± 0.1 | 1671 | 2.1 |
| MIPS464 | PL | 5.2 | 4.6 | 0.40 | -1.59 | 2.5 | 0.16 ± 0.70 | 1.9 ± 0.1 | 0.7 ± 0.1 | 1671 | 1.0 |
| MIPS227 | Bump | 10.4 | 7.7 | 0.54 | -1.84 | 3.0 | 0.03 ± 0.01 | 2.6 ± 0.1 | 1.6 ± 0.1 | 1671 | 1.7 |
| MIPS8196 | Bump | 8.5 | 9.0 | 0.54 | -2.09 | 3.7 | 0.07 ± 0.01 | 4.4 ± 0.2 | 4.0 ± 0.2 | 1671 | 1.8 |
| MIPS8327 | Bump | 5.9 | 5.6 | 0.51 | -1.44 | 2.8 | 0.00 ± 0.06 | 1.8 ± 0.1 | 3.4 ± 0.4 | 1671 | 1.4 |
| MIPS8245 | Bump | 3.2 | 3.5 | 0.44 | -0.96 | 2.2 | 0.00 ± 1.00 | 1.6 ± 0.1 | 0.4 ± 0.2 | 1670 | 1.7 |
| MIPS78 | PL | 2.2 | 6.5 | 0.43 | -0.84 | 2.5 | 0.21 ± 0.51 | 2.7 ± 0.3 | 0.3 ± 0.1 | 1671 | 1.5 |
| MIPS180 | Bump | 4.7 | 3.6 | 0.41 | -1.90 | 2.4 | 0.31 ± 0.82 | 1.6 ± 0.1 | 0.2 ± 0.2 | 1671 | 1.8 |
| MIPS42 | PL | 3.4 | 5.2 | 0.47 | -0.95 | 2.5 | 0.14 ± 0.18 | 2.2 ± 0.3 | 1.1 ± 0.5 | 1671 | 2.0 |
| MIPS8493 | Bump | 3.7 | 12.1 | 0.49 | -1.09 | 3.7 | 0.00 ± 0.07 | 5.3 ± 0.3 | 1.2 ± 0.1 | 1671 | 1.3 |
| MIPS22661 | Bump | 8.1 | 4.8 | 0.50 | -1.81 | 2.9 | 0.21 ± 0.04 | 1.8 ± 0.1 | 1.0 ± 0.1 | 1670 | 2.4 |
| MIPS22277 | Bump | 7.8 | 5.9 | 0.53 | -1.67 | 3.0 | 0.06 ± 0.03 | 2.0 ± 0.1 | 2.0 ± 0.1 | 1670 | 1.4 |
| MIPS22204 | PL | 11.6 | 3.4 | 0.51 | -1.60 | 2.9 | 0.17 ± 0.04 | 0.7 ± 0.1 | 3.7 ± 0.3 | 1671 | 1.5 |
| MIPS16080 | Bump | 5.5 | 9.4 | 0.57 | -1.39 | 3.5 | 0.03 ± 0.03 | 2.8 ± 0.1 | 2.8 ± 0.2 | 1671 | 1.4 |
| MIPS22303 | PL | 2.4 | 6.4 | 0.42 | -0.99 | 2.6 | 0.19 ± 0.29 | 2.6 ± 0.5 | 1.1 ± 0.3 | 1669 | 1.0 |
| MIPS15977 | Bump | 8.6 | 5.8 | 0.52 | -1.87 | 3.0 | 0.22 ± 0.04 | 2.5 ± 0.1 | 0.7 ± 0.1 | 1669 | 1.4 |
| MIPS15928 | Bump | 7.7 | 7.5 | 0.52 | -1.90 | 3.1 | 0.22 ± 0.05 | 3.2 ± 0.1 | 0.6 ± 0.1 | 1671 | 2.8 |
| MIPS15840 | PL | 4.4 | 4.8 | 0.45 | -1.47 | 2.8 | 0.18 ± 0.22 | 2.2 ± 0.1 | 0.6 ± 0.1 | 1671 | 1.1 |
| MIPS22651 | Bump | 6.0 | 7.7 | 0.58 | -2.00 | 3.3 | 0.11 ± 0.06 | 2.4 ± 0.1 | 1.6 ± 0.1 | 1671 | 1.2 |
| MIPS22558 | Bump | 4.8 | 3.6 | 0.51 | -1.84 | 3.4 | 0.16 ± 0.12 | 3.1 ± 2.2 | 10.9 ± 5.2 | 1671 | 0.8 |
| MIPS22699 | PL | 4.3 | 3.6 | 0.49 | -2.37 | 3.0 | 0.09 ± 1.00 | 0.9 ± 0.1 | 3.2 ± 0.9 | 1671 | 1.1 |
| MIPS16122 | PL | 2.4 | 7.6 | 0.46 | -1.26 | 3.0 | 0.04 ± 0.20 | 2.3 ± 0.1 | 1.2 ± 0.1 | 1671 | 1.6 |
| MIPS15949 | Bump | 4.0 | 8.6 | 0.61 | -1.52 | 3.7 | 0.28 ± 0.05 | 2.8 ± 0.2 | 1.7 ± 0.2 | 1671 | 1.0 |
| MIPS15880 | Bump | 4.0 | 8.8 | 0.46 | -1.08 | 2.3 | 0.03 ± 0.08 | 5.4 ± 0.3 | 0.7 ± 0.1 | 1671 | 1.8 |
| MIPS16113 | Bump | 1.6 | 9.0 | 0.47 | -0.66 | 1.8 | 0.02 ± 0.12 | 2.6 ± 0.2 | 1.5 ± 0.2 | 1671 | 1.6 |
| MIPS22530 | Bump | 2.4 | 10.0 | 0.47 | -1.42 | 2.5 | 0.03 ± 0.13 | 3.9 ± 0.3 | 0.9 ± 0.1 | 1664 | 1.5 |
| MIPS15958 | PL | 7.7 | 3.7 | 0.53 | -1.74 | 3.0 | 0.67 ± 0.10 | 1.6 ± 0.1 | 0.4 ± 0.1 | 1671 | 1.1 |
| MIPS16095 | Bump | 9.3 | 5.7 | 0.52 | -1.83 | 3.1 | 0.06 ± 0.04 | 1.9 ± 0.1 | 1.7 ± 0.1 | 1671 | 1.2 |

Table A.2 (cont'd)

| Source Name | Bump/PL | S/N | r_{P} (kpc) | G | M_{20} | C | PSF Fraction | R_{eff} (kpc) | n | N_{dof} | χ^2_{ν} |
|-------------|---------|-------|-------------------------|------|----------|-----|-----------------|---------------------------|---------------|------------------|----------------|
| MIPS16144 | Bump | 3.7 | 13.0 | 0.50 | -1.46 | 4.4 | 0.10 ± 0.04 | 5.6 ± 1.0 | 3.1 ± 0.6 | 1664 | 1.3 |
| MIPS16059 | Bump | 5.2 | 8.4 | 0.53 | -1.31 | 2.5 | 0.05 ± 0.05 | 2.9 ± 0.1 | 0.3 ± 0.1 | 1671 | 1.7 |

APPENDIX B

TESTS OF FOUR SPS LIBRARIES

Four SPS libraries have been tested in this analysis of the SEDs of DOGs and SMGs. The first SPS library used in this paper is from the Bruzual & Charlot (2003) population synthesis library. It uses the isochrone synthesis technique (Charlot & Bruzual, 1991) and the Padova 1994 evolutionary tracks (Girardi et al., 1996) to compute the spectral evolution of stellar populations at ages between 10^5 and 2×10^{10} yr. The STEllar LIBrary (STELIB Le Borgne et al., 2003) of stellar spectra offer a median resolving power of 2000 over the wavelength range 3200 to 9500 Å. Outside this wavelength range, the BaSeL 3.1 libraries (Westera et al., 2002) are used and offer a median resolving power of 300 from 91 Å to $160\mu\text{m}$.

The second SPS library used here is an updated version of the Bruzual & Charlot (2003) population synthesis library (Charlot & Bruzual, private communication, hereafter CB07). The primary improvement included in these models is a new prescription for the thermally pulsing asymptotic giant branch (TP-AGB) evolution of low- and intermediate-mass stars Marigo & Girardi (2007) and Marigo et al. (2008). This has the effect of producing significantly redder near-IR colors for young and intermediate-age stellar populations, which leads to younger inferred ages and lower inferred masses for a given observed near-IR color. These new models otherwise still rely on the Padova 1994 evolutionary tracks and the combination of BaSeL 3.1 and STELIB spectral libraries.

The third SPS library employed in this paper is called a Flexible Stellar Population Synthesis library (FSPS; Conroy et al., 2009, 2010; Conroy & Gunn, 2010). This library uses the isochrone synthesis technique as well, but with updated evolutionary tracks (Padova 2008 Marigo & Girardi, 2007; Marigo et al., 2008). FSPS

adopts the BaSeL 3.1 spectral library (Westera et al., 2002) but includes TP-AGB spectra from a compilation of more than 100 optical/near-IR spectra spanning the wavelength range $0.5 - 2.5\mu\text{m}$ (Lançon & Wood, 2000; Lançon & Mouhcine, 2002). One feature of this library that is not available in the others is the ability to input a custom IMF (e.g., a “bottom-light” IMF).

The fourth and final SPS library used here is from Maraston (2005). This library adopts the “fuel-consumption” approach, in which the integration variable is the amount of hydrogen or helium consumed by nuclear burning during a given post-main-sequence phase (unlike the isochrone synthesis approach, in which the integration variable is the stellar mass). This library features a strong contribution from TP-AGB stars ($\approx 40\%$ of the bolometric light) for age ranges of 0.2 - 2 Gyr. A comparison between this library and that of Bruzual & Charlot (2003) found that the near-IR colors of $z \sim 2$ galaxies were better fit by the former (Maraston et al., 2006), highlighting the importance of a proper treatment of the TP-AGB phase for intermediate age stellar populations.

All four libraries yield similar constraints (within the uncertainties) on A_V , M_* , and stellar population age. For example, using the most recent Charlot & Bruzual libraries and assuming a SSP SFH and a Chabrier IMF, the mass range for bump DOGs was found to be $M_* = (0.3 - 1.2) \times 10^{11} M_\odot$ (see Table 5.4). With the same assumptions but instead using the Conroy et al. (2009) libraries, the mass range is $M_* = (0.4 - 1.6) \times 10^{11} M_\odot$. The slightly higher upper limit on M_* from the Conroy et al. (2009) libraries is typical of the other libraries tested here as well (Bruzual & Charlot, 2003; Maraston, 2005). This is a reflection of the fact that the most recent Charlot & Bruzual libraries include the TP-AGB evolution prescription of Marigo et al. (2008) for low- and intermediate-mass stars. This prescription leads to significantly redder near-IR colors, and hence younger inferred ages and lower

masses, for intermediate-age stellar populations and younger (age < 300 Myr).

REFERENCES

- Abraham, R. G., Valdes, F., Yee, H. K. C., & van den Bergh, S. 1994, *ApJ*, 432, 75
- Abraham, R. G., van den Bergh, S., & Nair, P. 2003, *ApJ*, 588, 218
- Armus, L., Heckman, T., & Miley, G. 1987, *AJ*, 94, 831
- Ashby, M. L. N., Stern, D., Brodwin, M., Griffith, R., Eisenhardt, P., Kozłowski, S., Kochanek, C. S., Bock, J. J., Borys, C., Brand, K., Brown, M. J. I., Cool, R., Cooray, A., Croft, S., Dey, A., Eisenstein, D., Gonzalez, A. H., Gorjian, V., Grogin, N. A., Ivison, R. J., Jacob, J., Jannuzi, B. T., Mainzer, A., Moustakas, L. A., Röttgering, H. J. A., Seymour, N., Smith, H. A., Stanford, S. A., Stauffer, J. R., Sullivan, I., van Breugel, W., Willner, S. P., & Wright, E. L. 2009, *ApJ*, 701, 428
- Bershady, M. A., Jangren, A., & Conselice, C. J. 2000, *AJ*, 119, 2645
- Berta, S., Lonsdale, C. J., Polletta, M., Savage, R. S., Franceschini, A., Buttery, H., Cimatti, A., Dias, J., Feruglio, C., Fiore, F., Held, E. V., La Franca, F., Maiolino, R., Marconi, A., Matute, I., Oliver, S. J., Ricciardelli, E., Rubele, S., Sacchi, N., Shupe, D., & Surace, J. 2007, *A&A*, 476, 151
- Bertin, E. & Arnouts, S. 1996, *A&AS*, 117, 393
- Blain, A. W., Chapman, S. C., Smail, I., & Ivison, R. 2004, *ApJ*, 611, 725
- Bohlin, R. C., Savage, B. D., & Drake, J. F. 1978, *ApJ*, 224, 132
- Borne, K. D., Bushouse, H., Lucas, R. A., & Colina, L. 2000, *ApJL*, 529, L77
- Borys, C., Chapman, S., Halpern, M., & Scott, D. 2003, *MNRAS*, 344, 385

- Borys, C., Smail, I., Chapman, S. C., Blain, A. W., Alexander, D. M., & Ivison, R. J. 2005, *ApJ*, 635, 853
- Bower, R. G., Benson, A. J., Malbon, R., Helly, J. C., Frenk, C. S., Baugh, C. M., Cole, S., & Lacey, C. G. 2006, *MNRAS*, 370, 645
- Brand, K., Brown, M. J. I., Dey, A., Jannuzi, B. T., Kochanek, C. S., Kenter, A. T., Fabricant, D., Fazio, G. G., Forman, W. R., Green, P. J., Jones, C. J., McNamara, B. R., Murray, S. S., Najita, J. R., Rieke, M., Shields, J. C., & Vikhlinin, A. 2006, *ApJ*, 641, 140
- Brand, K., Dey, A., Desai, V., Soifer, B. T., Bian, C., Armus, L., Brown, M. J. I., Le Floch, E., Higdon, S. J., Houck, J. R., Jannuzi, B. T., & Weedman, D. W. 2007, *ApJ*, 663, 204
- Brand, K., Weedman, D. W., Desai, V., Le Floch, E., Armus, L., Dey, A., Houck, J. R., Jannuzi, B. T., Smith, H. A., & Soifer, B. T. 2008, *ApJ*, 680, 119
- Brodwin, M., Dey, A., Brown, M. J. I., Pope, A., Armus, L., Bussmann, S., Desai, V., Jannuzi, B. T., & Le Floch, E. 2008, *ApJL*, 687, L65
- Bruzual, G. & Charlot, S. 2003, *MNRAS*, 344, 1000
- Bruzual A., G. 1983, *ApJ*, 273, 105
- Bussmann, R. S., Dey, A., Borys, C., Desai, V., Jannuzi, B. T., Le Floch, E., Melbourne, J., Sheth, K., & Soifer, B. T. 2009a, *ApJ*, 705, 184
- Bussmann, R. S., Dey, A., Lotz, J., Armus, L., Brand, K., Brown, M. J. I., Desai, V., Eisenhardt, P., Higdon, J., Higdon, S., Jannuzi, B. T., LeFloch, E., Melbourne, J., Soifer, B. T., & Weedman, D. 2009b, *ApJ*, 693, 750

- Calzetti, D., Armus, L., Bohlin, R. C., Kinney, A. L., Koornneef, J., & Storchi-Bergmann, T. 2000, *ApJ*, 533, 682
- Caputi, K. I., Lagache, G., Yan, L., Dole, H., Bavouzet, N., Le Floch, E., Choi, P. I., Helou, G., & Reddy, N. 2007, *ApJ*, 660, 97
- Chabrier, G. 2003, *PASP*, 115, 763
- Chapman, S. C., Blain, A. W., Smail, I., & Ivison, R. J. 2005, *ApJ*, 622, 772
- Charlot, S. & Bruzual, A. G. 1991, *ApJ*, 367, 126
- Charlot, S. & Fall, S. M. 2000, *ApJ*, 539, 718
- Conroy, C. & Gunn, J. E. 2010, *ApJ*, 712, 833
- Conroy, C., Gunn, J. E., & White, M. 2009, *ApJ*, 699, 486
- Conroy, C., White, M., & Gunn, J. E. 2010, *ApJ*, 708, 58
- Conselice, C. J. 2003, *ApJS*, 147, 1
- Conselice, C. J., Chapman, S. C., & Windhorst, R. A. 2003, *ApJL*, 596, L5
- Conselice, C. J., Newman, J. A., Georgakakis, A., Almaini, O., Coil, A. L., Cooper, M. C., Eisenhardt, P., Foucaud, S., Koekemoer, A., Lotz, J., Noeske, K., Weiner, B., & Willmer, C. N. A. 2007, *ApJL*, 660, L55
- Conselice, C. J., Rajgor, S., & Myers, R. 2008, *MNRAS*, 386, 909
- Coppin, K., Chapin, E. L., Mortier, A. M. J., Scott, S. E., Borys, C., Dunlop, J. S., Halpern, M., Hughes, D. H., Pope, A., Scott, D., Serjeant, S., Wagg, J., Alexander, D. M., Almaini, O., Aretxaga, I., Babbedge, T., Best, P. N., Blain, A., Chapman, S., Clements, D. L., Crawford, M., Dunne, L., Eales, S. A., Edge,

- A. C., Farrah, D., Gaztañaga, E., Gear, W. K., Granato, G. L., Greve, T. R., Fox, M., Ivison, R. J., Jarvis, M. J., Jenness, T., Lacey, C., Lepage, K., Mann, R. G., Marsden, G., Martinez-Sansigre, A., Oliver, S., Page, M. J., Peacock, J. A., Pearson, C. P., Percival, W. J., Priddey, R. S., Rawlings, S., Rowan-Robinson, M., Savage, R. S., Seigar, M., Sekiguchi, K., Silva, L., Simpson, C., Smail, I., Stevens, J. A., Takagi, T., Vaccari, M., van Kampen, E., & Willott, C. J. 2006, *MNRAS*, 372, 1621
- Coppin, K., Halpern, M., Scott, D., Borys, C., & Chapman, S. 2005, *MNRAS*, 357, 1022
- Coppin, K., Halpern, M., Scott, D., Borys, C., Dunlop, J., Dunne, L., Ivison, R., Wagg, J., Aretxaga, I., Battistelli, E., Benson, A., Blain, A., Chapman, S., Clements, D., Dye, S., Farrah, D., Hughes, D., Jenness, T., van Kampen, E., Lacey, C., Mortier, A., Pope, A., Priddey, R., Serjeant, S., Smail, I., Stevens, J., & Vaccari, M. 2008, *MNRAS*, 384, 1597
- Cowie, L. L., Songaila, A., Hu, E. M., & Cohen, J. G. 1996, *AJ*, 112, 839
- Croton, D. J., Springel, V., White, S. D. M., De Lucia, G., Frenk, C. S., Gao, L., Jenkins, A., Kauffmann, G., Navarro, J. F., & Yoshida, N. 2006, *MNRAS*, 365, 11
- Daddi, E., Cimatti, A., Renzini, A., Fontana, A., Mignoli, M., Pozzetti, L., Tozzi, P., & Zamorani, G. 2004, *ApJ*, 617, 746
- Daddi, E., Renzini, A., Pirzkal, N., Cimatti, A., Malhotra, S., Stiavelli, M., Xu, C., Pasquali, A., Rhoads, J. E., Brusa, M., di Serego Alighieri, S., Ferguson, H. C., Koekemoer, A. M., Moustakas, L. A., Panagia, N., & Windhorst, R. A. 2005, *ApJ*, 626, 680

- Dasyra, K. M., Yan, L., Helou, G., Surace, J., Sajina, A., & Colbert, J. 2008, *ApJ*, 680, 232
- Davé, R. 2008, *MNRAS*, 385, 147
- Davé, R., Finlator, K., Oppenheimer, B. D., Fardal, M., Katz, N., Kereš, D., & Weinberg, D. H. 2010, *MNRAS*, 404, 1355
- de Vries, W. H., Morganti, R., Röttgering, H. J. A., Vermeulen, R., van Breugel, W., Rengelink, R., & Jarvis, M. J. 2002, *AJ*, 123, 1784
- Desai, V., Armus, L., Soifer, B. T., Weedman, D. W., Higdon, S., Bian, C., Borys, C., Spoon, H. W. W., Charmandaris, V., Brand, K., Brown, M. J. I., Dey, A., Higdon, J., Houck, J., Jannuzi, B. T., Le Floch, E., Ashby, M. L. N., & Smith, H. A. 2006, *ApJ*, 641, 133
- Desai, V., Soifer, B. T., Dey, A., Le Floch, E., Armus, L., Brand, K., Brown, M. J. I., Brodwin, M., Jannuzi, B. T., Houck, J. R., Weedman, D. W., Ashby, M. L. N., Gonzalez, A., Huang, J., Smith, H. A., Teplitz, H., Willner, S. P., & Melbourne, J. 2009, *ApJ*, 700, 1190
- Dey, A., Bian, C., Soifer, B. T., Brand, K., Brown, M. J. I., Chaffee, F. H., Le Floch, E., Hill, G., Houck, J. R., Jannuzi, B. T., Rieke, M., Weedman, D., Brodwin, M., & Eisenhardt, P. 2005, *ApJ*, 629, 654
- Dey, A., Soifer, B. T., Desai, V., Brand, K., Le Floch, E., Brown, M. J. I., Jannuzi, B. T., Armus, L., Bussmann, S., Brodwin, M., Bian, C., Eisenhardt, P., Higdon, S. J., Weedman, D., & Willner, S. P. 2008, *ApJ*, 677, 943

- Dey, A. & The NDWFS/MIPS Collaboration. 2009, in *Astronomical Society of the Pacific Conference Series*, Vol. 408, *Astronomical Society of the Pacific Conference Series*, ed. W. Wang, Z. Yang, Z. Luo, & Z. Chen, 411–+
- Donley, J. L., Rieke, G. H., Alexander, D. M., Egami, E., & Perez-Gonzalez, P. G. 2010, *ArXiv e-prints*
- Donley, J. L., Rieke, G. H., Pérez-González, P. G., Rigby, J. R., & Alonso-Herrero, A. 2007, *ApJ*, 660, 167
- Draine, B. T. 2003, *ARA&A*, 41, 241
- Dunne, L., Eales, S., Edmunds, M., Ivison, R., Alexander, P., & Clements, D. L. 2000, *MNRAS*, 315, 115
- Dunne, L. & Eales, S. A. 2001, *MNRAS*, 327, 697
- Dunne, L., Eales, S. A., & Edmunds, M. G. 2003, *MNRAS*, 341, 589
- Dye, S., Eales, S. A., Aretxaga, I., Serjeant, S., Dunlop, J. S., Babbedge, T. S. R., Chapman, S. C., Cirasuolo, M., Clements, D. L., Coppin, K. E. K., Dunne, L., Egami, E., Farrah, D., Ivison, R. J., van Kampen, E., Pope, A., Priddey, R., Rieke, G. H., Schael, A. M., Scott, D., Simpson, C., Takagi, T., Takata, T., & Vaccari, M. 2008, *MNRAS*, 386, 1107
- Eisenhardt, P. R., Stern, D., Brodwin, M., Fazio, G. G., Rieke, G. H., Rieke, M. J., Werner, M. W., Wright, E. L., Allen, L. E., Arendt, R. G., Ashby, M. L. N., Barmby, P., Forrest, W. J., Hora, J. L., Huang, J.-S., Huchra, J., Pahre, M. A., Pipher, J. L., Reach, W. T., Smith, H. A., Stauffer, J. R., Wang, Z., Willner, S. P., Brown, M. J. I., Dey, A., Jannuzi, B. T., & Tiede, G. P. 2004, *ApJS*, 154, 48

- Elvis, M., Wilkes, B. J., McDowell, J. C., Green, R. F., Bechtold, J., Willner, S. P., Oey, M. S., Polomski, E., & Cutri, R. 1994, *ApJS*, 95, 1
- Erb, D. K., Steidel, C. C., Shapley, A. E., Pettini, M., Reddy, N. A., & Adelberger, K. L. 2006, *ApJ*, 646, 107
- Faber, S. M., Phillips, A. C., Kibrick, R. I., Alcott, B., Allen, S. L., Burrous, J., Cantrall, T., Clarke, D., Coil, A. L., Cowley, D. J., Davis, M., Deich, W. T. S., Dietsch, K., Gilmore, D. K., Harper, C. A., Hilyard, D. F., Lewis, J. P., McVeigh, M., Newman, J., Osborne, J., Schiavon, R., Stover, R. J., Tucker, D., Wallace, V., Wei, M., Wirth, G., & Wright, C. A. 2003, in Presented at the Society of Photo-Optical Instrumentation Engineers (SPIE) Conference, Vol. 4841, Instrument Design and Performance for Optical/Infrared Ground-based Telescopes. Edited by Iye, Masanori; Moorwood, Alan F. M. *Proceedings of the SPIE*, Volume 4841, pp. 1657-1669 (2003)., ed. M. Iye & A. F. M. Moorwood, 1657–1669
- Farrah, D., Lonsdale, C. J., Borys, C., Fang, F., Waddington, I., Oliver, S., Rowan-Robinson, M., Babbedge, T., Shupe, D., Polletta, M., Smith, H. E., & Surace, J. 2006, *ApJL*, 641, L17
- Farrah, D., Lonsdale, C. J., Weedman, D. W., Spoon, H. W. W., Rowan-Robinson, M., Polletta, M., Oliver, S., Houck, J. R., & Smith, H. E. 2008, *ApJ*, 677, 957
- Fazio, G. G., Hora, J. L., Allen, L. E., Ashby, M. L. N., Barmby, P., Deutsch, L. K., Huang, J.-S., Kleiner, S., Marengo, M., Megeath, S. T., Melnick, G. J., Pahre, M. A., Patten, B. M., Polizotti, J., Smith, H. A., Taylor, R. S., Wang, Z., Willner, S. P., Hoffmann, W. F., Pipher, J. L., Forrest, W. J., McMurty, C. W., McCreight, C. R., McKelvey, M. E., McMurray, R. E., Koch, D. G., Moseley, S. H., Arendt, R. G., Mentzell, J. E., Marx, C. T., Losch, P., Mayman,

- P., Eichhorn, W., Krebs, D., Jhabvala, M., Gezari, D. Y., Fixsen, D. J., Flores, J., Shakoorzadeh, K., Jungo, R., Hakun, C., Workman, L., Karpati, G., Kichak, R., Whitley, R., Mann, S., Tollestrup, E. V., Eisenhardt, P., Stern, D., Gorjian, V., Bhattacharya, B., Carey, S., Nelson, B. O., Glaccum, W. J., Lacy, M., Lowrance, P. J., Laine, S., Reach, W. T., Stauffer, J. A., Surace, J. A., Wilson, G., Wright, E. L., Hoffman, A., Domingo, G., & Cohen, M. 2004, *ApJS*, 154, 10
- Fiolet, N., Omont, A., Polletta, M., Owen, F., Berta, S., Shupe, D., Siana, B., Lonsdale, C., Strazzullo, V., Pannella, M., Baker, A. J., Beelen, A., Biggs, A., De Breuck, C., Farrah, D., Ivison, R., Lagache, G., Lutz, D., Tacconi, L. J., & Zylka, R. 2009, *A&A*, 508, 117
- Fiore, F., Grazian, A., Santini, P., Puccetti, S., Brusa, M., Feruglio, C., Fontana, A., Giallongo, E., Comastri, A., Gruppioni, C., Pozzi, F., Zamorani, G., & Vignali, C. 2008, *ApJ*, 672, 94
- Fiore, F., Puccetti, S., Brusa, M., Salvato, M., Zamorani, G., Aldcroft, T., Aussel, H., Brunner, H., Capak, P., Cappelluti, N., Civano, F., Comastri, A., Elvis, M., Feruglio, C., Finoguenov, A., Fruscione, A., Gilli, R., Hasinger, G., Koekemoer, A., Kartaltepe, J., Ilbert, O., Impey, C., Le Floch, E., Lilly, S., Mainieri, V., Martinez-Sansigre, A., McCracken, H. J., Menci, N., Merloni, A., Miyaji, T., Sanders, D. B., Sargent, M., Schinnerer, E., Scoville, N., Silverman, J., Smolcic, V., Steffen, A., Santini, P., Taniguchi, Y., Thompson, D., Trump, J. R., Vignali, C., Urry, M., & Yan, L. 2009, *ApJ*, 693, 447
- Ford, H. C., Bartko, F., Bely, P. Y., Broadhurst, T., Burrows, C. J., Cheng, E. S., Clampin, M., Crocker, J. H., Feldman, P. D., Golimowski, D. A., Hartig, G. F., Illingworth, G., Kimble, R. A., Lesser, M. P., Miley, G., Neff, S. G., Postman, M., Sparks, W. B., Tsvetanov, Z., White, R. L., Sullivan, P., Krebs, C. A.,

- Leviton, D. B., La Jeunesse, T., Burmester, W., Fike, S., Johnson, R., Slusher, R. B., Volmer, P., & Woodruff, R. A. 1998, in Presented at the Society of Photo-Optical Instrumentation Engineers (SPIE) Conference, Vol. 3356, Proc. SPIE Vol. 3356, p. 234-248, Space Telescopes and Instruments V, Pierre Y. Bely; James B. Breckinridge; Eds., ed. P. Y. Bely & J. B. Breckinridge, 234–248
- Franceschini, A., Aussel, H., Cesarsky, C. J., Elbaz, D., & Fadda, D. 2001, *A&A*, 378, 1
- Franx, M., Labbé, I., Rudnick, G., van Dokkum, P. G., Daddi, E., Förster Schreiber, N. M., Moorwood, A., Rix, H.-W., Röttgering, H., van de Wel, A., van der Werf, P., & van Starkenburg, L. 2003, *ApJL*, 587, L79
- Gallagher, S. C., Brandt, W. N., Chartas, G., Garmire, G. P., & Sambruna, R. M. 2002, *ApJ*, 569, 655
- Genzel, R., Burkert, A., Bouché, N., Cresci, G., Förster Schreiber, N. M., Shapley, A., Shapiro, K., Tacconi, L. J., Buschkamp, P., Cimatti, A., Daddi, E., Davies, R., Eisenhauer, F., Erb, D. K., Genel, S., Gerhard, O., Hicks, E., Lutz, D., Naab, T., Ott, T., Rabien, S., Renzini, A., Steidel, C. C., Sternberg, A., & Lilly, S. J. 2008, *ApJ*, 687, 59
- Girardi, L., Bressan, A., Chiosi, C., Bertelli, G., & Nasi, E. 1996, *A&AS*, 117, 113
- Glasser, G. J. 1962, *Journal of the American Statistical Association*, 57, 648
- Greve, T. R., Bertoldi, F., Smail, I., Neri, R., Chapman, S. C., Blain, A. W., Ivison, R. J., Genzel, R., Omont, A., Cox, P., Tacconi, L., & Kneib, J.-P. 2005, *MNRAS*, 359, 1165

- Greve, T. R., Ivison, R. J., Bertoldi, F., Stevens, J. A., Dunlop, J. S., Lutz, D., & Carilli, C. L. 2004, *MNRAS*, 354, 779
- Hainline, L. J., Blain, A. W., Smail, I., Alexander, D. M., Armus, L., Chapman, S. C., & Ivison, R. J. 2010, *ArXiv e-prints*
- Hainline, L. J., Blain, A. W., Smail, I., Frayer, D. T., Chapman, S. C., Ivison, R. J., & Alexander, D. M. 2009, *ApJ*, 699, 1610
- Helou, G., Khan, I. R., Malek, L., & Boehmer, L. 1988, *ApJS*, 68, 151
- Hildebrand, R. H. 1983, *QJRAS*, 24, 267
- Holland, W. S., Robson, E. I., Gear, W. K., Cunningham, C. R., Lightfoot, J. F., Jenness, T., Ivison, R. J., Stevens, J. A., Ade, P. A. R., Griffin, M. J., Duncan, W. D., Murphy, J. A., & Naylor, D. A. 1999, *MNRAS*, 303, 659
- Hopkins, P. F., Cox, T. J., Kereš, D., & Hernquist, L. 2008a, *ApJS*, 175, 390
- Hopkins, P. F., Hernquist, L., Cox, T. J., Di Matteo, T., Robertson, B., & Springel, V. 2006, *ApJS*, 163, 1
- Hopkins, P. F., Hernquist, L., Cox, T. J., & Kereš, D. 2008b, *ApJS*, 175, 356
- Houck, J. R., Roellig, T. L., van Cleve, J., Forrest, W. J., Herter, T., Lawrence, C. R., Matthews, K., Reitsema, H. J., Soifer, B. T., Watson, D. M., Weedman, D., Huisjen, M., Troeltzsch, J., Barry, D. J., Bernard-Salas, J., Blacken, C. E., Brandl, B. R., Charmandaris, V., Devost, D., Gull, G. E., Hall, P., Henderson, C. P., Higdon, S. J. U., Pirger, B. E., Schoenwald, J., Sloan, G. C., Uchida, K. I., Appleton, P. N., Armus, L., Burgdorf, M. J., Fajardo-Acosta, S. B., Grillmair, C. J., Ingalls, J. G., Morris, P. W., & Teplitz, H. I. 2004, *ApJS*, 154, 18

- Houck, J. R., Soifer, B. T., Weedman, D., Higdon, S. J. U., Higdon, J. L., Herter, T., Brown, M. J. I., Dey, A., Jannuzi, B. T., Le Floch, E., Rieke, M., Armus, L., Charmandaris, V., Brandl, B. R., & Teplitz, H. I. 2005, *ApJL*, 622, L105
- Huang, J., Faber, S. M., Daddi, E., Laird, E. S., Lai, K., Omont, A., Wu, Y., Younger, J. D., Bundy, K., Cattaneo, A., Chapman, S. C., Conselice, C. J., Dickinson, M., Egami, E., Fazio, G. G., Im, M., Koo, D., Le Floch, E., Papovich, C., Rigopoulou, D., Smail, I., Song, M., Van de Werf, P. P., Webb, T. M. A., Willmer, C. N. A., Willner, S. P., & Yan, L. 2009, *ApJ*, 700, 183
- Hughes, D. H., Dunlop, J. S., & Rawlings, S. 1997, *MNRAS*, 289, 766
- Hughes, D. H., Gear, W. K., & Robson, E. I. 1994, *MNRAS*, 270, 641
- Hutchings, J. B. & Neff, S. G. 1987, *AJ*, 93, 14
- Iglesias-Páramo, J., Buat, V., Hernández-Fernández, J., Xu, C. K., Burgarella, D., Takeuchi, T. T., Boselli, A., Shupe, D., Rowan-Robinson, M., Babbedge, T., Conrow, T., Fang, F., Farrah, D., González-Solares, E., Lonsdale, C., Smith, G., Surace, J., Barlow, T. A., Forster, K., Friedman, P. G., Martin, D. C., Morrissey, P., Neff, S. G., Schiminovich, D., Seibert, M., Small, T., Wyder, T. K., Bianchi, L., Donas, J., Heckman, T. M., Lee, Y., Madore, B. F., Milliard, B., Rich, R. M., Szalay, A. S., Welsh, B. Y., & Yi, S. K. 2007, *ApJ*, 670, 279
- Jannuzi, B. T. & Dey, A. 1999, in *Astronomical Society of the Pacific Conference Series*, Vol. 191, *Photometric Redshifts and the Detection of High Redshift Galaxies*, ed. R. Weymann, L. Storrie-Lombardi, M. Sawicki, & R. Brunner, 111–+
- Jonsson, P., Cox, T. J., Primack, J. R., & Somerville, R. S. 2006, *ApJ*, 637, 255

- Juneau, S., Glazebrook, K., Crampton, D., McCarthy, P. J., Savaglio, S., Abraham, R., Carlberg, R. G., Chen, H., Le Borgne, D., Marzke, R. O., Roth, K., Jørgensen, I., Hook, I., & Murowinski, R. 2005, *ApJL*, 619, L135
- Kauffmann, G., Heckman, T. M., White, S. D. M., Charlot, S., Tremonti, C., Peng, E. W., Seibert, M., Brinkmann, J., Nichol, R. C., SubbaRao, M., & York, D. 2003, *MNRAS*, 341, 54
- Kenter, A., Murray, S. S., Forman, W. R., Jones, C., Green, P., Kochanek, C. S., Vikhlinin, A., Fabricant, D., Fazio, G., Brand, K., Brown, M. J. I., Dey, A., Jannuzi, B. T., Najita, J., McNamara, B., Shields, J., & Rieke, M. 2005, *ApJS*, 161, 9
- Koekemoer, A. M., Fruchter, A. S., Hook, R. N., & Hack, W. 2002, in *The 2002 HST Calibration Workshop : Hubble after the Installation of the ACS and the NICMOS Cooling System*, Proceedings of a Workshop held at the Space Telescope Science Institute, Baltimore, Maryland, October 17 and 18, 2002. Edited by Santiago Arribas, Anton Koekemoer, and Brad Whitmore. Baltimore, MD: Space Telescope Science Institute, 2002., p.337, ed. S. Arribas, A. Koekemoer, & B. Whitmore, 337–+
- Kornei, K. A., Shapley, A. E., Erb, D. K., Steidel, C. C., Reddy, N. A., Pettini, M., & Bogosavljević, M. 2010, *ApJ*, 711, 693
- Kovács, A. 2006, PhD thesis, Caltech
- Kovács, A., Chapman, S. C., Dowell, C. D., Blain, A. W., Ivison, R. J., Smail, I., & Phillips, T. G. 2006, *ApJ*, 650, 592

- Kovács, A., Omont, A., Beelen, A., Lonsdale, C., Polletta, M., Fiolet, N., Greve, T. R., Borys, C., Cox, P., De Breuck, C., Dole, H., Dowell, C. D., Farrah, D., Lagache, G., Menten, K. M., Bell, T. A., & Owen, F. 2010, *ApJ*, 717, 29
- Kreysa, E., Gemünd, H., Gromke, J., Haslam, C. G. T., Reichertz, L., Haller, E. E., Beeman, J. W., Hansen, V., Sievers, A., & Zylka, R. 1999, *Infrared Physics and Technology*, 40, 191
- Kroupa, P. 2001, *MNRAS*, 322, 231
- Labbé, I., Franx, M., Rudnick, G., Schreiber, N. M. F., Rix, H.-W., Moorwood, A., van Dokkum, P. G., van der Werf, P., Röttgering, H., van Starkenburg, L., van de Wel, A., Kuijken, K., & Daddi, E. 2003, *AJ*, 125, 1107
- Lacy, M., Wilson, G., Masci, F., Storrie-Lombardi, L. J., Appleton, P. N., Armus, L., Chapman, S. C., Choi, P. I., Fadda, D., Fang, F., Frayer, D. T., Heinrichsen, I., Helou, G., Im, M., Laine, S., Marleau, F. R., Shupe, D. L., Soifer, B. T., Squires, G. K., Surace, J., Teplitz, H. I., & Yan, L. 2005, *ApJS*, 161, 41
- Lançon, A. & Mouhcine, M. 2002, *A&A*, 393, 167
- Lançon, A. & Wood, P. R. 2000, *A&AS*, 146, 217
- Laurent, G. T., Glenn, J., Egami, E., Rieke, G. H., Ivison, R. J., Yun, M. S., Aguirre, J. E., Maloney, P. R., & Haig, D. 2006, *ApJ*, 643, 38
- Law, D. R., Steidel, C. C., Erb, D. K., Larkin, J. E., Pettini, M., Shapley, A. E., & Wright, S. A. 2007, *ApJ*, 669, 929
- Le Borgne, J., Bruzual, G., Pelló, R., Lançon, A., Rocca-Volmerange, B., Sanahuja, B., Schaerer, D., Soubiran, C., & Vílchez-Gómez, R. 2003, *A&A*, 402, 433

- Le Floch, E., Papovich, C., Dole, H., Bell, E. F., Lagache, G., Rieke, G. H., Egami, E., Pérez-González, P. G., Alonso-Herrero, A., Rieke, M. J., Blaylock, M., Engelbracht, C. W., Gordon, K. D., Hines, D. C., Misselt, K. A., Morrison, J. E., & Mould, J. 2005, *ApJ*, 632, 169
- Leong, M., Peng, R., Houde, M., Yoshida, H., Chamberlin, R., & Phillips, T. G. 2006, in *Society of Photo-Optical Instrumentation Engineers (SPIE) Conference Series*, Vol. 6275, Society of Photo-Optical Instrumentation Engineers (SPIE) Conference Series
- Lisker, T. 2008, *ApJS*, 179, 319
- Lonsdale, C. J., Polletta, M. d. C., Omont, A., Shupe, D., Berta, S., Zylka, R., Siana, B., Lutz, D., Farrah, D., Smith, H. E., Lagache, G., DeBreuck, C., Owen, F., Beelen, A., Weedman, D., Franceschini, A., Clements, D., Tacconi, L., Afonso-Luis, A., Pérez-Fournon, I., Cox, P., & Bertoldi, F. 2009, *ApJ*, 692, 422
- Lotz, J. M., Jonsson, P., Cox, T. J., & Primack, J. R. 2008, *MNRAS*, 391, 1137
- . 2009a, *ArXiv e-prints*
- . 2009b, *ArXiv e-prints*
- Lotz, J. M., Madau, P., Giavalisco, M., Primack, J., & Ferguson, H. C. 2006, *ApJ*, 636, 592
- Lotz, J. M., Primack, J., & Madau, P. 2004, *AJ*, 128, 163
- Lutz, D., Yan, L., Armus, L., Helou, G., Tacconi, L. J., Genzel, R., & Baker, A. J. 2005, *ApJL*, 632, L13
- Madau, P., Ferguson, H. C., Dickinson, M. E., Giavalisco, M., Steidel, C. C., & Fruchter, A. 1996, *MNRAS*, 283, 1388

- Magnelli, B., Elbaz, D., Chary, R. R., Dickinson, M., Le Borgne, D., Frayer, D. T., & Willmer, C. N. A. 2009, *A&A*, 496, 57
- Magorrian, J., Tremaine, S., Richstone, D., Bender, R., Bower, G., Dressler, A., Faber, S. M., Gebhardt, K., Green, R., Grillmair, C., Kormendy, J., & Lauer, T. 1998, *AJ*, 115, 2285
- Maraston, C. 2005, *MNRAS*, 362, 799
- Maraston, C., Daddi, E., Renzini, A., Cimatti, A., Dickinson, M., Papovich, C., Pasquali, A., & Pirzkal, N. 2006, *ApJ*, 652, 85
- Marigo, P. & Girardi, L. 2007, *A&A*, 469, 239
- Marigo, P., Girardi, L., Bressan, A., Groenewegen, M. A. T., Silva, L., & Granato, G. L. 2008, *A&A*, 482, 883
- Melbourne, J., Bussman, R. S., Brand, K., Desai, V., Armus, L., Dey, A., Jannuzi, B. T., Houck, J. R., Matthews, K., & Soifer, B. T. 2009, *AJ*, 137, 4854
- Melbourne, J., Desai, V., Armus, L., Dey, A., Brand, K., Thompson, D., Soifer, B. T., Matthews, K., Jannuzi, B. T., & Houck, J. R. 2008, *AJ*, 136, 1110
- Menéndez-Delmestre, K., Blain, A. W., Smail, I., Alexander, D. M., Chapman, S. C., Armus, L., Frayer, D., Ivison, R. J., & Teplitz, H. 2009, *ApJ*, 699, 667
- Michałowski, M., Hjorth, J., & Watson, D. 2010, *A&A*, 514, A67+
- Mihos, J. C. & Hernquist, L. 1996, *ApJ*, 464, 641
- Murphy, Jr., T. W., Armus, L., Matthews, K., Soifer, B. T., Mazzarella, J. M., Shupe, D. L., Strauss, M. A., & Neugebauer, G. 1996, *AJ*, 111, 1025

- Murray, S. S., Kenter, A., Forman, W. R., Jones, C., Green, P. J., Kochanek, C. S., Vikhlinin, A., Fabricant, D., Fazio, G., Brand, K., Brown, M. J. I., Dey, A., Jannuzi, B. T., Najita, J., McNamara, B., Shields, J., & Rieke, M. 2005, *ApJS*, 161, 1
- Muzzin, A., Marchesini, D., van Dokkum, P. G., Labbé, I., Kriek, M., & Franx, M. 2009, *ApJ*, 701, 1839
- Narayanan, D., Dey, A., Hayward, C., Cox, T. J., Bussmann, R. S., Brodwin, M., Jonsson, P., Hopkins, P., Groves, B., Younger, J. D., & Hernquist, L. 2009, *ArXiv e-prints*
- Neugebauer, G., Habing, H. J., van Duinen, R., Aumann, H. H., Baud, B., Beichman, C. A., Beintema, D. A., Boggess, N., Clegg, P. E., de Jong, T., Emerson, J. P., Gautier, T. N., Gillett, F. C., Harris, S., Hauser, M. G., Houck, J. R., Jennings, R. E., Low, F. J., Marsden, P. L., Miley, G., Olton, F. M., Pottasch, S. R., Raimond, E., Rowan-Robinson, M., Soifer, B. T., Walker, R. G., Wesselius, P. R., & Young, E. 1984, *ApJL*, 278, L1
- Novak, G. S., Cox, T. J., Primack, J. R., Jonsson, P., & Dekel, A. 2006, *ApJL*, 646, L9
- Oke, J. B., Cohen, J. G., Carr, M., Cromer, J., Dingizian, A., Harris, F. H., Labrecque, S., Lucinio, R., Schaal, W., Epps, H., & Miller, J. 1995, *PASP*, 107, 375
- Papovich, C., Dickinson, M., & Ferguson, H. C. 2001, *ApJ*, 559, 620
- Papovich, C., Rudnick, G., Le Floch, E., van Dokkum, P. G., Rieke, G. H., Taylor, E. N., Armus, L., Gawiser, E., Huang, J., Marcillac, D., & Franx, M. 2007, *ApJ*, 668, 45

- Pascale, E., Ade, P. A. R., Bock, J. J., Chapin, E. L., Devlin, M. J., Dye, S., Eales, S. A., Griffin, M., Gundersen, J. O., Halpern, M., Hargrave, P. C., Hughes, D. H., Klein, J., Marsden, G., Mauskopf, P., Moncelsi, L., Netterfield, C. B., Olmi, L., Patanchon, G., Rex, M., Scott, D., Semisch, C., Thomas, N., Truch, M. D. P., Tucker, C., Tucker, G. S., Viero, M. P., & Wiebe, D. V. 2009, ArXiv e-prints
- Peng, C. Y., Ho, L. C., Impey, C. D., & Rix, H.-W. 2002, *AJ*, 124, 266
- Pérez-González, P. G., Rieke, G. H., Egami, E., Alonso-Herrero, A., Dole, H., Papovich, C., Blaylock, M., Jones, J., Rieke, M., Rigby, J., Barmby, P., Fazio, G. G., Huang, J., & Martin, C. 2005, *ApJ*, 630, 82
- Petrosian, V. 1976, *ApJL*, 209, L1
- Pierce, C. M., Lotz, J. M., Primack, J. R., Rosario, D. J. V., Griffith, R. L., Conselice, C. J., Faber, S. M., Koo, D. C., Coil, A. L., Salim, S., Koekemoer, A. M., Laird, E. S., Ivison, R. J., & Yan, R. 2010, *MNRAS*, 455
- Polletta, M., Weedman, D., Hönig, S., Lonsdale, C. J., Smith, H. E., & Houck, J. 2008, *ApJ*, 675, 960
- Pope, A., Borys, C., Scott, D., Conselice, C., Dickinson, M., & Mobasher, B. 2005, *MNRAS*, 358, 149
- Pope, A., Bussmann, R. S., Dey, A., Meger, N., Alexander, D. M., Brodwin, M., Chary, R., Dickinson, M. E., Frayer, D. T., Greve, T. R., Huynh, M., Lin, L., Morrison, G., Scott, D., & Yan, C. 2008a, *ApJ*, 689, 127
- Pope, A., Chary, R.-R., Alexander, D. M., Armus, L., Dickinson, M., Elbaz, D., Frayer, D., Scott, D., & Teplitz, H. 2008b, *ApJ*, 675, 1171

- Ravindranath, S., Giavalisco, M., Ferguson, H. C., Conselice, C., Katz, N., Weinberg, M., Lotz, J., Dickinson, M., Fall, S. M., Mobasher, B., & Papovich, C. 2006, *ApJ*, 652, 963
- Rieke, G. H. 1978, *ApJ*, 226, 550
- Rieke, G. H., Alonso-Herrero, A., Weiner, B. J., Perez-Gonzalez, P. G., Blaylock, M., Donley, J. L., Marcillac, D., & . 2008, ArXiv e-prints
- Rieke, G. H. & Lebofsky, M. J. 1981, *ApJ*, 250, 87
- Rieke, G. H. & Low, F. J. 1972, *ApJL*, 176, L95+
- Rieke, G. H., Young, E. T., Engelbracht, C. W., Kelly, D. M., Low, F. J., Haller, E. E., Beeman, J. W., Gordon, K. D., Stansberry, J. A., Misselt, K. A., Cadien, J., Morrison, J. E., Rivlis, G., Latter, W. B., Noriega-Crespo, A., Padgett, D. L., Stapelfeldt, K. R., Hines, D. C., Egami, E., Muzerolle, J., Alonso-Herrero, A., Blaylock, M., Dole, H., Hinz, J. L., Le Floch, E., Papovich, C., Pérez-González, P. G., Smith, P. S., Su, K. Y. L., Bennett, L., Frayer, D. T., Henderson, D., Lu, N., Masci, F., Pesenson, M., Rebull, L., Rho, J., Keene, J., Stolovy, S., Wachter, S., Wheaton, W., Werner, M. W., & Richards, P. L. 2004, *ApJS*, 154, 25
- Rigopoulou, D., Lawrence, A., & Rowan-Robinson, M. 1996, *MNRAS*, 278, 1049
- Sajina, A., Yan, L., Armus, L., Choi, P., Fadda, D., Helou, G., & Spoon, H. 2007a, *ApJ*, 664, 713
- Sajina, A., Yan, L., Lacy, M., & Huynh, M. 2007b, *ApJL*, 667, L17
- Sajina, A., Yan, L., Lutz, D., Steffen, A., Helou, G., Huynh, M., Frayer, D., Choi, P., Tacconi, L., & Dasyra, K. 2008, *ApJ*, 683, 659

- Salpeter, E. E. 1955, *ApJ*, 121, 161
- Sanders, D. B., Mazzarella, J. M., Kim, D., Surace, J. A., & Soifer, B. T. 2003, *AJ*, 126, 1607
- Sanders, D. B. & Mirabel, I. F. 1996, *ARA&A*, 34, 749
- Sanders, D. B., Soifer, B. T., Elias, J. H., Madore, B. F., Matthews, K., Neugebauer, G., & Scoville, N. Z. 1988a, *ApJ*, 325, 74
- Sanders, D. B., Soifer, B. T., Elias, J. H., Neugebauer, G., & Matthews, K. 1988b, *ApJL*, 328, L35
- Sargsyan, L. A., Weedman, D. W., & Houck, J. R. 2010, *ApJ*, 715, 986
- Sault, R. J., Teuben, P. J., & Wright, M. C. H. 1995, in *Astronomical Society of the Pacific Conference Series*, Vol. 77, *Astronomical Data Analysis Software and Systems IV*, ed. R. A. Shaw, H. E. Payne, & J. J. E. Hayes, 433–+
- Schade, D., Lilly, S. J., Crampton, D., Hammer, F., Le Fevre, O., & Tresse, L. 1995, *ApJL*, 451, L1+
- Sersic, J. L. 1968, *Atlas de galaxias australes* (Cordoba, Argentina: Observatorio Astronomico, 1968)
- Shapley, A. E., Steidel, C. C., Erb, D. K., Reddy, N. A., Adelberger, K. L., Pettini, M., Barmby, P., & Huang, J. 2005, *ApJ*, 626, 698
- Shen, Y., Strauss, M. A., Ross, N. P., Hall, P. B., Lin, Y., Richards, G. T., Schneider, D. P., Weinberg, D. H., Connolly, A. J., Fan, X., Hennawi, J. F., Shankar, F., Vanden Berk, D. E., Bahcall, N. A., & Brunner, R. J. 2009, *ApJ*, 697, 1656
- Silva, L., Granato, G. L., Bressan, A., & Danese, L. 1998, *ApJ*, 509, 103

- Smail, I., Chapman, S. C., Blain, A. W., & Ivison, R. J. 2004, *ApJ*, 616, 71
- Smail, I., Ivison, R. J., & Blain, A. W. 1997, *ApJL*, 490, L5+
- Soifer, B. T., Sanders, D. B., Neugebauer, G., Danielson, G. E., Lonsdale, C. J., Madore, B. F., & Persson, S. E. 1986, *ApJL*, 303, L41
- Spergel, D. N., Bean, R., Doré, O., Nolta, M. R., Bennett, C. L., Dunkley, J., Hinshaw, G., Jarosik, N., Komatsu, E., Page, L., Peiris, H. V., Verde, L., Halpern, M., Hill, R. S., Kogut, A., Limon, M., Meyer, S. S., Odegard, N., Tucker, G. S., Weiland, J. L., Wollack, E., & Wright, E. L. 2007, *ApJS*, 170, 377
- Steidel, C. C., Giavalisco, M., Pettini, M., Dickinson, M., & Adelberger, K. L. 1996, *ApJL*, 462, L17+
- Swinbank, A. M., Chapman, S. C., Smail, I., Lindner, C., Borys, C., Blain, A. W., Ivison, R. J., & Lewis, G. F. 2006, *MNRAS*, 371, 465
- Swinbank, A. M., Smail, I., Chapman, S. C., Blain, A. W., Ivison, R. J., & Keel, W. C. 2004, *ApJ*, 617, 64
- Swinbank, A. M., Smail, I., Chapman, S. C., Borys, C., Alexander, D. M., Blain, A. W., Conselice, C. J., Hainline, L. J., & Ivison, R. J. 2010a, *MNRAS*, 405, 234
- Swinbank, M., Smail, I., Chapman, S., Borys, C., Alexander, D., Blain, A., Conselice, C., Hainline, L., & Ivison, R. 2010b, *ArXiv e-prints*
- Tacconi, L. J., Genzel, R., Smail, I., Neri, R., Chapman, S. C., Ivison, R. J., Blain, A., Cox, P., Omont, A., Bertoldi, F., Greve, T., Förster Schreiber, N. M., Genel, S., Lutz, D., Swinbank, A. M., Shapley, A. E., Erb, D. K., Cimatti, A., Daddi, E., & Baker, A. J. 2008, *ApJ*, 680, 246

- Tacconi, L. J., Neri, R., Chapman, S. C., Genzel, R., Smail, I., Ivison, R. J., Bertoldi, F., Blain, A., Cox, P., Greve, T., & Omont, A. 2006, *ApJ*, 640, 228
- Thompson, R. I., Rieke, M., Schneider, G., Hines, D. C., & Corbin, M. R. 1998, *ApJL*, 492, L95+
- Toft, S., van Dokkum, P., Franx, M., Labbe, I., Förster Schreiber, N. M., Wuyts, S., Webb, T., Rudnick, G., Zirm, A., Kriek, M., van der Werf, P., Blakeslee, J. P., Illingworth, G., Rix, H.-W., Papovich, C., & Moorwood, A. 2007, *ApJ*, 671, 285
- Trauger, J. T., Ballester, G. E., Burrows, C. J., Casertano, S., Clarke, J. T., Crisp, D., Evans, R. W., Gallagher, III, J. S., Griffiths, R. E., Hester, J. J., Hoessel, J. G., Holtzman, J. A., Krist, J. E., Mould, J. R., Scowen, P. A., Stapelfeldt, K. R., Watson, A. M., & Westphal, J. A. 1994, *ApJL*, 435, L3
- Tyler, K. D., Floc'h, E. L., Rieke, G. H., Dey, A., Desai, V., Brand, K., Borys, C., Jannuzi, B. T., Armus, L., Dole, H., Papovich, C., Brown, M. J. I., Blaylock, M., Higdon, S. J. U., Higdon, J. L., Charmandaris, V., Ashby, M. L. N., & Smith, H. A. 2009, *ApJ*, 691, 1846
- van Dokkum, P. G. 2008, *ApJ*, 674, 29
- van Dokkum, P. G., Labbé, I., Marchesini, D., Quadri, R., Brammer, G., Whitaker, K. E., Kriek, M., Franx, M., Rudnick, G., Illingworth, G., Lee, K., & Muzzin, A. 2009, *PASP*, 121, 2
- Viana, A., Wiklind, T., Koekemoer, A., Thatte, D., Dahlen, T., Barker, E., de Jong, R., & Pirzkal, N. 2009, *NICMOS Instrument Handbook Volume 11*, 11, 1
- Wake, D. A., Nichol, R. C., Eisenstein, D. J., Loveday, J., Edge, A. C., Cannon, R., Smail, I., Schneider, D. P., Scranton, R., Carson, D., Ross, N. P., Brunner, R. J.,

- Colless, M., Couch, W. J., Croom, S. M., Driver, S. P., da Ângela, J., Jester, S., de Propriis, R., Drinkwater, M. J., Bland-Hawthorn, J., Pimbblet, K. A., Roseboom, I. G., Shanks, T., Sharp, R. G., & Brinkmann, J. 2006, *MNRAS*, 372, 537
- Wang, R., Carilli, C. L., Wagg, J., Bertoldi, F., Walter, F., Menten, K. M., Omont, A., Cox, P., Strauss, M. A., Fan, X., Jiang, L., & Schneider, D. P. 2008, *ApJ*, 687, 848
- Weedman, D., Polletta, M., Lonsdale, C. J., Wilkes, B. J., Siana, B., Houck, J. R., Surace, J., Shupe, D., Farrah, D., & Smith, H. E. 2006a, *ApJ*, 653, 101
- Weedman, D. W., Soifer, B. T., Hao, L., Higdon, J. L., Higdon, S. J. U., Houck, J. R., Le Floch, E., Brown, M. J. I., Dey, A., Jannuzi, B. T., Rieke, M., Desai, V., Bian, C., Thompson, D., Armus, L., Teplitz, H., Eisenhardt, P., & Willner, S. P. 2006b, *ApJ*, 651, 101
- Westera, P., Lejeune, T., Buser, R., Cuisinier, F., & Bruzual, G. 2002, *A&A*, 381, 524
- White, S. D. M. & Frenk, C. S. 1991, *ApJ*, 379, 52
- White, S. D. M. & Rees, M. J. 1978, *MNRAS*, 183, 341
- Wilson, C. D., Petitpas, G. R., Iono, D., Baker, A. J., Peck, A. B., Krips, M., Warren, B., Golding, J., Atkinson, A., Armus, L., Cox, T. J., Ho, P., Juvela, M., Matsushita, S., Mihos, J. C., Pihlstrom, Y., & Yun, M. S. 2008, *ArXiv e-prints*, 806
- Yan, L., Helou, G., Fadda, D., Marleau, F. R., Lacy, M., Wilson, G., Soifer, B. T., Drozdovsky, I., Masci, F., Armus, L., Teplitz, H. I., Frayer, D. T., Surace, J.,

- Storrie-Lombardi, L. J., Appleton, P. N., Chapman, S., Choi, P., Fan, F., Heinrichsen, I., Im, M., Schmitz, M., Shupe, D. L., & Squires, G. K. 2004, *ApJS*, 154, 60
- Yan, L., Sajina, A., Fadda, D., Choi, P., Armus, L., Helou, G., Teplitz, H., Frayer, D., & Surace, J. 2007, *ApJ*, 658, 778
- Yang, M. & Phillips, T. 2007, *ApJ*, 662, 284
- Younger, J. D., Omont, A., Fiolet, N., Huang, J., Fazio, G. G., Lai, K., Polletta, M., Rigopoulou, D., & Zylka, R. 2009, *MNRAS*, 394, 1685
- Zirm, A. W., van der Wel, A., Franx, M., Labbé, I., Trujillo, I., van Dokkum, P., Toft, S., Daddi, E., Rudnick, G., Rix, H.-W., Röttgering, H. J. A., & van der Werf, P. 2007, *ApJ*, 656, 66